

UNIVERSITY OF READING

Deborah Josie Putt

Northern hemisphere snow: measurement,  
modelling and predictability

A Thesis submitted for the degree of Doctor of Philosophy

Environmental Systems Science Centre

September 2008

# Declaration

I confirm that this is my own work and the use of all material from other sources has been properly and fully acknowledged.

D.J.Putt

# Abstract

Northern hemisphere snow water equivalent (SWE) distribution from remote sensing (SSM/I), the ERA40 reanalysis product and the HadCM3 general circulation model are compared. Large differences are seen in the February climatologies, particularly over Siberia. The SSM/I retrieval algorithm may be overestimating SWE in this region, while comparison with independent runoff estimates suggest that HadCM3 is underestimating SWE. Treatment of snow grain size and vegetation parameterizations are concerns with the remotely sensed data. For this reason, ERA40 is used as ‘truth’ for the following experiments. Despite the climatology differences, HadCM3 is able to reproduce the distribution of ERA40 SWE anomalies when assimilating ERA40 anomaly fields of temperature, sea level pressure, atmospheric winds and ocean temperature and salinity. However when forecasts are released from these assimilated initial states, the SWE anomaly distribution diverges rapidly from that of ERA40. No predictability is seen from one season to another. Strong links between European SWE distribution and the North Atlantic Oscillation (NAO) are seen, but forecasts of this index by the assimilation scheme are poor. Longer term relationships between SWE and the NAO, and SWE and the El Niño-Southern Oscillation (ENSO) are also investigated in a multi-century run of HadCM3. SWE is impacted by ENSO in the Himalayas and North America, while the NAO affects SWE in North America and Europe. While significant connections with the NAO index were only present in DJF (and to an extent SON), the link between ENSO and February SWE distribution was seen to exist from the previous JJA ENSO index onwards. This represents a long lead time for SWE prediction for hydrological applications such as flood and wildfire forecasting. Further work is required to develop reliable large scale observation-based SWE datasets with which to test these model-derived connections.

# Acknowledgements

Firstly I would like to acknowledge my supervisors, Robert Gurney and Keith Haines, for their support and input into this thesis from the start. The Grid for Coupled Ensemble Prediction project, to which this PhD is tied, has been funded by an e-science grant from the Natural Environment Research Council. The support of NERC has been invaluable, both financially, and in giving me the opportunity to take courses such as GRAD which have added enormously to my experience over the past three years.

I would like to acknowledge the National Snow and Ice Data Center who have been the source of many datasets used in this thesis, most importantly the Global Monthly SWE Climatology. ERA40 data was provided by Kevin Hodges at ESSC. Running the model would not have been possible without the help and persistence of the rest of the GCEP group, especially Chunlei Liu, Alan Iwi and Doug Smith.

I am grateful to Jim Foster, Ed Kim and all the Hydrology branch at NASA Goddard for the opportunity to visit them for 2 weeks during this thesis. Similarly I would like to thank Phil Arkin and Matt Sapiano of the Earth Systems Science Interdisciplinary Center, University of Maryland, for inviting me to give a seminar. I would also like to thank Marco Tedesco for the first invited conference talk of my career, at the European Geophysical Union General Assembly in 2008.

My thanks also go to all at ESSC for being an approachable and enthusiastic community to work in; almost everyone has made a contribution to this thesis through helpful comments, and questions both asked and answered. I would also like to acknowledge the continuing support of my monitoring committee: Liz Morris, Anne Verhoef and Lennart Bengtsson.

Finally I must also thank my fiancé Matt, who has shown unceasing interest in and enthusiasm for my research, which has kept me on track for the last 3 years.

The more it snows  
*(Tiddely pom)*  
The more it goes  
*(Tiddely pom)*  
The more it goes  
*(Tiddely pom)*  
On snowing.

And nobody knows  
*(Tiddely pom)*  
How cold my toes  
*(Tiddely pom)*  
How cold my toes  
*(Tiddely pom)*  
Are growing.

Early discourse on the predictability of snowfall and its consequences, from A.A. Milne's 'The House at Pooh Corner', 1928.

# Chapter 1

## Introduction

### 1.1 Why is snow important?

Snow has an important role in the Earth's climate, as it is part of both the surface energy and water balances. The presence or absence of snow accounts for the largest change in surface albedo on both seasonal and interannual timescales (Bagnoud et al., 2005). A snowpack insulates the ground, keeping the top layer of soil relatively warm. Snowmelt, and the associated latent heat flux, also significantly affects the surface energy balance. The influence of snow is not limited to those areas in which it falls; snowmelt often feeds rivers that are vital in providing water to more arid areas (Frei et al., 2005). The atmosphere also takes up moisture from snowpacks through sublimation.

Snow is an important component in terrestrial water storage, and for water resources, both for drinking water and industry. It is estimated that snow accounts for 10% of mean continental water storage globally, and 16% of the interannual variability (Guntner et al., 2007). Examples of the economic importance of snow in the USA were presented by Carroll et al. (2003). The largest surface water user in the US is manufacturing, and the contribution of snow to US manufacturing revenue was estimated as \$1.6 trillion annually. Agriculture is dependent on snowmelt for irrigation, which supports a net US revenue exceeding \$33 billion annually. 10% of the USA's electricity is provided by hydropower, 30% of which comes from snow. Snow also supplies water estimated as worth about \$25 billion to the coal-fired, oil-fired and nuclear power plants that supply the rest of the country's electricity demands.

The importance of studying snow, and the wider cryosphere, has been underlined in several reports. The IPCC Fourth Assessment Report (Randall et al., 2007) highlights the magnitudes of cryospheric feedbacks as a crucial uncertainty in determining climate sensitivity. Priority hydrological science questions for the first decade of

the 21st century were set out in Entekhabi et al. (1999), and included, “What are the mechanisms and pathways by which the coupling between surface hydrologic systems and the overlying atmosphere modulate weather and climate variability?”. Important contemporary issues such as global environmental change, an increasing population’s access to drinking water, risks from flooding, wildfire and drought, all require an understanding of the role of snow in the Earth system. Spatially continuous observations of many land surface elements, particularly snow, are now becoming available on global scales, and the strengths and limitations of both the observations and the models must be understood in order to exploit them appropriately, and potentially to produce useful long term forecasts.

The Grid for Coupled Ensemble Prediction (GCEP) project was funded as part of the Natural Environment Research Council’s e-Science programme, and uses cluster computing to investigate seasonal to decadal prediction. While the the upward trend in global temperatures with climate change is the dominant forcing over centuries, natural variability can have more impact on seasonal to decadal timescales. This thesis compares output from GCEP climate model runs with observations, to gain understanding of large scale snow and its predictability on these timescales.

## 1.2 Hypotheses and approach

The main aims of this project are:

- To investigate the variability of Northern hemisphere snow data as observed by satellites
- To investigate the variability of Northern hemisphere snow data as modelled by a general circulation model
- To understand the differences between the observed and modelled snow distributions
- To assess the ability of a general circulation model to reproduce observed snow anomalies
- To assess the predictability of snow anomalies

The hypotheses are as follows:

1. Information on the distribution of snow in the Northern hemisphere can be reliably obtained from remote sensing and GCMs

2. Snow distribution in coupled models will be better forecast from an initial state that is constrained by observations of fields such as surface temperature.
3. Seasonal forecasts of snow anomalies can be made with knowledge of large scale patterns of climate variability such as the El Niño-Southern Oscillation

### 1.3 Chapter summary

- Chapter 2 introduces the concepts used in the thesis.
- Chapter 3 describes the theory and practice of measuring snow distribution at large scales, with emphasis on remote sensing using passive microwave radiometers. EOF analysis is applied to the remotely sensed snow product to assess interannual variability.
- Chapter 4 describes the modelling of snow at large scales, concentrating on the land surface component of the general circulation model HadCM3. Runs of the climate model, performed at ESSC, are investigated and compared to previous studies. The concept of reanalysis, and the reanalysis product ERA40, are introduced.
- Chapter 5 compares the measured and modelled snow distribution, assessing the reasons for any differences between them. Many other remote sensing and modelling studies are referenced. A study of runoff generated by HadCM3 (performed by researchers at the Met Office) is used as a further comparison.
- Chapter 6 uses data assimilation to reproduce snow anomalies with HadCM3. The experiments and all the analysis were performed at ESSC.
- Chapter 7 uses a multi-century run of HadCM3 to assess potential snow predictability. This multi-century run and the analysis of it were performed at ESSC.
- Chapter 8 draws together the conclusions of this work and makes suggestions for future studies.

# Chapter 2

## Background

The material in this chapter provides context and general background information on the work that will be presented in this thesis. First, the challenges of investigating snow at large scales are introduced. This is followed by discussion of seasonal forecasting and predictability, together with the definition of some large-scale climate modes used in later chapters. The interactions between snow and atmospheric dynamics are then discussed, followed by an introduction to general circulation models, and the representation of these interactions within them. Finally, remote sensing is presented as a means of making observations at large scales, and data assimilation is introduced as a way of combining these large-scale data with climate models.

### 2.1 Investigating snow at large scales

While many studies of snow are at field or catchment scale, snow has an important role at larger scales, both hydrologically and as part of the climate system. Water stored as snow is an important component of the hydrological cycle on regional to global scales, but is poorly characterised due to a lack of large scale information. Much of the impact on climate comes from the high albedo of snow-covered surfaces, with the exact value depending on the snowpack's colour, age, depth, wetness and grain size. Additional effects include the snowpack's insulating properties, keeping the top layer of soil relatively warm. Heat flux from the soil to the snow is small, although it can have a cumulative effect on the timing of melt. This snowmelt not only affects river discharge, but also significantly affects the surface energy balance, through the associated latent heat flux.

Many snow properties can be measured, including depth, extent, grain size, albedo and density. Here we are considering depth measurements, but even still there is a choice: snow depth or snow water equivalent (SWE)? The former is simply the distance

from the ground surface to the top of the snowpack, while the latter is the amount of water that the snowpack would produce if melted. The two are related by the snow density. The latter is the more widely-used variable in water resource forecasting and land surface models (as it is equivalent to lying snow in  $\text{kg m}^{-2}$ ) and is the variable considered in this thesis.

Snow is highly variable both spatially (laterally and through the depth of the snowpack) and temporally. While snow extent datasets are available and have been well-studied, snow depth variability is less well understood. Gong et al. (2004) showed that depth anomalies are as important as snow extent anomalies in affecting atmospheric circulation. They perform three sets of ensemble experiments with a GCM, one with both snow cover and depth forcing, one eliminating the snow depth forcing, and one suppressing the surface albedo change due to the presence of snow. Their analysis of the surface energy balance in each of the cases shows that snow depth anomalies are important in local and remote feedbacks, and not purely due to an increased albedo, as other thermodynamic mechanisms such as thermal conductivity, thermal emissivity and phase changes are significant.

Ge and Gong (2008) showed that this large scale snow depth variability cannot be inferred from snow extent variability, as is often done, for instance by using empirical snow depletion curves that link SWE to snow extent. They even suggest that previous results linking spring snow extent with summer climate (see discussion below) may actually follow instead from winter snow depths influencing summer climate.

Many of the physical properties of snow are dependent on the size and shape of the snow grains, which are usually expressed as a snow grain radius which can vary from 0.1 to 10mm, and is referred to simply as the ‘grain size’. However, in reality the snow grains are irregular, with shapes ranging from dendritic, to quasi-spherical, to large, faceted crystals (Domine et al., 2006). While alternative approaches to a catch-all ‘grain size’ have been explored, such as surface area to volume ratios, or the specific surface area (surface area per unit mass), it is the grain size approach that persists both in snow modelling and retrieval algorithms for the interpretation of remotely sensed data.

The density, albedo, conductivity, depth of light penetration and amount of wind transport all depend on the grain size, which itself can be transformed by settling and metamorphism (Jones et al., 2001). The size of freshly fallen snow grains will hence be different to those in a mature snowpack. Large vertical temperature gradients exist in snowpacks, as the low thermal conductivity of snow means that the soil temperature stays high when the air temperature above the snowpack is low. This temperature gradient is the main driver for metamorphism in dry snow, with the resulting size and

shape of the crystals depending on the strength of the gradient. With a temperature gradient of less than  $5^{\circ}\text{C m}^{-1}$ , the grains will tend to be small and rounded, whereas a gradient higher than  $15^{\circ}\text{C m}^{-1}$  will drive the formation of quick-growing depth hoar crystals (Jones et al., 2001).

Unfortunately, grain size is very difficult to measure in the field, and almost impossible over large areas. An alternative approach is to classify snowpacks in different regions according to their various characteristics, which can then be related back to measurable fields such as temperature and windspeed. A commonly-used classification of seasonal snow covers is that proposed by Sturm et al. (1995). The six classes are defined on the basis of their textural and stratigraphic properties including the thickness of snow layers, their density, crystal morphology and grain characteristics. The Sturm classes are:

- Tundra: thin, cold, wind-blown snow, usually above or north of the tree line. The layers consist of a basal depth hoar overlain by wind slabs. Max depth  $\approx$  75cm.
- Taiga: thin to moderately deep low density cold snow cover. Present in cold forest areas with low wind and initial snow density. Up to 50-80% depth hoar by late winter covered by low density new snow. Max depth  $\approx$  120cm.
- Alpine: intermediate to deep cold snow cover. Often consists of alternate thick and thin layers, with basal depth hoar and wind crusts common. Max depth  $\approx$  250cm.
- Maritime: Warm, deep snow cover with melting features such as basal melting. Ubiquitous coarse grains due to wetting. Max depth can be greater than 300cm.
- Prairie: Thin, moderately cold snow cover with some deep drifts. Wind slabs common. Max depth  $\approx$  100cm.
- Ephemeral: Thin and extremely warm snow cover, which melts as soon as it falls, often replaced by the next snowfall.

Global maps of Sturm classes are available to guide algorithm design and interpretation. The maps are derived using an algorithm taking into account precipitation, temperature, wind speed and vegetation data. The Sturm classes have been widely used in the literature both as part of a variety of studies of remote sensing (Dong et al., 2005; Langlois et al., 2004; Josberger and Mognard, 2002; Hall et al., 2001), modelling (Liston and Elder, 2006; Strack et al., 2004; Slater et al., 2001) and reanalysis (Brown et al., 2003).

## 2.2 Climate indices and predictability

Advance information on the large-scale characteristics of the seasonal snowpack would be useful for many applications, such as predictions of streamflows for water resource management, and forecasts of the risk of wildfire and flooding. In order to produce this sort of long range forecast, the climate must demonstrate predictability.

The day to day variations in weather patterns follow from the chaotic behaviour of the atmosphere, but not all components of the climate system are as variable as the atmosphere on short time scales. The ocean circulation varies much more slowly, and has a strong influence on the atmosphere from below, mainly via the temperature of the sea surface. Knowledge of this sea surface temperature (SST) is therefore crucial in forecasting weather patterns, so if these temperatures are themselves predictable, there is potential for some information on future atmospheric states.

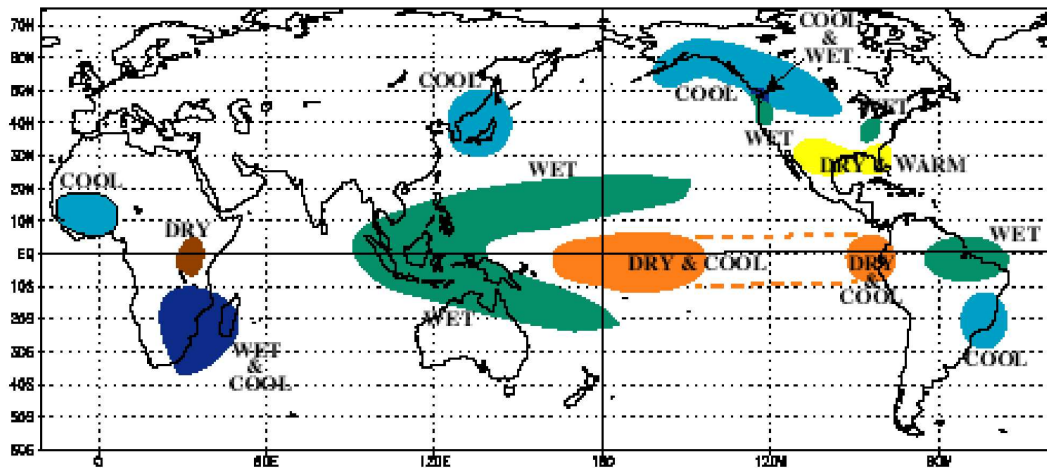
The best understood link between ocean variability and weather is the El Niño-Southern Oscillation (ENSO). Warmer than usual sea surface temperatures occur in the eastern tropical Pacific every 3 to 8 years, warming the globe and triggering a pattern of weather which brings droughts to some areas and floods to others. Forecasts of ENSO events can therefore provide important information on likely weather in the coming seasons. ‘El Niño’ is the name given to the positive phase, where tropical Pacific SSTs are warmer than average, and ‘La Niña’ refers to the negative phase, with cooler than average SSTs. In this thesis, ‘ENSO events’ includes both positive and negative phases.

Figure 2.1 shows that when La Niña conditions exist during the Northern hemisphere winter (DJF), cool and wet weather is brought to northwestern North America, with drier and warmer conditions in the south east of the continent. Cooler conditions are also seen over Japan and eastern China. The opposite is true in El Niño winters.

The strongest impacts of ENSO are in the Tropics, rather than the mid- to high latitudes where snow is more extensive. The variability in the Northern hemisphere, particularly during winter, is dominated by the North Atlantic Oscillation (NAO). Sometimes the storms track across northern Europe, bringing wet and windy weather to northern countries, while at other times the storms track south across the Mediterranean, making southern Europe wetter and northern Europe colder and drier. It is through forecasts of this oscillation index that average conditions for Europe in the coming months are usually predicted.

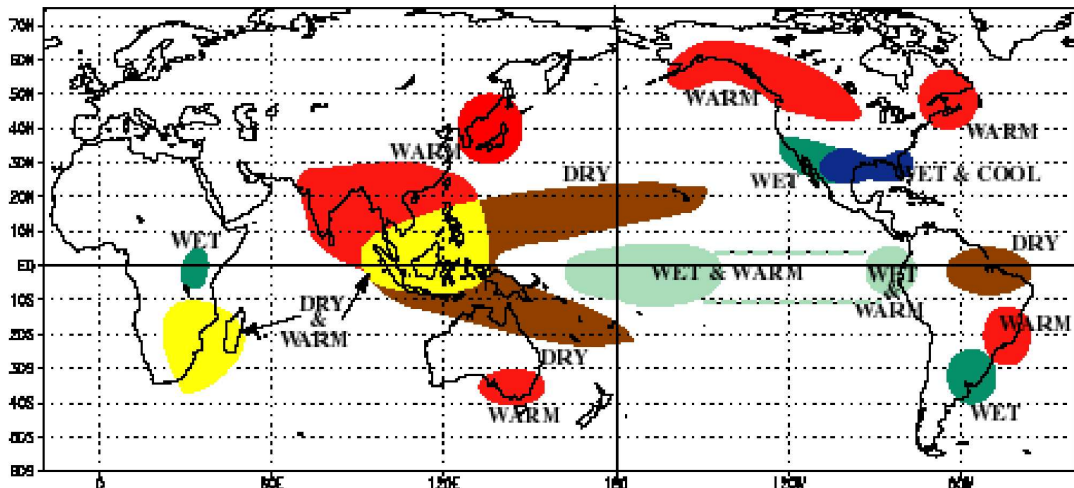
Figure 2.2 shows the impact of the different NAO phases on the weather of the North Atlantic. In the positive phase, the jet stream is drawn to the North, making

### COLD EPISODE RELATIONSHIPS DECEMBER - FEBRUARY



(a) La Niña

### WARM EPISODE RELATIONSHIPS DECEMBER - FEBRUARY



(b) El Niño

Figure 2.1: Effect of cold (upper) and warm (lower) ENSO episodes during Northern hemisphere winter (DJF).

Source: <http://www.ngdc.noaa.gov/paleo/ctl/images/>

northern Europe wetter and northeastern Canada colder, with reduced snow in the eastern United States. This pattern is reversed in the negative phase.

The related Arctic Oscillation (AO) has also received much attention as a potentially important mode of climate variability. It is identified as the first EOF of the mean sea level pressure field, and consists of an annular mode, with anticorrelated centres of action at mid- and high latitudes. Debate continues about the interpretation of these large scale modes, as to whether the NAO is the Atlantic signature of the more spatially extensive AO pattern, or whether the AO paradigm is misleading in indicating related behaviour between the North Atlantic and Pacific sectors, the NAO being a more physically robust index (Wallace, 2000; Deser, 2000; Ambaum et al., 2001).

Operational seasonal forecasting is an emerging area of research, with major operational centres such as the UK Met Office, the Climate Prediction Center in the United States, Environment Canada and the Australian Bureau of Meteorology now issuing seasonal forecasts to the public. However, the field is not new; potential links between Eurasian snow cover and the Indian summer monsoon have been investigated for over a hundred years. Blanford (1884) was the first to propose that the varying extent and thickness of snow could affect the thermal regime of the land and hence alter the onset of the Asian summer monsoon. This ‘Blanford hypothesis’ suggested a negative correlation between the snow in the Himalayas and rainfall in the plains of western India. Further correlations between monsoon strength and snow depth by Walker (1910) led to the adoption of Himalayan snow as an operational monsoon predictor by the Indian Meteorological Service until the 1960s, when it was removed after an extended period of poor performance. Interest in the topic was revived in the 1970s when Hahn and Shukla (1976) found an inverse relationship between Eurasian DJFM mean snow cover and monsoon strength. Many studies have followed which support this conclusion, although a lack of long term data means that the conclusions are rarely statistically significant, and many of the results are based on model, rather than observational, data. More recent studies using satellite observations of snow (e.g. Bamzai and Shukla (1999)) only find strong inverse correlations between Indian rainfall and climatic conditions in western Eurasia, remote from the areas studied previously. A study of the historical Soviet snow depth data record (Kripalani and Kulkarni, 1999) also finds an inverse correlation between snow depth in western Eurasia and Indian monsoon rainfall, but also sees a positive correlation between the rainfall and snow depth in Siberia. Robock et al. (2003) show that the relationship between all-India rainfall and North Atlantic variability in the 1880s supported some aspects of Blanford’s hypothesis. A similar link between SWE and the variability of the North American monsoon was performed by Zhu et al. (2005). Despite testing several

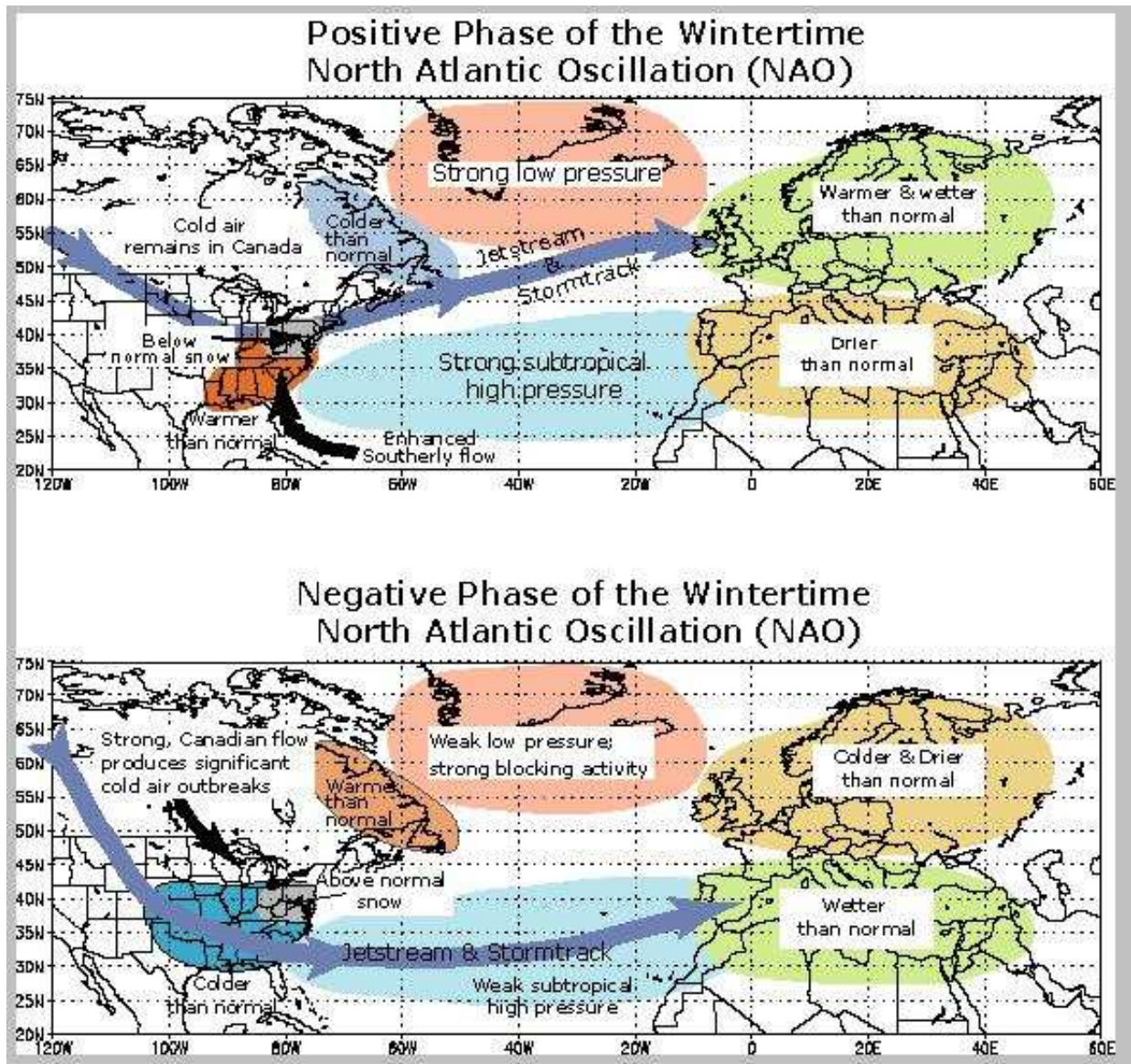


Figure 2.2: Effect of positive (upper) and negative (lower) NAO index on North Atlantic winter climate.

Source: <http://www.ncdc.noaa.gov/paleo/ctl/clisci100.html>

hypothesised mechanisms linking SWE with the following year's monsoon, via changes in soil moisture content, no stable relationship between the two was found. A study using NOAA/NESDIS satellite snow cover data by Fasullo (2004) found that negative correlations between snow cover and monsoon rainfall were robust and statistically significant only in weak ENSO years. The findings suggest that the Blanford hypothesis is correct, but the effect is overwhelmed during ENSO events.

## 2.3 Snow and the atmosphere

While it is the long timescales in the ocean that have received the most attention for seasonal to decadal forecasting, slowly-varying water storage variables like snow and soil moisture may also exhibit predictability at longer timescales. Anomalies of these variables could potentially persist for weeks or even months, acting as a source of 'memory' within the climate system, and be able to drive the atmosphere in a predictable way by controlling the surface temperature and fluxes of energy and water.

The presence of snow has a direct effect on the energy balance at the surface, and hence the surface temperature: the high albedo can reduce the solar energy available to heat the atmosphere by 50% (Foster and Chang, 1993). Snow can induce strong temperature inversions in the boundary layer by absorbing energy via melting or sublimating the snowpack (Marshall et al., 2003), with the impact of the high albedo most noticeable in spring when snow cover is still extensive but insolation is high (Groisman et al., 1994). As it cools, the thickness of the air mass is reduced, causing an atmospheric trough which can lead to persistence of the snow cover (Derksen et al., 1997). This is one proposed mechanism by which snow information can be exploited for longer term forecasting.

Marshall et al. (2003) set up a series of ensemble experiments with a general circulation model to investigate the persistence and predictability of snow cover in the western United States. The experiments were of two forms: the initial state was either an extreme anomaly across the experimental domain, or a particularly high or low instance of snow cover taken from a previous model run. Ensembles were created by imposing the atmospheric state from a series of different days onto the start conditions. Experiments were started in December and February and run for a season. Their results suggest that in order to predict the coming snow cover, the initial snow cover is much more important than the initial atmospheric state for runs beginning in February. Results for December are less clear-cut, as a low snow anomaly in December does not inhibit the accumulation of snow as the season progresses. However, the snow state is shown to be more important than the atmospheric state for the maintenance

of a snow extent anomaly, suggesting the presence of memory in the snow cover which could be used for medium-range prediction.

Leathers and Robinson (1993) show that the presence of positive snow extent anomalies in the United States leads to negative anomalies in surface temperature, modifying the air mass above and extending a temperature anomaly far to the south, often as far as the Gulf of Mexico. Clark and Serreze (2000) demonstrate that snow extent anomalies in east Asia show little persistence, so knowledge of anomalies in this area is more suited to short range range than interseasonal forecasts. However, they also find that relatively small snow extent anomalies in east Asia are associated with large and significant changes in downstream circulation, suggesting that signals associated with these short-term snow extent anomalies are amplified by the atmosphere. By examining NOAA snow charts and NCEP-NCAR atmospheric reanalysis fields, they suggest that these model-derived associations between snow extent and circulation are present in observations.

Yang et al. (2001) investigate the relationship between snow cover and ENSO over North America. The paper uses a suite of atmospheric general circulation model experiments to assess how the continental surface temperature response is modulated through snow-albedo feedback. They find that the response of the surface to ENSO is magnified by local feedbacks, particularly at midlatitudes where there is sufficient winter insolation and variability in snow amount to result in a significant change to the surface energy balance. They emphasise that both the parameterization of albedo and the initialisation of snow depths are therefore important in seasonal-to-interannual climate predictions.

Cohen and Entekhabi (1999) propose that anomalous snow cover in the Northern hemisphere is influential in the Northern hemisphere wintertime general circulation, and that it affects extratropical storm tracks. Investigation of snow cover with various climate indices showed that Eurasian snow cover showed stronger correlations with the climate indices than did North American or Northern hemisphere snow cover. An empirical orthogonal function (EOF) analysis of Eurasian snow cover with observed 500mb heights over a 23 year period produced the North Atlantic Oscillation (NAO) and Pacific North American (PNA) mode as the first two modes of variability. The authors went on to find that Eurasian SON snow cover correlated more strongly with the DJF 500mb heights than did the DJF snow cover. This suggests that early season snow cover could be forcing the atmosphere, and hence could be used as a predictor of the Northern hemisphere winter climate. A mechanism for this coupling is suggested by Cohen et al. (2007). By examining NCEP-NCAR reanalysis data, they found that Eurasian snow anomalies in October can influence sea level pressure in January, via the

vertical component of lower-stratospheric wave activity. Extensive October snow causes a upward-propagating tropospheric wave which interacts with the polar stratosphere, which in turn leads to high geopotential heights at the surface in January. A schematic of this proposed mechanism is shown in figure 2.3. Fletcher et al. (2007) subsequently show that a weak polar vortex is required for this coupling.

Gong and Entekhabi (2002) perform two ensemble experiments to determine the effect of snow perturbations on the Arctic Oscillation. One experiment has monthly climatological SSTs, sea ice and snow mass, whereas in the other experiment snow is allowed to evolve. Both ensembles contained twenty members each beginning on 1 September, with the initial conditions coming from a 20-year control integration. They show that in the fixed experiment, the atmosphere still exhibits the classic AO dipole structure, supporting the hypothesis that this mode arises through internal climate processes, not external forcing from the land or sea surface. However, the difference between the free and fixed experiments shows that some enhancement of the AO-NAO occurs with the variable snowpack, with relatively stronger climate variability over Siberia and the North Atlantic.

Gong et al. (2003) perform two ensemble experiments to assess the effect of realistic Siberian snow anomalies on Northern hemisphere winter climate. They find that a positive SWE and extent anomaly over Siberia results in a statistically significant decrease in the winter AO mode throughout the atmosphere. However, the magnitude of the atmospheric response is only a third of that seen in observational studies. This underestimation may be due to the poor stratospheric resolution in the model used (ECHAM3) which inhibits the response of the atmosphere to the Siberian anomalies. The experiment was then extended to examine the model response to North American snow anomalies (Gong and Entekhabi, 2003), where it was shown that an anomaly of comparable extent in North America does not have the same AO response as the Siberian anomaly. This difference is ascribed to the different activity of the atmosphere over North America, and supports the assertion that Siberia is a particularly important region for snow-forced winter climate variability.

Foster et al. (1983) also find differences in the temperature response of the continents to snow cover anomalies: autumn snow cover and winter temperature are more correlated over Eurasia, while winter snow cover and winter temperature are more correlated over North America. The authors explain that this is because of the greater continentality of Eurasia: the Siberian anticyclone is more pronounced and persistent because of the extensive area of snow cover that forms in the autumn over Siberia, and so there is a longer-lasting impact on circulation.

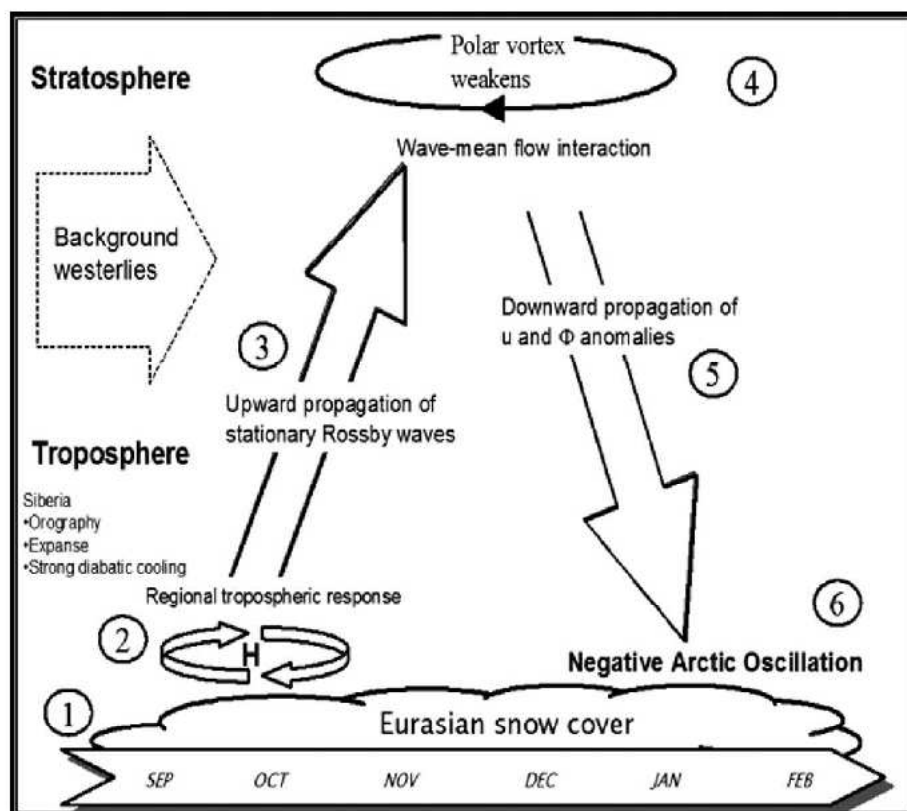


Figure 2.3: Schematic and text from Cohen et al. (2007), figure 6: Conceptual model for how autumn snow cover modifies winter circulation in both the stratosphere and the troposphere; case for extensive snow cover illustrated: 1) Snow cover increases rapidly in the fall across Siberia, when snow cover is above normal. 2) Diabatic cooling helps strengthen the Siberian high and leads to below normal temperatures. 3) Snow-forced diabatic cooling in proximity to the high topography of Asia increases upward flux of wave activity from the troposphere, which is absorbed in the stratosphere. 4) Strong convergence of the Wave Activity Flux leads to higher geopotential heights, a weakened polar vortex, and warmer temperatures in the stratosphere. 5) Zonal mean geopotential height and wind anomalies propagate down from the stratosphere into the troposphere all the way to the surface. 6) Dynamic pathway culminates with strong negative phase of the Arctic Oscillation at the surface.

## 2.4 General circulation models and land-atmosphere coupling

To perform experiments of the sort described above, scientists require large scale models. A general circulation model, or GCM, is a three-dimensional computer model of the major components of the climate system. An atmospheric-GCM (AGCM) is a model of the atmosphere, with boundary conditions provided by SSTs and the land surface (often an interactive land surface model). A coupled atmosphere-ocean-GCM (AOGCM) is an AGCM fully coupled to an ocean model. GCMs are used both to predict the climate and to investigate the complex interactions within it. Much effort has focussed on accurately modelling the oceans, particularly the tropical Pacific, which is critical in obtaining good seasonal predictions of the ENSO phenomenon.

As such, there has been little research into the sensitivity of the modelled climate to the representation of the land surface, and the land surface components themselves are generally very crude. The land surface is an important part of coupled climate models, not merely in providing boundary conditions for the atmosphere but also because it is the part of the earth system that we, as humans, have most interaction with. As such, forecasts of land surface conditions are particularly important and relevant economically and politically, especially when examining impacts from climate change scenarios.

The recent fourth assessment report by the Intergovernmental Panel on Climate Change (IPCC) highlights the main advances in the development of coupled models in recent years: the model dynamics have improved, including increased horizontal and vertical resolutions, the physical parameterizations have been improved, and more processes have been added, in particular with respect to aerosols, sea ice and the land surface (Randall et al., 2007). However, there have been few studies assessing the capability of land surface models in GCMs, which the report ascribes in part to a lack of suitable observations. This has implications for the reliability of predictions under climate change scenarios, especially as the magnitude of cryospheric feedbacks are uncertain, which contributes to the range of model responses at mid- to high latitudes. It is often assumed (Jones et al., 2001; Brown, 2000; Frei et al., 2003) that increased surface temperatures with climate change produce a positive feedback effect, with reduced snow cover due to warming resulting in increased absorption of more incident radiation and hence more warming, and vice versa. However, Cess et al. (1991) argue that this is too simplistic an assumption, and that by including cloud interactions and longwave feedback the sign of the overall feedback can be reversed.

As described in the previous section, feedbacks between snow and the atmosphere

have been the subject of both observational and model studies, which could have important implications for seasonal to interannual predictions. For this predictability to exist within a certain model, the atmosphere must be responsive to anomalies in the land surface. The degree of responsiveness is referred to as the ‘coupling strength’ between the land surface and the atmosphere. As coupling strength has not been determined in reality, it is only the relative strength between different models that can be compared (Koster et al., 2002).

While snow, and the boreal winter in general, has not been studied in this context, there have been many recent investigations using summer soil moisture. It is hypothesised that precipitation anomalies could be transmitted back to the atmosphere through the increased evaporation following a rainfall event that has increased the moisture content of the soil. Koster et al. (2002) perform a set of AGCM experiments designed to test the strength of land-atmosphere coupling across the globe in boreal summer. For each of four models, a 16-member ensemble of runs each lasting one month were run with prescribed SSTs, where the atmospheres were initialised independently and allowed to evolve. A corresponding set of ensemble runs were then made, but with the land surface of each member updated at each time step with conditions from one of the previous freely-evolving runs. In this way, the effect of the land surface conditions could be isolated from the SST forcing. By comparing the difference in precipitation across the two ensembles, an estimate of the strength of land-atmosphere coupling was obtained.

A further examination of land-atmosphere coupling was made by Dirmeyer (2005). A series of ensemble experiments, with different initialization schemes and flux replacement (with observed fluxes), were carried out to assess the role of the land surface in communicating climate anomalies back to the atmosphere. The results show that due to errors in downward fluxes, the climate model’s land surface state drifts sufficiently after a month to ‘forget’ the soil moisture initial conditions, and that only in arid areas do anomalies in initial soil wetness persist without flux replacement. Hence systematic errors in the atmospheric model which generates these fluxes will lead to an insensitivity to the land surface initialisation.

The impact of land surface conditions on the atmosphere also depends on the model orography: Sobolowski et al. (2007) find that the representation of North American orography in the ECHAM3 GCM affects how snow cover anomalies in North America impact circulation over Eurasia. A series of experiments in which the mountains in North America were removed showed a pronounced reduction in the response of the sea level pressure field to snow anomalies. This implies a nonlinear coupling between

snow forcing and orographic forcing of the atmosphere, both of which will need to be well-represented in a GCM to produce realistic responses to snow distribution.

## 2.5 Remote sensing and data assimilation

As noted in the IPCC report, the main obstacle to improving the land surface components of GCMs is the lack of suitable land surface data. It is logistically and economically impossible to use in situ data to provide spatially and temporally continuous monitoring of climate variables such as snow. An important advance in the second half of the twentieth century was the ability to monitor the Earth from space, using instruments mounted on satellites.

Most spaceborne instruments are measuring the energy fluxes from the Earth's surface and atmosphere. As the temperature of the Earth is above absolute zero it emits some amount of radiation at all frequencies. A radiometer measurement is generally expressed as a brightness temperature  $T_B$ , which is a function of the physical temperature of the scene and the emissivity of the various components within that scene. The radiation arriving at the radiometer can be decomposed into two orthogonal components: horizontally polarized, or parallel to the plane of incidence, and vertically polarized, perpendicular to the plane of incidence.

Some frequencies are more appropriate to viewing the surface, while others provide information on different layers in the atmosphere. Of those channels that 'see' the surface, different frequencies are sensitive to different land surface components. Measurements have been made at frequencies appropriate for obtaining snow information for several decades, while instruments that could measure frequencies responsive to changes in soil moisture are yet to be launched. This is part of the motivation for this thesis: while both snow and soil moisture show potential for exploitation in seasonal forecasting, it is only snow that has a time series of measurements long enough to use for this purpose.

A different type of remote sensing campaign, which has also been proposed as a source of snow information, is the Gravity Recovery and Climate Experiment (GRACE; Tapley et al. (2004)). Twin satellites, launched in 2002, make detailed measurements of the Earth's gravity fields. Changes in this field are due, in part, to mass variations on the Earth's surface, including changes in continental water storage (Guntner et al., 2007). However, isolating the contribution of SWE variations to this integrated measurement will be a challenge, in particular the difficulty in untangling the seasonal cycles. For instance, in snow-dominated river areas, the seasonal cycle of groundwater storage is opposite to that of total water storage, which is dominated by the snow.

Obtaining snow estimates is therefore difficult without accurate information on the other components of total water storage such as groundwater, which are currently unavailable.

The most widely-used snow products from remote sensing are snow cover datasets from visible-band sensors and SWE/snow depth/snow mass from microwave radiometers. The former are more numerous, and more accepted within the scientific community as reliable datasets for validation than the SWE datasets. However, without this depth information, satisfactory forecasts will be impossible. It is also important to bear in mind that although a SWE (or air temperature, or rainfall, etc.) dataset is provided, the radiometer is only ever measuring energy fluxes, and the SWE ‘measurement’ is derived using a model based on assumptions about how SWE affects the radiation reaching the satellite.

One way of exploiting a spatially extensive observational product is through assimilation into a spatial model. There are many techniques that have been developed for data assimilation. The simplest method is direct insertion, where model fields are replaced by observed fields. This method is used by Rodell and Houser (2004), who argue that by inserting snow extent data into a land surface model they can produce accurate, high resolution maps of snow water equivalent in near-real time. The land surface model that they use in their study, Mosaic, has explicit subgrid-scale variability but a simple snow formulation. Snow cover in the model is updated daily using remotely sensed snow extent data. They find that their updating scheme is good at removing superfluous snow, but only rarely adds additional snow. This is explained by the fact that the updates began on 1 January, once the snowpack was already established, and the fact that in their scheme an added layer of snow was only 5mm thick, and would quickly melt away if the surface temperature remained above freezing. They suggest that a more sophisticated updating scheme involving SWE observations, or coupling the land surface model to an atmospheric model, could improve results.

However, this direct insertion method assumes that the observations are perfect, and that the model-generated fields contain no useful information, which is not necessarily true. It can also introduce biases in other state variables which have to adjust to the newly inserted information. More sophisticated methods of incorporating data into a model have also been developed, such as the Kalman filter and variational methods, which account for the relative confidence in the modelled and observed fields (Walker et al., 2003). These approaches usually rely on continuous relationships between model states and observations which are not always appropriate, depending on the model used. They also require comprehensive analysis of the errors in both the model and the observations.

Sun et al. (2004) use a Kalman filter to assimilate synthetic SWE ‘observations’. They present and demonstrate a methodology, though do not propose a treatment of the observation and model biases, which they note is an important task for the future. Their results suggest that the assimilation of SWE data improves model state variables, and the fluxes of energy and water, and can negate the effect of poor initial condition data. Recently, this Kalman filter approach has been applied to real remotely sensed SWE data. Dong et al. (2007) use an error analysis of the observed SWE to inform the method of Sun et al. (2004) described above. Assimilation improves simulation of SWE in the land surface model, so that SWE estimates from the assimilation showed better agreement with station data than either the modelled or observed states alone.

Assimilation of remotely-sensed SWE data into models is at an early stage, and the success of the approach will be highly dependent on the quality of both the observations and the models. Schlosser and Mocko (2003) suggest that improvements to the physical parameterizations within GCMs need to be made before all the advantages of including snow observations can be realized. They performed a pair of experiments with the COLA and GEOS GCMs to investigate the impact of snow conditions on seasonal prediction. Pairs of runs starting in each of the years from 1982-1998 are run from March to June, one with prescribed snow from a daily, global snow depth analysis, and one where the snow is allowed to evolve interactively. The results show that the prescribed snow has a positive effect on the local climate, reducing errors in near-surface air temperature, but that this improvement in skill was not transferred to non-local effects. They suggest that this highlights the problems of parameterization in GCMs, as to generate a realistic non-local response to snow forcings requires the ability to represent boundary layer processes such as advection.

A Kalman filter approach was recently used by Andreadis and Lettenmaier (2006) to assimilate remotely sensed SWE data into a macroscale hydrology model, but the output appeared to be dominated by retrieval errors. Foster et al. wrote in 1996 that SWE retrievals needed to improve before this remotely-sensed data could be assimilated into GCMs; clearly there still need to be further improvements in the method of obtaining SWE data from space in order to exploit it fully in GCMs.

## 2.6 Summary

Snow is a complex and highly variable component of the land surface water and energy balances. Many snow properties depend on its crystal structure, commonly parameterized using a ‘grain size’, which is difficult to measure in the field.

Snow has been suggested as playing a role in the large scale circulation of the atmosphere, which could be exploited for seasonal forecasting. Much of the impact comes from the high albedo, although other effects such as the insulation of the ground and latent heat fluxes associated with snowmelt are also important. The importance of these other factors illustrate the fact that it is the depth of snow on the ground, rather than its mere presence, that can have an influence on the atmosphere.

Siberia in particular has emerged as an influential area in the wintertime circulation, and differences in the atmospheric response to snow anomalies over North America and Eurasia have been demonstrated. It is this large scale behaviour, and the fact that the continental snow distribution will be influenced by large scale climate modes such as ENSO, that requires an appreciation of the distribution of, and variability of, snow across the whole Northern hemisphere.

Large-scale snow information is therefore required to understand the role of snow in the circulation, and the impact of circulation changes upon snow distribution. The two main sources of information at these scales are remote sensing and general circulation modelling. The development of better land surface models is hampered by the lack of large scale observations. While remote sensing observations appropriate to retrieving snow data have been gathered for many years, the observations appear dominated by retrieval errors. Better understanding of both model and retrieval is required to exploit both fully and close the cryosphere feedback loop.

This thesis examines the distribution of SWE at hemispheric scale, from both remotely sensed observations and general circulation models. It is hypothesised that a better understanding of this SWE distribution would lead to better seasonal and decadal predictions.

# Chapter 3

## Measuring snow at large scales

### 3.1 Introduction

In order to understand the climate system, and constrain and validate models at all scales, scientists require frequent, good quality observations. Ground-based snow measurements have been made at meteorological stations in many parts of the world, and time series of up to 100 years exist at certain locations (Derksen et al., 2004; Jones et al., 2001). In the last half of the 20th century, observations of snow began to be obtained from satellites, providing more complete spatial and temporal coverage than was possible with ground stations.

This chapter briefly describes some techniques for measuring snow in situ, before considering the main measurement method in this work, satellite remote sensing. While in situ measurements can provide detailed measurements at a point, the only way to gather large scale near-simultaneous observations is with remote sensing. The two main snow properties that are regularly derived from satellite measurements are snow extent (also referred to as snow-covered area, or SCA) and snow water equivalent (SWE). Methods for retrieving both snow extent and SWE information are introduced, and the limitations of each are described. Finally the remotely sensed snow product used in this thesis is introduced and a first analysis is performed, using empirical orthogonal functions (EOFs). This method is used both to assess the noise and spatial coherence within the data, and investigate patterns of interannual variability.

### 3.2 In situ monitoring

Measurements of snow depth can be made in situ, using rulers, fixed snow stakes and snow boards. Measurements of SWE can also be made in situ, for instance by melting a sample or by weighing it and using a measured or assumed density to calculate the

water equivalent. In situ measurements are subject to a number of errors: systematic biases can be introduced through the measurer's choice of location (with respect to topography, vegetation density, ease of access etc.), and any error in the measuring process. Furthermore, a point measurement, although accurate for that locality, is not always representative of a wider area. Snow is particularly variable on relatively small spatial scales. Trujillo et al. (2007) measured snow depths in five 1km<sup>2</sup> areas, and found that this spatial variability was driven by the interaction of the wind with surface features and vegetation, or by vegetation when wind redistribution was minimal. This leads to characteristic scales of variability of 15m or less.

Scaling point measurements up to provide large scale gridded products will always be subject to sampling errors, because of this large spatial variability. Chang et al. (2005) suggest that to obtain an error of less than 5cm in a 1 degree by 1 degree grid cell, at least ten measurements are required. This density of measurements is unlikely to be achieved over a wide area, particularly as many snow-covered areas are dangerous or otherwise inaccessible (Gupta et al., 2005).

## **3.3 Remote sensing**

### **3.3.1 Snow extent**

The monitoring of snow from space began in 1966 with USA's National Oceanic and Atmospheric Administration (NOAA) satellites providing data in the visible and near infra-red wavelengths (Matson and Wiesnet, 1981). This dataset provided the first global spatially and temporally continuous measurements of snow, and weekly snow extent charts are still being produced today. The method is simple: snow has a very high albedo in the visible part of the spectrum so shows up clearly next to the (low albedo) snow-free surface. Snow cover is interpreted manually using data from the Advanced Very High Resolution Radiometer (AVHRR), the Geostationary Observational Environmental Satellite (GOES) and station data, with a pixel designated as snow-covered when more than 50% is covered with snow. A major drawback is that clouds are also highly reflective in this part of the spectrum and obscure the view of the ground. Careful discrimination is required between snow-covered and cloud-covered surfaces; the data for clouded areas has to be estimated by interpolating between neighbouring values. This can lead to biases, particularly during periods of snowmelt where the timing of melt can be crucial, for instance in flood forecasting. The data is also affected by low solar illumination in winter, making the satellite pictures harder to interpret (Frei et al., 2003).

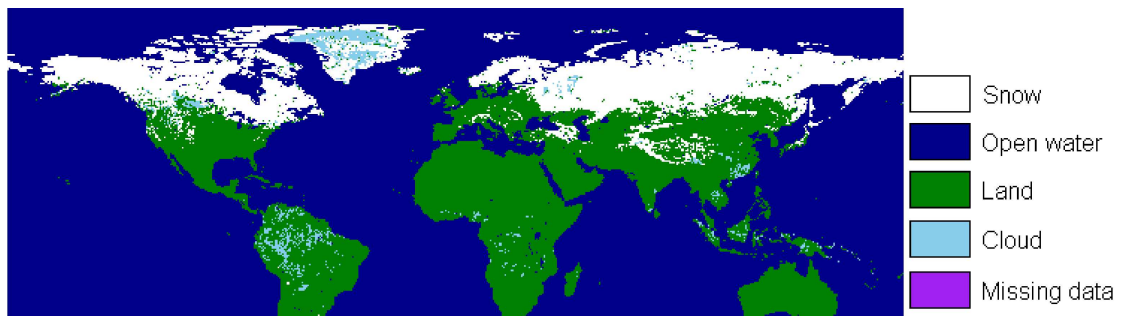


Figure 3.1: Global 8-day snow extent from MODIS, 30 March to 06 April 2003. Data available from NSIDC.

An important addition to visible band remote sensing is the MODIS instrument, launched in 2000. MODIS has a fully automated algorithm for determining snow extent, unlike the NOAA product, and daily products at 500m resolution are available. The data are based on the difference between various measurements in the visible band, and are masked for the presence of cloud. An example MODIS image is shown in figure 3.1. Masking of the snow due to vegetation, however, can be a problem for visible band sensors. Hall et al. (2001) assess errors in the MODIS snow cover retrieval due to land cover type by assigning percentage errors for each of seven land cover classes, plus additional errors due to mixed pixel effects. These errors are then aggregated according to the land cover types north of the snowline each month. They estimate that the Northern hemisphere snow extent mapping error is 8%, largely due to the amount of forest cover north of the snowline.

Other large scale snow extent products include a North America-only 1km dataset from the National Operational Hydrologic Remote Sensing Center (NOHRSC), also based on AVHRR and GOES data, and products derived from microwave radiometers such as the Special Sensor Microwave/Imager (SSM/I) and the Scanning Multichannel Microwave Radiometer (SMMR). The detection of snow cover using microwave frequencies has a number of advantages over using visible-band imagery. Data does not have to be interpreted manually, and can be obtained during darkness or when the sky is overcast, as clouds are fairly transparent at microwave frequencies. However, the microwave measurements are not sensitive to thin snow, so will underestimate the total extent.

A number of hemispheric-scale comparisons of snow extent have been performed. A comparison of data from MODIS, NOHRSC and SSM/I was undertaken by Hall et al. (2002). They found that MODIS and NOHRSC often agree well, although MODIS nearly always maps a larger area as snow-covered. As expected, SSM/I shows the lowest snow-covered area although agreement between MODIS and SSM/I increases

as the snow season progresses. Armstrong and Brodzik (2001) found that data from visible and passive microwave sensors showed similar interannual variability, but that the microwave measurements underestimated the extent by up to eight million square kilometres, compared to the visible data. The largest differences were found in autumn with some improvement in winter and the most agreement in spring.

Despite the drawbacks, the NOAA weekly snow charts have been judged by some to be the most reliable snow dataset (Foster et al., 1996). However, this dataset can only provide estimates of snow extent and not snow water equivalent or mass.

### 3.3.2 Snow water equivalent (SWE)

#### Theory

Information on SWE can be obtained by measuring the amount of energy reaching the satellite at microwave frequencies. If a snowpack is present, it will scatter and attenuate the radiation emitted by the Earth, so a different emission signature is recorded by the satellite (Foster et al., 1987). This scattering is from a combination of physical characteristics, such as grain size, and thermodynamic control of the snow's dielectric constant. Different algorithms are required to retrieve snow over ice sheets and sea ice instead of snow over ice-free land, and it is only the latter that is considered in this thesis.

Most SWE retrievals are empirically-derived, using the difference in brightness temperature between two frequency channels, referred to as the 'spectral gradient'. At frequencies less than 25GHz, the snowpack is virtually transparent, so the signal is dominated by emission related to the temperature of the scene. Above 25GHz the response is affected by scattering from the snowpack. By comparing the brightness temperatures at frequencies either side of this threshold, the amount of scattering due to the snowpack, and hence its water equivalent, can be inferred. This method is simple, however there are many important factors to take into account.

Passive microwave methods are unable to detect very thin snow cover (less than  $\approx 5$ cm, Armstrong and Brodzik (2002)), as the difference between the two frequencies is not large enough to detect. The signal is also unable to penetrate a depth of snow 10-100 times the microwave wavelength, so for a 37GHz signal, with a corresponding wavelength of 0.8cm, the signal saturates at depths greater than 800mm (SWE  $\approx 250$ mm) (Foster et al., 2005).

Snow pack morphology affects the emission through changes in grain size, which is controlled by temperature and water vapour. The presence of large, plate-like depth hoar crystals can result in artificially high SWE retrievals (Derksen et al., 2005), as the

radiometer ‘sees’ a deep snowpack, whereas in fact it is looking at a shallow but dense one. In wet snow, large grains grow at the expense of smaller ones which rapidly melt. However, water has an emissivity close to 1 at microwave frequencies and the signal from any liquid water present (either in the snowpack or as an open body of water) will overwhelm the decreased signal from the Earth, and low or no snow depth values are retrieved. Ice crust layers, resulting from melt-refreeze cycles or wind compaction, can also cause increased microwave scattering and an overestimation of SWE.

When Mie scattering theory and conventional radiative transfer equations were applied to modelling snow microwave retrievals, it was found that the amount of scattering should be strongly dependent on grain size. However, algorithms using a constant grain size assumption appeared to do much better than expected under a wide range of conditions. Armstrong et al. (1993) suggest that the assumption of independent scatterers in the conventional theory is not rigorous, and that dense medium transfer theory, which accounts for correlated scattering in a dense material such as snow, shows a much less sensitive response to grain size. Despite the high degree of sensitivity to grain size, Foster et al. (1999) found that scattering appears relatively insensitive to grain shape.

The emissive properties of the soil beneath the snowpack will also influence the brightness temperature. The dielectric behaviour of dry soils is roughly the same as for frozen soils (Kelly et al., 2003), but any wetness will raise the emissivity towards 1. Surface roughness also becomes more influential for a wet soil. It is assumed that the soil temperature will be at or below freezing for most snowpacks, although these factors will become important when the snow is thin or in maritime areas where temperatures can rise above freezing (Kelly et al., 2003; Pulliainen, 2006). Therefore air temperature will also affect SWE retrieval, by driving the metamorphism of snow grains, and by causing melt.

Forest cover also affects the microwave measurement, as vegetation has the effect of masking the signal from underlying snow cover by contributing scatter, absorption and emission through snow interception and the water content of the vegetation itself (Derksen and MacKay, 2006). This effect is usually thought to result in an underestimation of SWE of up to 50% (e.g. Foster et al. (2005); Brown et al. (2003)). It is important to account for vegetation in the retrieval, as at the scale of a satellite pixel (many kilometres square) the scene is unlikely to be free of vegetation.

### **Retrievals in practice**

The regular recording of passive microwave brightness temperatures from space began in 1978 with the Scanning Multichannel Microwave Radiometer (SMMR),

which functioned until 1987 when the Special Sensor Microwave/Imager (SSM/I) was launched on NASA's F8 satellite. It has now been operational on five satellites (F8, F10, F11, F12 and F13). The Advanced Microwave Scanning Radiometer for the Earth observing system (AMSR-E) began recording brightness temperatures in 2002.

A simple algorithm for SWE retrieval was developed by Chang et al. (1987) for SMMR:

$$\text{SWE (mm)} = c(T_B18H - T_B37H) \quad (3.1)$$

where  $H$  refers to the horizontally polarized channel,  $T_B$  is brightness temperature in degrees Kelvin and the gradient of the linear fit,  $c$ , is  $4.8\text{mmK}^{-1}$ , a constant derived from radiative transfer models. Two important assumptions in this derivation are a constant snow grain radius of  $0.3\text{mm}$  and a constant density of  $300\text{kg m}^{-3}$ . Defining these variables as constants in the retrieval, independent of space or time, means that this is a 'static' retrieval. This is the most common form of SWE retrieval, though 'dynamic' retrievals, where the changing grain size over time is taken into account, have also been developed and will be discussed below.

Defining an appropriate grain size and density for use in any retrieval algorithm is difficult. Foster et al. (1996) showed that a representative snow density for mature snow packs in North America is  $300\text{kg m}^{-3}$ , however, in reality the grain size and snow density can be highly variable both temporally and spatially. As snow grains tend either to grow or to remain the same size over a snow season, the constant grain size assumption will lead to an overestimation of SWE, all other things being equal (Foster et al., 2005). Although snow density is related to the snow grain size, its influence on retrievals is much smaller (Pulliainen, 2006). The use of a difference algorithm minimises certain errors in the retrieval, such as the effect of snow temperature, the dielectric constant of the soil and the surface roughness (Kelly et al., 2003). However, Chang et al. (1987) suggest that application of their algorithm should be limited to snow depths of less than  $1\text{m}$ , and any retrieved depths less than  $25\text{mm}$  should be set to zero. To apply the Chang algorithm (equation 3.1) to SSM/I data, a modification for the difference between the  $18\text{GHz}$  and  $19\text{GHz}$  channels is needed. Armstrong and Brodzik (2001) suggest:

$$\text{SWE (mm)} = 4.77(T_B19H - T_B37H - 5) \quad (3.2)$$

Unfortunately, the SMMR and SSM/I operational periods overlap for only six weeks of the Northern hemisphere summer, limiting the amount of data that could be used to compare the readings from the two systems. Derksen and Walker (2003) show that

Table 3.1: Land cover specific algorithms for SWE retrieval used by the Meteorological Service of Canada

Open	$\text{SWE (mm)} = -20.7 - 2.59[(T_B37V - T_B19V)/18]$
Coniferous	$\text{SWE (mm)} = 16.81 - 1.96(T_B37V - T_B19V)$
Deciduous	$\text{SWE (mm)} = 33.5 - 1.97(T_B37V - T_B19V)$
Sparse	$\text{SWE (mm)} = -1.95 - 2.28(T_B37V - T_B19V)$

there is a systematic bias in the cross-platform time series, with SSM/I measurements systematically higher than those from SMMR. They also show that this bias is regional, so a global adjustment factor would be inappropriate

Rather than apply the same algorithm at every point, the Meteorological Service of Canada (MSC) has developed a suite of land cover-specific SWE retrieval algorithms, following airborne passive microwave and ground measurement campaigns (Goodison et al., 1984; Sellers et al., 1997). Weekly maps of Canadian SWE are derived from SSM/I brightness temperatures in near-real time. The four land cover types used are open prairie, coniferous forest, deciduous forest and sparse forest, and the grid cell land cover fractions are determined using the IGBP 1km land cover data set. The four difference algorithms are shown in table 3.1.

The open prairie algorithm has been well validated, producing results within  $\pm 15\text{mm}$  of observed values (Derksen and Walker, 2003). Higher uncertainty of  $\pm 30\text{--}50\text{mm}$  exists in forested areas, and the problem of SWE retrieval uncertainty in very dense forest is still present. Despite most errors in the static retrieval tending towards underestimation, Chang et al. (2005) found no bias in whether SSM/I results over- or underestimate SWE in a 10 year record. Similarly, but in a spatial rather than temporal context, Derksen et al. (2005) subsampled a single SSM/I grid cell ( $25 \times 25\text{km}$ ) and found that the microwave estimate lay in the centre of a highly variable but normally distributed set of in situ measurements, suggesting that the spatial averaging performed over a pixel by the radiometer leads to a representative brightness temperature for that pixel.

Alternative approaches to the static retrieval have also been attempted. Kelly et al. (2003) derive a new form of the coefficient  $c$  in the snow depth version of the SSM/I retrieval algorithm (equation 3.2). Rather than a continent-wide static approach, assuming a constant grain size and density, Kelly et al. (2003) use a dynamic approach. Simple empirical models of grain size evolution and density are used to derive the coefficient  $c$  and predict its spatial and temporal variation.

This new dynamic algorithm estimates snow depth with greater root mean square error (RMSE) but a generally smaller bias than the static algorithm of equation 3.2

when compared to ground station data (the larger RMSE is believed to be due to a few stations exerting a strong influence on the results). No account was taken in this study of the effects of vegetation.

Josberger and Mognard (2002) also used a dynamic approach that takes into account the temperature history of the snowpack. They define a temperature gradient index (TGI), based on the integral of the bulk temperature gradient, and find a high correlation between this index and the SSM/I spectral gradient. This allowed them to derive a new snow depth retrieval dependent on air temperature and the TGI, which works well in the Great Plains region of North America. The algorithm was then tested in Siberia (Grippa et al., 2004) and appears to improve estimates compared to the static case, although the lack of frequent in situ observations in the region limits calibration and validation.

More deterministic retrievals have also been attempted, by coupling radiative models of the snowpack to hydrological models (e.g. Chen et al. (2001)). So far this approach requires site-specific parameterizations which are unavailable at large scales, and obtaining detailed snowpack properties for areas the size of an SSM/I pixel is not practical.

### **3.3.3 Summary**

Remote sensing using satellites emerged in the second half of the twentieth century as a means of gathering spatially and temporally continuous datasets of both snow extent and SWE. Snow extent datasets are derived from a range of different instruments and require differing amounts of manual processing. SWE data is only retrieved from microwave instruments, which generally use a linearized difference between two frequency channels to derive a SWE measurement. This retrieval method is sensitive to assumptions regarding grain size, and the frequency difference saturates in deep snowpacks and is insensitive to very shallow ones. The masking effect of vegetation has also to be taken into account. Most operational retrievals use a ‘static’ approach, where the algorithm uses a constant grain size both spatially and throughout the season. ‘Dynamic’ approaches, where the grain size used is dependent on, for example, the temperature history of the pixel, have also been developed but are not as widely used.

## 3.4 Analysis of passive microwave data

### 3.4.1 Data

The only available global snow water equivalent product based entirely on observations is the Global Snow Water Equivalent Climatology, provided by the National Snow and Ice Data Center (Armstrong et al., 2005). The climatology is produced from a combination of SMMR, SSM/I and visible data, with the passive microwave data providing the SWE information, and visible data is used to fill in any pixels that were seen to be snow covered but not detected by the microwave radiometer. Only data from the 37GHz and 19GHz channels are used, first re-sampled to the 19GHz -3dB footprint of 69x43km and then gridded to the 25km Equal Area Scalable Earth (EASE) grid (Brodzik and Knowles, 2002). The dataset comprises monthly means from November 1978 to March 2005. An example of a month's worth of Northern hemisphere data is shown in figure 3.2 (note that ice sheets such as Greenland and parts of the Canadian Arctic are masked).

Equation 3.2 is used for SWE retrieval. To avoid overmeasure due to melting snow, only data from the “cold” pass (the 0600 ascending equator crossing) are used. Any SWE values less than 7.5mm are deemed unreliable and set to zero, and areas with permanent ice according to the MODIS dataset are masked. Missing data are interpolated from surrounding days, and the monthly mean is calculated from interpolated daily values.

To account for the masking effect of vegetation, the algorithm is adjusted by a forest factor  $ff$  using the 25km EASE-grid version of MODIS land cover.  $ff$  increases on a linear scale with forest cover percentage, up to a maximum value of 0.5 for forest cover fraction of 50% or above. SWE is then adjusted according to equation 3.3.

$$SWE_{adjusted} \text{ (mm)} = SWE \text{ (mm)} / (1 - ff) \quad (3.3)$$

Only in one area does the microwave data indicate snow where the visible data does not, which is over the Tibetan plateau, an area of extremely high elevation. Most SWE retrieval algorithms assume that the atmosphere is transparent at 37GHz and 19GHz, i.e. the radiation leaving the snowpack reaches the radiometer in space unaffected by the atmosphere in between. Recent studies comparing data from airborne and spaceborne radiometers have found that this may not be the case (Pulliainen and Hallikainen, 2001; Wang and Tedesco, 2007), and Armstrong et al. (2004) suggest that this may be the cause of the discrepancy over the Tibetan plateau. Since this area has a mean elevation of over 4000m, there is a much reduced atmosphere between the snowpack and the radiometer, so the calibration using data gathered at low elevation

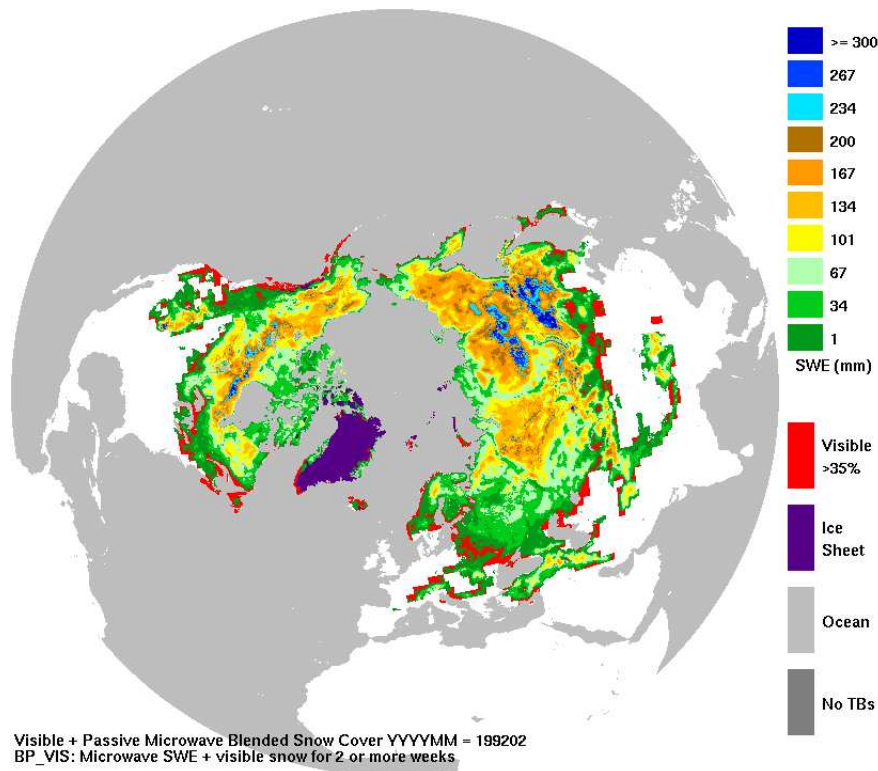


Figure 3.2: February 1992 from the Global Monthly Snow Water Equivalent Climatology. Note that ice sheets are masked out (purple), and that the product is supplemented with data from visible band satellites (red) where the snow is not sufficiently deep to be detected by the microwave radiometer

may not be appropriate. A correction is being developed but is not yet part of the released product.

For this study, it was decided to use only the data from the SSM/I radiometers, which starts in August 1987, due to the systematic biases found between the data from the SMMR and SSM/I instruments (Derksen and Walker, 2003). It was also decided to remove the visible data from the dataset. Firstly this allows the monthly data to be easily averaged, as all the data are provided in the same units, and secondly it allows conclusions to be drawn about the quality of the passive microwave data and retrieval algorithm.

Figure 3.3 shows the average monthly climatology for the SSM/I data. In August, the only snow-covered pixels are found in the Himalayas. Snow begins to develop in Alaska and northeast Siberia in September and extends across high latitudes in October. By December most of Siberia, Canada and the Tibetan Plateau are snow-covered, with the deepest values still found in Alaska and northeast Siberia. SWE values peak at over 300mm in eastern Siberia and central Canada in February and March. The US and Europe become mainly snow-free in April, and the snowline

retreats northwards on both continents until in June it is only the high Arctic regions of Canada and Siberia and the high altitude Himalayas that are snow-covered. The latter still have some snow-covered pixels in July where the rest of the hemisphere is snow-free.

In the data documentation (Armstrong et al., 2005), the authors suggest overmeasure due to depth hoar could be occurring in eastern Siberia, although sufficient snow depth data were not available to verify whether this was the case. They also note that persistently high SWE values are measured between the western edge of Hudson’s Bay and North Alaska. Few measurements are available for this region, but those that exist suggest that this gradient is real, but perhaps of a smaller magnitude than the passive microwave measurements indicate (Derksen and MacKay, 2006).

### 3.4.2 Empirical Orthogonal Function analysis

Nearly 20 years of SSM/I data are now available, making the study of interannual patterns possible. This section assesses the coherence and interannual variability of this SWE dataset using empirical orthogonal functions (EOFs). EOFs are used to quantify spatial patterns of variability, with the method also returning a time series of that variability, and a measure of the importance of that pattern in the overall variability within the original dataset.

Jin et al. (2006) use EOF analysis of station data in the western United States. They compare the EOF patterns with patterns found by stratifying the station data according to climate indices such as ENSO, to establish how much of the variability in SWE data is caused by these climate indices. Derksen et al. (2002) use EOFs to characterize the spatial variability of in situ SWE in central North America, to assess the accuracy of the MSC SWE algorithms (shown above). These studies have concentrated on regional or catchment-scale analysis of SWE, where the patterns are potentially more influenced by the sensitivity of the retrieval to local features such as snow grain size. By looking at patterns on the continental and hemispheric scale we hope to minimise these sensitivities, and understand SWE patterns on the hemispheric scale.

The aim of Empirical Orthogonal Function (EOF) analysis in this context is to find patterns of variability in SWE and snow cover, from seasonal to decadal scales. The method works by decomposing the original monthly ‘snapshots’ into static spatial patterns (EOFs) with an associated time series. This is somewhat similar to the decomposition of, for instance, a time series into orthogonal sine and cosine functions, however in this case the orthogonal functions in the EOF method are not chosen *a priori*, but so as to maximise the amount of variance in the dataset that they explain.



The first EOF thus explains the most variance, the second EOF the next largest amount of variance and so on, until all the variance has been explained. It is essentially an eigenvector-eigenvalue problem, with the eigenvector being the EOF pattern, and the eigenvalue the proportion of the variance explained. The time series associated with each EOF pattern, here referred to as the principal component (PC), is constructed by projecting the pattern onto each of the original monthly snapshots. The method produces as many EOF patterns as there are timesteps in the data, though only those explaining significant proportions of the data are retained for analysis (this is discussed in the Results section below). The method followed here was that of Bjornsson and Venegas (1997), described as singular value decomposition for very non-square matrices.

To reconstruct the original dataset, you would multiply each EOF pattern by its PC and then sum. EOF analysis is often used to reduce noise in datasets by retaining only the first few EOFs in this summing procedure, and rejecting the remaining EOFs as containing noise uncorrelated to the dominant patterns. In many studies, the orthogonal condition is relaxed by rotating the first few EOF patterns to maximise the variance each explains. We chose not to perform any rotation of the EOFs, as this procedure can favour local modes of variability at the expense of global modes (Dommenges and Latif, 2002).

### **EOFs of SSM/I data**

To prepare the data for analysis, the time mean of each pixel is removed, so the PCs are each centred around zero. As the data were obtained in an equal area grid, no area weighting was required. To calculate the seasonal cycle, an ‘average year’ was produced by finding the mean of all Januaries, all Februaries and so on. This average year was then used to calculate anomaly fields by subtracting the appropriate monthly mean from each month. EOF analysis was performed on both the seasonal cycle and anomaly datasets, for the entire Northern hemisphere, and for Eurasia and North America separately.

When applying this method to the SSM/I SWE dataset, it is important to recognise where the sources of error are, whether they are random or systematic, and how they affect the output of the analysis:

- Strong dependence on vegetation is assumed to have been removed by the forest factor, although the EOFs should be inspected for any evidence of correlation with vegetation type

- Signal contamination due to open water is expected to be large but constant throughout the dataset, and therefore to have a limited effect on patterns of variability
- Areas likely to develop depth hoar (particularly eastern Siberia) are expected to show overestimated SWE values, and hence an enhanced variability between snow-free and snow-covered seasons
- Seasons when snowpacks become warm and wet will exhibit SWE underestimation, masking the true variability of the area
- The absence of thin snow cover is not expected to affect the SWE EOF patterns, as the variance will be dominated by areas with deep snow in winter and shallow or no snow in summer.
- Areas affected by signal saturation at large SWE values may show a reduced variability as the whole range of SWE values may be missed. This also means that large negative anomalies are captured by the retrieval, but large positive anomalies may be missed.

It is also important to note that not all the error to be taken account of in the analysis will come from the retrieval algorithm. Previous studies referenced in this report have used pentads (five-day averages), not the monthly averages to be used in the EOF analysis. The approach here will smooth out some of the higher frequency errors, but lead to the amplification of some anomalies as a timing error. As this study uses a multi-decadal dataset, it was felt to be computationally too intensive to use 5-day data.

## Results

Figure 3.4 shows the first four EOFs, and their associated PCs. The EOF patterns are presented as correlation maps, where each pixel shows the correlation of that gridpoint's time series with the respective PC, while the PC's themselves are normalized by their variance.

EOF1 accounts for over 80% of the variance, and contains a coherent pattern of the SWE seasonal cycle. This is the dominant spatial pattern in the data, showing an annual cycle peaking in February, with some interannual variability in the amplitude of that peak. EOF2 and EOF3 show dipole structures accounting for accumulation and melt in the seasonal cycle, as seen by the frequencies present in the time series, and figure 3.7 shows a closer view of a few years of the time series. EOF3 removes

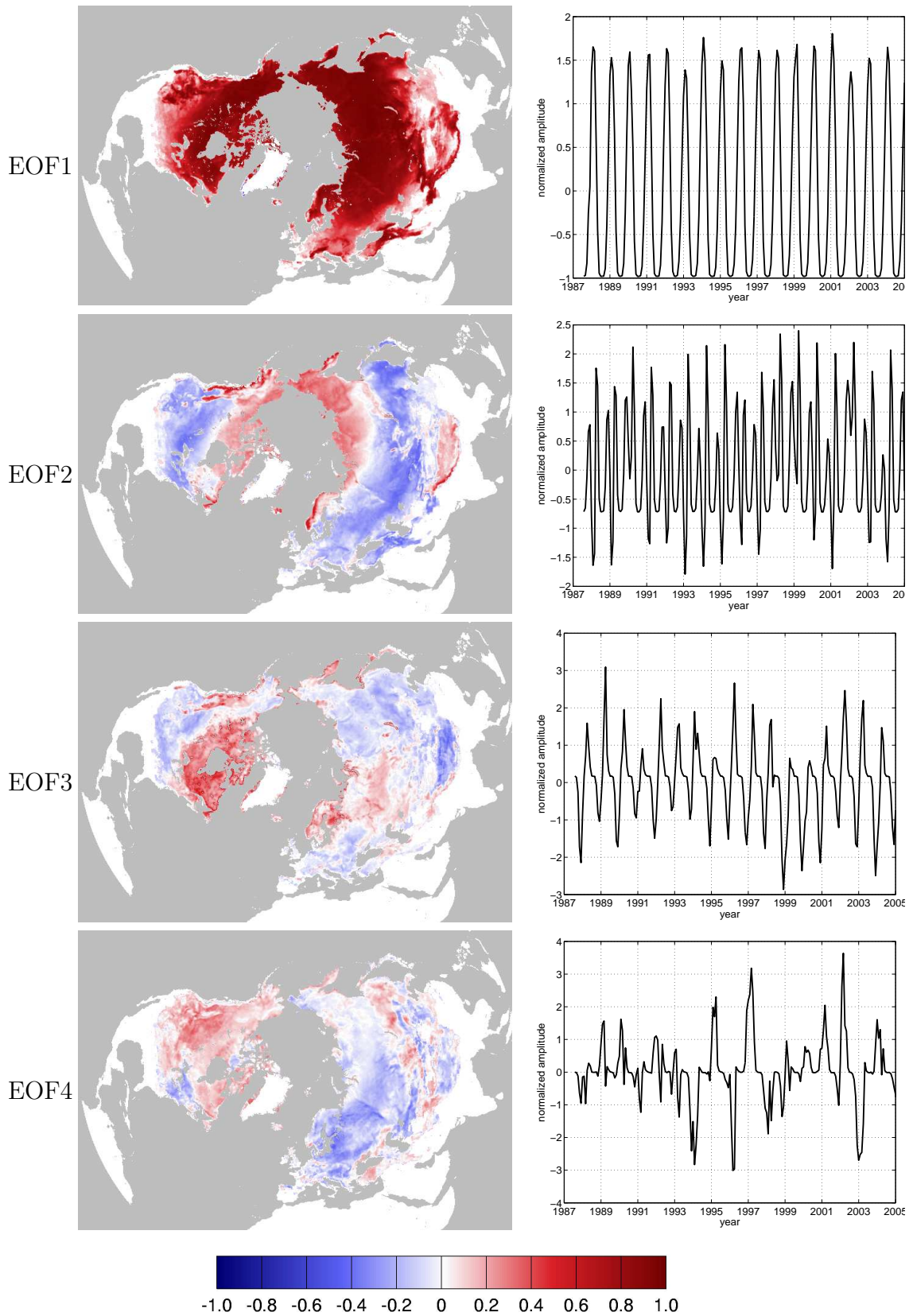


Figure 3.4: Correlation maps of the first four empirical orthogonal function patterns and associated principal component time series of monthly SWE data. The percentage variance explained by the patterns is, in order, 81%, 3.9%, 1.9% and 1.3%.

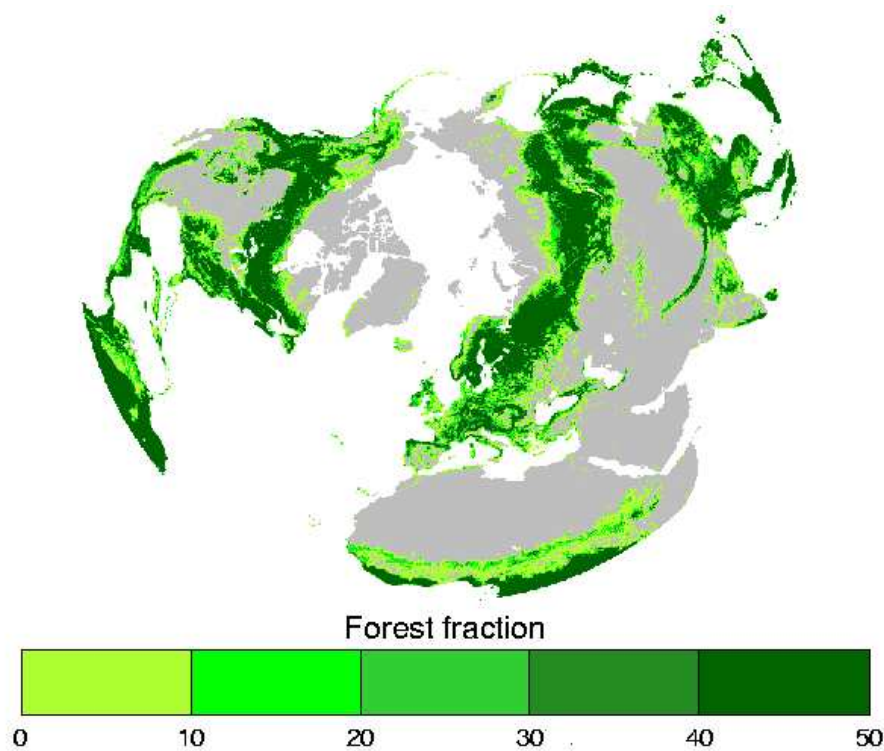


Figure 3.5: Forest cover percent per pixel from BU-MODIS data, capped at 50%. This is the map used to determine the adjustment to the SWE retrieval in the Global Snow Water Equivalent Climatology product.

SWE in the red areas in early winter and adds snow to these areas in spring - these are areas in the dataset that retain snow longer in spring than is captured by EOF1 alone. EOF2 has two peaks per year, in winter and spring, relating to accumulation and melt respectively (the latter peak being larger in almost every case). Hence EOF3 shows areas that have snow in spring but not autumn, whereas EOF2 peaks in autumn and spring, showing areas that have a longer snow season than those picked up in EOF1. These areas are mountains, such as the Rockies and those in Norway, and the high latitudes. The Alps are visible in EOF1, presumably because of their lower latitude and hence shorter snow season. All the first three EOFs contribute to the seasonal cycle, as shown by the periodic PCs (figure 3.4). The PC for EOF4 however is dominated by an interannual pattern.

The EOF method will only remove uncorrelated noise; any contamination in the signal that is correlated to the main pattern will remain. None of the leading patterns look like the map of forest cover (figure 3.5) or grain size (figure 3.6). Therefore, this analysis does not reveal a separable pattern in the data that relates only to forest cover or grain size.

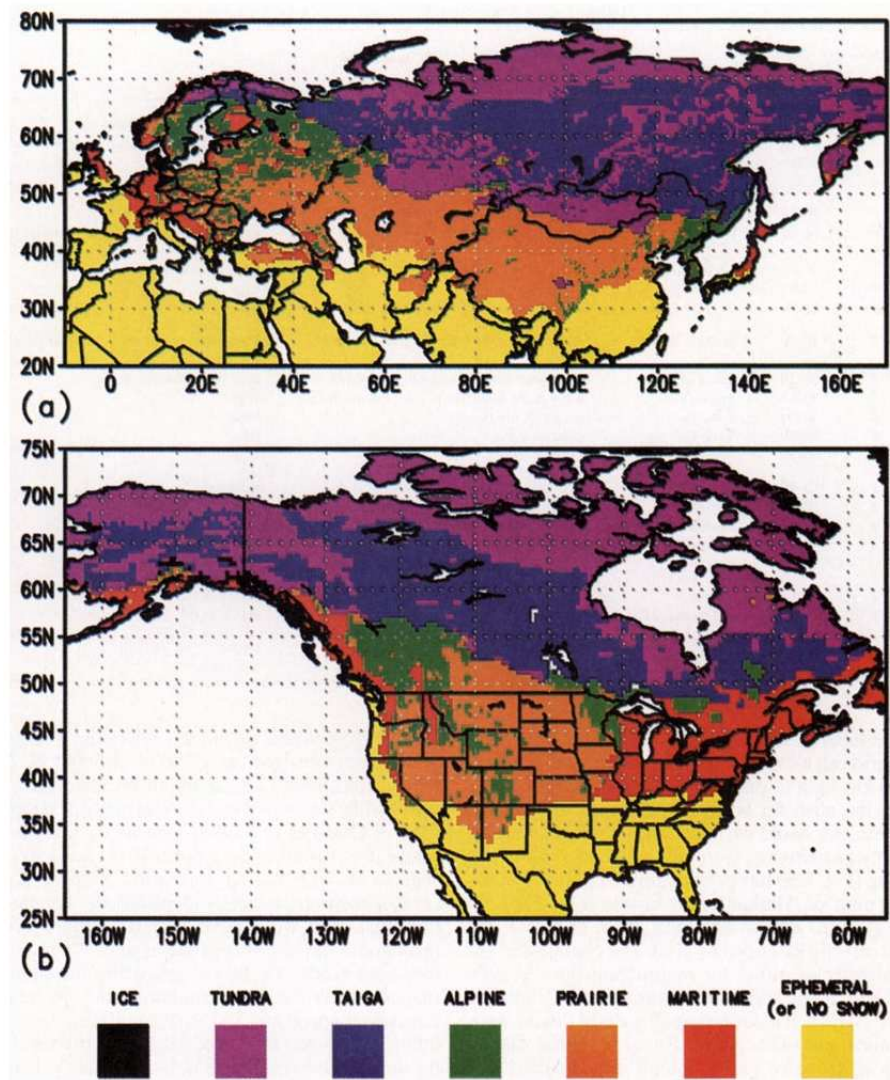


Figure 3.6: Snow type classes over Eurasia and North America, taken from Sturm et al. (1995).

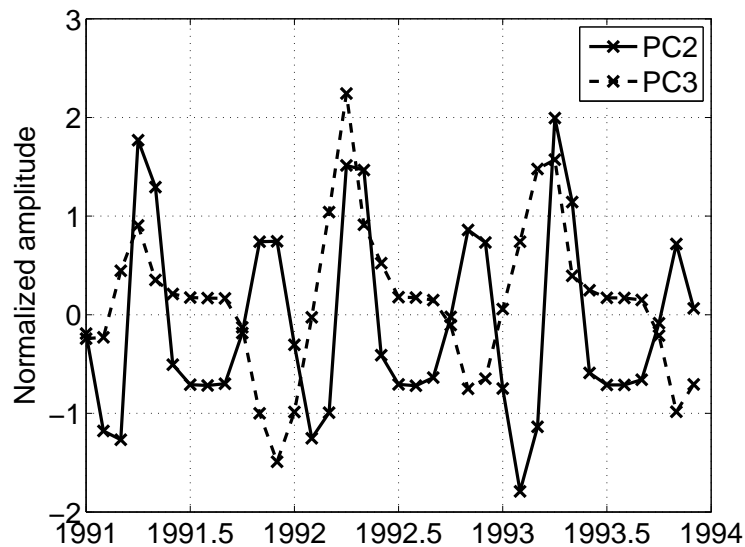


Figure 3.7: Close-up of three years of the second and third principal component time series of monthly SWE data.

The upper panel of figure 3.8 shows the first 20 eigenvalues obtained from the analysis of the Northern hemisphere, North American and Eurasian datasets: as the larger Eurasian landmass dominates the first EOF, the analysis was repeated on the continents separately. Clearly all three are dominated by the annual cycle which explains around 80% of the variance in each case. To examine interannual patterns, the seasonal cycle was removed as described above. The lower panel of figure 3.8 shows the first 20 eigenvalues obtained from the analysis of Northern hemisphere, North American and Eurasian anomalies. Here the eigenvalues are more closely spaced, though the first eigenvalue is well separated from those following in each dataset. EOF1 in North America explains nearly 16% of the interannual variability, and EOF1 in Eurasia explains just over 13%. These two leading patterns are shown in figure 3.9. EOF1 for North America is shown in the upper panel with its PC. The main area of action of this pattern is in the boreal forest band stretching between southern Alaska and Hudson Bay. Where the PC is positive, anomalies in this region were negative (*e.g.* winter 1988, spring 1993 and late winter 2003), and vice versa. The lower panel shows EOF1 for Eurasia, where the centre of action again lies in the boreal forest region, stretching from northern Scandinavia and across northern central Siberia. These first EOF patterns for the anomaly time series over North America and Eurasia are negatively correlated at -0.2 which is low (although statistically significant at 95%). If just the February values are used, the correlation changes sign to 0.36. No correlation is seen with either ENSO or the NAO.

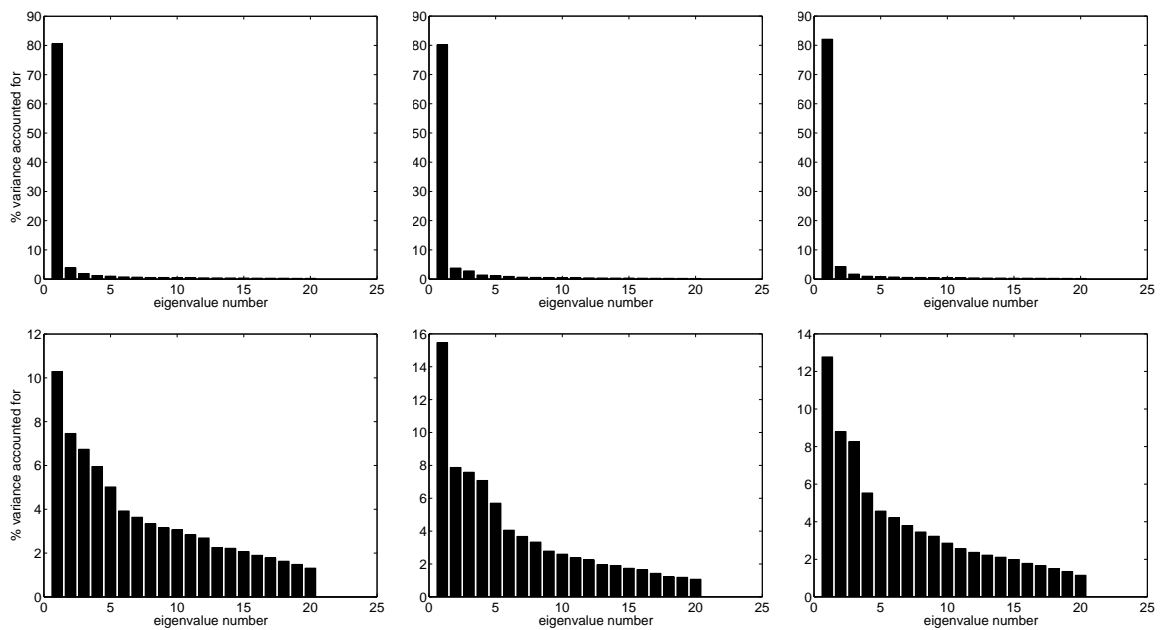


Figure 3.8: Eigenvalues of the first twenty EOFs from the whole Northern hemisphere (left), North America (middle) and Eurasia (right). Top row shows the original dataset, the bottom row shows the anomaly data.

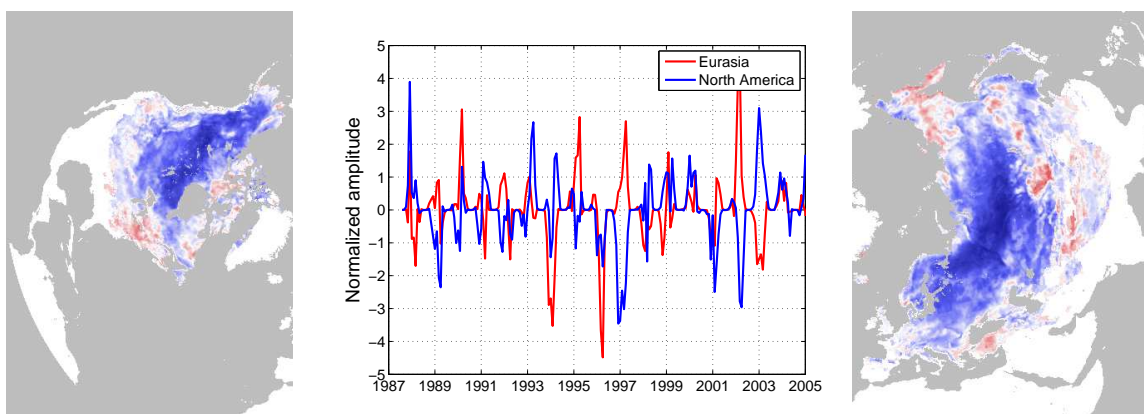


Figure 3.9: EOF1 and PC1 from North American (upper) and Eurasian (lower) regional analysis

## 3.5 Discussion

Spatially and temporally continuous snow data have been retrieved from space since the 1960s. While snow extent data from space are reliable and well-studied, for a complete picture of the Earth system we also require reliable information on SWE.

The only readily available long term global SWE dataset is derived from passive microwave data from the SMMR and SSM/I satellites. The SMMR data period is 1978-1987, although this thesis concentrates on the data from the SSM/I satellite only (1987-2005). The dataset makes use of an empirical retrieval first derived by Chang et al. (1987) and makes two important assumptions: a constant grain size, and SWE underestimation wherever there is forest cover. Despite many newer approaches being proposed, these static retrievals are often found to be the most consistently reliable choice at large scales (Koenig and Forster, 2004; Armstrong and Brodzik, 2002; Foster et al., 1997).

The SSM/I-derived SWE product analysed in this chapter is dominated by a coherent annual signal. This signal gives a plausible representation of the pattern of SWE across the Northern hemisphere. The effect of topography on the snow variability is more easily visible once the data are decomposed into EOFs.

Although no obvious contamination of signals from the forest cover or grain size were found, we would expect the SWE to be correlated in some way to both. The presence of forest will not only mask the snow from the radiometer, it will also affect the amount of snow that lies there, so a correlation between the distribution of forest and the seasonal pattern of SWE would not be entirely due to errors in the remote sensing technique. Similarly, there will also be a relationship between grain size and SWE that could be revealed or masked by the remote sensing technique and the retrieval used. Until more is understood about the interaction of both grain size and vegetation with SWE and microwave radiation, these components are difficult to decompose and the reliability of this SWE product difficult to assess.

As well as a means of assessing the noise in the SSM/I data, the EOF analysis is a way of finding patterns of interannual variability in the data. The most prominent interannual pattern is active over central Eurasia, and accounts for 1.3% of the variance of the entire dataset, and 13% with the seasonal cycle removed.

As the Eurasian land mass dominates this result, the continents were then analysed separately with the seasonal cycle removed, to form ‘anomaly’ datasets. The anomaly patterns in North America and Eurasia appear to have different characteristics. The dominant North American anomalies are a modulation of the seasonal cycle, whereas the Eurasian pattern occurs over a different portion of the continent to the seasonal maximum. Neither are correlated with either ENSO or the NAO, although February

values for the two PC time series are correlated at 0.36. This suggests that there may be some relationship between high and low years, although there are evidently other factors contributing to the extremes on each continent. These patterns could be related to westerly storm tracks across each continent, and there could also be a relationship with the boreal forests (see figure 3.5). As the seasonal cycle has been removed and it is now an anomaly dataset we are analysing, the effect of the forest factor vegetation correction has been removed. If this first anomaly EOF pattern is indeed related to the vegetation map, then this suggests that it is SWE in the boreal forests that dominates the interannual variability of SWE anomalies.

Before attempting further validation of the SSM/I-derived SWE distribution, the next chapter will introduce the model to be used in this thesis. Chapter 5 will then return to the issues presented here, as part of a more detailed evaluation of the observed SWE with respect to both the model climatology and other sources of SWE information.

# Chapter 4

## Modelling snow at large scales

### 4.1 Introduction

Although observations are important, good models are a vital tool for understanding physical processes, and filling in gaps where observations are unavailable. Snow modelling is required in many applications at many scales; these include avalanche, flood and wildfire forecasting, water resource management and climate prediction. Different applications require different modelling approaches and varying complexity, many of which are being investigated in the snow modelling intercomparison project (SnowMIP, Etchevers (2004)). SnowMIP compares snow models on a ‘stand alone’ basis, driven by meteorological forcing data and producing 1D output for a point in space. Most snow modelling studies have been performed at this point scale, or using data from field sites of a limited size for validation (Essery, 1998; Slater et al., 2001; Boone et al., 2006); validation of distributed snow models on a large (continental to hemispheric) scale is more difficult as suitable observation data are limited.

Boundary conditions for the atmosphere are provided by the land surface, as summarised by Bagnoud et al. (2005):

“The role of the land surface in climate models is primarily to partition available radiative energy between the sensible and latent heat fluxes (the surface energy balance), to partition available water between evaporation and runoff (the surface water balance) and to simulate momentum and, most recently, carbon exchange between the land surface and the atmospheric boundary.”

Snow is recommended by Foster et al. (1996) as a challenging diagnostic for climate models, as both the temperature and precipitation must be realistic to ensure good predictions of snow cover and depth. The representation of snow processes varies

between GCMs. Typically, precipitation occurs as snow when the temperature of the lowest atmospheric level is at or below freezing. The energy balance of the snowpack dictates melt, and many models add a sublimation term to the evaporative flux from surface to atmosphere. However, computational constraints limit the complexity that can be included in a snow model to be used as part of a GCM. This leads to parameterization, and a problem in land surface models is that snow is heterogeneous on a smaller scale than the model grid, and so is particularly sensitive to parameterization choices (Essery et al., 2003).

Model structure influences the physics of the snow model; an illustration of common structures is shown in figure 4.1 (from Slater et al. (2001)). A model with a single snow layer above the soil, known as a ‘bulk-layer model’, will allow the snow to be thermodynamically separate to the soil, with an explicit temperature and separate fluxes calculated for the snow-covered fraction of the gridbox. A multi-layer snow model will, in addition, be able to represent more complicated compaction and melting processes. Some models have a composite snow-soil layer, where the snow will still occupy a fraction of the gridbox, but thermally the snow and soil will not be independent. Alternatively, an implicit scheme is one where the properties of the upper soil layer(s) are modified to allow for the difference between snow and soil, for instance in albedo or thermal conductivity. In this scheme, the grid box thus becomes an aggregate of the different components within it.

An alternative to using models alone for large scale information is to use a reanalysis product, where the aim is to recreate climate fields by exploiting the best features of both the model and observing system. An estimate of the state of the atmosphere, ocean or land surface for a point in time, often prepared in real time for operational forecasting, is referred to as an ‘analysis’. Subsequently, observations collected at that point in time can be assimilated into that analysis, providing a retrospective ‘best estimate’ of the state of the climate system. This is known as a ‘reanalysis’. The first generation of reanalysis products were proposed in the late 1980s and became available in the mid-1990s (see section 4.5.2 for details). Since then, improvements in data assimilation, observing systems and computing resources has led to a second generation of reanalyses with improved resolution and parameterizations.

This chapter comprises an introduction to the general circulation model that has been used in this thesis. A brief overview of the general features of the GCM is followed by a more detailed assessment of the land surface component, and the representation of snow in particular. Some examples of snow climatologies from runs of the model with differing boundary conditions are also presented.

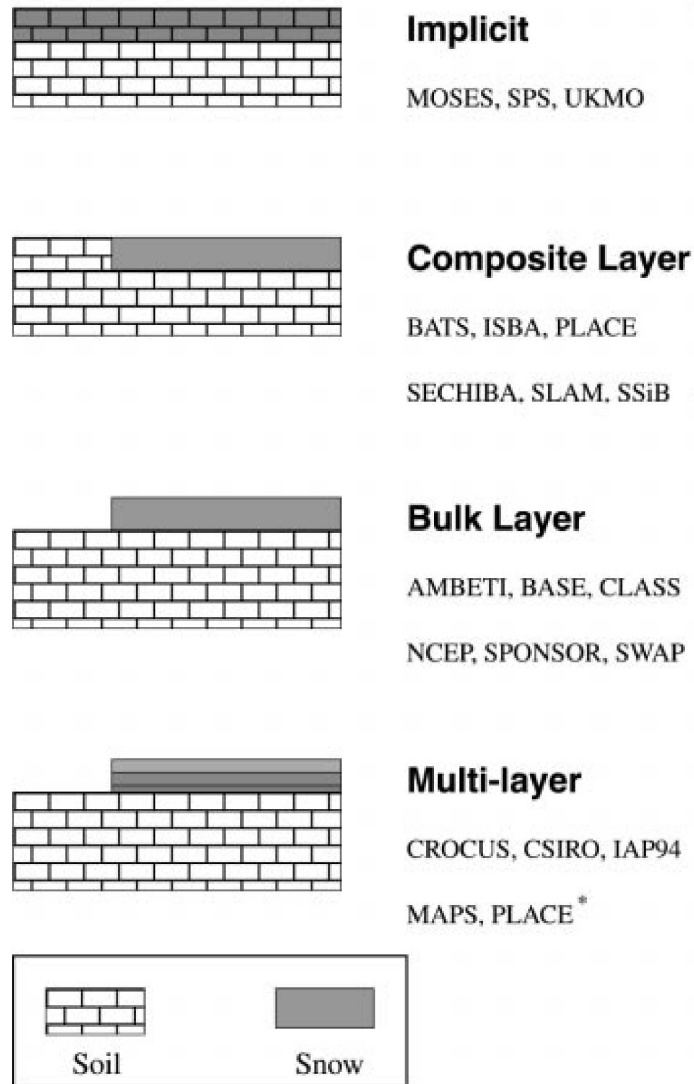


Figure 4.1: Classification of GCM snow model structure, after Slater et al. (2001), figure 5. Note that MOSES is an implicit scheme; other land surface model acronyms are listed in the original reference.

The GCEP project also uses the ERA40 reanalysis product (Uppala et al., 2005) both as a source of fields for assimilation into the model and for validation of model output. ERA40 is also introduced in this chapter, and a similar assessment of the product's climatology and snow distribution is presented.

## 4.2 Choosing a GCM

To study snow at continental to global scales, and as part of the climate system as a whole, it is necessary to use a GCM. Many different centres have developed GCMs and all will have particular strengths and weaknesses. A further choice is between AGCMs and AOGCMs, *i.e.* whether or not the model should have an interactive ocean component. While atmosphere-only models (most of which also comprise an interactive land surface) are widely used for weather forecasting, the much longer runs to be performed in GCEP require the seasonal to decadal variability of the ocean to be represented, which demands a fully-coupled AOGCM.

The GCM chosen for the GCEP project is HadCM3, an AOGCM developed in the 1990s by the Hadley Centre (Gordon et al., 2000; Collins et al., 2001). The atmospheric component of HadCM3 has a resolution of  $3.75^\circ$  longitude by  $2.5^\circ$  latitude, producing  $96 \times 73$  grid boxes. There are 19 vertical levels, and it is coupled to the Met Office Surface Exchange Scheme (MOSES, described below). The ocean component of HadCM3 has a horizontal resolution of  $1.25^\circ$  by  $1.25^\circ$  with 20 vertical levels.

The GCEP project required a GCM that could be run on a PC cluster, rather than a supercomputer. The relatively low resolution of HadCM3 allows multiple runs to be performed on the ESSC computing cluster (typically on 4 processors). The model has also been shown to have a good representation of longer term variability, as represented by phenomena such as ENSO, the NAO and Atlantic Meridional Overturning Circulation. Many aspects of the model, particularly the ocean, have been well-studied, but the land surface model has received little attention, particularly at large scales.

One area of concern with respect to the Hadley Centre models is the land-atmosphere coupling strength, as determined by Koster et al. (2002). The AGCM HadAM3 participated in this experiment and showed very little coupling strength anywhere (in terms of soil moisture anomalies influencing anomalies of precipitation). The effect of land surface conditions on the model's evaporative fluxes was stronger, but it seemed that this did not translate into effects on precipitation. This suggests that the influence of land surface initial conditions on decadal predictions will be minimal with this model, however seasonal and decadal variability in circulation patterns are

expected to affect the distribution of lying snow. It is also important to note that the land-atmosphere coupling strength is yet to be determined in reality, so while small, the coupling in HadCM3 cannot be definitively ‘wrong’. In any case, the benefits of HadCM3 for GCEP overall outweigh this limitation, and sections 4.3 to 4.4.3 will concentrate on this GCM.

### 4.3 The Coupled Model Intercomparison Project

HadCM3 was one of over 20 AOGCMs used in the Fourth Assessment Report from the Intergovernmental Panel on Climate Change (IPCC, Randall et al. (2007)). The analysis and intercomparison of these state of the art climate models also formed part of the third phase of the Coupled Model Intercomparison Project (CMIP3, Covey et al. (2003)), during which a comprehensive database of model output from standardised experiments was collected. Figure 4.2 shows output from HadCM3 compared to the mean of all participating models from a 140-year run beginning in 1860, including forcing from both natural and anthropogenic sources. Shown is the annual mean surface temperature (upper panel) and annual mean precipitation (lower panel), expressed as the model field minus observations. HadCM3 displays a slight cold bias over the continents of one to two °C, and a cold bias of up to 5 °C in the annual mean temperature of northwestern Russia and northern Scandinavia. There is a warm bias of a few degrees in the Arctic. This is similar to the distribution of biases in the mean model.

The precipitation plots in figure 4.2 show large differences between the model climatology and observed precipitation in the tropics, particularly over the maritime continent (Indonesia) where there is a wet bias of greater than 150cm in the annual mean. Biases are much lower at high latitudes, but a lack of data in this region, either from satellites or in situ monitoring, makes reliable error quantification almost impossible. While the precipitation differences in the Tropics are a long way from areas that become snow-covered in winter, changes in precipitation over the maritime continent were shown by Neale and Slingo (2003) to have an impact across North America and northeast Eurasia. However, this study was performed with HadAM3, the atmosphere-only counterpart to HadCM3, which shows large dry biases over the maritime continent (*i.e.* of the opposite sign to biases in the coupled model). This highlights the dangers in comparing atmosphere-only GCM output (driven by predefined SSTs) to output from a GCM with a fully coupled ocean that allows feedbacks. Nevertheless, it is likely that the maritime continent has an important

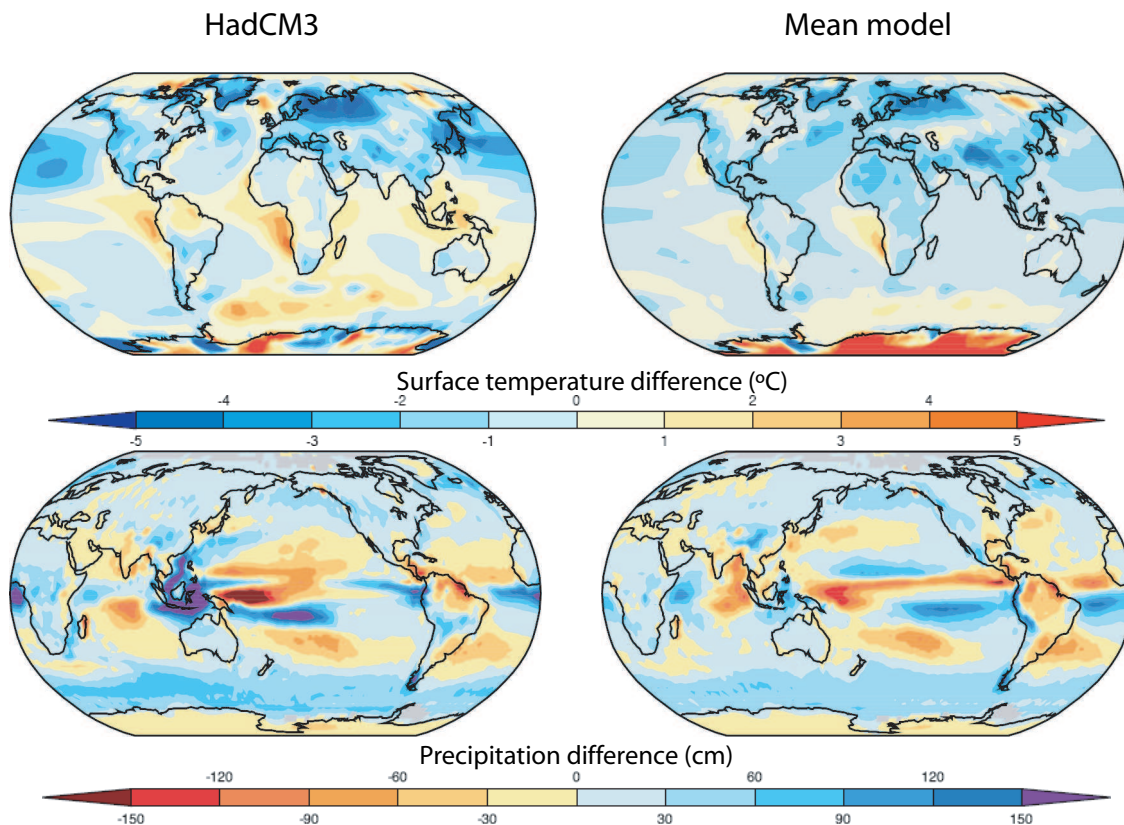


Figure 4.2: Annual mean surface temperature (top) and annual mean precipitation (bottom) difference fields from HadCM3 (left) and mean of all IPCC models (right). Difference fields are model-observations, computed for the periods where the selected observational validation datasets were available. Further details of model runs and observational datasets in Randall et al. (2007).

role in the circulation patterns of the Pacific, and biases in this region will affect the climatology of more remote regions.

Figure 4.3 shows the zonally-averaged mean sea level pressure (MSLP) from the CMIP models, taken from Covey et al. (2003). HadCM3 (dashed brown) shows good agreement with the observations (thick black) for latitudes below  $50^{\circ}\text{N}$ , almost all the way to the South Pole, where there is a small low pressure bias. Above  $50^{\circ}\text{N}$  the model displays a zonally-averaged high pressure bias of around 10hPa. This will impact the circulation pattern and hence the snow cover, although with a zonally-averaged metric it is impossible to tell how that bias is distributed around the hemisphere. The position of storm tracks is a more local measure of circulation biases, and according to Slingo et al. (2003), the model has a generally good representation of wintertime Northern hemisphere storm tracks, when compared to reanalysis products. However it is again important to bear in mind that measurements at high latitudes are sparse and the reanalysis products used for validation will be poorly constrained in these areas.

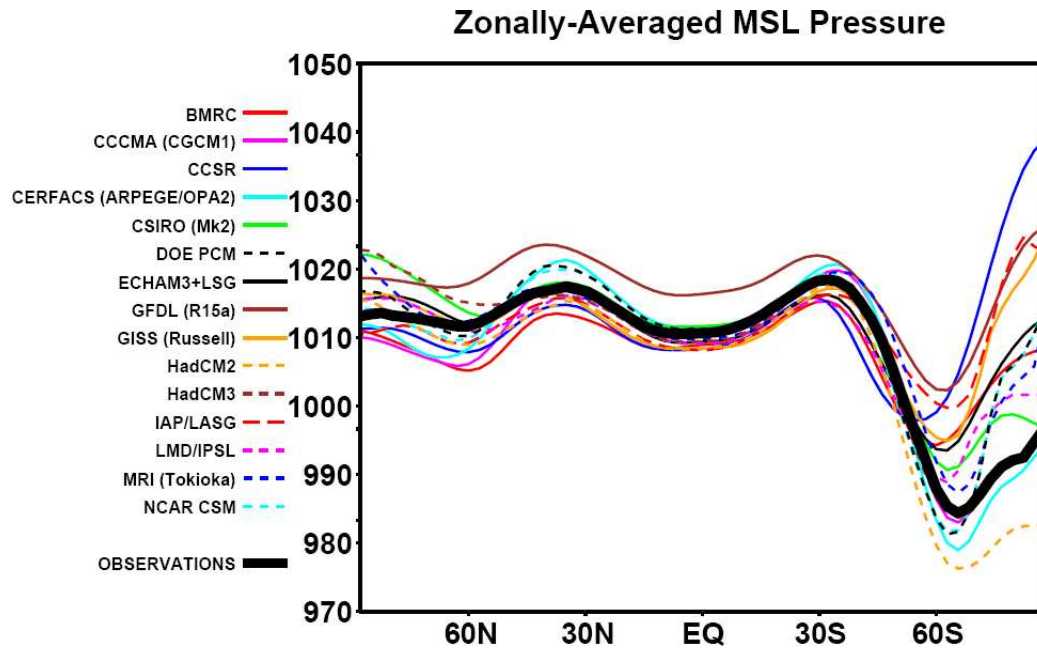


Figure 4.3: Zonally-averaged mean sea level pressure from CMIP models, after Covey et al. (2003).

## 4.4 The land surface in HadCM3

### 4.4.1 MOSES

The interactive land surface model MOSES provides boundary conditions to the atmosphere in both HadCM3 and HadAM3 (a detailed description of the model is found in Cox et al. (1999)). The seasonal cycle of air temperature in HadCM3 is very similar to that in HadAM3, showing the dominant role of land surface temperatures (Slingo et al., 2003) and hence the importance of the land surface model. The prognostic variables in MOSES are canopy water, mass of lying snow and the temperature and moisture contents of each soil layer. The scheme has inputs of rainfall, snowfall and net radiation and returns moisture and energy fluxes and skin temperature to the atmospheric model. MOSES performs calculations with only one surface type simulated for each gridbox, so effective parameters are calculated by an area-weighted mean (except roughness length, which is calculated using a blending height approach). A schematic of MOSES is shown in figure 4.4.

The soil model is comprised of four layers, at depths below the surface of 0.1, 0.25, 0.65 and 2.0m. Moisture input to the soil comes from throughfall through the canopy and snowmelt, and is lost at the surface via surface runoff, and from the lowest soil layer via subsurface flow. Surface runoff occurs when the water flow into the top layer exceeds the saturated hydraulic conductivity of the soil. The subsurface flow is equal

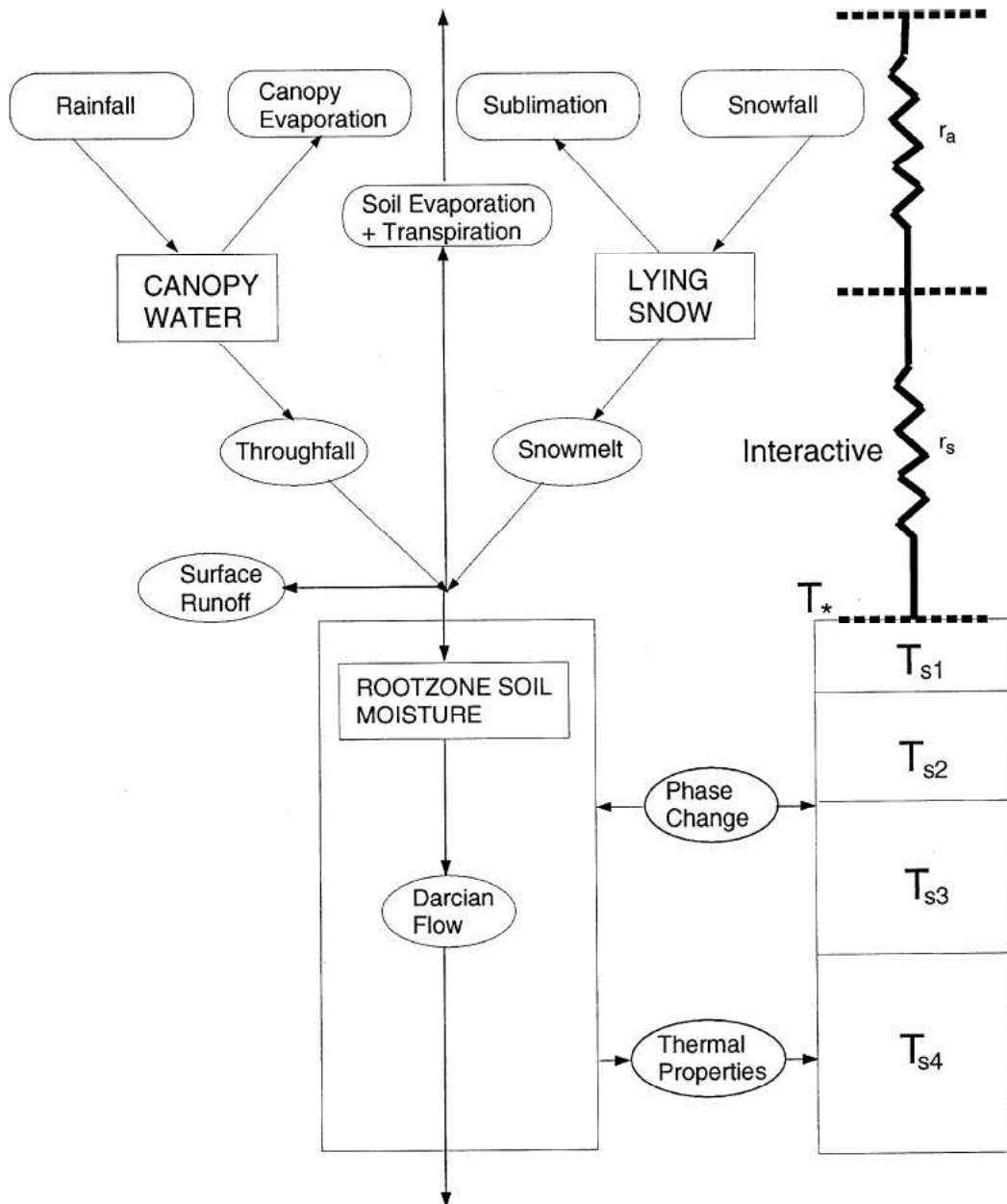


Figure 4.4: Schematic representation of the Meteorological Office surface exchange scheme (MOSES). Prognostic variables are denoted by rectangles. After Cox et al. (1999), figure 1.

to the hydraulic conductivity of the lowest layer ('free drainage'). HadCM3 has no river routing model, so any surface or subsurface flow is instantaneously transported to the river mouth appropriate to that gridbox.

The surface temperature is reduced in the presence of snow, due to its high albedo, until the snow begins to melt. In snow-free areas the surface temperature will be strongly dependent on soil moisture and its impact on the surface energy balance. The evaporation from bare soil depends on the soil moisture concentration in the top soil layer: if the top layer begins to dry out and is not recharged from below, evaporation will tend towards zero and sensible heat fluxes will increase. In vegetated regions, soil moisture controls transpiration, with the moisture content in each layer determining the fraction of the total transpiration extracted from each layer within the rootdepth (which depends on vegetation type). Photosynthesis also depends on the soil moisture availability, which feeds back into fluxes of water and carbon from the canopy.

#### 4.4.2 Snow in HadCM3

The snow model in HadCM3 is a simple one. MOSES has an implicit snow layer structure, so as snow falls, the top two subsurface layers become combined snow/soil layers, and the snow is assumed to be evenly distributed across the gridbox. The depth of snow, where required, is calculated by dividing the snow mass by an assumed snow density, fixed at  $250\text{kg m}^{-3}$ . Important parameterizations in the model include the following, many of which depend on the skin temperature  $T_*$  (shown in figure 4.4):

- Albedo is adjusted from a snow-free value, which is dependent on soil colour, to its deep snow value at large snow depths. This deep snow value is also temperature-dependent if  $T_*$  rises above  $2^\circ\text{C}$ .
- The insulating properties of snow are modelled by adjusting the soil thermal conductivity. This impacts on the soil heat flux, reducing its contribution to the surface energy balance.
- Snowmelt occurs if either  $T_*$  or the temperature of the top snow/soil layer exceeds the melting point of water,  $T_m$ . If  $T_*$  exceeds  $T_m$ , sufficient snowmelt occurs to restore the surface energy balance.
- When snow is present, all the evaporative demand is met by sublimation from the snowpack, setting canopy transpiration and evaporation from the soil to zero.
- The aerodynamic roughness of the surface is also reduced to account for the smoothing effect of snow cover.

SnowMIP categorises participating models according to complexity, from simple (1) to very complex (4). MOSES is given a 2 on this scale. It was found that the model complexity has a strong impact on the simulation of net longwave radiation, through the difficulty of simulating the snow surface temperature accurately with a simple model (Etchevers, 2004). In contrast, it is possible to parameterize the albedo successfully, leading to good simulations by simple models.

An investigation of snow in land surface models was made as part 2(d) of the Project for the Intercomparison of Land-Surface Parameterization Schemes (PILPS). Slater et al. (2001) compare the snow output of 21 land surface schemes at point scale. The models are driven by 18 years of forcing data for a grassland catchment in Valdai, Russia, and are able to reproduce the broad features of the observed SWE, though there is considerable inter-model and inter-annual spread. In general, MOSES tends to estimate a lower SWE than many of the other models when driven by identical meteorological data (including prescribed snowfall amounts). MOSES also melts SWE too quickly, which is a consequence of the implicit scheme: as the albedo of the aggregate grid box is raised by the soil portion, more energy is absorbed (and hence more snow melted) than if the energy balance calculation were performed on snow-covered and snow-free parts of the grid box separately (Essery et al., 2005). A more recent version of MOSES, version 2.2, includes subgrid tiling which goes some way to remedying this problem, but it is the older version that was available for use in the configuration of HadCM3 in this project.

Many models in Slater et al. (2001) were shown to decouple from the atmosphere under very stable conditions. As net radiation becomes negative during winter, surface temperature drops and turbulent fluxes of sensible and latent heat can drop to zero (this is dependent upon the Richardson number, a dimensionless number expressing the degree of turbulent transfer under given conditions of boundary layer stability). At this point the soil heat flux becomes very negative to balance the net radiation, which cools the surface further, hence a positive feedback loop is set up. In the suite of simulations at Valdai, while the sensible heat in MOSES never dropped to zero, there was 70mm more SWE in spring during runs where net radiation was allowed to become negative, compared to control simulations where it did not. This is mainly due to the colder environment allowing the SWE to persist for longer.

A further PILPS study (part 2(e); Bowling et al. (2003a)) tested the land surface schemes' simulation of hydrological processes in a high latitude basin (the Torne-Kalix basin in northern Scandinavia). The 21 models that participated showed large variation in the simulation of the energy budget, and were grouped according to the partitioning of sensible and latent heat fluxes. MOSES was placed in group 4: models with high

annual average latent heat and low annual average sensible heat. In fact MOSES simulated the highest latent heat of all participating models, around 50% higher than that measured at the site. This could explain why MOSES SWE estimates are low, if there is excessive sublimation of fallen snow from the surface, which could in turn be related to the parameterization of atmospheric resistance (Bowling et al., 2003b).

A limitation of the PILPS experiments is the lack of feedback between atmosphere and land surface, as the land surface schemes are driven by observed fluxes. To include these feedbacks, comparisons of the schemes as part of coupled models are required. There have been several investigations into the ability of GCMs to model snow (Foster et al., 1996; Cess et al., 1991; Etchevers, 2004; Frei and Robinson, 1998; Frei et al., 2003, 2005). Foster et al. (1996) compare seven GCMs and find that snow was generally well simulated, except in October, when snow cover begins to extend. Snow mass is also better modelled during winter than during the transitional periods of spring and autumn, when the temperature and precipitation fields are less reliable. This could also be due in part to the parameterization of the albedo; Etchevers (2004) found that a temperature-dependent parameterization, as found in many GCMs, only works well during non-melting periods. While a Hadley Centre model was part of this study, it was a much older version than that used in this thesis.

Snow was considered in the Atmospheric Model Intercomparison Project (AMIP). The atmosphere-only GCM, HadAM3 (which includes MOSES), took part in the second round, AMIP-2. Frei et al. (2003) describe the results with respect to snow covered area (SCA). The suite of AGCMs showed little seasonal bias and improved representation of interannual variability with respect to the older models in AMIP-1 (as discussed in Frei and Robinson (1998)), although it remains underestimated. Regional biases are apparent, however, with overestimates of SCA in eastern Eurasia and underestimates in western Eurasia. Suggestions for improvement include better simulation of the climate of central Asia, and improved parameterizations of precipitation and sublimation in cold, dry regions of high elevation.

Frei et al. (2005) went on to consider AMIP-2 simulations of SWE over North America, using a gridded dataset of interpolated in situ snow depth observations for validation, and snow density estimated from a simple snowpack model. Most of the models reproduced the seasonal timing and relative patterns of continental-scale SWE well, with simulated values peaking in the correct month. However, there was significant inter-model variability found in all diagnostics, and the rate of spring snowmelt tended to be overestimated. HadAM3 slightly underestimated snow mass over North America, and the interannual variability was much less than observed. In estimating climatological means, the median result from all models tended to perform

better than any individual model, which supports the use of ensembles of models in studies of this kind. It is also suggested that SSTs, the primary boundary conditions in the AMIP studies, do not play a significant role in determining the interannual variability of the snowpack in atmospheric models. Frei et al. suggest that coupled ocean-atmosphere models are required to produce accurate predictions of snow cover, particularly at midlatitudes. This is supported by the work of Yang et al. (2001) described in chapter 2, where important feedbacks between ENSO and snow cover were found.

### 4.4.3 Snow in GCEP runs

To investigate the seasonal cycle of snow in HadCM3, three separate runs were performed on the compute cluster at ESSC.

**Control run** This 545-year run includes solar and prescribed volcanic forcings, but fixed greenhouse gas forcings.

**Transient run** This 150-year run begins in 1860 and includes increasing concentrations of greenhouse gases and aerosols to match that observed.

**Flux adjustment run** This short run from December 1994 - November 2004 includes spatially and seasonally varying flux adjustments over the oceans. Fluxes are adjusted so that the sea surface temperatures match those observed. This accounts for ocean circulation patterns not simulated in the model, and corrects imbalances in the surface heat flux (Collins et al., 2006). The method still allows SSTs to vary in response to influences such as changing CO<sub>2</sub> amounts.

The need for flux adjustment arises from model errors; flux adjustments were necessary in many GCMs to stop the model drifting away from the observed climate. HadCM3 was one of the first coupled atmosphere-ocean models to run without the need for flux adjustments, although the successful simulations of large-scale SST features comes at the expense of regional biases (Gordon et al., 2000). This can reduce the plausibility of predicted changes in, for example, circulation patterns in longer climate runs, as SST biases will impact crucial feedback processes, however the flux adjustment will inevitably constrain the model's ability to respond to the changes in forcing. Nevertheless, some authors (for instance Collins et al. (2006)) suggest continuing to use flux adjustments particularly for applications where the remaining biases could reduce the usefulness of model fields, for instance as initial conditions for shorter runs.

To derive the adjustments used here, the model is run for around 100 years, during which SST and sea surface salinity are relaxed to climatology. The fluxes from this are

stored and then applied as flux adjustments. This is done for about 300 years, before starting runs from 1860 with increasing greenhouse gas forcings. Details follow those found in Collins et al. (2006).

Figure 4.5 shows the seasonal cycle of monthly SWE from the control run. As for the passive microwave data in chapter 3, areas of permanent ice, such as Greenland and parts of the Canadian Arctic, have been masked out. Thin snow cover begins to form in September at high latitudes and deepens during Autumn, particularly along coastal areas with high elevation, such as the Rockies and Kamchatka. By February snow has accumulated to depths of over 150mm of water equivalent across Scandinavia, western and central Russia, the Himalayas and Canada. The most widespread deep values are found along the western coast of Canada in March. The snowline recedes during April, May and June, leaving a few gridpoints with snow cover at high latitude or high elevation. By July the hemisphere is almost entirely snow-free.

Figure 4.6 shows the difference in the SWE seasonal cycle between the control run and the transient run (as transient minus control). Differences are small (less than 40mm maximum, generally less than 10mm), with the largest of these occurring over the mountainous west coast of North America. There is also no clear effect of increasing greenhouse gases on the snow line, as has been suggested in the literature (Groisman et al., 1994; Brown, 2000; Dye, 2002), though this is unlikely to be discernable in a climatology averaged over the whole run. Figure 4.7 shows the Northern hemisphere mean SWE as seasonal means for the transient run. Some declining trend may be present in the JJA and SON averages, although the mean SWE present in the Northern hemisphere over these seasons is very low. Continental means will also average out regional differences: Hamlet et al. (2005) found that in North America, the sign of regional trend varied, as while some areas associated declining SWE with a warming trend, others showed increasing SWE due to an upward trend in precipitation. Figure 4.8 shows the same as figure 4.7 except for snow-covered area (SCA). Again, no clear trend is seen, though there may be some decrease with time in the SON average.

Figure 4.9 shows the seasonal cycle of SWE from the run with flux adjustments, expressed as departures from the control run climatology (flux adjusted minus control). This run shows much larger departures from the control run climatology (more than 150mm at certain gridboxes), and almost all negative, showing that the impact of realistic SSTs (or alternatively the inhibition of ocean feedbacks) is to reduce the depth of snow across much of the hemisphere. Reductions are mainly found along the west coast of North America but also in western Russia, where some of the largest land surface temperature biases occur (as shown in figure 4.2; note that the run used to produce this plot of surface temperature errors was a transient run, similar to the one

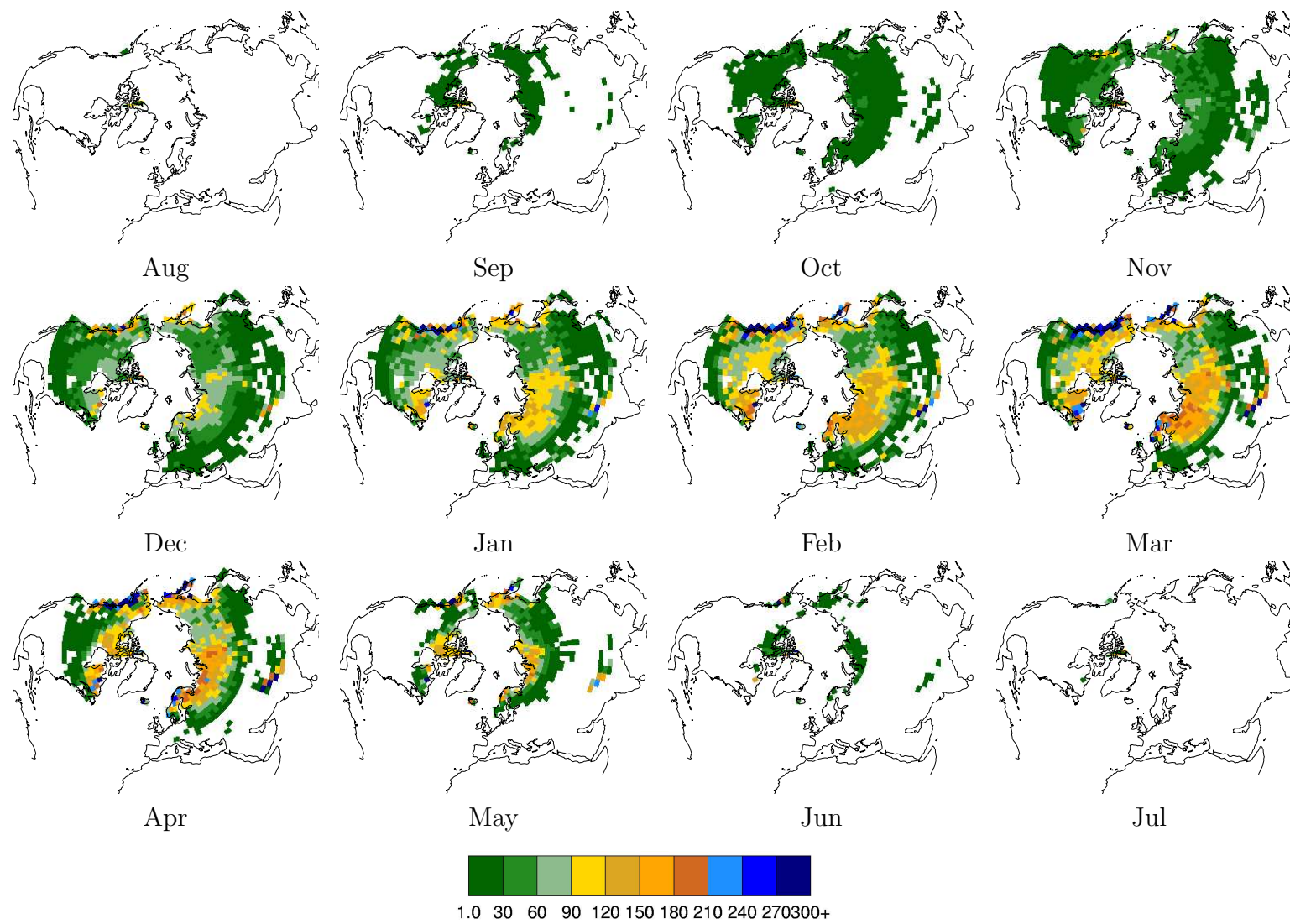


Figure 4.5: Seasonal cycle of snow water equivalent (mm) for a 545-year control run of HadCM3. Note that permanent ice sheets such as Greenland are masked.

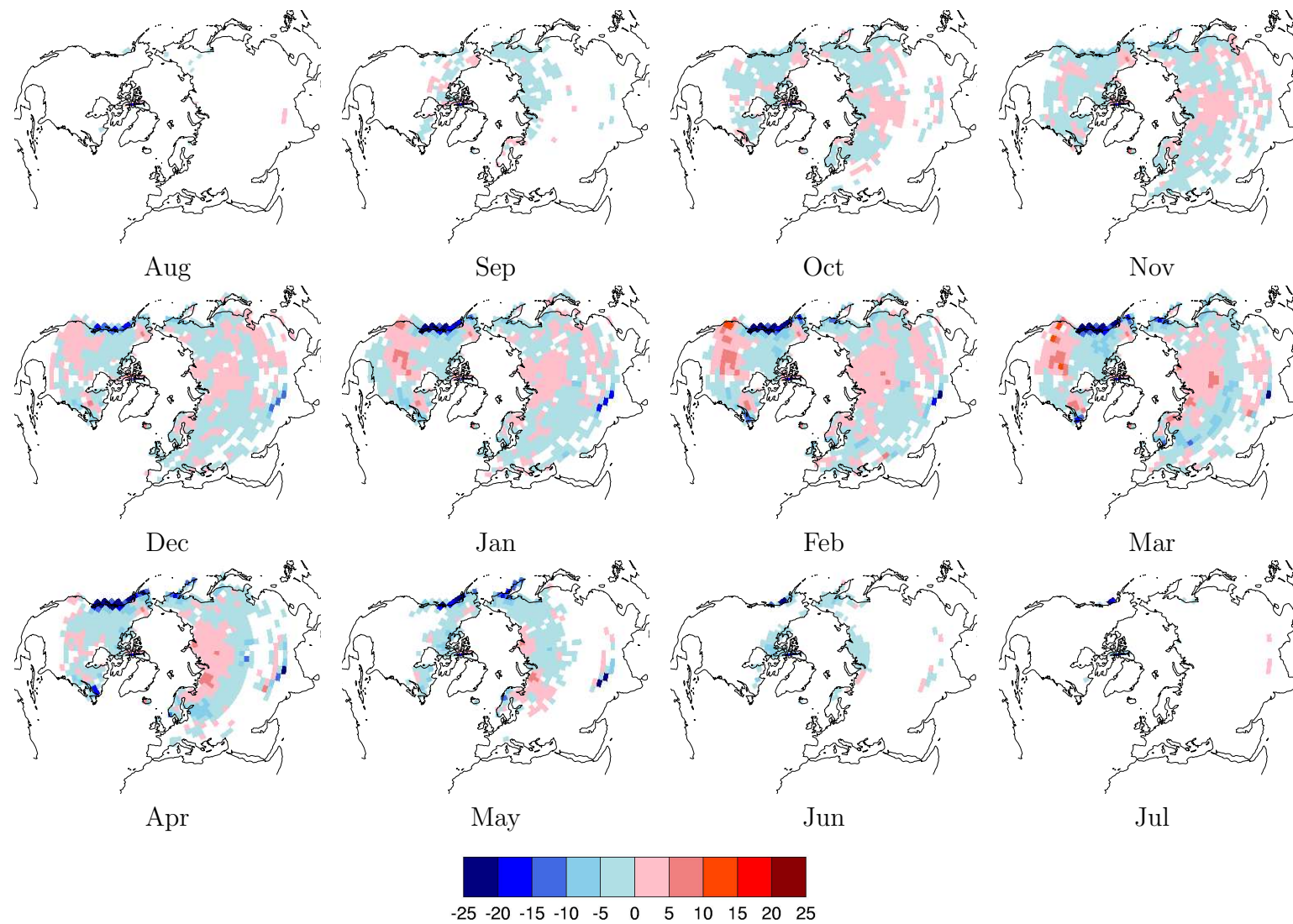


Figure 4.6: Seasonal cycle of monthly snow water equivalent (mm) for a transient run of HadCM3, expressed as departures from the control climatology in figure 4.5. The transient run is 150 years from 1860 including the best estimate of greenhouse gas forcing.

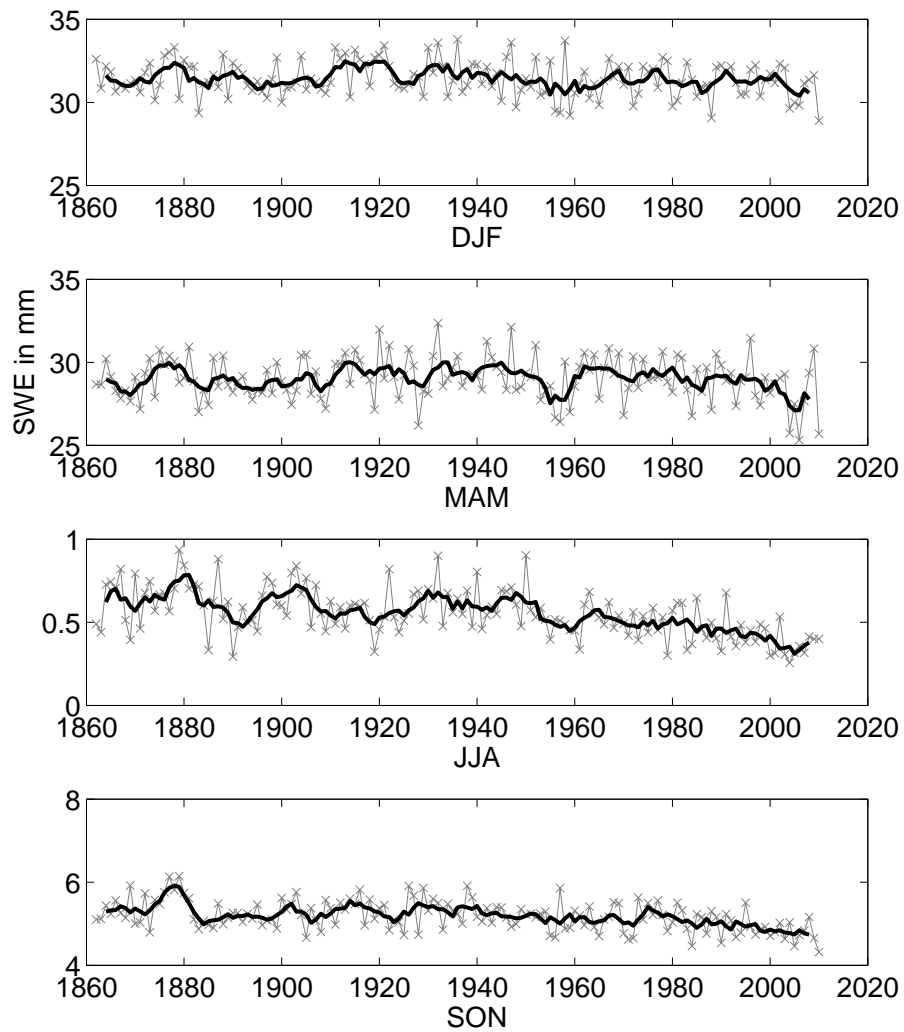


Figure 4.7: Northern hemisphere mean monthly snow water equivalent (mm) by season for a 50-year transient run of HadCM3. Thick line: ten-year running average. Top to bottom: DJF, MAM, JJA, SON

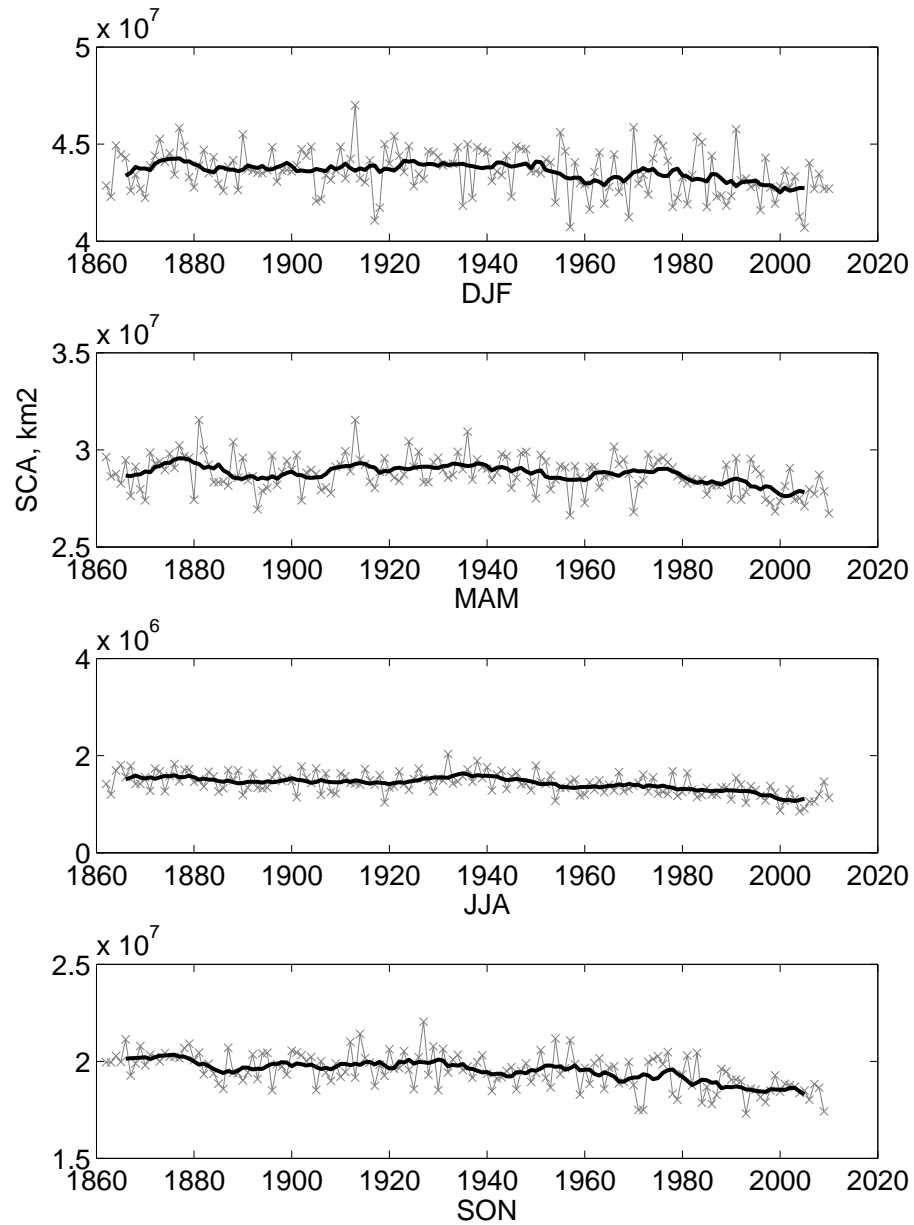


Figure 4.8: Northern hemisphere monthly snow-covered area ( $\text{km}^2$ ) by season for a 150-year transient run of HadCM3. Thick line: ten-year running average. Top to bottom: DJF, MAM, JJA, SON

performed at ESSC, and that figure 4.9 shows differences relative to a pre-industrial control run. Since the snow climatology for the control and transient runs in figures 4.5 and 4.6 are so similar it is reasonable to assume that the differences between the flux-adjusted and transient climatologies would look much the same as those plotted in 4.9, particularly over Eurasia).

## 4.5 Snow in reanalyses

### 4.5.1 ERA40

ERA40 is a widely-used second generation reanalysis product from the European Centre for Medium Range Weather Forecasting (ECMWF, Uppala et al. (2005)). It provides the atmospheric data for the GCEP project to constrain and validate HadCM3. This section describes the product and its snow component.

ERA40 provides global climatologies of a range of surface and atmospheric variables for the time period mid-1957 to 2001. The ERA40 system produces a new analysis every 6 hours. A background field is generated as a short range forecast from the previous analysis, and observations are assimilated into this analysis, using statistically-based estimates of the errors in both the observations and the background model. Three dimensional variational assimilation (3DVar) is the method used in ERA40, a process which minimises the sum of deviations of the analysis from both the observation and background fields. The biases in the reanalysis will depend on the model physics and the dynamical and physical relationships within the statistical error estimates, and will vary spatially and temporally, and from variable to variable.

The model used to produce the analysis is based on the ECMWF's Integrated Forecast System (IFS), the operational medium-range weather forecasting system used at the Centre. Observations come from a range of satellites, radiosondes and ground observations, which are described in more depth on the ERA40 project website<sup>1</sup>. Snow depths from surface synoptic reports are assimilated, and while many SSM/I brightness temperatures are assimilated, no retrieved snow products are used. As the IFS has no ocean component, SST data are needed to supply boundary conditions to the atmospheric model over the oceans. These data come from the UK Met Office's HADISST1 (until November 1981) and the NOAA/NCEP 2D-Var dataset (thereafter until June 2001).

There are a number of known problems with the ERA40 dataset, in particular that the rain rate over the tropical oceans is too high, and too low over the extratropics.

---

<sup>1</sup>ERA website: <http://www.ecmwf.int/research/era/ERA-40/Observations/index.html>

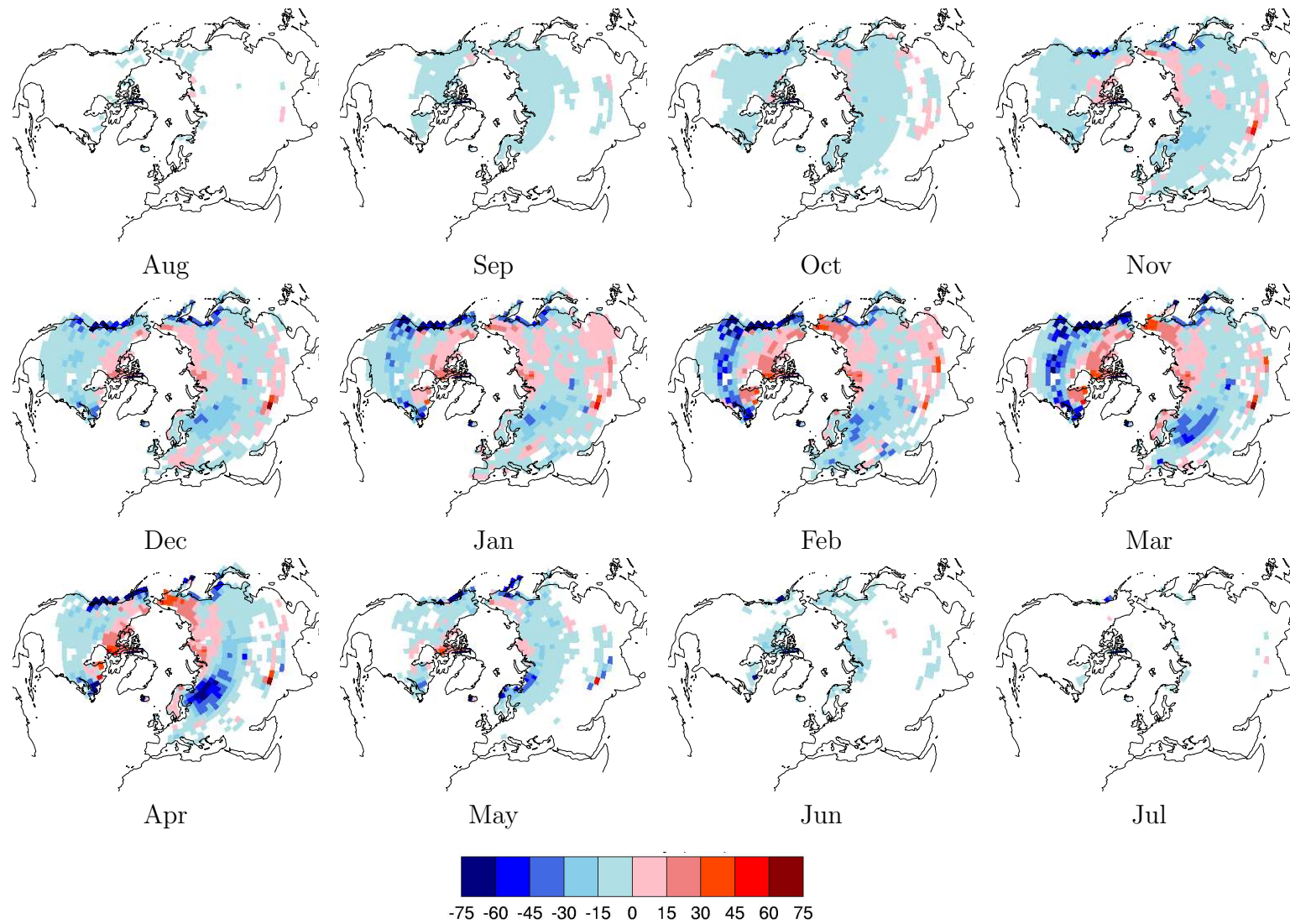


Figure 4.9: Seasonal cycle of monthly snow water equivalent (mm) for a flux-adjusted run of HadCM3, expressed as departures from the control climatology in figure 4.5. The flux adjustment run is for 1994-2004.

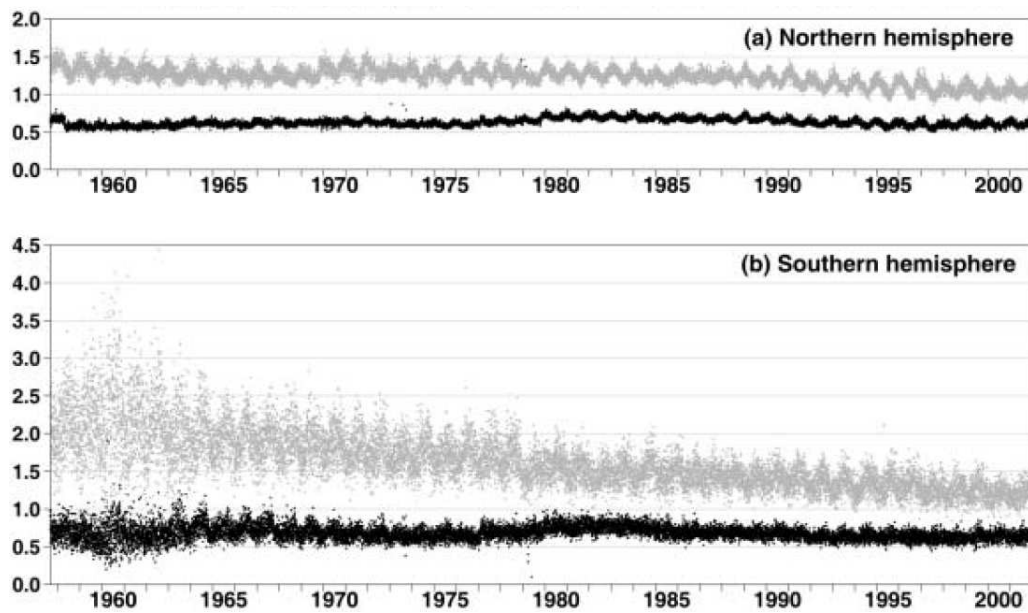


Figure 4.10: Daily values of the ERA40 RMS background (grey) and analysis (black) fits to daily 500hPa extratropical radiosonde measurements of temperature (K) for (a) Northern hemisphere and (b) Southern hemisphere. After Uppala et al. (2005).

Constraining the model at high latitudes is difficult, especially as there are few radiosonde measurements over Russia through the 1990s. At the start of the ERA40 epoch, a lack of reports from surface stations adversely affects 2m temperature estimates which leads to biases in the soil moisture in particular. Despite these issues, the ERA40 dataset compares well against many independent observations. Figure 4.10 shows one example: RMS fits to daily temperature measurements at 850hPa. The background field is shown in black, and the reanalysis in grey. The assimilated observations are clearly improving the RMS fit in both hemispheres, with particularly improvement seen in the Southern hemisphere in the later part of the time series, as more satellite observations become available. Reichler and Kim (2008) have undertaken a systematic assessment of the time mean errors and uncertainties of a number of reanalysis products over the period 1979-1999, and find that the ERA40 dataset is the best match for the observations used, which include a wide variety of both dynamical and physical atmospheric quantities.

### ERA40 land surface

A new surface scheme was designed for the ERA40 project, and a series of offline experiments are described in van den Hurk et al. (2000). The main innovation in the new scheme is the use of tiled surface characteristics to represent sub-gridscale

heterogeneity. Each land surface gridbox is comprised of appropriate areal fractions of bare soil, high vegetation, low vegetation, high vegetation with snow underneath, snow on low vegetation and a canopy interception layer. Snow water equivalent is a prognostic variable, and the fraction of the gridbox covered by snow is linearly related to the SWE in that gridbox. The scheme has an explicit snowpack layer with prognostic equations for the snow albedo and density. The snow albedo is only used for exposed snow; snow under vegetation has a reduced albedo of 0.2. This was found to dramatically reduce errors in the 850hPa temperatures in March and April in the boreal forest regions (Viterbo and Betts, 1999).

Evaluation of the land surface scheme in snow conditions was performed with data from the BOREAS field campaign (Sellers et al., 1997). The results (figure 4.11) showed that in this offline simulation, snow depth in the new (tiled) model was improved over the previous (control) model, though was still an underestimate of the actual snow depth. This was more likely due to inaccurate precipitation forcing data suffering from gauge under-catch than model bias. The tiled scheme delays snowmelt realistically, as seen in other studies with tiled models (Essery et al., 2005). The addition of soil freezing leads to large runoff peaks not seen in the control runs (figure 4.12), and the temperature of the top soil layer is increased due to the insulating effect of the separate snowpack above. These changes were shown to make particular improvements to the turbulent fluxes above boreal forests, with beneficial impacts on the surface Bowen ratio and the atmospheric boundary layer.

The ECMWF land surface scheme, like MOSES above, took part in part 2(e) of the PILPS study (Bowling et al., 2003a). While one configuration of the scheme was run with calibration for the basin, it is the uncalibrated run that is considered here, as this will better reflect the performance of the scheme globally in the ERA40 product. Like MOSES, the uncalibrated ECMWF scheme was also placed in group 4. The average annual latent heat was high (though not as high as MOSES), and the average annual sensible heat flux was low, almost equal to that of MOSES. Basin average snow water equivalent, however, was higher. Total runoff was similar to that of MOSES, though a greater proportion was subsurface flow.

Uppala et al. (2005) note that there is an error in the ERA40 snow analysis between 1992 and 1994. Figure 4.13 shows the time series of anomaly SWE values in North America and Eurasia (referenced to the 1958-1987 monthly climatology). This suggests that the error is present from 1989 onwards, so for the rest of this thesis all ERA40 SWE data between 1989 and 1994 are omitted. The ERA40 SWE climatology for 1958-2001, with these years omitted, is shown in figure 4.14.

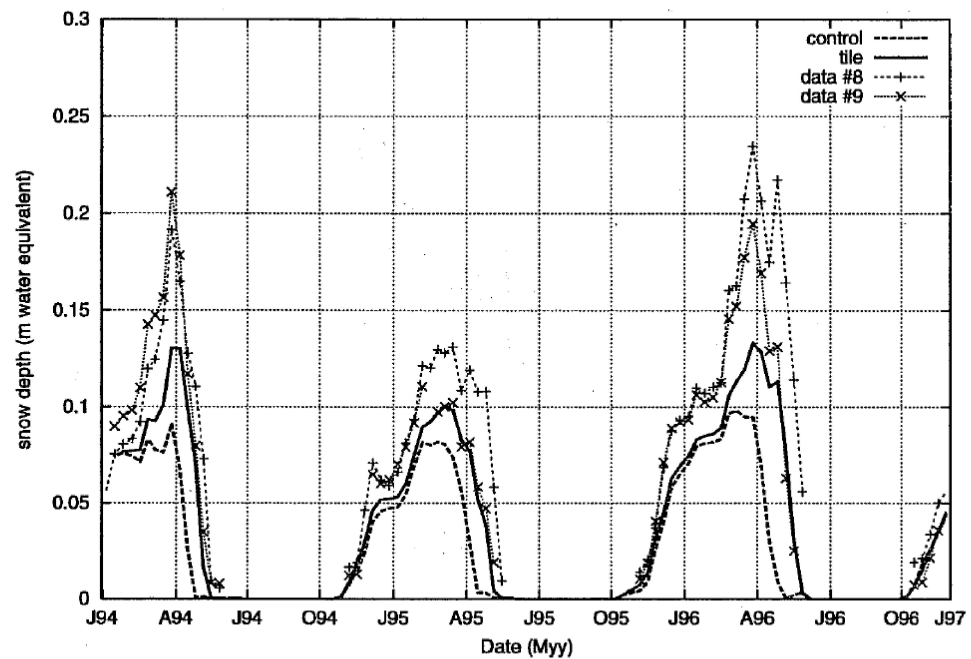


Figure 4.11: Improvement of snow water equivalent predictions in the tiled version of the ERA40 land surface scheme (solid line) as compared to the control version (dashed), after van den Hurk et al. (2000). In situ data comes from the BOREAS field experiment (dashed with crosses).

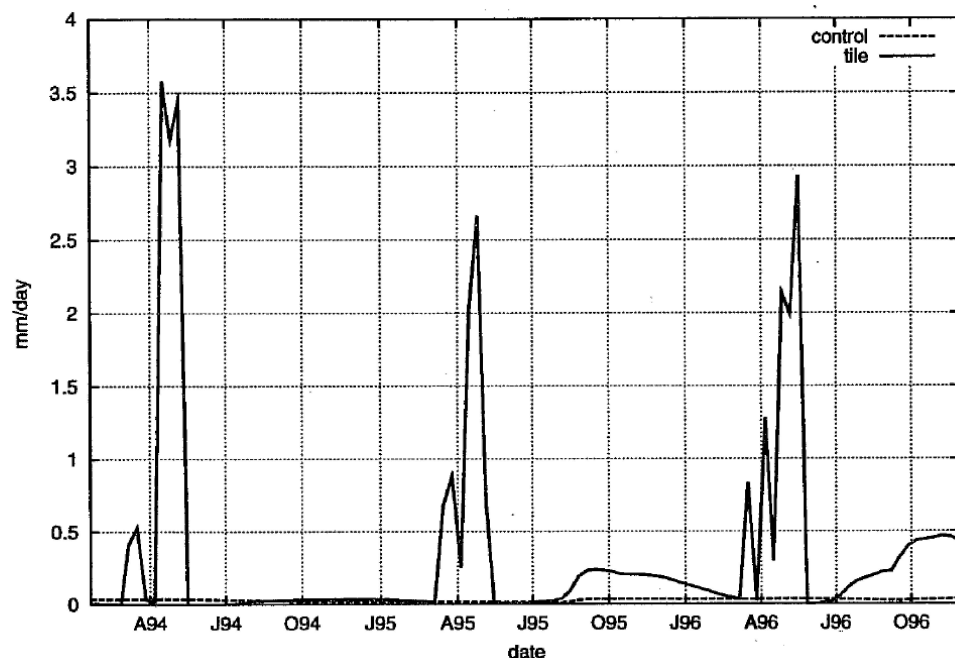


Figure 4.12: Differences in simulated runoff between the tiled version of the ERA40 land surface scheme (solid line) as compared to the control version (dashed), after van den Hurk et al. (2000).

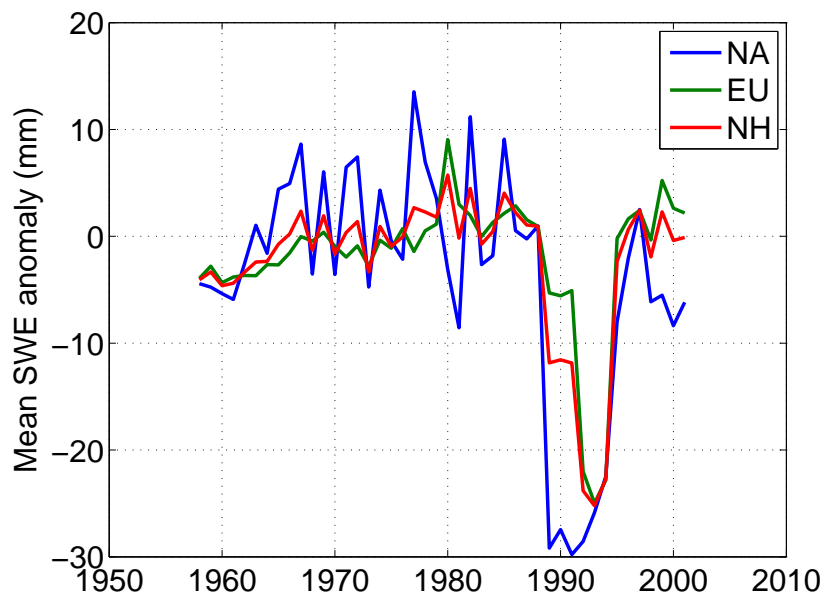


Figure 4.13: ERA40 North American (blue), Eurasian (green) and Northern hemisphere (red) mean SWE anomaly time series (mm). Anomalies are referenced to 1958-1987 climatology.

SWE begins to accumulate in September in the Canadian Archipelago, north-eastern Siberia and the Himalayas. The snowline spreads southwards through October and water equivalents of greater than 100mm begin to appear in Alaska and northern central and far northeastern Siberia in November. Water equivalent values reach a maximum in March in central Siberia and northeastern Canada. The snowline recedes fairly rapidly during Spring with the only snow cover remaining in June at highest latitudes and over the Himalayas. July and August are almost entirely snow-free.

#### 4.5.2 Other reanalysis products

A number of other global reanalysis products are available. Prior to ERA40, ECMWF produced a 15-year reanalysis beginning in 1979, called ERA15 (Gibson et al., 1997). This first generation reanalysis contained several deficiencies which were specifically addressed in the creation of ERA40, and hence the earlier reanalysis will not be considered further in this thesis.

The United States National Centre for Environmental Prediction (NCEP), in collaboration with the National Center for Atmospheric Research (NCAR), produce a reanalysis which stretches back to 1948 and is ongoing in near-real time (Kalnay et al., 1996). A later collaboration between NCEP and the Department of Energy improved

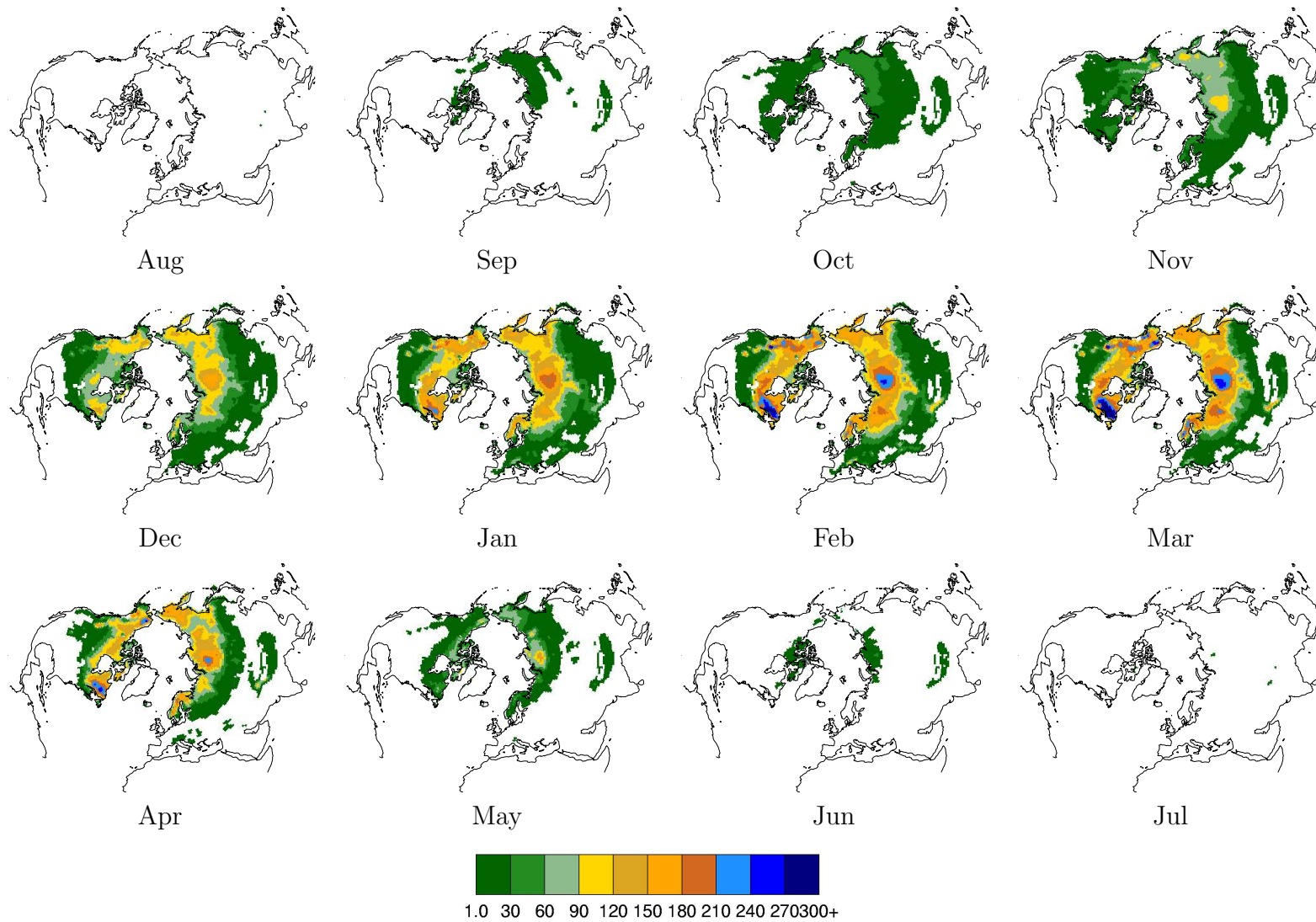


Figure 4.14: ERA40 monthly SWE climatology (mm) for the years 1958-2001, omitting 1989-1994 which contained an error in the snow analysis. Note that permanent ice sheets such as Greenland are masked.

upon the earlier product and has data for 1979 onwards. This revised reanalysis system aimed to fix errors and improve parameterizations in the earlier reanalysis, although it is not considered a ‘second generation’ reanalysis product as it remains at low resolution and there is no direct assimilation of satellite brightness temperatures (Kanamitsu et al., 2002).

A North American snow reanalysis at 0.25 degree resolution was produced by Brown et al. (2003) to provide a dataset for AMIP model evaluation. A first-guess SWE field was produced using a simple snow model driven by meteorological forcing data from ERA15, then snow depth observations from 8000 meteorological stations across the US and Canada were blended into this background field using optimal interpolation. Evaluation using independent in situ and satellite data showed the product successfully captured the main features of continental SWE and snow extent variations, although the product is less reliable at latitudes greater than 50° N as station data here are sparse. Unfortunately no equivalent product exists for Eurasia.

The Brown et al. reanalysis data is plotted in figure 4.15. Note that the product does not extend across Alaska to the edge of the continent. Some SWE is present all year round in the Canadian Arctic and parts of Alaska, but becomes more extensive in September. Through October and November the snowline advances and at the highest latitudes deepens to over 60mm. In December and January deeper snow becomes more extensive along the west coast and to the east of Hudson Bay, and through February and March the coasts are joined by a band of deeper SWE (>150mm in places) along the boreal forest region. The snowline retreats in April, although SWE on the west and NE coasts continues to deepen. The snowline continues to retreat through May and June until only a few patches of SWE remain in July. At high latitudes, the product shows many ‘bullseye’ features which are a consequence of the interpolation of sparse in situ data points in these areas.

A further reanalysis product is under generation at ECMWF. The ERA-Interim analysis implements a higher model resolution than ERA40, and 4D variational data assimilation, where the influence of an observation extends through time as well as space. Improvements to physical parameterizations and the use of satellite brightness temperatures are also included, though the observation database is largely the same as ERA40. Ten years of this new product became available in early 2008. ERA40 data are used in preference in this thesis for consistency with the rest of the GCEP project.

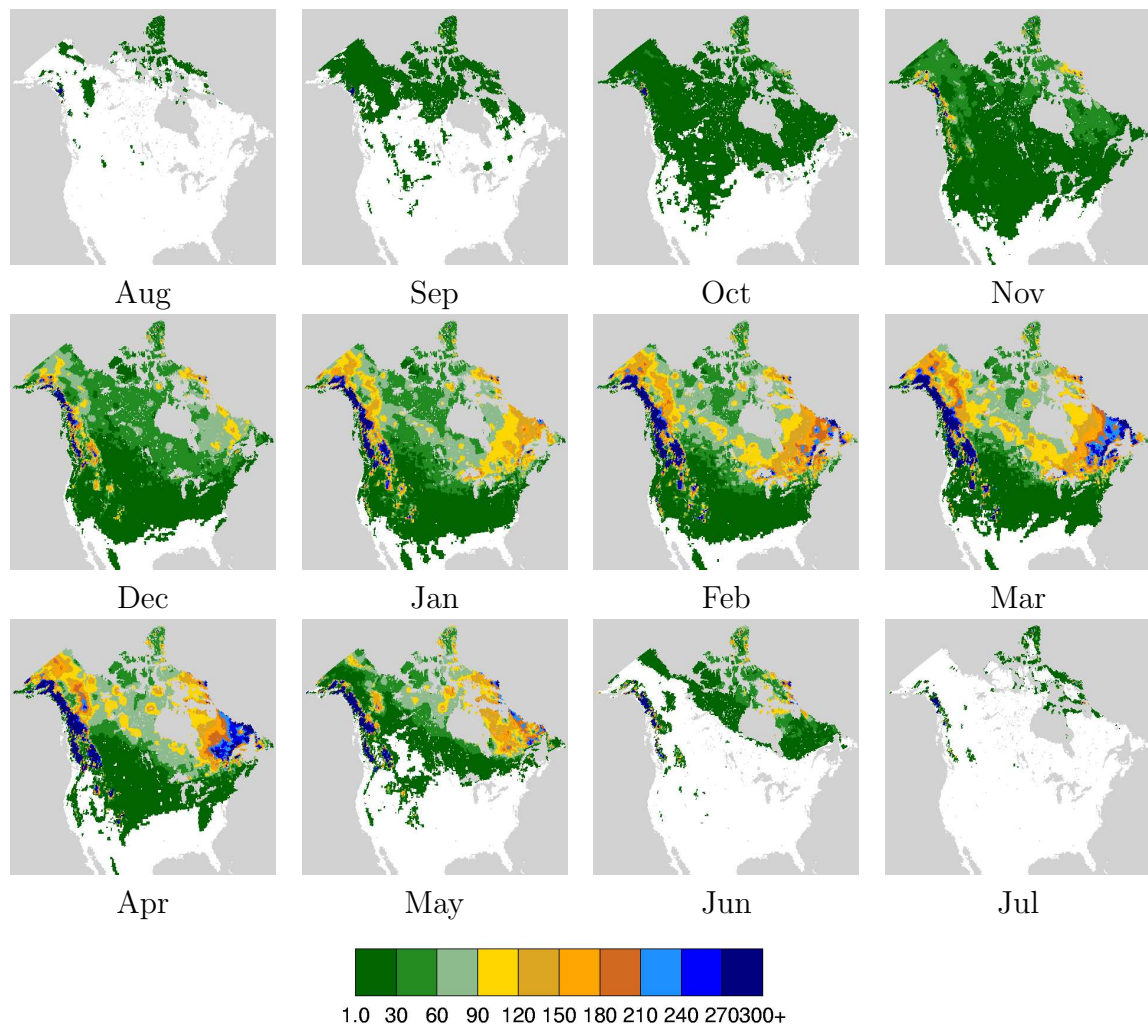


Figure 4.15: Monthly SWE climatology (mm) for North America from Brown et al. (2003).

## 4.6 Discussion

A GCM is required to study the role of snow in the global climate. HadCM3 has been chosen for the GCEP project thanks to a combination of its low resolution (to allow it to be run on a compute cluster instead of a supercomputer) and good representation of seasonal to decadal variability. A disadvantage of this GCM for studies of the land surface is its low land-atmosphere coupling strength. This suggests that initial conditions over the land surface will have little impact on the evolution of longer term model runs, although the impact of the variability of other fields (such as temperature and precipitation) on snow can still be studied.

This chapter has examined the climatology of HadCM3 and its land surface component, MOSES, with respect to snow. HadCM3 produces deep SWE along the Pacific coasts of North America and Eurasia, and also in the western half Eurasia and northeastern Canada. Little snow is seen in Siberia. The SWE distribution is little changed in a transient run with increasing greenhouse gases when compared to a pre-industrial control. A run with flux adjustments generally reduces SWE across the hemisphere, with increases confined to the higher latitudes.

The land surface component, MOSES, has been studied independently of the GCM by Slater et al. (2001). It produces a lower SWE in a 1D analysis at a grassland site compared to other land surface models driven by the same forcing data. MOSES has a simplistic snow scheme based around an implicit snow layer, which means that when snow falls, the top layers of the land surface model become combined snow/soil layers. This leads to the model melting snow too quickly, because the increased albedo of the merged snow and soil leads to additional solar energy being absorbed by the layer. MOSES also produced low SWE estimates for a high latitude basin compared to other schemes (Bowling et al., 2003a), and overestimates latent heat flux.

While HadCM3 is an older model, many aspects of it have been well-studied, and its participation in CMIP3 allows comparison with other state of the art climate models. Although the snow cover in the atmosphere-only GCM has been studied as part of AMIP2, the biases in the AOGCM are very different and should not be compared. The land surface model is crude and less well-studied than the atmosphere and ocean components, so a study of snow is an important addition to the body of work surrounding this coupled model.

The outcome of CMIP is encouraging with respect to GCMs: in general, the difference between a typical model simulation and observations is comparable to the differences between observational datasets from different sources. Some fields are better simulated than others, however, which can be related to the quality of observational

datasets with which to validate the models. Surface temperature is observed and modelled with some confidence, while precipitation remains a challenge in both respects (Covey et al., 2003).

Observations of many different fields are used to constrain the ERA40 reanalysis product. This includes in situ snow data from meteorological stations around the world, although these stations are sparse at high latitudes. The land surface scheme was compared to that of HadCM3 in part 2(e) of PILPS (Bowling et al., 2003a), and the results were very similar to that of MOSES, despite the greater complexity of the ECMWF scheme.

ERA40 has been well-studied, and the analysis of Reichler and Kim (2008) supports the use of ERA40 in this thesis as the best available reanalysis product. Further work by the same authors suggests that HadCM3 also performs well against other coupled climate models (Reichler, pers. comm. 2008), although snow fields were not used in this comparison.

Hemispheric-scale comparison of snow distribution from models, reanalysis products and observations is required in order to use the model for understanding climate interactions and producing reliable forecasts. The evaluation of the HadCM3 snow climatology against both ERA40 and the SSM/I-derived SWE is the subject of the next chapter.

# Chapter 5

## Comparison of hemispheric-scale snow climatologies

### 5.1 Introduction

Three sources of global SWE data used in this thesis have been introduced in the last two chapters: satellite observations from SSM/I, the HadCM3 coupled climate model and the ERA40 reanalysis product. Comparing datasets at large scales is a difficult task, and attempts with snow mass data have been infrequent. Biases in both the modelled and observed datasets are known to exist, but are difficult to quantify, particularly for remote regions. Foster et al. (1996) used SMMR-derived SWE data to validate snow distribution in seven GCMs, including a Hadley Centre model which was a precursor to HadCM2. SMMR data was also used by Yang et al. (1999) in a study of NCAR's CCM3 climate model, and the authors concluded that the GCM distribution was more reliable. Both studies used a global snow dataset from the US Air Force Environmental Technical Applications Center (Foster and Davy, 1988), which used synoptic stations, literature searches and climatological records to reconstruct manually a gridded hemispheric snow depth product. While this constitutes an independent, observation-based data source, Foster and Davy themselves acknowledge low confidence in data at high latitudes, and systematic biases have been identified by Brown and Frei (2007), which are particularly problematic over Eurasia. Brown and Frei go on to note that “there is no detailed snow depth of SWE reanalysis available for evaluating...SWE results for Eurasia”.

With new generations of climate models emerging all the time, the evaluation of global snow distribution is a topic which must be returned to, particularly in the context of understanding how it may be affected by climate change. In this chapter the climatologies of SSM/I, HadCM3 and ERA40 are compared. While a full quantitative

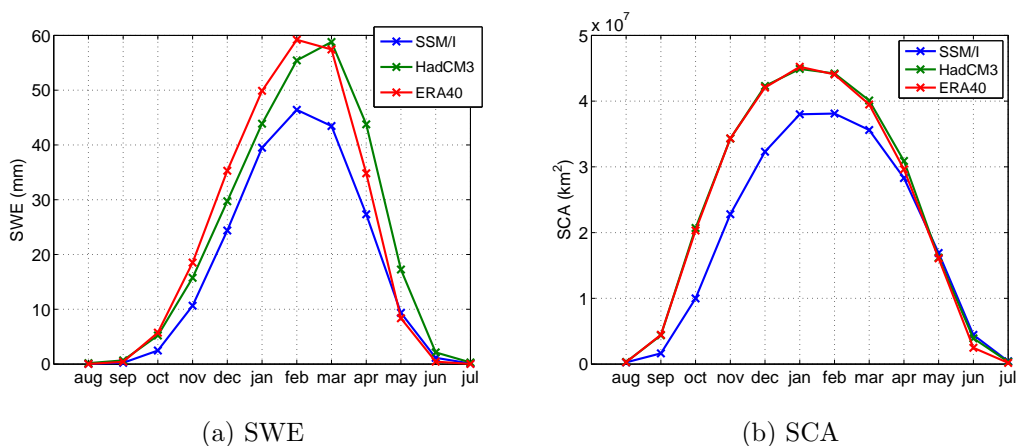


Figure 5.1: Northern hemisphere average climatologies of SWE (mm) and SCA (km<sup>2</sup>) from SSM/I (blue), HadCM3 (green) and ERA40 (red).

error assessment of the three datasets is outside the scope of this thesis, attempts are made to understand the sources of the differences between them. To do this, we examine alternative models and retrieval algorithms, and use long-term runoff data as an independent estimate of winter snow mass.

## 5.2 Climatologies in SSM/I, HadCM3 and ERA40

Figure 5.1 shows the average seasonal cycle for Northern hemisphere SWE and snow-covered area (SCA) for all three datasets. ERA40 has the deepest SWE values during the accumulation period, followed by HadCM3, with SSM/I the lowest. SSM/I and ERA40 both produce peak SWE in February while the HadCM3 peak is in March. HadCM3 then has the most SWE during the melting period with SSM/I again showing the lowest values, although SSM/I and ERA40 are almost equal in May. Examining the seasonal cycle of SCA (figure 5.1b), HadCM3 and ERA40 are almost identical throughout the season, with a peak SCA in January of around 45 million square kilometres. SSM/I shows less than 40 million square kilometres at its peak (also in January), although the three datasets agree from April onwards. It is not surprising that SSM/I shows the lowest values of SCA, as the retrieval is unable to detect very thin snow cover. Data from the MODIS instrument suggest a maximum value of 47 million square kilometres in January, supporting the values seen in HadCM3 and ERA40 (Armstrong and Brodzik, 2001).

Previous chapters have shown the month-by-month climatologies for the three global datasets (figures 3.3, 4.5 and 4.14). Plotting February values side by side in figure

5.2, together with the February climatology for North America from the reanalysis of Brown et al., it is clear that the climatologies for this month are quite different. The model produces much more snow over western Eurasia and very little ( $< 60\text{mm}$ ) over Siberia, whereas in contrast the satellite observations show the deepest snow in Siberia ( $> 150\text{mm}$ ) and shallower snow in western Eurasia. ERA40 is more similar to the SSM/I retrievals than the model, although the maximum is located further west than in the SSM/I data. ECMWF have been investigating this, and have found that an improvement to the parameterization of the aerodynamic surface roughness over snow shifts the location of this maximum further east (G. Balsomo, pers. comm., 2008). In North America, very deep values are seen along the west coast and northeastern Canada in HadCM3, with less in the boreal forests in between. This is also seen in the Brown reanalysis; although in situ data from Canada are sparse, this product relies more on model data at high latitudes. HadCM3 shows more SWE in the United States than the Brown reanalysis, which is well-constrained in this region. Chapter 4 showed climatologies from both a normal control run of HadCM3, and a similar one with sea surface flux adjustments (figures 4.5 and 4.9 respectively). The flux adjustments reduced the SWE in the United States, the west coast of North America and western Eurasia, while adding SWE in eastern Siberia and the Canadian Arctic. These changes bring the model climatology closer to that of ERA40 and the Brown reanalysis.

ERA40 shows a similar pattern to HadCM3 with some deeper snow in the boreal forests. SSM/I, in contrast, shows its deepest values in the boreal forests, as part of a deep SWE band crossing the continent. Ground investigations by Derksen and MacKay (2006) confirmed the presence of this SWE gradient across the northern boreal forest, and their simulations with a climate model suggested it is formed each autumn by lower tropospheric frontal activity aligned with the boreal forest.

A study of long term in situ daily snow depth and SWE data was performed by Kitaev et al. (2005). They found that SWE values  $> 250\text{mm}$  are typical for western North America (due to the effect of the Aleutian Low and orography), while maximum Eurasian values are in Western Siberia (133mm) and the Eastern European plain (110mm), with values of 90mm found in Eastern Siberia. The ERA40 data comes closest to this distribution, which is to be expected since the ERA40 system assimilates the in situ data from WMO stations. In situ data from the Former Soviet Union (as distributed by the NSIDC (Krenke, 2004) and discussed in Kripalani and Kulkarni (1999)) also find that snow depths of over 60cm in Siberia are not uncommon.

Figure 5.3 reproduces EOF and PC3 from the EOF analysis of SSM/I data performed in chapter 3. Interestingly, this pattern is reminiscent of the distribution of SWE in HadCM3, with red areas corresponding to regions of deeper SWE (western

Eurasia, Kamchatka, northern and eastern Canada and the west coast of North America), and blue areas corresponding to region of reduced SWE. The PC shows that in the SSM/I dataset, this pattern is expressed positively (more snow in the red areas) in Spring and negatively (less snow in the red areas) in Autumn. This could be interpreted in two different ways: the model could be reproducing only part of the seasonal cycle of SWE, due to errors or deficiencies in the model, or the SSM/I data are contaminated by the seasonal cycle of other fields, such as vegetation, reducing the proportion of variance explained by this pattern. A closer examination of both the retrieval and the model are required to determine which of these interpretations is correct.

Gong and Entekhabi (2002) suggest that Siberian snow, particularly as it forms in autumn, is important in influencing the circulation across the Northern hemisphere. In a later paper, Gong et al. (2003) go so far as to describe Siberia as “the region with the greatest potential for snow-forced climate modulation”. It is clear that the differences between these datasets across this crucial region must be understood, however there is a lack of data to do so. Various SWE reanalyses have been produced for North America using different sources of observations and models of varying complexity (Brown et al., 2003; Brasnett, 1999; Foster and Davy, 1988), however no such reanalysis exists for Eurasia. In the next section (5.3), runoff data is examined as a means of validating SWE in the region. In the following two sections (5.4 and 5.5), the errors in both the satellite retrieval and climate model will be discussed in more detail. Particular attention will be paid to the differences that have emerged in Siberia and the boreal forests.

### 5.3 Comparison with runoff data

Patterns at this large scale are difficult to validate with point SWE measurements, so as an alternative, summer runoff data is presented here as an integrated in situ measurement of the previous winter’s snow accumulation. The Global Runoff Data Center provide monthly average discharge rates for 35 large catchments worldwide, based on decades of in situ measurements (Dumenil Gates et al., 2000). Relevant Siberian catchments included in the dataset are shown in figure 5.4, together with each catchment’s average measured hydrograph. All three show a distinct peak in June, characteristic of snowmelt. The runoff observations are multidecadal averages, and the Lena values in particular show tight confidence limits.

A ‘water equivalent’ value can be derived for each catchment by summing the May, June and July discharges and dividing them by the area of the catchment. These water

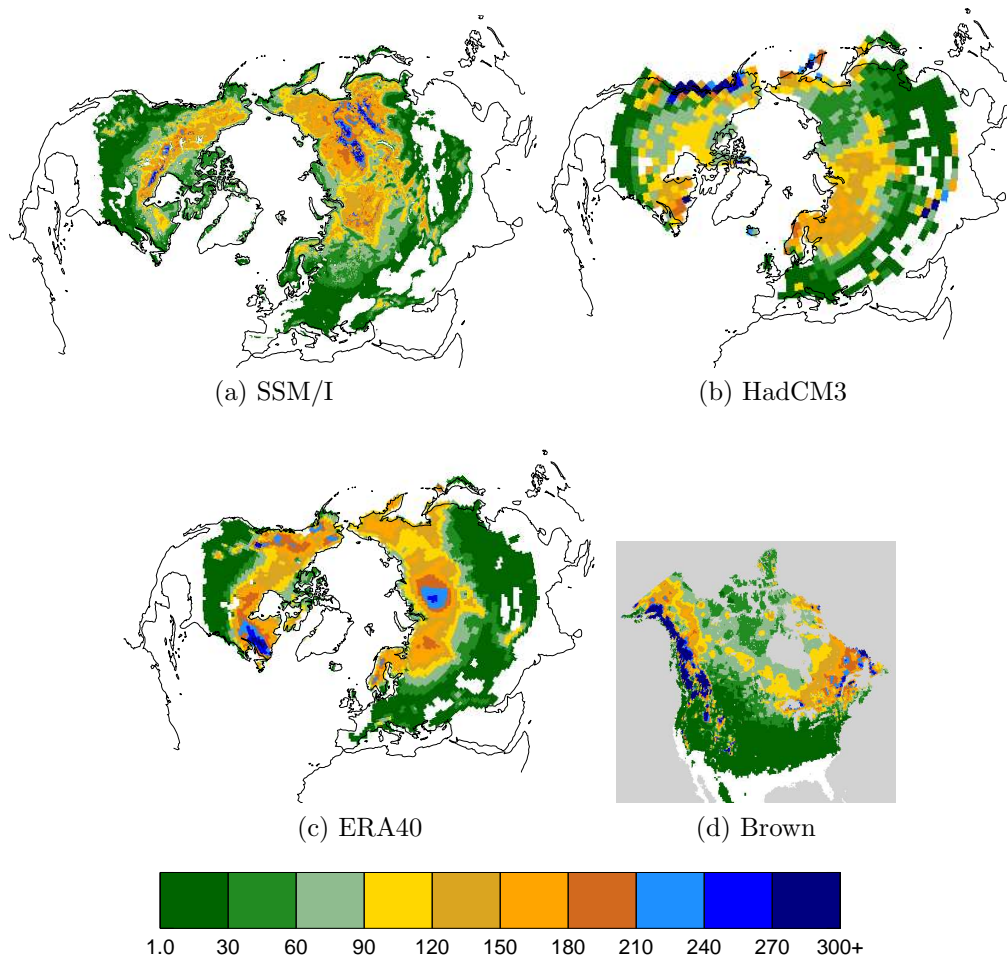


Figure 5.2: February SWE climatology (mm) from SSM/I, HadCM3, ERA40 and the Brown et al. reanalysis.

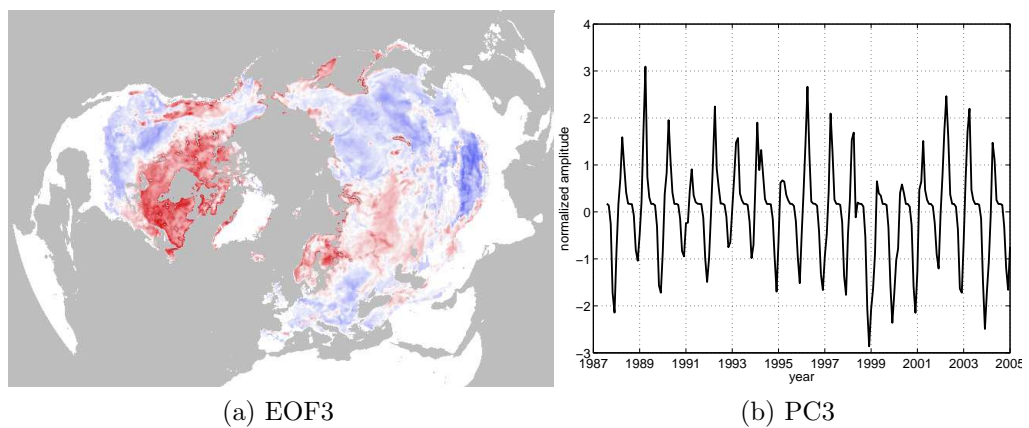


Figure 5.3: EOF3 and PC3 of SSM/I SWE data, as presented previously in chapter 3.

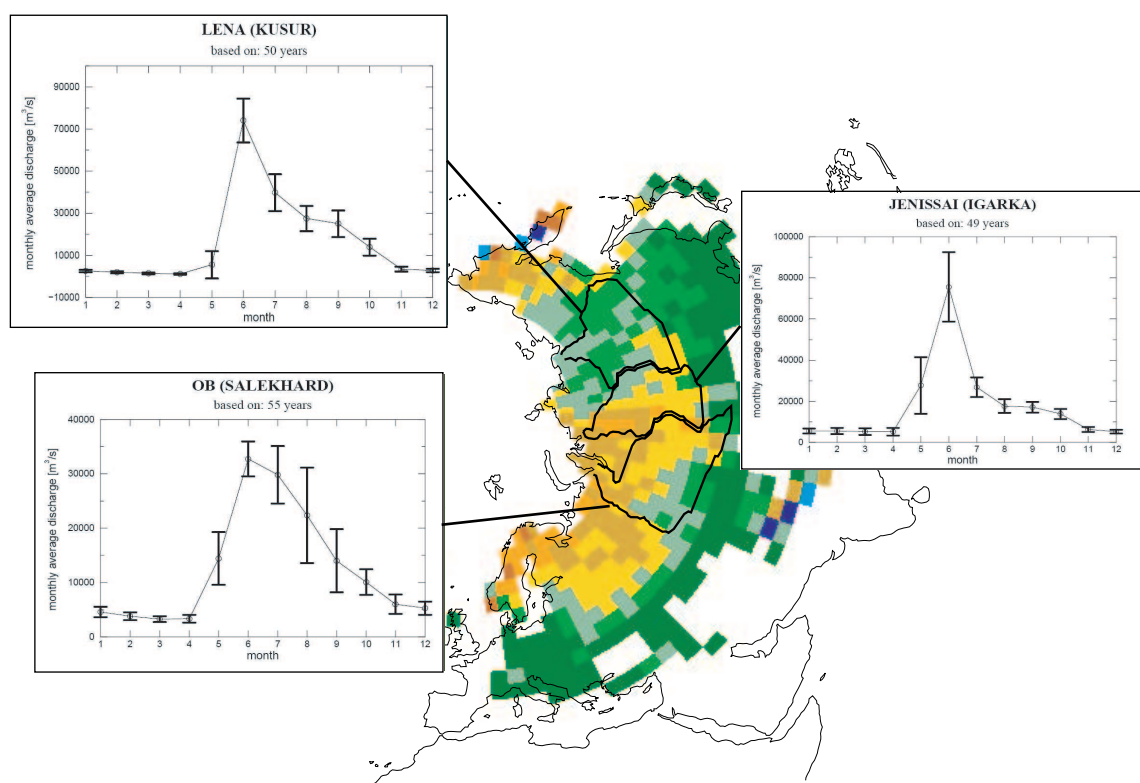


Figure 5.4: Three large Siberian catchments (the Ob, Yenisey and Lena) and their hydrographs from Dumenil Gates et al. (2000).

equivalent values are shown in table 5.1. The largest water equivalent is found for the Yenisey river, which coincides with the location of maximum SWE in ERA40. The value for the Lena catchment (where the maximum SWE from the satellite data is found) is almost as large, and is double the value for the Ob catchment - the opposite way round to the model.

The Met Office have used a river routing model to generate hydrographs from HadCM3. Results from this comparison for the large Eurasian catchments are shown in figure 5.5 (paper submitted to Journal of Hydrology). Discharge in the Ob is well-modelled, but HadCM3 is not generating enough summer discharge to match the

Table 5.1: Water equivalents required across the Siberian catchments to produce observed May+June+July discharge found in the average hydrograph

River	Catchment Area (km <sup>2</sup> )	Discharge (m <sup>3</sup> /s)			Water equivalent (mm)
		May	June	July	
Lena	2430000	5000	75000	40000	<b>130</b>
Yenisey	24400000	30000	75000	30000	<b>150</b>
Ob	2950000	15000	33000	30000	<b>70</b>

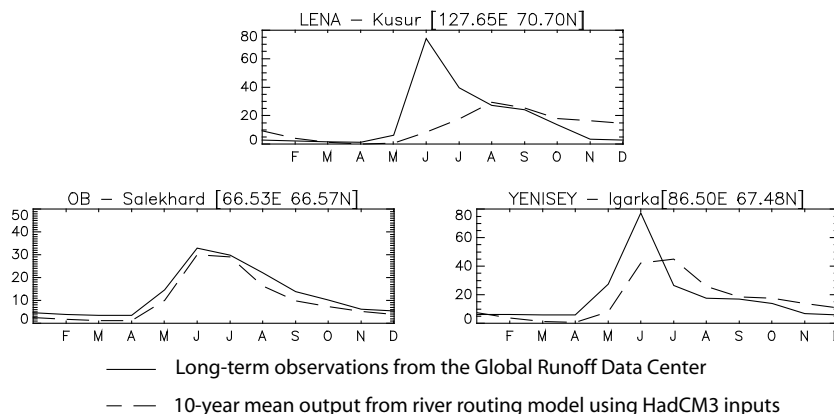


Figure 5.5: Comparison of discharge from HadCM3 (dashed) and observations (solid), after Falloon and Betts (in press, 2008)

observations in the Lena and Yenisey catchments. The HadCM3 hydrograph for the Lena shows no distinct snowmelt peak, which is consistent with the lack of snow in the region. The study of runoff generated by land surface schemes in part 2(e) of PILPS (Bowling et al., 2003a) showed that MOSES tended to underestimate runoff, mainly due to low snow accumulation. This study was performed at a high latitude basin, and while the Lena is a much larger catchment, many of the characteristics are shared, such as the dominance of snow in the land surface hydrology and limited energy input over winter.

Yang et al. (2007) also investigate SWE in the Lena basin. The authors compile weekly SWE accumulation measurements from microwave data in the Lena, Ob and Yenisey basins, and discuss the impact of catchment management (such as damming) on Lena runoff data. SWE in the Lena appears deeper than SWE in the other catchments, but melts more quickly. The authors also state that the Lena basin is completely permafrost, and that this leads to high summer runoff and very low winter runoff. This again supports the observed hydrograph over the modelled hydrograph of HadCM3.

Although these runoff measurements appear to support the distribution in the SSM/I data, this result should be treated with some caution. The Siberian rivers are hydrologically complex, with large deltas and layers of sediment containing up to 80% ice which can collapse in summer and release large amounts of water unexpectedly into rivers. Furthermore, Yang et al. (2002) suggest that summer discharge in the Lena river is only weakly correlated to snow depth, suggesting that other factors may be contributing to discharge in this catchment. However, using a dynamic retrieval algorithm, Grippa et al. (2005) find a correlation of 0.61 between SSM/I-derived snow depths and discharge in the Ob river in June, and a correlation of -0.92 between May runoff and snowmelt date, which suggests that snow depth is linked to runoff in May

and June, and to SSM/I measurements in the basin. Fukutomi et al. (2003) also state that the peak Lena runoff is due to snowmelt not summer precipitation.

## 5.4 A closer look at microwave retrievals

### 5.4.1 Errors in the static retrieval

While the analysis of runoff data presented above appears to support the larger values of the SSM/I data when compared to the model, a closer examination of the retrieval and other studies using microwave data are required to give confidence in the data. Could the large retrieved SWE values in Siberia and the boreal forests be an overestimate? The limitations of static difference retrievals were noted in chapter 3 and the treatment of grain size and vegetation are particularly important in this region.

Foster et al. (2005) propose a modified version of the original Chang algorithm (eqn. 3.1) to investigate the errors due to the effect of vegetation cover and the assumption of constant grain size. The new algorithm is:

$$\text{SWE}_{new} \text{ (mm)} = Fc(T_B19H - T_B37H) \quad (5.1)$$

$F$  and  $c$  are time- and space-varying coefficients, relating to forest cover and grain size respectively.  $F$  is a function of fractional forest cover, derived from the IGBP Land Cover data set (Loveland et al., 2000), and assumes an underestimation of SWE with increasing forest cover in the pixel. A new grain size coefficient,  $c$ , was estimated for each of the six characteristic Sturm classes (introduced in chapter 2) and evolved month by month. As expected, the new algorithm estimates more snow in densely forested areas. In general, during the months of January, February and March the increase was between 30 and 120mm, up to a maximum of 180mm in the extreme northern taiga region. When validated using meteorological station data across Canada, the new algorithm shows considerable improvement in the tundra and taiga classes, and some improvement in the maritime and alpine classes. The new algorithm also captures melting and ablation phases well. However there are still problems observed in dense maritime forests and alpine regions around the Great Lakes. It is suggested that this may be to do with the proximity to open water, warmer air temperatures and/or depth hoar.

Figure 3.6 showed the map of Sturm snow classes for Eurasia. Siberian snow is shown to be a mixture of tundra and taiga snow, which have significant amounts of depth hoar. These large depth hoar crystals scatter microwave radiation disproportionately, leading to an overestimation of the water equivalent: the radiometer ‘sees’

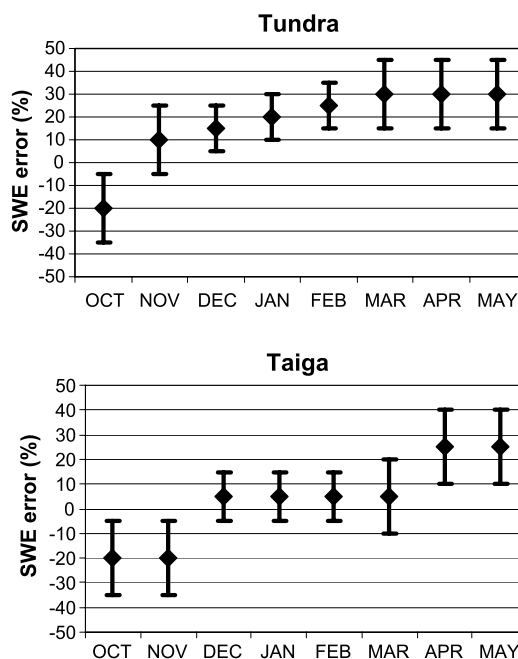


Figure 5.6: Estimate of SWE overestimation (%) per month by SSM/I retrieval due to the assumption of constant grain size in tundra and taiga regions, taken from Foster et al. (2005).

a deep snowpack, whereas in fact the snowpack is shallow and dense. But is this effect enough to explain the difference between the modelled snow and the satellite observations of Siberia? Figure 5.6 shows the attempt of Foster et al. (2005) to quantify the error in the retrieval due to the assumption of constant grain size in tundra and taiga areas. The maximum overestimation, according to their estimate, is 30%. Taking 180mm as a representative value of the satellite-derived SWE in Siberia in February, a revised estimate would be 120mm, which is still twice the modelled SWE in that area. The static algorithm has also been tested against observations in the tundra region: an investigation of passive microwave retrievals in the Kuparuk River Watershed in Alaska, a snowpack that is dominated by depth hoar, found that the Chang algorithm produced estimates within 30mm of the spatially averaged SWE for the watershed, despite large pixel-to-pixel errors (Koenig and Forster, 2004). This suggests that the assumption of a constant grain size becomes more representative at larger areas.

If the difference between the model and observational data were purely due to the effect of grain size on the retrievals, then we would expect it to manifest in late winter/early spring, when conditions are favourable for the formation of depth hoar. On the contrary, examining figures 3.3 and 4.5 it is clear that the difference is established as soon as the snowpack forms, when depth hoar would not yet be present.

Table 5.2: Summary of the error analysis of SWE retrieved from SMMR by Dong et al. (2005). Relative bias is the bias of a given half-degree pixel divided by the mean SWE retrieval for the 9 years used in the study.

Snow pack mass	90% SWE estimation bias for snowpacks deeper than 150mm. This error drops to less than 70% when values greater than 100mm are excluded.
Air temperature	Relative bias underestimation increases from less than 10% at -20°C to over 40% at 0°C
Distance to open water	Relative bias underestimation tends towards zero as the distance from open water increases, with a sharp improvement at a distance of 200km, where the relative bias is 50%
Roughness	Slight increases in relative errors are found with increasing roughness, but no obvious retrieval contamination
Forest fraction	No trend with forest fraction was observed, though there were large biases at some heavily forested stations. When pixels close to water and at higher air temperatures were omitted, the relative bias dropped to almost zero.

A quantified error analysis was performed using the equation derived above (eqn. 5.1) applied to brightness temperatures obtained from SMMR (Dong et al., 2005). The study was restricted to Canada, where in situ measurements for validation are much more dense than across Eurasia. In their analysis, the researchers considered snow pack mass, air temperature, distance to water, roughness, forest cover, snow class and aspect as factors contributing to errors in the retrieval. They found the error to be dominated by snow pack mass, with secondary factors being distance to open water and air temperature. Their results suggest that the adjustments to the retrieval for forest cover and grain size have removed the influence of these factors on the SWE error, with the exception of heavily forested pixels. They also show that much of the error in the maritime class can be attributed to higher air temperatures and the proximity of open water. A summary of their results is shown in table 5.2.

These results suggest that the forest cover adjustment  $F$  of Foster et al. reduces the effect of vegetation significantly, however Derksen et al. (2005) disagree with this practice of adjusting SWE retrievals purely according to the fraction of forest cover within a grid cell (a forest factor). Results from transects in Canada suggested that there is little or no correlation between fractional forest cover and SWE underestimation: forest inventory variables such as stem volume and canopy closure are suggested as more physically relevant to the retrieval. A forest factor approach is used in the SWE product considered here (see equation 3.3). A map of the forest

cover fraction, derived from MODIS data, was shown in figure 3.5. Much of Siberia is subject to large corrections (doubling wherever the pixel at least 50% forested), and if this approach is inappropriate, this could be a large overestimation. In fact, any values greater than  $\sim 150\text{mm}$  must come from the application of this forest correction, as the signal saturates around this value. If this is the case, and the forest factor approach is wrong, then this could explain the large biases seen for deep snowpacks (as noted in table 5.2).

### 5.4.2 Alternative retrieval techniques and satellite climatologies

The errors in this SSM/I SWE product derive from both the brightness temperature measurements and the retrieval algorithm used to derive the SWE value. Although no other satellite-based SWE product is freely available for comparison, other retrieval techniques have been tested using SSM/I data. Most SSM/I retrievals are performed with a static algorithm very similar to the one used in the NSIDC product and will not be considered separately here. Instead, presented here are two climatologies derived using dynamic retrieval algorithms (*i.e.* the algorithm is adjusted over time, usually with respect to a surface temperature history).

The dynamic retrieval of Josberger and Mognard (2002), described in chapter 3, has been used to derive a snow depth climatology for a portion of Siberia (Grippa et al., 2004). The January climatologies from the new ‘combined’ algorithm and the old ‘static’ algorithm are shown in figure 5.7. Both algorithms show maximum snow depths of over 60cm and a mean of around 30cm, which (assuming a snow density of  $250\text{ kg m}^{-3}$ ) equate to snow water equivalents of 240mm and 120mm respectively. The static retrieval locates the maximum snow depth about  $15^\circ$  eastward of the dynamic one, which the authors ascribe to the effect of depth hoar. Interestingly though, the dynamic retrieval does show a reduction in snow depth travelling east into the Lena catchment similar to HadCM3, although the values here are still much deeper than the shallow snow produced by the model.

An alternative dynamic retrieval derived by Kelly et al. (2003), and also introduced in chapter 3, has been applied to data from the SSM/I instrument. Figure 5.8 shows the retrieved snow depth (note, not snow water equivalent) using this revised dynamic algorithm compared to the static algorithm for one day in January 2000. The dynamic algorithm produces less snow over Siberia than both the static algorithm and the dynamic algorithm of Josberger and Mognard described above. It also produces shallower snow across the boreal forest region of Canada. Kelly et al. (2003) use snow depth data from over 1000 WMO stations to assess the spatial errors of the retrieved

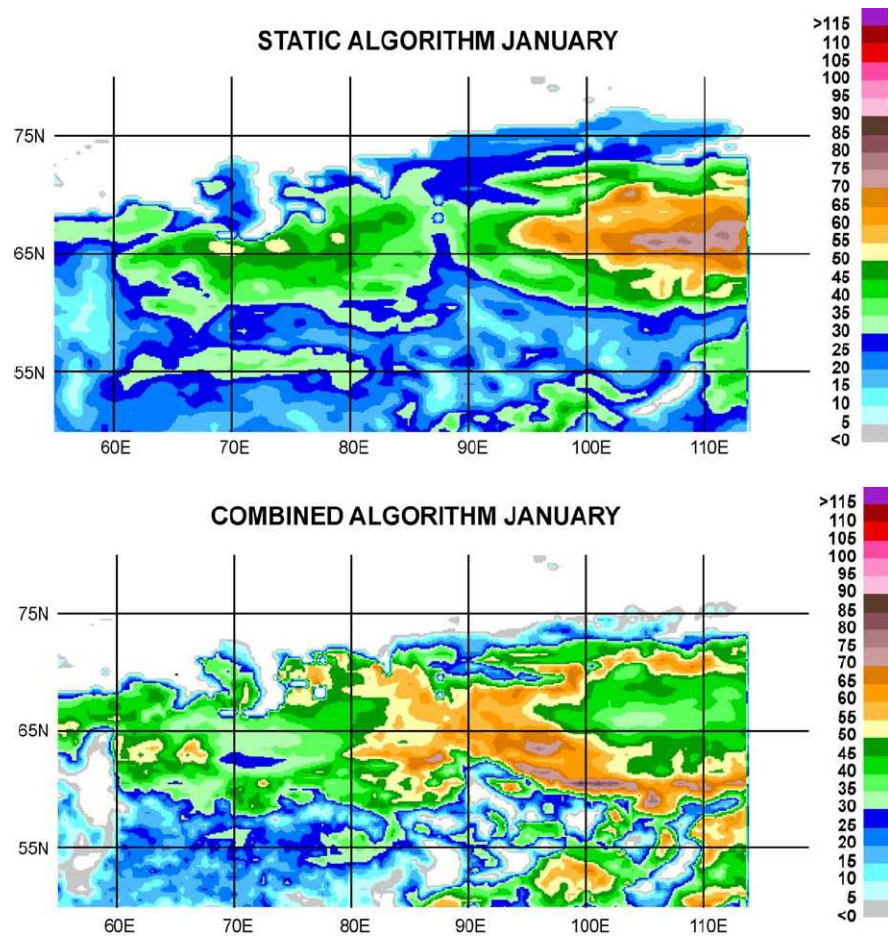


Figure 5.7: January Siberian snow depth climatologies from SSM/I (cm), using (upper) static and (lower) dynamic algorithms. Taken from Grippa et al. (2004).

snow depth. Both the static and dynamic algorithms underestimate the snow depth, particularly in boreal forest areas (no forest correction was used in this study). The mean error is smaller for the dynamic algorithm than for the static, although the root mean square error is larger, as a few locations are significantly biasing the overall value. This study shows that a dynamic algorithm is an improvement over the static version in most locations, although the effect of vegetation still hampers the accuracy of the data.

### 5.4.3 Retrievals summary

This section has looked in more detail at the static retrieval used in the global SSM/I SWE product in terms of its errors, and comparisons with other retrievals. Grain size and vegetation are identified as important sources of error in the static retrieval. While the assumption of a constant grain size at every location and time is clearly unphysical, the retrieval performs well over large areas (Derksen et al., 2005). Heterogeneity in the grain size within passive microwave satellite footprints, however, could explain why retrievals over larger areas are more representative than those applied at a point.

Retrievals that attempt to account for changes in grain size over a season (the dynamic approach) do show a reduction in SWE compared to the static retrieval over Siberia.

The effect of vegetation on SWE is poorly understood, and hence difficult to account for in the retrieval. Some authors (Dong et al., 2005; Foster et al., 2005) support the use of the forest factor approach applied in this global dataset, while others have questioned its validity (Derksen et al., 2005).

## 5.5 A closer look at GCM SWE modelling

### 5.5.1 HadCM3 and ERA40 SWE errors

Having examined the retrieval more closely, we now assess the limitations of the HadCM3 land surface model. The participation of MOSES in the PILPS intercomparison project was described in chapter 4. It was shown that for the same precipitation forcing, MOSES produces a lower SWE than other models, and that it melts SWE too quickly. Its simple representation of snow is also unlikely to simulate the surface temperature of the snow correctly, as shown by the SnowMIP study (Etchevers, 2004), leading to errors in the net longwave radiation. The surface could also become decoupled from the atmosphere under the conditions in Siberia in winter as the surface temperature and net radiation drop (Slater et al., 2001). These errors in the surface

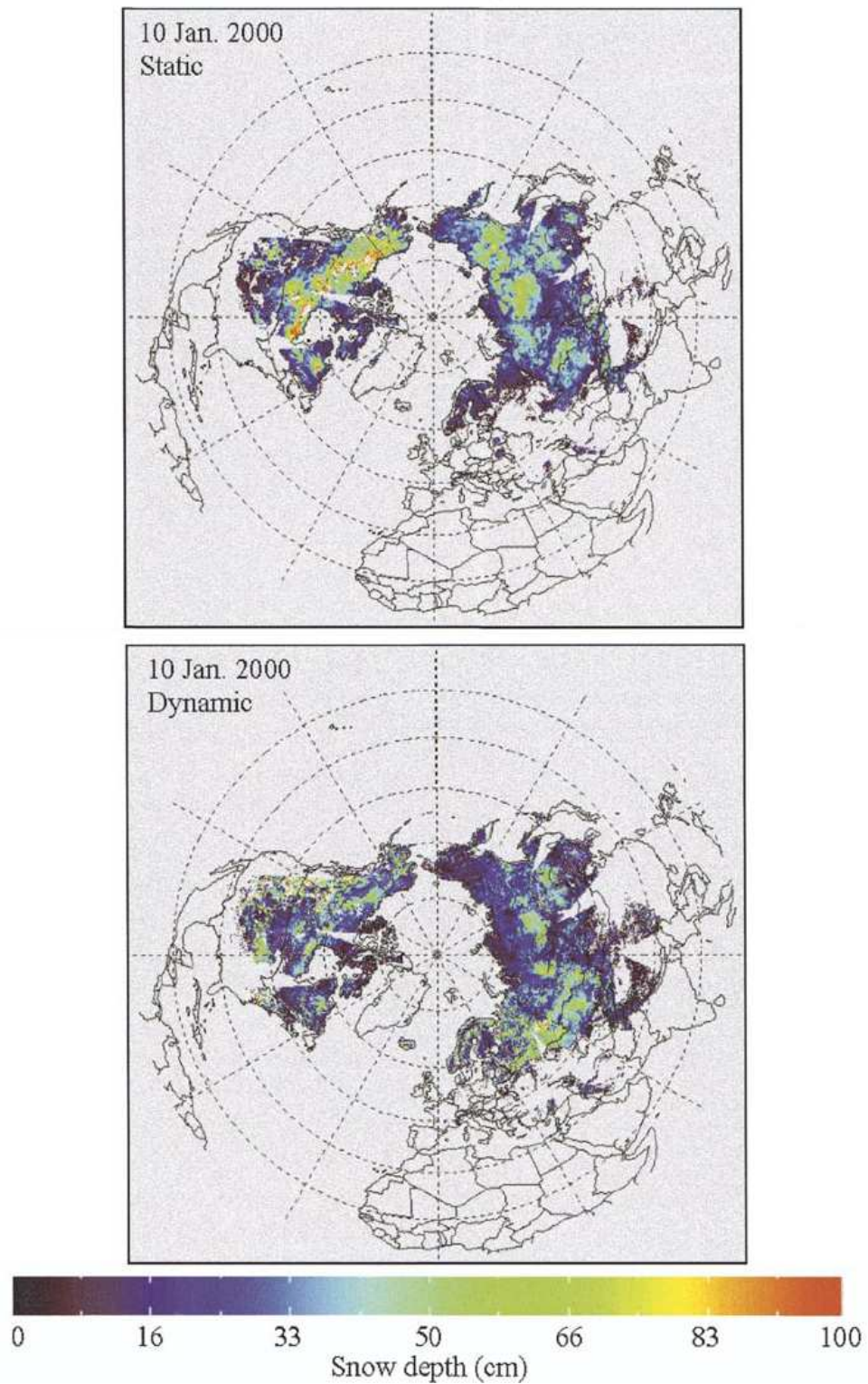


Figure 5.8: Snow depth from SSM/I data for 10th January 2000 using (upper) static and (lower) dynamic retrieval algorithms. Taken from Kelly et al. (2003). Note that as this shows data for only one day, the gaps between satellite overpasses can be seen.

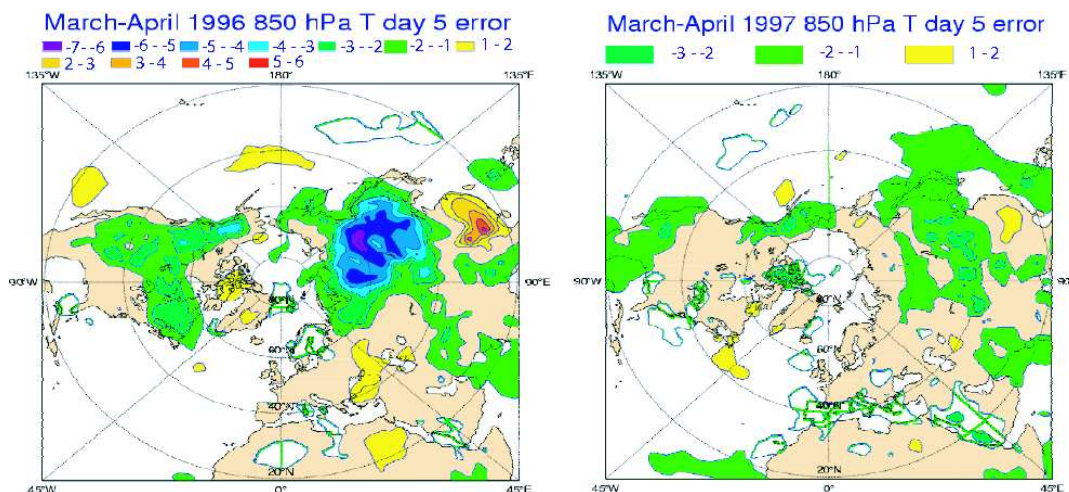


Figure 5.9: ECMWF operational 5-day 850hPa temperature bias when using a deep snow albedo of (left) 0.8 and (right) 0.2 under forests, after Viterbo and Betts (1999).

energy budget will affect the formation and persistence of the snowpack as well as the feedback to the atmosphere.

While boreal forests make the interpretation of satellite measurements difficult, they are also a challenging environment for models. Limited data exist on the behaviour of snow in dense forests, particularly in Siberia. Essery (1998) showed, using an earlier version of the Met Office land surface model, that simulated fluxes are highly dependent on whether the snow is modelled as being in the canopy or on the ground. The presence of a canopy makes snow modelling more complex, mainly due to the energy exchange between the snow and the canopy. This is being investigated in the second round of the Snow Model Intercomparison Project, where simulations by many different snow models in open and forested sites are compared. The presence of the canopy leads to greater disagreement between models, even when calibration data has been provided (N. Rutter, pers comm, 2008).

Adjustments to the ERA40 land surface model for boreal forests were noted in chapter 4. ECMWF altered the surface scheme to use a reduced albedo of 0.2 for snow under tall vegetation. This had a large impact on the errors in 5-day forecasts of temperature at the 850hPa pressure level over Siberia, as shown in figure 5.9. The original version displayed a cold bias of up to 7°C in the region, which is comparable to that found for HadAM3 in the AMIP project (Neale and Slingo, 2003). While both HadAM3 and the climate model used in ERA40 are atmospheric models, and the biases in coupled ocean-GCMs are likely to be different, this does demonstrate the large influence of the land surface, and specifically snow, on the atmosphere.

A further challenge in modelling the distribution of snow is that of wind redistribution. Areas of snowdrifts (increased SWE) and scour (reduced SWE) are formed over large areas where windspeeds are high (Trujillo et al., 2007), which is not represented in a climate model. Strack et al. (2004) drove a land surface scheme at five BOREAS stations and found that the modelled snow depth at the wind-blown station was considerably worse than that of the other four. This will certainly be a challenge for models at individual stations in Siberia, as wind speeds are high in many areas, though the effect should be averaged out over the large gridbox in a climate model run.

Although the snow distribution will be influencing the atmosphere above it, and may therefore have an impact on the circulation, it is also clear that the circulation will be driving the snow distribution. However crude or sophisticated the land surface model is, it can only process the amount of precipitation that falls as snow in that gridbox. While in chapter 4 the precipitation and temperature climatologies of HadCM3 were compared to the CMIP3 multi-model climatology, here we compare HadCM3's winter mean sea level pressure, and winter precipitation with available observation-based data (figure 5.10). Mean sea level pressure in DJF is compared to ERA40, as the latter is constrained by many pressure observations. The comparison shows that HadCM3 has a high pressure bias at northern high latitudes, and a low pressure bias along the west coast of North America. No clear pattern emerges over Siberia, although it is important to note that the ERA40 product will be less well constrained in this area. Rikiishi et al. (2004) investigate the sources of snow in Russia by correlating snowfall data at particular stations (Krenke, 2004) with sea level pressures and 500hPa heights from the U.S. National Meteorological Center. They suggest that snowfall in the European Russian plain is caused by travelling disturbances from the Baltic or North Sea, whereas it is synoptic disturbances from the Arctic ocean that causes snowfall over Siberia. A high pressure bias at these high latitudes could therefore be causing a lack of snow over Siberia, by diverting travelling disturbances from the region, and by causing the air to be too cold for snowfall.

The model's snowfall climatology (figure 5.14) shows that most solid precipitation over Siberia in HadCM3 falls in October, with small amounts falling during the rest of the winter. This reduction in snowfall occurs when the surface temperature drops below  $\sim 240\text{K}$ , so a cold bias in this region could be 'switching off' the precipitation too early. In fact, a comparison of DJF precipitation amount to the CPC Merged Analysis of Precipitation (CMAP, Xie and Arkin (1997)) (figure 5.10b) suggests that HadCM3 does a very good job across Siberia. However, the satellite data used in the CMAP project is of limited use over snow-covered regions, so at high latitudes the observations are merged with the NCEP-NCAR reanalysis product. This product is unlikely to be

well-constrained in Siberia due to the lack of ground measurements, and the problems of gauge under-catch when measuring solid precipitation, so the reanalysis product and hence CMAP will be more model-dependent in this area (Xie and Arkin, 1997). This highlights the difficulty in assessing model validity independently in this important geographical region.

### 5.5.2 Alternative models and modelling approaches

In contrast to the lack of alternative SWE products for comparison, there is a wide variation in approaches used to derive SWE fields from models. The climatologies depend on the physics of the model and the data used to drive it: a selection of alternative models and previous studies are presented here, beginning with higher resolution climate models.

Precipitation is dependent on topography, so a model with a coarse resolution such as HadCM3 could not be expected to produce completely accurate distributions of snow. For comparison, HiGEM is a high resolution coupled atmosphere-ocean GCM also from the Hadley Centre (although model physics are slightly changed from HadCM3), with a gridbox size of 1.25 by 0.83 degrees in longitude and latitude in the atmosphere. Figure 5.11 shows the 10-year average SWE climatology from HiGEM. The distribution is very similar to that in HadCM3 (except of course at a much higher resolution), suggesting that this distribution is not driven by the low-resolution topography but by the atmospheric circulation pattern.

The direct effect of resolution on SWE distribution can be assessed easily with the ECHAM5 model. While this model is an atmosphere-only GCM, results of equivalent physical model runs at very different resolutions are available for comparison. Figure 5.12 shows the 10-year average SWE seasonal cycle from the T63 version of the model (roughly equivalent to the resolution of HadCM3). This can be compared to figure 5.13, showing a 10-year average SWE from the T213 model (closer in resolution to the satellite data). As expected, the higher resolution model shows much more local detail in snow distribution, particularly over the Rockies, although the overall pattern is very similar. ECHAM5, in either resolution, shows a much more zonal pattern of SWE than HiGEM, with a smaller area snow-covered each month, and while ECHAM5 also produces the ‘SWE hole’ over Siberia, it does show deeper SWE values than either of the Hadley Centre models both here and in the Canadian boreal forest.

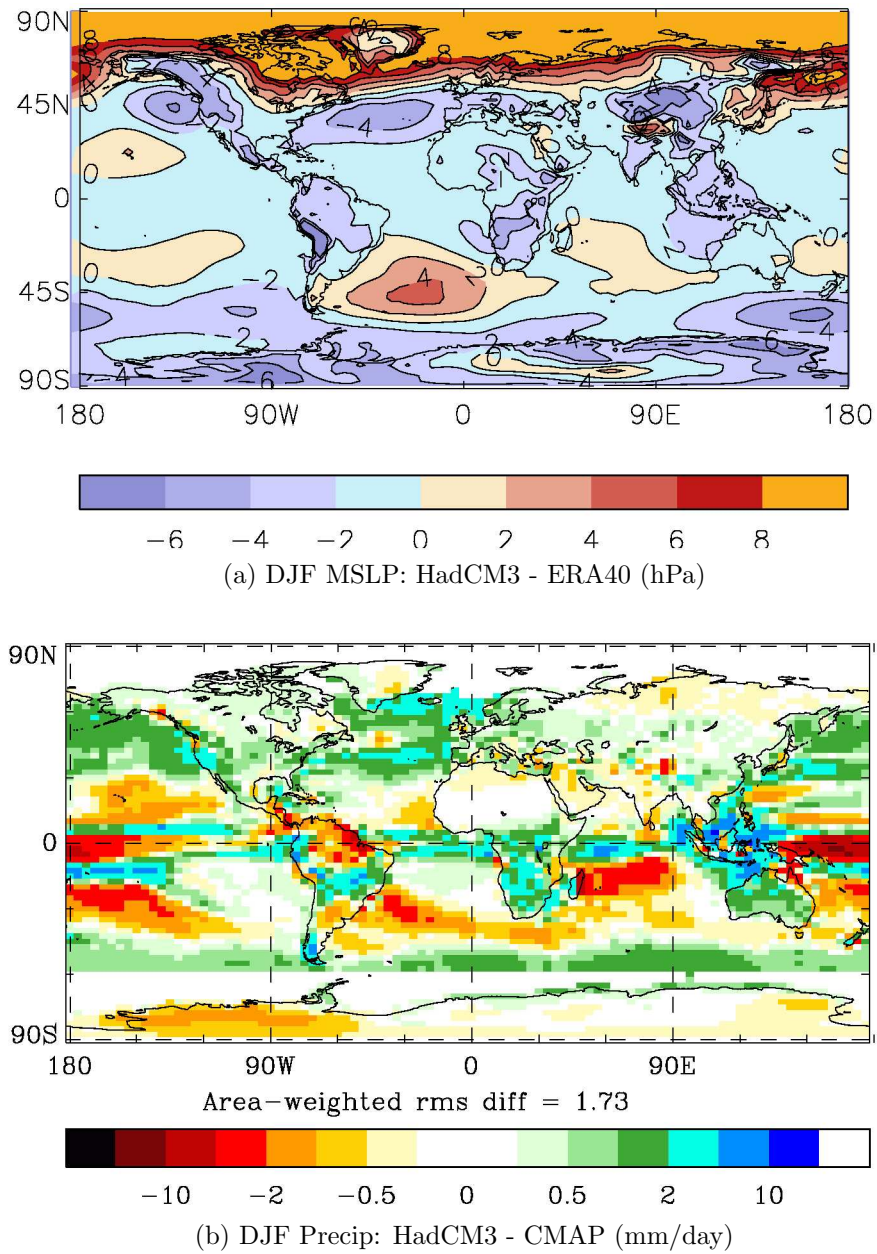


Figure 5.10: HadCM3 errors in mean sea level pressure (MSLP in hPa) and DJF precipitation (in mm/day), relative to ERA40 and CMAP respectively.

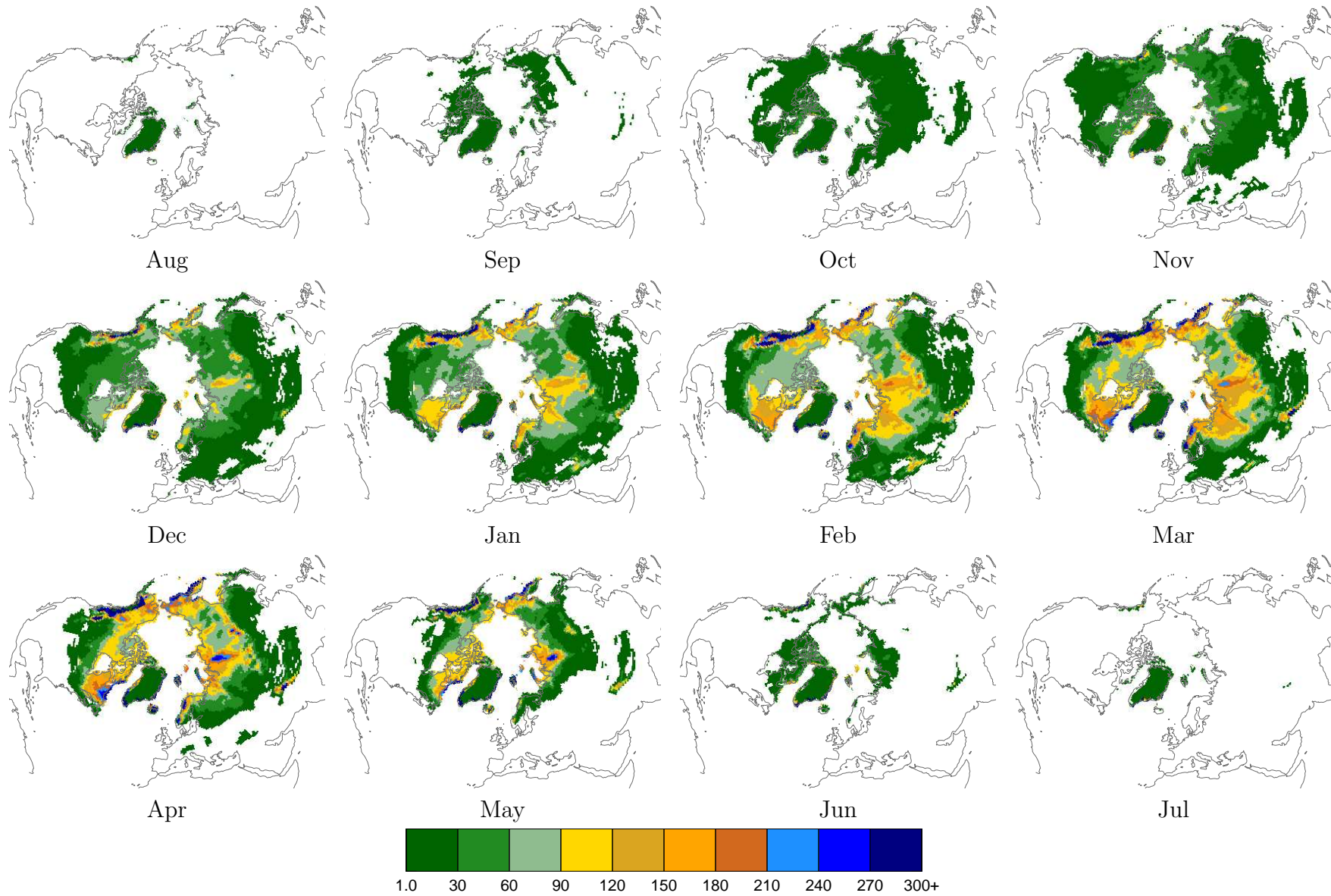


Figure 5.11: Seasonal cycle of snow water equivalent (mm) for HiGEM.

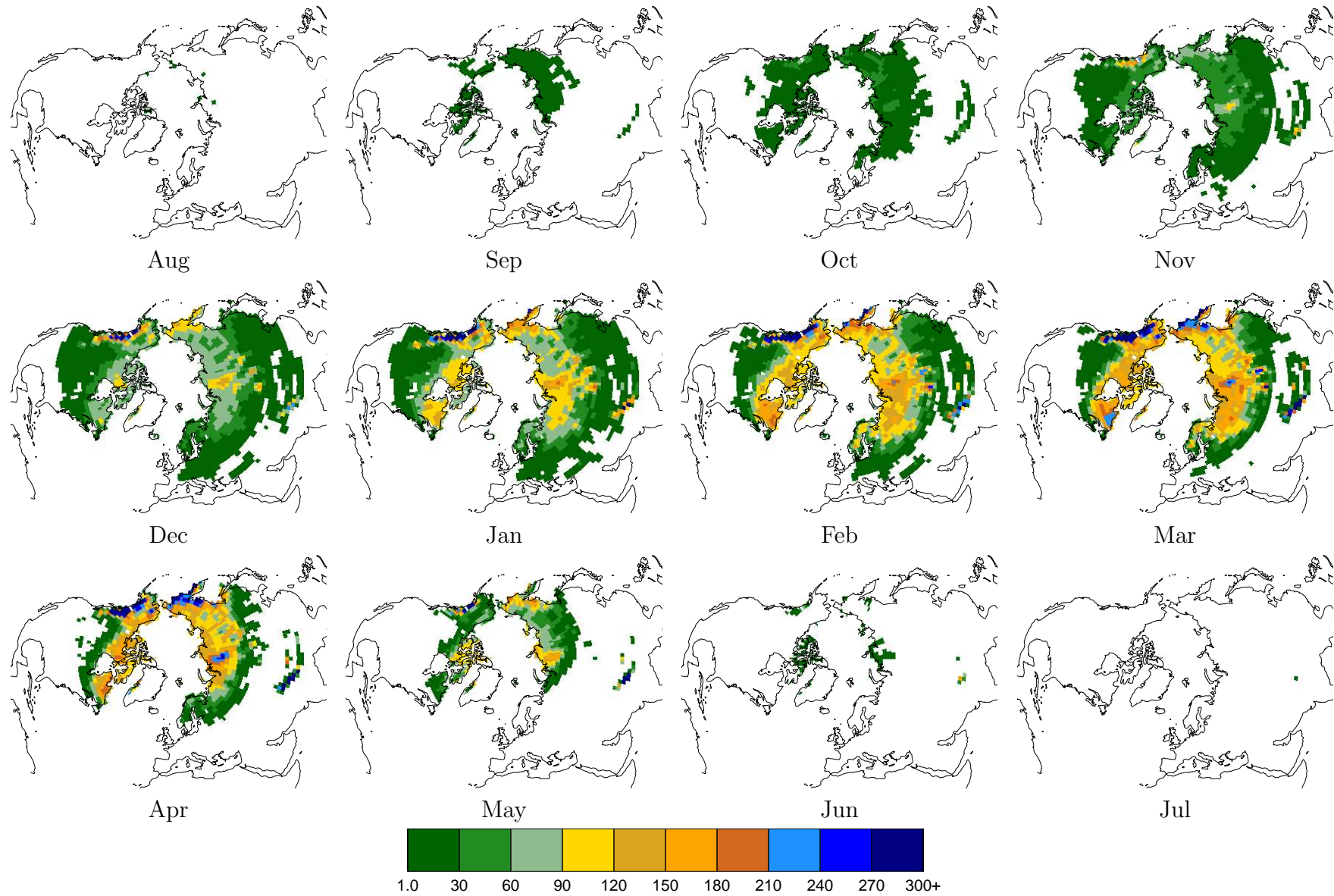


Figure 5.12: Seasonal cycle of SWE (mm), from ECHAM5 at T63 resolution

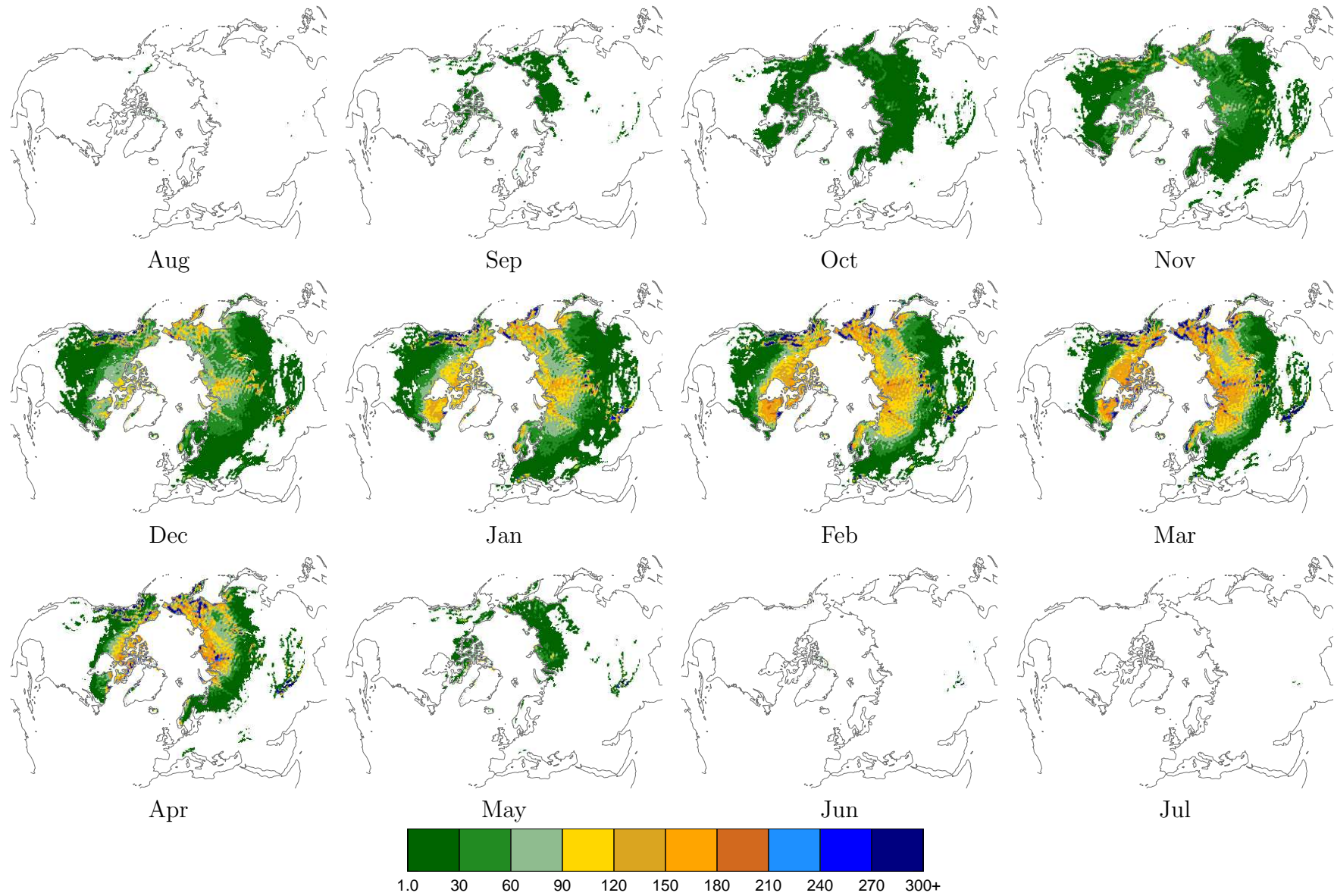


Figure 5.13: Seasonal cycle of SWE (mm), from ECHAM5 at T213 resolution

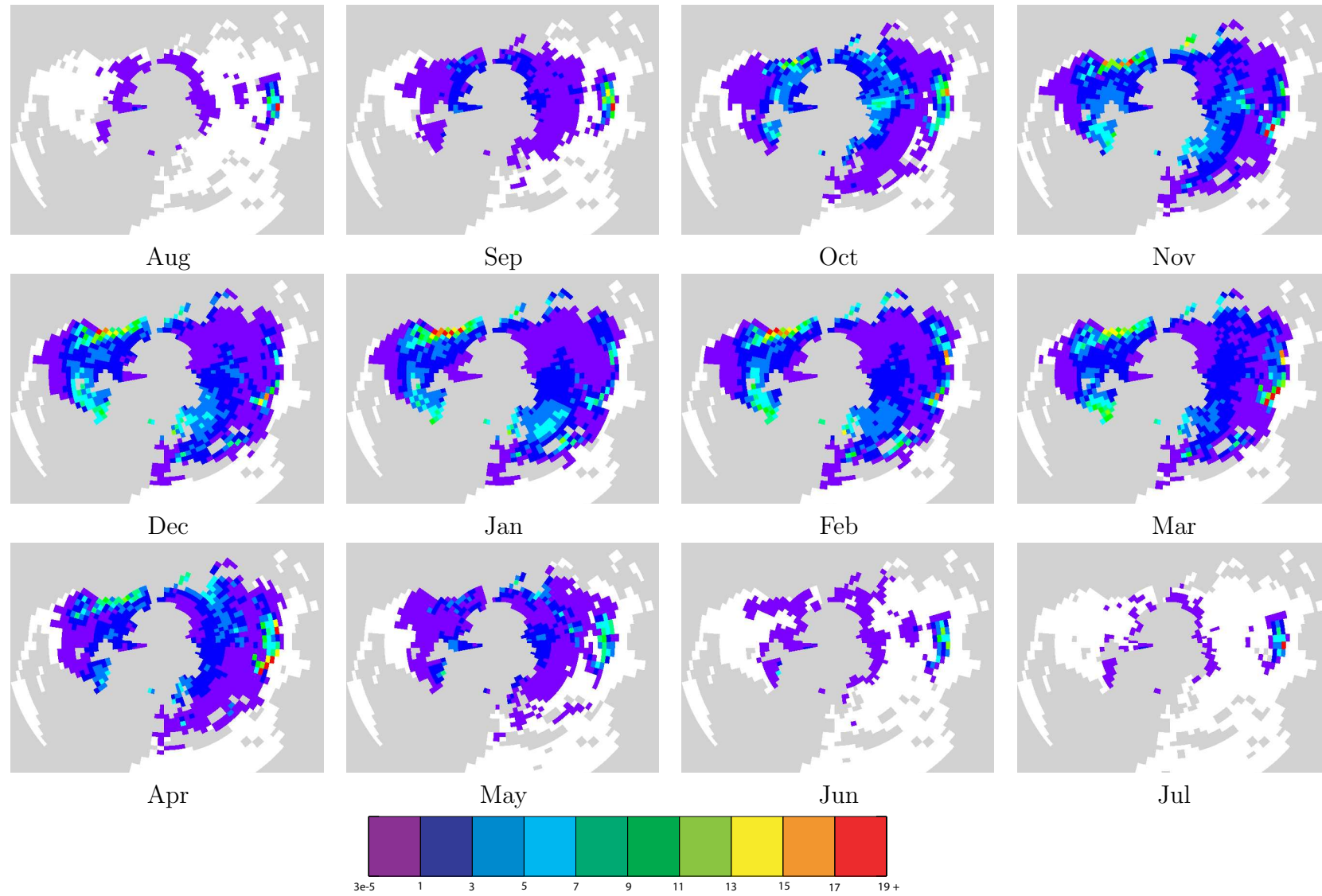


Figure 5.14: Snowfall climatology from HadCM3 (mm/day)

A more focussed study of SWE modelling in Siberia was carried out by Boone et al. (2006). A land surface scheme was run for ten years with three types of atmospheric forcing data over the region (50 to 80 degrees N and 55 to 115 degrees E). The forcing data used were:

1. The Global Soil Wetness Project 2 control simulation, hybridized with observed and satellite based precipitation data
2. ERA40 - the reanalysis product from the ECMWF
3. As (1), but without gauge under-catch corrections applied

The results of the ten year average (1986-1995) are shown in figure 5.15. The result of the ten year average for the same area from the flux replacement HadCM3 run is shown in figure 5.16. While the HadCM3 run produces its largest SWE values in the right area, all three of the offline model runs in figure 5.15 show much greater peak values, supporting the idea that HadCM3 is not snowing enough in this area.

As described in chapter 4, HadCM3 took part in the third round of the Coupled Model Intercomparison project. A first investigation of the snow distribution in 14 of these models has been completed by Brown and Mote (in press). They note the difficulty in validating large-scale SWE patterns due to a lack of a reliable global SWE climatology, and choose as their reference dataset the daily snow depth analyses produced by the Canadian Meteorological Center (Brasnett, 1999), converting to SWE using a density climatology based on Sturm classes. Figure 5.17 shows the comparison of the CMIP3 models with this SWE product. Again, the GCM consensus (middle panel) is for reduced SWE in the Lena basin compared to surrounding regions, which is not so evident in the validation data (upper panel). The largest differences however are seen over the Himalayas and the west coast of North America (lower panel). The main aim of the study was to analyse the changes in Northern hemisphere snow in the CMIP3 models with climate change. While snow cover duration was shown to be more sensitive to climate change than SWE, there was agreement between the models about the location of increases in SWE. Figure 5.18 shows where the 14 models agree that the maximum SWE increases with respect to a 1970-1999 reference. Increases are seen in almost all models in northern Eurasia, in particular the Lena basin, and in northern Canada. One explanation could be that in a warmer climate, a cold bias over Siberia is reduced, allowing the model to precipitate in this area more freely.

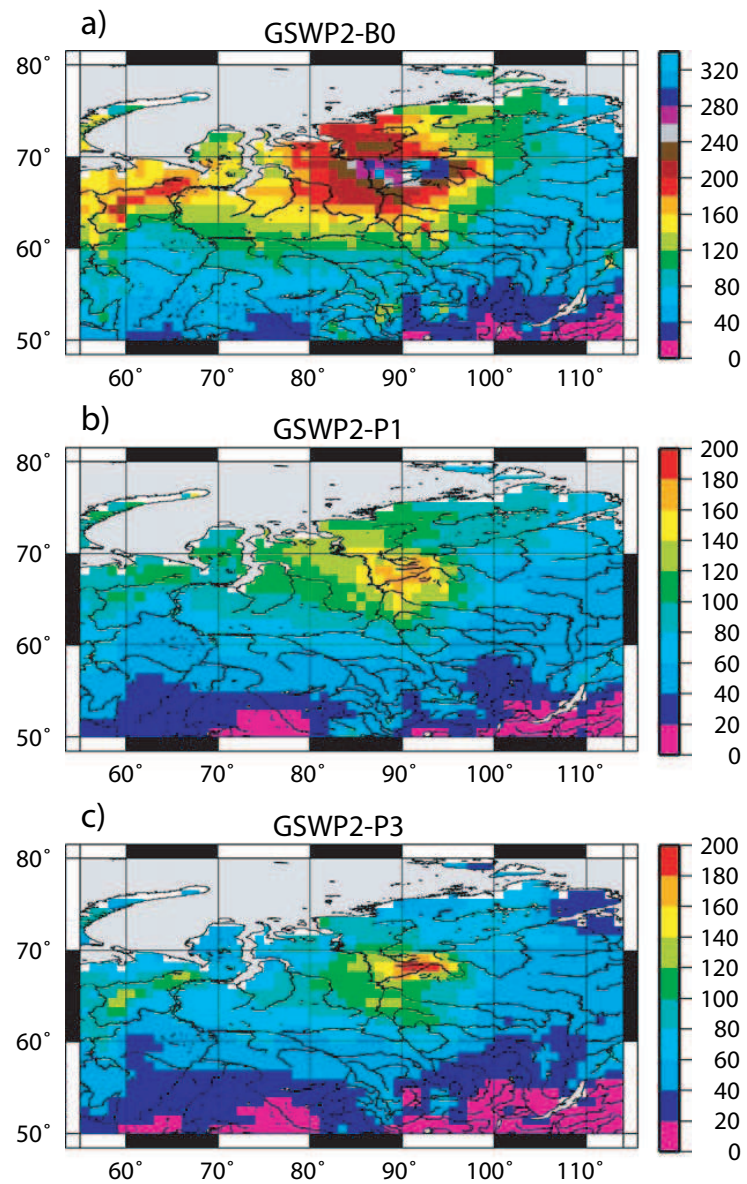


Figure 5.15: 10-year average SWE (mm) from the three Siberian modelling experiments in Boone et al. (2006). Simulations driven by forcing data from (top) Global Soil Wetness Project 2, (middle) ERA40, (bottom) GSWP-2 without gauge under-catch corrections applied.

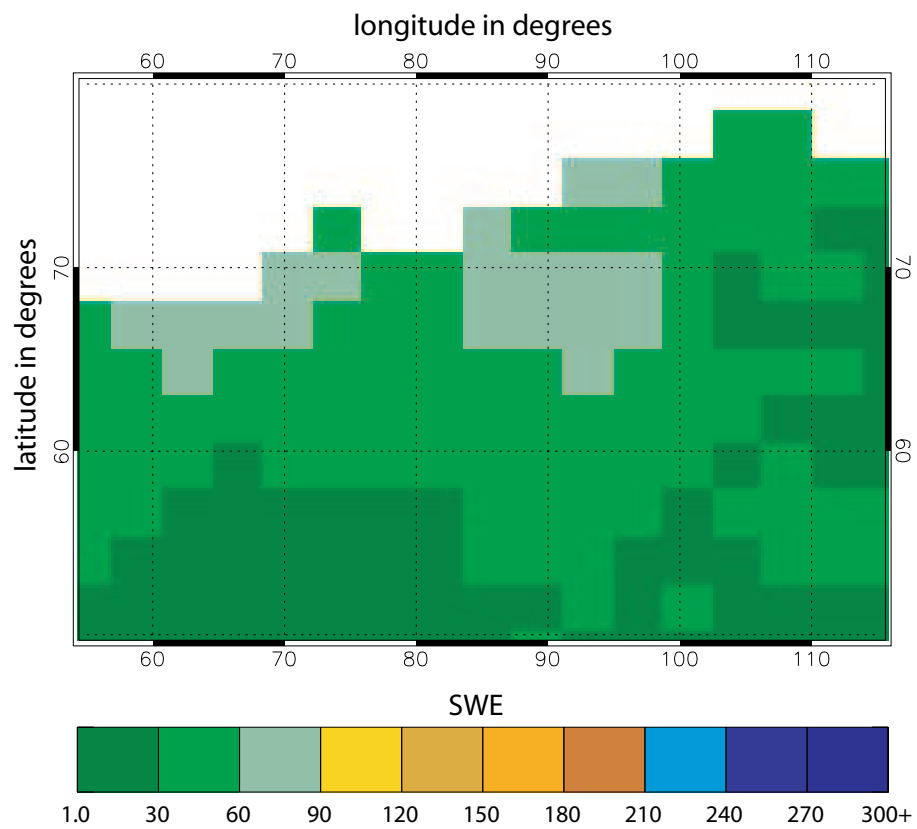


Figure 5.16: 10-year average SWE (mm) from the HadCM3 flux replacement run, for the area of northern Russia studied in Boone et al. (2006).

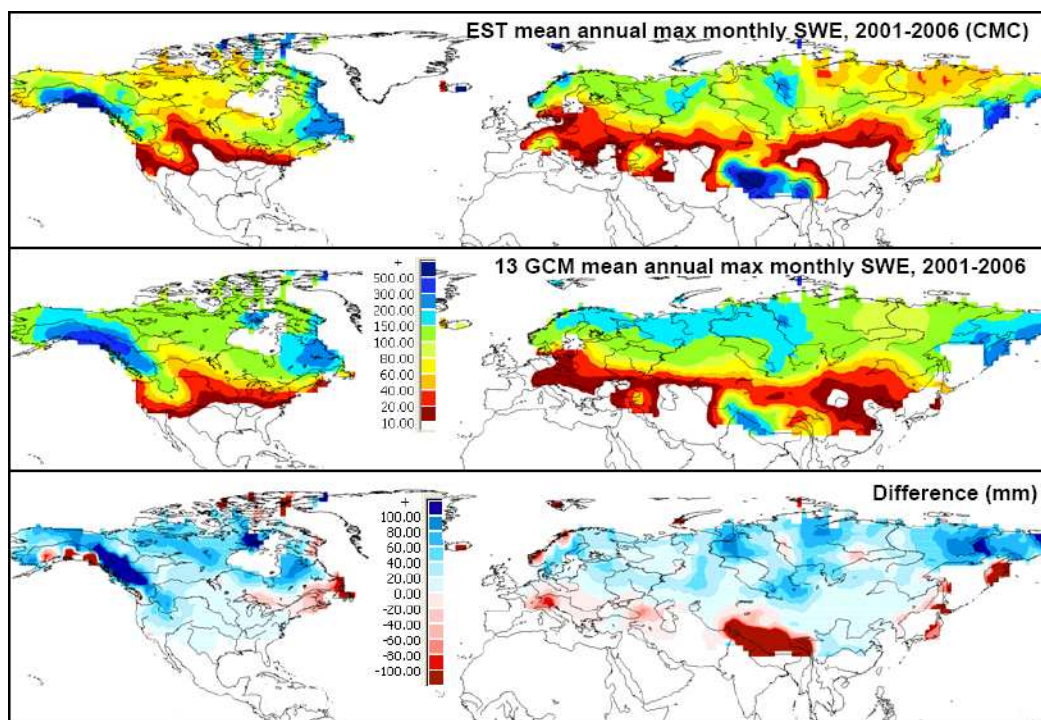


Figure 5.17: Maximum SWE (mm) from the CMIP3 multi-model average (14 models), compared to the daily snow depth analyses from the Canadian Meteorological Center for 2001-2006. After Brown and Mote (in press).

### 5.5.3 Modelling summary

The land surface model in HadCM3 has been discussed more closely, and compared to alternative modelling approaches. While similar patterns of SWE distribution are seen across a range of models, in every case, HadCM3 produces the lowest values of SWE across Siberia. This is likely to be due to the physics of the model rather than its low resolution. The model does exhibit a high pressure bias at the high northern latitudes which could be responsible for a lack of snowfall over Siberia. Large biases were also seen in this area in a previous version of the ERA40 land surface, which were improved by a reduction to the albedo of snow under vegetation.

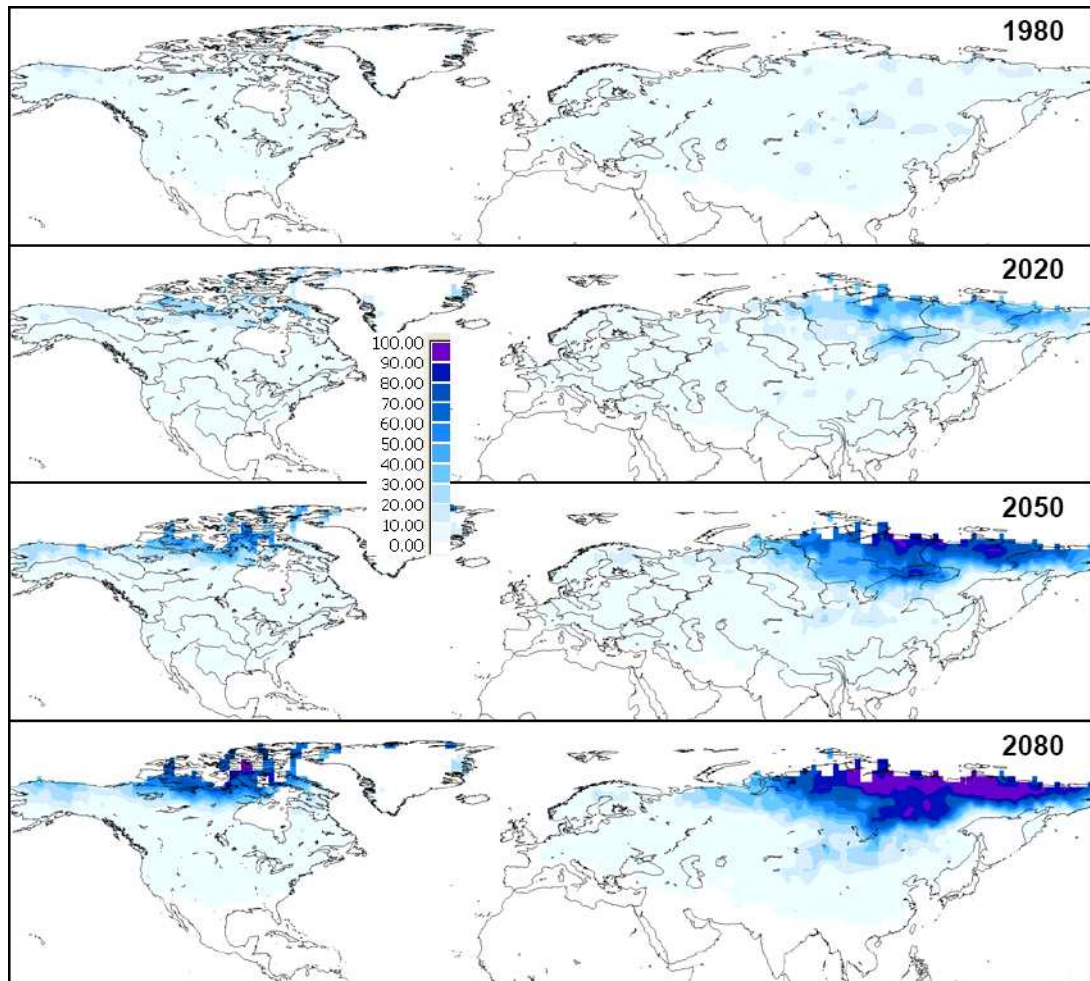


Figure 5.18: Percentage agreement between the fourteen CMIP3 models about significant increases in maximum SWE compared to a 1970-1999 reference. After Brown and Mote (in press).

---

## 5.6 Discussion

The only purely observation-based global SWE product shows a very different distribution of SWE across the Northern hemisphere when compared to the leading reanalysis product, ERA40, and a fully coupled ocean-atmosphere GCM, HadCM3. The differences are largest across Siberia, where the SSM/I data shows very deep SWE values and HadCM3 very little. Similar differences are seen when using a range of GCMs, with all showing lower SWE than SSM/I.

The comparison of modelled and observed hydrographs for large Siberian catchments highlight a lack of runoff from the model in the Lena catchment. The hydrographs show a large peak in early summer and many authors relate this to snowmelt (Fukutomi et al., 2003; Grippa et al., 2005; Su et al., 2005). However, the Lena is hydrologically complex and the runoff measurements are subject to many uncertainties, although the large size of the basin will smooth out many of the variations caused by dam regulations (Su et al., 2005). The Yang et al. (2007) analysis of microwave data confirm higher retrieved SWE values in the Lena basin compared to the Ob and the Yenisey, but SWE in this basin also melts the fastest. This could be indicative of an erroneously deep snowpack from the retrieval, where in fact the snowpack is shallow and composed of depth hoar, which then melts more quickly than the snowpacks in the other basins.

The assumption of a constant grain size in the microwave retrieval will be contributing to bias in the depth hoar-dominated tundra region, although the differences between the datasets are established before conditions become favourable for the formation of depth hoar. Examining climatologies from dynamic retrievals show differences to the static algorithm, demonstrating the sensitivity of the retrieved product to the algorithm used and the influence of the constant grain size assumption on the retrieved product. The dynamic retrievals show reduced SWE going east across Siberia, which is the pattern seen in the models, although the absolute values from the retrievals are much higher.

Of more concern is the influence of vegetation on the retrieval, and the application of a simple forest factor correction to the observed data. The unfactored SSM/I SWE data are very likely an underestimate of the true values, but the degree of this underestimation is not known well enough to justify a doubling of the retrieved value in many areas.

The boreal forests are also problematic for land surface models, due to the complicated energy exchange between the snow and the canopy, and the presence of snow both on the ground and in the canopy. The distribution of SWE in the model is driven by precipitation and hence the atmospheric circulation. While the mean sea level

pressure compares favourably to ERA40 (which is constrained by observations), large scale precipitation is harder to validate due to the paucity of measurements and the inherent difficulty in making them, especially at high latitudes. Low SWE in the Lena basin appears to be a common feature to GCMs, though HadCM3 has the lowest values of all the models studied here. The agreement between GCMs as to the distribution of SWE is not unexpected, as many will share the same atmospheric physics that drive the precipitation and temperature patterns, and hence snow distribution. The lack of observations at high latitudes mean that these fields are relatively unconstrained in all models, so all could be suffering from the same biases. Likewise, the improved agreement between ERA40 and HadCM3 with the addition of flux adjustments in the latter is also expected, as the reanalysis will be using the same SST observations as were used to provide the climatology for deriving the flux adjustments.

As a combination of both a climate model and observations, it is difficult to diagnose the errors in the ERA40 product. As the fields with more global observations (such as surface temperature and sea level pressure) are better constrained than in a climate model, it is reasonable to assume that the precipitation and resulting SWE climatology will exhibit lower average bias. The SWE climatology lies somewhere between the climatologies from SSM/I and HadCM3, which is encouraging given that the comparison with both other models and runoff data suggests that, on balance, SWE in the Lena basin is too low in HadCM3 and too high in SSM/I.

Siberia has been shown to have potential in modulating Northern hemisphere circulation patterns (Gong and Entekhabi, 2002; Gong et al., 2003). Due to its remoteness and harsh climate, remote sensing is the only feasible way of getting consistent, large-scale observational information on snow distribution here. Tying up the large differences between the model and the remotely sensed data requires a detailed study and is outside the scope of this project, but clearly must be done to exploit both sources of data properly. It is also required for a correct interpretation of GCM predictions of increased SWE in Siberia with climate change.

It is difficult to have confidence in any one dataset globally with so many factors unconstrained and unvalidated. There is no ‘truth’ to compare with at these very large scales. While we call the SSM/I SWE ‘observations’, they are really brightness temperature observations which have been passed through a retrieval - a simple, and flawed, model. What we are actually doing when comparing SSM/I SWE data to HadCM3 output is comparing one model to another; approximations to the truth from different perspectives. As a ‘middle ground’ between in situ observations and a climate model, ERA40 will be used as the truth in the assimilation studies that follow, although the independent SSM/I estimates are still an important dataset for comparison.

# Chapter 6

## Anomaly prediction using assimilation in HadCM3

### 6.1 Introduction

The previous chapter showed that the HadCM3 SWE climatology is very different to the climatologies of the observations and ERA40 in a number of respects. We could still get useful snow information from the model, however, if it can be driven by, for instance, well-constrained observed temperatures which would generate realistic snow anomalies. Predictions of future anomalous SWE would be useful for many hydrological applications, such as water resource management and streamflow forecasting. If the method is successful in its generation of SWE anomalies, it could also be used to provide SWE data for model initialisation for cases where atmospheric data is available but reliable land surface data is not.

To forecast future conditions of any field, the forecast model needs to be constrained in some way to the current observed state. This can be provided by the assimilation of initial condition data and/or the assimilation of boundary condition fields throughout the forecast, such as sea surface temperatures. Inevitably the introduction of outside data into a model will interrupt the model's preferred evolution, and step changes in model fields can introduce large errors into the analysis. A related problem is the tendency of a model to evolve away from the previously assimilated field and towards its own preferred climatology, known as 'climate drift' (Stockdale, 1997).

Forecasting is often performed using an ensemble approach, with many forecasts released with subtly different initial or boundary conditions in an attempt to sample the error from incomplete knowledge of observed states. 'Forecasts' released at dates in the past are known as hindcasts, and can be assessed against the subsequent observations.

This chapter builds on decadal forecast work performed at the Met Office (Smith et al. (2007), and discussed below) using atmospheric and oceanic data assimilation. The ability of climate models to forecast the temporal and spatial variability of the land surface, particularly important water storage variables such as snow, has been little studied. This is partly because of the lack of reliable global estimates of snow, however global reanalyses of atmospheric states are readily available and have been well studied. This chapter assesses the ability of HadCM3 to reproduce and forecast SWE distributions via assimilation of well-constrained fields from atmospheric and oceanic reanalyses. SWE anomalies in both assimilation and hindcast runs are compared to observations from ERA40 and SSM/I at lead times of up to two years.

## Techniques in seasonal forecasting

Short-term weather forecasting is an initial value problem, in that the outcome depends on the initial conditions, rather than the boundary conditions. Climate predictions spanning decades to hundreds of years are dependent on the boundary conditions, but forecasting at seasonal to interannual timescales lies somewhere in between. Predicting the onset or development of an ENSO event, for instance, is an initial value problem, but the influence of the ENSO is felt as changing boundary conditions through a longer-term seasonal forecast. The accuracy of this forecast therefore depends on the initial state of the model as well as the boundary conditions: the two are not necessarily independent.

Collins and Allen (2002) analyse decadal predictions in terms of their relative dependence on initial conditions - the state of the ocean, atmosphere and land surface at the start of the run - and boundary conditions - forcings such as greenhouse gases and varying sea surface temperatures. The authors generate ensembles of a coupled GCM (HadCM2, an earlier Hadley Centre model) with perturbations to either the forcing or the initial conditions. The smaller the ensemble, the more noisy it will be (*i.e.* the more the different weather in each run will influence the ensemble mean), but the authors show that, for seasonal forecasting, this weather noise is minimised through averaging over ensembles of more than 4 members.

Collins and Allen first examine the ensembles of varying boundary conditions. Northern hemisphere land temperatures have a discernable response to the changing boundary conditions only after a decade (prior to this any signal is indistinguishable from climatological noise), with the influence of the snow-albedo feedback leading to winters being more predictable than summers. No signal in the SSTs is detectable at lead times of less than 20 years from these boundary condition experiments.

Turning to the initial condition ensembles, Collins and Allen show that in an idealised system with perfect knowledge of initial states, global temperatures may be predictable up to 2 years ahead. The authors note that this figure is likely to be state dependent; certain initial conditions, such as a developing strong ENSO event, are likely to impart more predictability than others, and push this predictability beyond the 2 year average. They also find that while North Atlantic SSTs may show decadal predictability, temperatures over land are not predictable after around a month.

Hermanson and Sutton (2008) look at an ensemble of forecasts starting on 1st December 1981 with initial states that show large regional differences in ocean heat content. Differences in temperature, precipitation and mean sea level pressure are examined in the second year of each forecast. Significant differences are found over Europe and much of the Tropics, demonstrating the importance of the initial condition differences at lead times of two years.

Latif et al. (1993) use a GCM to investigate the predictability of tropical SSTs during ENSO events in the 1970s and 1980s. To eliminate the problem of model climate drift, an approach is used where observed anomalies are introduced into the model, rather than the complete fields. Oceanic initial conditions are supplied from an uncoupled run of the ocean model, forced by observed wind stress at the sea surface. This forcing field is derived by adding the observed wind stress anomalies to the wind stress climatology of the model running in coupled mode. This anomaly-based approach aims to reduce the tendency of the model to drift away from the observed state by allowing its own climatology to persist. Latif et al. produce a total of 20 predictions spanning 5 ENSO events, and find high correlations ( $>0.6$ ) for lead times of up to a year, and beyond in some cases.

This method was questioned by Stockdale (1997), who expressed concern that the observed anomalies may not be compatible with the mean state to which they are applied. Stockdale uses a different approach, estimating the model's drift from a set of control forecasts and subtracting it as an *a posteriori* mean bias correction. The approach is demonstrated using 12-month ENSO forecasts which exhibit considerable drift after the initial state was applied. The system produces skilful forecasts after the bias correction is used, prompting the author to note that climate drift "should not cause undue despair". However, it is also noted that errors in the model's basic climatology are nevertheless likely to impact the skill in anomaly prediction through nonlinear interactions, and it is likely that forecasts would be improved if the climate drift was limited or constrained. This method is now used by ECMWF for seasonal forecasting.

Ensembles of multi-model seasonal forecasts were performed in the EU project Prediction of Climate Variations on Seasonal to Interannual Timescales (PROVOST; and its “sister” project, Dynamical Seasonal Predictions in the United States). 4-month hindcasts were run with nine ensemble members per model, and considerable inter-model variability was seen, despite all runs using the same prescribed SSTs. The multi-model average was shown to have greater skill than any of the individual model hindcasts.

Following this, a further EU project “Development of a European multi-model ensemble system for seasonal to inter-annual prediction”, or DEMETER, was begun (Palmer et al., 2004). This project ran seven GCMs on the same supercomputer with standardised output diagnostics, the aim being to advance understanding of model-to-model variability at seasonal timescales. For each model, 6-month hindcasts were released each year on 1 Feb, 1 May, 1 Aug, 1 Nov, with ensembles created using a mixture of wind stress and SST perturbations to ERA40 reanalyses. Hindcasts were validated against ERA40 as ‘truth’ (an assumption that we are ‘in ERA40 world’). The investigators found that while the skill of the hindcasts was linked to ENSO (as before), the identity of the most skilful model varied in time and space. Once again, the multi-model ensemble mean was found to perform the best overall. The output from these multi-model hindcasts was used to produce probabilistic forecasts for other applications that depend on weather data as inputs, such as crop yield forecasting and modelling the spread of diseases such as malaria.

The decadal variability of snow extent in several of the IPCC-AR4 GCMs was investigated by Frei and Gong (2005). They used data from ensemble runs under different emission scenarios to assess the decadal to century scale variability and trends of North American snow, comparing the results to the reconstructed snow extent datasets of Brown (2000) and Frei and Robinson (1999). Although ensemble mean variability was too low compared to observations, the individual ensemble member variability was much closer. They found no temporal correlation between ensemble members, or between model runs and observations. They propose therefore that the decadal variability of snow extent in these models is due to the internal variability within the models rather than the changing boundary conditions of the different emissions scenarios.

## DePreSys

In order to extend seasonal forecasting to decadal timescales, a way of predicting the natural variability in a GCM must be found. The Met Office have used HadCM3 in developing the Decadal Prediction System, DePreSys (Smith et al., 2007), which

makes interannual forecasts starting from assimilated initial conditions, to account for the state of important modes of internal variability such as El Niño at the release of a forecast. Assimilation of this initial condition information is achieved via an anomaly assimilation scheme, rather than the a posteriori bias correction approach of Stockdale (1997), above, since errors in the bias calculation required for the latter method risk masking the smaller predictable signal at decadal timescales. The assimilated fields are ocean temperature and salinity, atmospheric winds, atmospheric temperature and surface pressure.

The accuracy of the system was tested using 10-year hindcasts, released 4 times a year between 1982 and 2001 (a total of 80 start dates). The predictions from these hindcast runs were compared against observations, and averaged over all lead times the root mean square error (RMSE) in surface temperature hindcasts was  $0.105^{\circ}\text{C}$ . To assess the impact of initial conditions, these hindcasts with assimilated initial conditions were compared to an equivalent set of hindcasts with initial states taken from four transient runs of HadCM3 with no assimilation, and therefore independent of the observations. These ‘NoAssim’ hindcasts had an RMSE averaged over all lead times of  $0.132^{\circ}\text{C}$ , 20% higher than the hindcasts with assimilated initial conditions. The improvement in the RMSE of the DePreSys hindcasts compared to NoAssim was even greater when only the longer lead times were considered (e.g. an improvement of 49% at a lead time of 9 years).

The success of the DePreSys hindcasts is very likely to be coming from the initialisation of the ocean, as the internal variability of the atmosphere is only predictable up to a few weeks. Smith et al. show that the main source of improvement in the assimilated system is through the initialisation of the upper ocean heat content, with atmospheric feedbacks maintaining the difference between the DePreSys hindcasts and the NoAssim hindcasts at lead times of many years.

## **GCEP**

The Grid for Coupled Ensemble Prediction (GCEP) project (Haines et al., 2008) uses the assimilation and hindcast method of DePreSys for investigating seasonal to decadal predictions. A compute cluster at ESSC runs the HadCM3 climate model both with and without oceanic and atmospheric data assimilation, with model anomalies relaxed towards observed anomalies using a simple nudging scheme, as in DePreSys.

Early GCEP results investigate known patterns of variability in ocean heat content to test timescales over which HadCM3 exhibits predictability. Ensembles were initialised from naturally-occurring extremes of ocean phenomena such as the Interdecadal Pacific Oscillation and Southern Oscillation. The two ensemble plumes

remain separate for a certain period before converging to the background climatology of the model, and this separation time is an indication of the predictability within the model. Predictability was found to be higher for ocean heat content than SSTs, and despite the external forcing from increasing greenhouse gases, the initial conditions were often found to have an impact for 5 years or occasionally even more (Haines et al., 2008; Hermanson and Sutton, 2008).

The regional nature of skill in hindcasts of surface temperature has also been investigated. The mean error from the second year of the hindcasts was improved over much of the globe compared to a set of hindcasts released from a run without assimilation. As expected, improvement was clear in the tropical Pacific (with improved representation of ENSO events via assimilation) although there was also skill over land areas (Haines et al., 2008).

Here we investigate whether snow anomalies within HadCM3 are realistically reproduced by the DePreSys method, and also whether improved snow forecasts can be made on monthly to seasonal timescales. This tests one simple method of initialising land surface conditions for climate predictions, and also allows comparisons with independent SSM/I data. Note that in the studies described above, the fields used for assessment of the scheme (often surface temperature) are those that were constrained by the assimilation. Here we assess a field that has not been assimilated, thus it is a test of whether the assimilation of a limited set of atmospheric and oceanic fields have a beneficial impact on other fields within the model.

## 6.2 Assimilation

### 6.2.1 Assimilation scheme

In order to produce the anomalies for assimilation into the model, a climatology is required. In all model runs presented here, the time period December 1989 - November 2001 is used to define the climatology of the atmospheric and oceanic fields for assimilation.

**Ocean data** 3D anomaly fields of *temperature* and *salinity* are assimilated 6hr-ly.

**Atmospheric data** ERA40 3D anomaly fields of *temperature* and *winds* (u and v), plus *surface pressure* (2D field) are assimilated 6hr-ly.

**External forcing** All observed *greenhouse gas*, *ozone* and *volcanic* and *solar* forcings are included and are identical in both the assimilation and no assimilation runs.

**Flux adjustment** Adjustments are applied to all runs, following the method described previously (chapter 4).

Atmospheric data is taken from the ERA40 reanalysis product. The ocean data is from the dataset that was created for the DePreSys project: covariances from HadCM3 climatologies were used to perform a four-dimensional, multivariate optimal interpolation of sub-surface observations and the Hadley Centre’s HadISST surface temperature dataset, to construct a temperature and salinity analysis. For details see Smith and Murphy (2007).

This ‘assimilation run’ tests the ability of the model to reproduce land surface anomalies given some limited meteorological constraints. An ensemble of runs for the same period, but without assimilation, is also performed, to derive a ‘No assimilation ensemble mean’. This ensemble is thus the best estimate of the climate that can be made without the use of direct ocean or atmospheric conditions. These No assimilation ensemble members are initialised from a transient run started in 1860, with noise added to the SST initial conditions. All runs begin in December 1989 and finish in November 2001, and fields are output on a monthly basis.

Monthly anomalies of SWE are calculated for the assimilation run and the No assimilation ensemble. The period December 1989 - November 2001 is used to define the climatology of SWE in the No assimilation ensemble mean, which forms the reference climatology for all model anomalies (including the assimilation run). The same period is used to define anomalies for SSM/I SWE data. An exception is ERA40: SWE anomalies are calculated with respect to a 1984-2001 climatology, but omitting five years due to the previously-noted error in the snow analysis during the period 1989-1994 (see chapter 4).

Time series of ENSO index and the NAO index have also been calculated. The ENSO index used here is the seasonal SST anomaly in the Nino3.4 box (defined as between 5S, 5N and 170W, 120W). The NAO index is calculated seasonally by subtracting mean sea level pressure in an Azores box (5 gridboxes wide, centred on 26W, 37.5N) minus that in an Iceland box (also 5 gridboxes wide, but centred on 34W, 60N).

## 6.2.2 Assimilation run performance

Figure 6.1 shows an example of the assimilation scheme working. Anomalies of surface air temperature (over land and ocean) are plotted for the observations and the assimilation run. While we would not expect the observations and model anomalies to

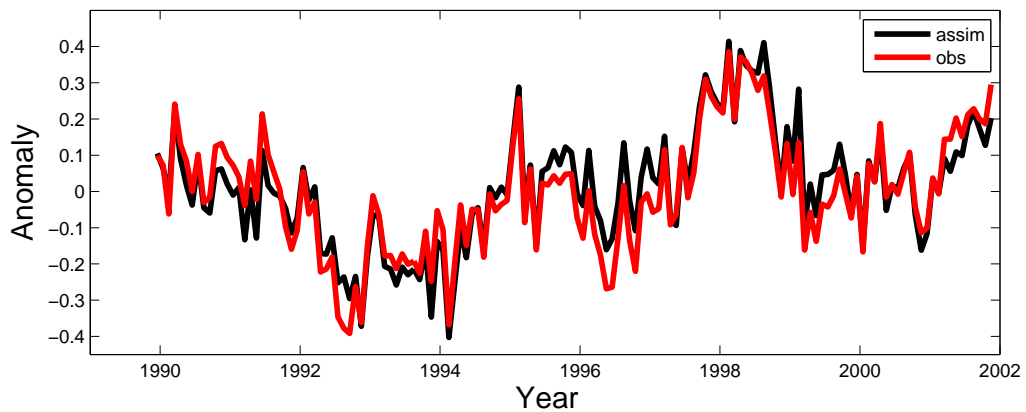


Figure 6.1: Surface temperature anomalies in K for the observations (in black) and the assimilation run (in red).

be exactly the same, they are very close and the interannual variability in particular is well captured.

Biases in assimilation run SWE are calculated with respect to SWE in ERA40, as it is ERA40 atmospheric data that are used in the assimilation scheme. Comparison with the independent SSM/I anomalies will be performed when examining the case studies below (section 6.4).

Figure 6.2 shows the mean seasonal bias for the assimilation run SWE anomalies, calculated by subtracting the No assimilation ensemble mean anomalies from those of the assimilation run, and constructing seasonal averages of this quantity.

For winter (figure 6.2a) the biases are predominantly positive (assimilation run has more SWE than ERA40) in Europe, eastern Siberia, the Canadian Arctic and the west coast of North America. Negative biases are seen in central North America, central Eurasia and the Himalayas. A very similar pattern is seen in spring (figure 6.2b). Smaller biases are seen in autumn (figure 6.2d), with the largest values being over the Himalayas, the Pacific coasts and northern Siberia.

Figure 6.3a shows the root mean square error (RMSE) between the SWE anomalies in the assimilation run (relative to the climatology of the no assimilation ensemble mean) and the ERA40 SWE anomalies. The RMSE is higher for the assimilation run than the No assimilation ensemble mean, which suggests that the assimilation scheme is doing a poor job of reproducing SWE anomalies. However, examining the spatial correlation (figure 6.3b), the assimilation run shows better correspondence with the ERA40 anomalies in almost all months than the No assimilation ensemble mean. The RMSE is a pointwise comparison of gridboxes; the anomalies in the assimilation run and ERA40, while having a similar spatial pattern, are not exactly coincident, and so large gridbox-to-gridbox errors occur. As the No assimilation field is an ensemble

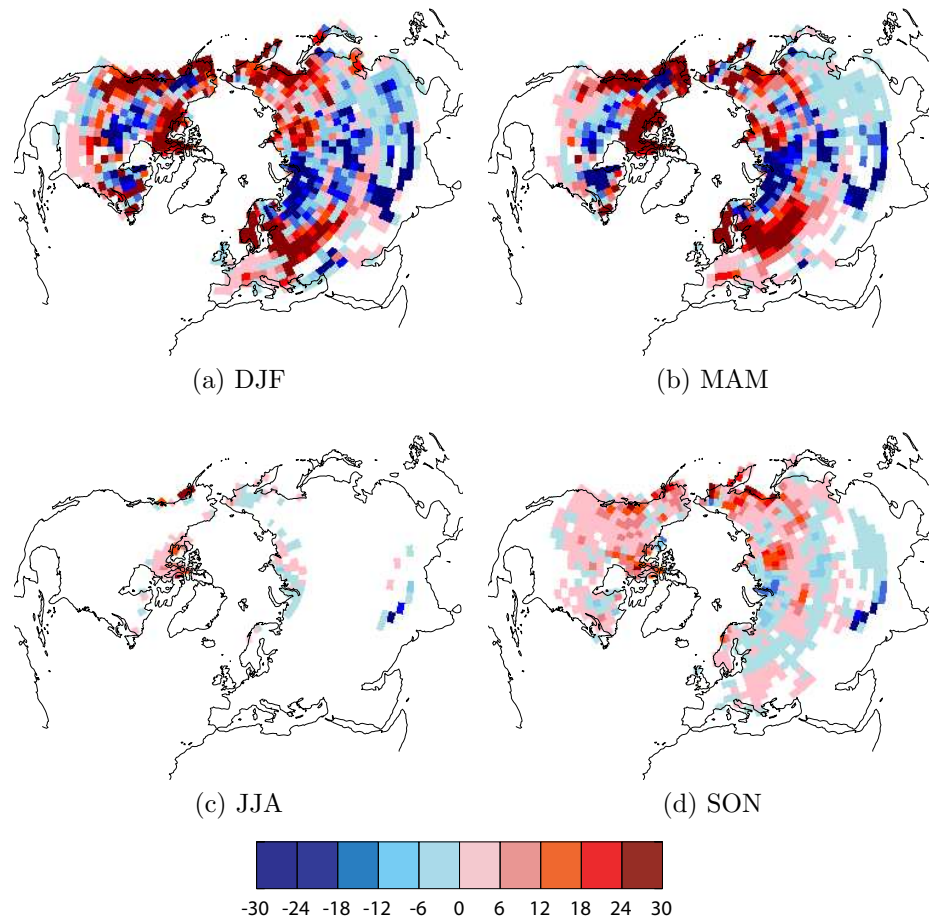


Figure 6.2: Mean seasonal bias of SWE (mm) of assimilation run anomalies with respect to ERA40 anomalies.

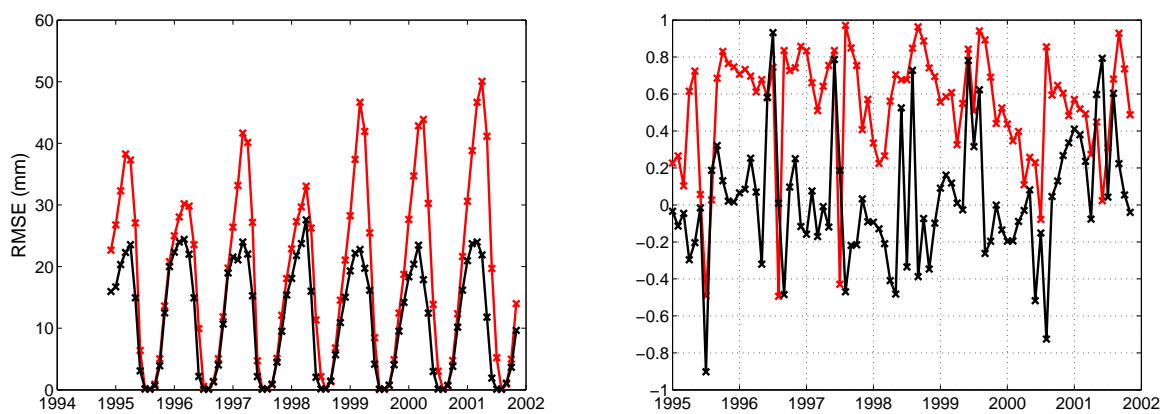


Figure 6.3: Monthly root mean square error of SWE (left, mm) and spatial correlation (right) between ERA40 and the assimilation run (red) and the no assimilation ensemble mean (black).

mean of a noisy field, the anomalies are much smaller and smoother, so the RMSE is generally lower. The superior performance of the assimilation run in reproducing SWE anomaly patterns when compared to runs without assimilation is evident when examining the case studies (below, section 6.4).

## 6.3 Hindcasts

### 6.3.1 Hindcast scheme

A well-constrained initial state may produce more reliable forecasts than those made without initialisation. This will be tested using a hindcast approach, with hindcasts released from the assimilation run. These hindcasts are therefore constrained by the observations up to release, but after release are allowed to evolve freely. Hindcasts are released twice a year, on the 1st May and 1st November, and run independently for 2 years. Each hindcast result presented here is the mean of a 4-member ensemble, generated by adding noise (of amplitude 0.05K) to the SST field at the point of release.

As the hindcasts are meant as a test of the scheme's forecasting ability, the external forcings are 'unknown' for the period of the hindcast. The solar forcing repeats the forcing from the last 10 years (i.e. the 2-year hindcast will be forced with a repeat of the first 2 years of the pattern starting 10 years prior to the date of release). Volcanic aerosols in the atmosphere decay exponentially with an e-folding timescale of 1 year from the point of release. No future information is used, so for example a hindcast released before the Pinatubo eruption (May 1991) would not include the Pinatubo aerosols, but a similar hindcast launched after the eruption (November 1991) would do so. Anthropogenic forcing is taken from the intermediate IPCC SRES B2 scenario.

In total there are 10 hindcasts over the period 1995-2001 (the period when ERA40 SWE anomalies are available), with 5 released in May and 5 in November. An equivalent set of hindcast ensembles with identical solar, volcanic and greenhouse gas forcings are also released from the No assimilation ensemble each May and November.

### 6.3.2 Hindcast performance

Figure 6.4 shows the biases averaged across all hindcasts for the first and second year of each hindcast separately. The upper panels shows results for the hindcasts released from the assimilation run, while the lower panel shows results from the hindcasts released from the No assimilation ensemble mean. Note that the absolute values of the biases in this figure are lower than those in 6.2 as this is an average across 12 months, and the very low values for JJA will bring the average down.

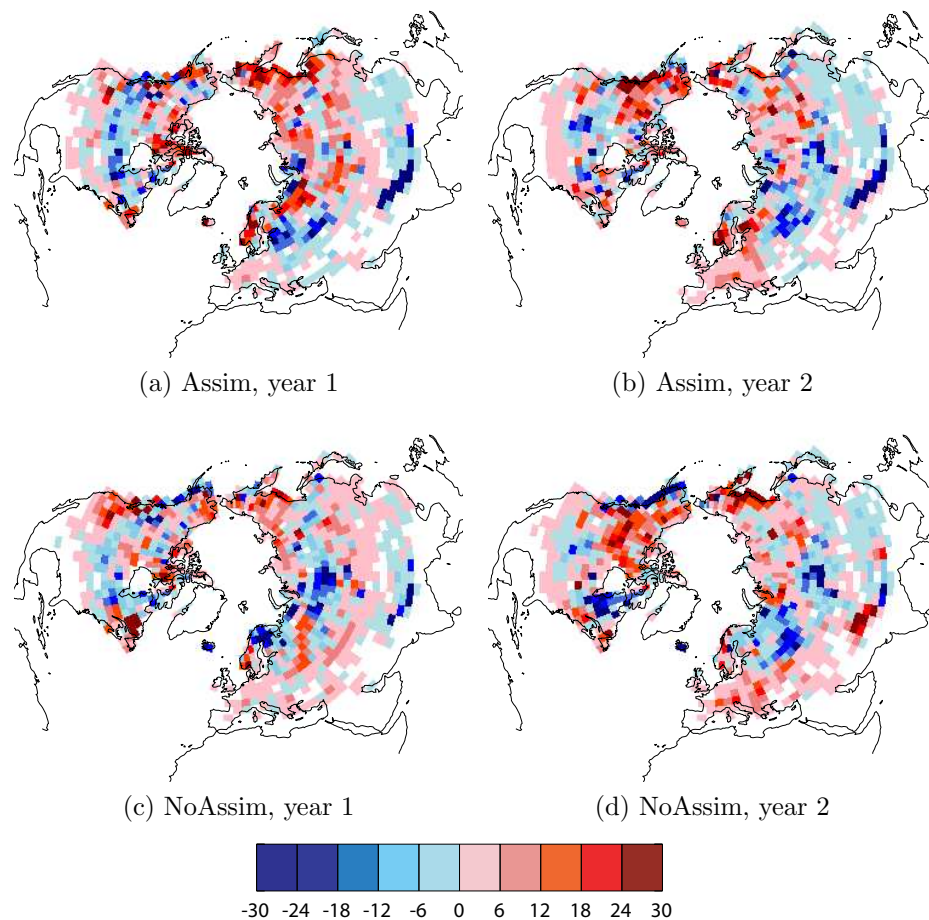


Figure 6.4: Mean bias of SWE anomalies (mm) from hindcasts released from the assimilation run (upper) and the No assimilation ensemble (lower), with respect to ERA40 anomalies, for year 1 (left) and year 2 (right).

Figures 6.4c and 6.4d show different patterns of biases in the first and second years of the hindcasts released from the No assimilation ensemble mean. As these hindcasts are not initialised using observations, we would expect that the biases would look similar in each case. The differences could be a consequence of the small ensemble size (only 10 hindcasts).

The pattern of biases in figures 6.4b and 6.4d are similar, with positive biases in northwestern North America, eastern Siberia and Europe, and negative biases in central and western Asia. This could be an indication that the Assim hindcasts look similar to the No Assim hindcasts by the second year since their release, but since the biases in the first and second years of the No Assim hindcasts look quite different, this is more likely to be down to chance (and variability across the small number of hindcasts).

The standard deviation calculation subtracts the mean bias from the month-to-month errors, so acts as a bias correction which is tuned to the duration of the model run. By comparing the standard deviation maps from the hindcasts launched

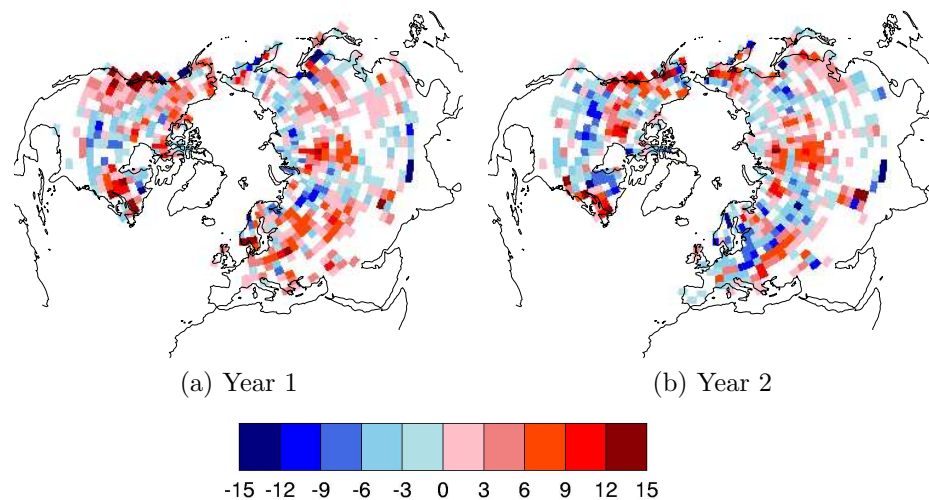


Figure 6.5: Difference in standard deviation of SWE errors (mm) for hindcast anomalies with and without assimilation, for year 1 (left) and year 2 (right). Calculated as NoAssim minus Assim, so positive gridboxes are those where the hindcasts released from the assimilation run have a lower standard deviation than the hindcasts released from the No assimilation ensemble.

from the assimilation run with those launched from the No assimilation ensemble, the regions where the assimilation hindcasts are performing better than the no assimilation hindcasts can be seen. Figure 6.5 shows the difference between standard deviations (No assim hindcasts minus assim hindcasts) for year 1 and year 2.

Figure 6.5a shows this difference in standard deviations for the first year of the hindcasts. The assimilation hindcasts perform better than the No assimilation hindcasts wherever values are positive: Europe, central Siberia and the coasts of North America. There is a similar pattern when assessing the second year of hindcasts (figure 6.5b), with some additional improvement in central Canada but worsening performance in Europe. These areas also showed the largest biases in figures 6.4 and 6.2, but with the bias correction applied they are revealed to be areas of improved skill over the No assimilation runs. However, the fields remain noisy, and the small number of hindcasts limit the statistical significance of this result.

Figure 6.6 shows RMSE and spatial correlation scores for the hindcasts with and without assimilation. The clear seasonal cycle in the SWE anomaly biases can be seen in figures 6.6a and 6.6c. RMSE scores are similar across all hindcasts, with or without assimilation, generally peaking at 30-35mm. The largest RMSE for the assimilation hindcasts in figure 6.6a is for the May 1997 hindcast over the winter of 97-98, which featured a large ENSO event. A lack of knowledge of the developing event after release may explain the large RMSE.

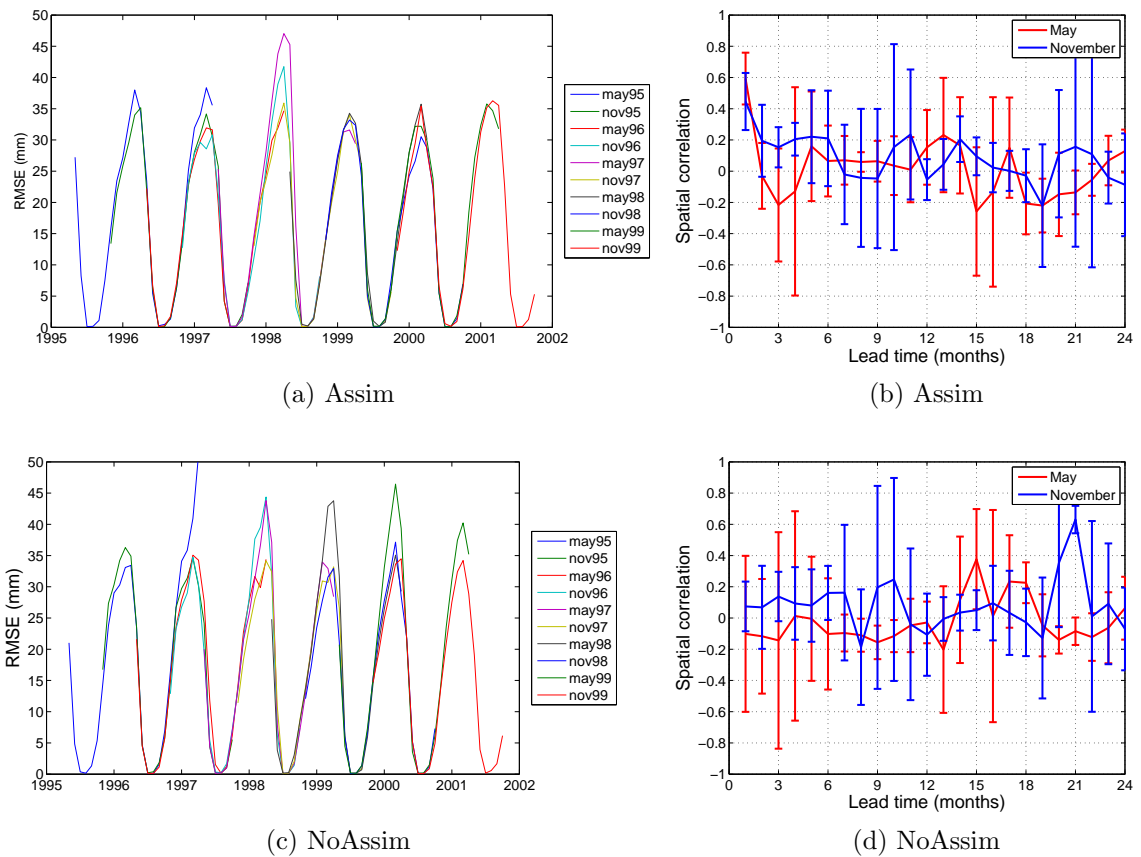


Figure 6.6: Monthly root mean square error (left column, mm) and mean spatial correlation (right column) of SWE anomalies between ERA40 and the hindcasts released from the assimilation run and the no assimilation ensemble mean. Spatial correlations are averaged over May and November hindcasts separately, and error bars show one standard deviation of the hindcast ensemble.

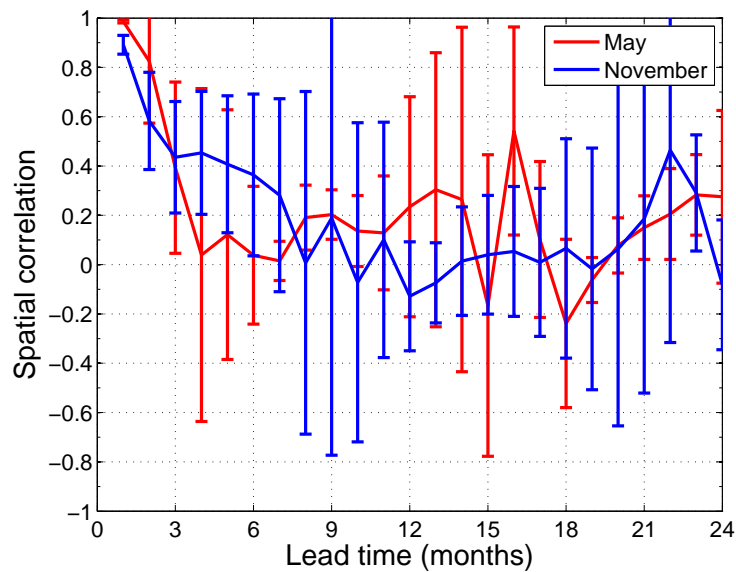


Figure 6.7: Spatial correlation of SWE anomalies between hindcasts and assimilation run

The spatial correlations for the hindcasts launched from the assimilation run (figure 6.6b) start high for the first month, but within 3-6 months the spatial correlations are around zero. The No assimilation hindcasts (figure 6.6d) have spatial correlations with ERA40 of around zero at all lead times. For comparison, the correlations between the hindcasts released from the assimilation run and the assimilation run itself are also plotted in figure 6.7. As expected, the correlations for the first month are very high but again the correlations drop to zero, in 3-6 months for the May hindcasts and 8-10 months for November. In both cases this coincides with the start of the new snow season, between August and October, and suggests there is little memory in the snow state carried over from the previous season.

## 6.4 Case Studies

Having now examined the overall statistics of the assimilation runs and hindcasts, we now examine some case studies month-by-month. The aim here is to assess whether the broad features of the anomaly patterns in each dataset are similar, rather than attempting more detailed gridbox-to-gridbox comparisons.

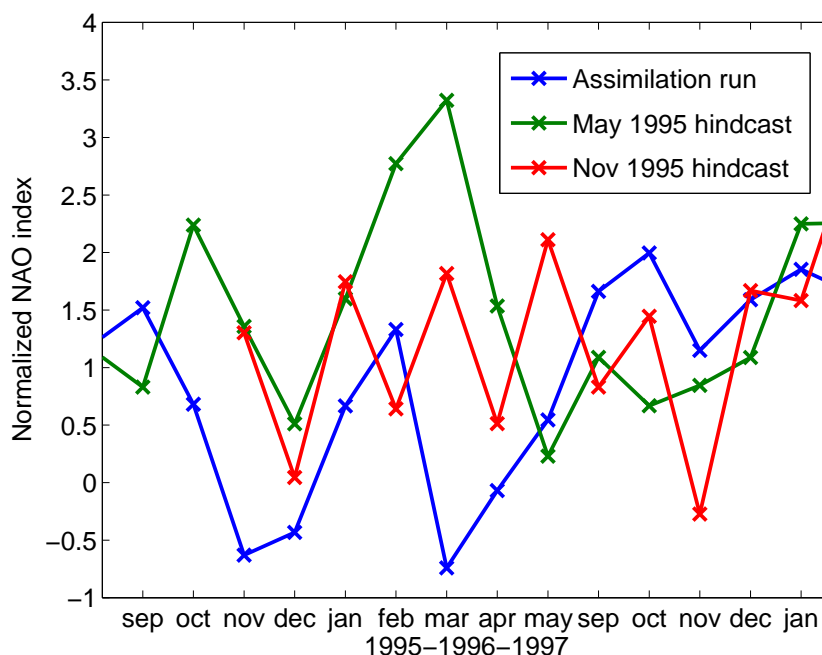


Figure 6.8: NAO during 1995-1997 from assimilation run and hindcasts

### 6.4.1 Negative NAO event: 1995-6

The North Atlantic Oscillation (NAO) characterises variability in atmospheric pressure and storm tracks in the North Atlantic, and forms the basis for much seasonal forecasting research in the region. The winter of 1995-6 exhibited a large negative NAO event: the DJFM average NAO index was highly negative<sup>1</sup>. Figure 2.2 in chapter 2 showed the effect of the NAO on winter climate. During the negative phase, northern Europe is drier than normal, so negative snow anomalies would be expected. Southern Europe is wetter than normal, so positive anomalies would be expected. In North America, the negative phase brings above normal snow to the eastern United States, while less snow than normal is found in northeastern Canada.

The monthly NAO index for the assimilation run (assumed close to truth as mean sea level pressure anomalies are assimilated) and hindcasts launched in May and November 1995 are shown in figure 6.8. The lowest values are seen in the assimilation run for November, December and March, with higher values between these months. The hindcasts follow a similar pattern but are generally higher, with the November 1995 hindcast oscillating between positive and negative NAO index and the May 1995 hindcast being generally positive.

<sup>1</sup>Tim Osborn's page, Climate Research Unit at the University of East Anglia: <http://www.cru.uea.ac.uk/timo/projpages/nao.update.htm>.

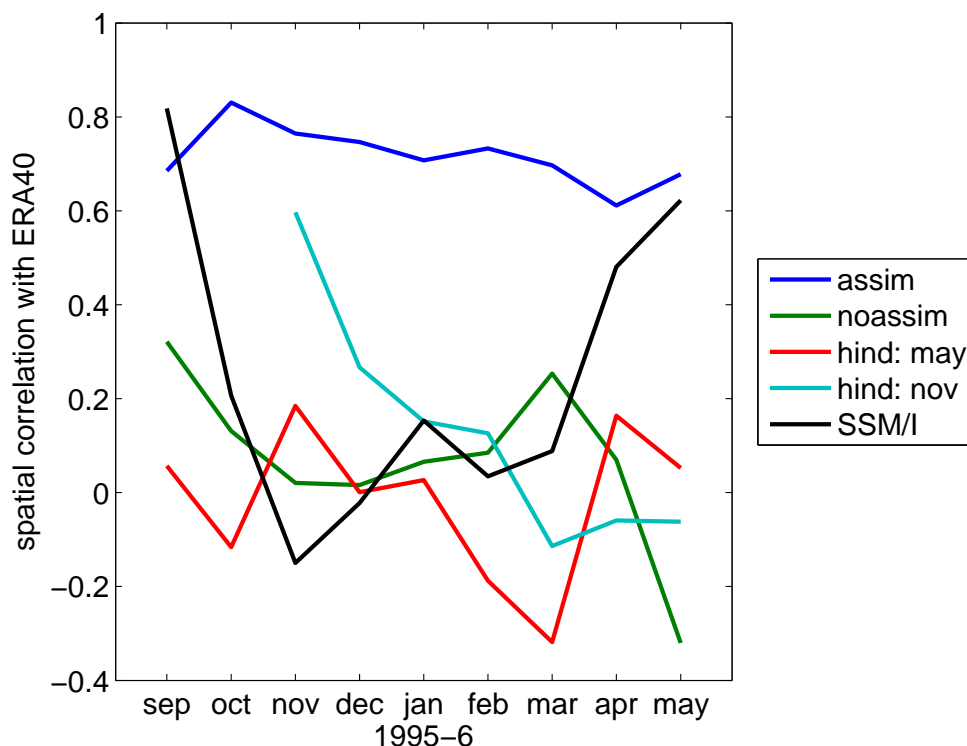


Figure 6.9: Spatial correlation between anomalies of ERA40 and the assimilation run, no assimilation ensemble mean, hindcasts launched in May 1995 and November 1995 and SSM/I, for the negative AO event in 1995-6

Figure 6.9 shows the spatial correlations of SWE anomalies during the NAO event in 1995-6 between ERA40 and the different model runs, plus correlations between ERA40 and SSM/I. As would be expected (and as seen previously in figure 6.3b, the assimilation run shows a high correlation ( $>0.7$ ) with ERA40 for all months. Correlation between ERA40 and SSM/I is also high in September, but this rapidly drops to zero before improving again in April and May. The hindcast released in November 1995 shows fairly high correlations with ERA40 for the first month (November) but this also drops to zero within two months. By the start of this case study in September, the hindcast released the previous May is showing low correlations with ERA40. The No assimilation ensemble mean shows low correlations throughout.

The spatial distribution of SWE anomalies during the case study period are now examined. Figure 6.10 shows SWE anomalies from the model runs, SSM/I and ERA40. The No assimilation ensemble mean is plotted for each month as an illustration of the impact of assimilation.

## Autumn 1995

In September, ERA40 and the assimilation run both show widespread negative anomalies, with a positive anomaly in far northern Russia. SSM/I also shows a positive anomaly here, although the negative anomalies are not nearly as widespread, due to the retrieval's limitations in detecting very thin snow cover (as discussed in chapter 3).

In October, the positive anomaly in Russia in the assimilation run has got much larger. The anomaly is still present in both ERA40 and SSM/I but is not so large. ERA40 and the assimilation run also share small positive anomalies in northern Scandinavia, central Asia and far northern Canada. The May 1995 hindcast is showing a large positive anomaly further west which is not seen in either ERA40 or SSM/I.

By November, the positive anomaly over Russia in the assimilation run is even larger, and still bigger than in SSM/I or ERA40. Negative anomalies are developing to the south and east of this, and are seen in both ERA40 and SSM/I. Agreement between ERA40 and the assimilation run also exists over northern Scandinavia, although this is not seen in SSM/I. Broadly similar patterns are also seen over North America, especially around Hudson Bay, although SSM/I anomalies are still much smaller than those in the assimilation run and ERA40. The November 1995 hindcast, launched at the start of this month, is still very similar to the assimilation run at this point.

Throughout Autumn, the anomalies from the hindcast launched in May 1995 look somewhat different to the other runs, with the main feature being a widespread positive anomaly developing in northwestern Russia throughout the season. The No assimilation ensemble mean also shows no correlation with the observations or the assimilation run, and much smaller anomalies across the hemisphere.

## Winter 1995-6

In December, the assimilation run anomalies have a similar distribution to the ERA40 anomalies over both continents. The pattern of anomalies in eastern North America and Russia are particularly well-correlated, though the positive anomaly in northern Russia is still too large. However, large negative anomalies are present in the Himalayas which are not seen in ERA40, and are of the opposite sign in SSM/I. ERA40 and SSM/I show similarities around Hudson Bay and northern Scandinavia, but the anomalies are rather different across Russia. The November 1995 hindcast still shares many features with the assimilation run, but these are diverging from the ERA40 observations. The May 1995 hindcast again looks very different to either the assimilation run, ERA40 or SSM/I, with the persistent positive anomaly in northwestern Russia, and predominantly negative anomalies in North America.

In January, agreement is widespread over North America between the assimilation run and ERA40, particularly towards the two coasts. ERA40 also shows agreement with SSM/I in eastern Canada, and about the presence of a band of positive anomalies across central North America. In Eurasia, the anomalies in central Russia are still too large in the assimilation run, although the spatial distribution is still similar to ERA40. Agreement is seen between SSM/I and ERA40 in eastern Europe, but there is no clear agreement over the rest of the continent. The November 1995 hindcast still shows reasonable correspondence with ERA40 in western North America and eastern Eurasia but there is little agreement elsewhere. The sign of the NAO is positive in the two hindcasts, so the anomalies in the North Atlantic region show little correspondence to the assimilation run, where the NAO index is more neutral for this month (but has been negative throughout autumn). In the May 1995 hindcast, the SWE anomaly dipole in Europe is clearly opposite to that in the assimilation run.

February shows continuing agreement between ERA40 and the assimilation run in eastern North America. Across Eurasia, the anomalies in the assimilation run are much more zonal than in ERA40, although the dipole over western Russia is of the correct sign, with negative anomalies further north and positive anomalies further south. Further east in Eurasia, there is much less agreement. SSM/I and ERA40 again look similar over North America, but the Eurasian SSM/I pattern for February is dominated by a large positive anomaly over eastern Europe/western Russia, and there is no negative counterpart as seen in ERA40. The November 1995 hindcast shows reasonable agreement with ERA40 in western North America and Siberia, and shows some positive anomalies in southern Europe. Once again, the dipole of positive anomalies in northern Europe and negative anomalies to the south is seen in the May 1995 hindcast, indicative of the positive NAO phase during this month in this hindcast.

Throughout winter the No assimilation ensemble mean has much smaller SWE anomalies across the hemisphere, indicating that by averaging over the ensemble members the patterns have been smoothed.

## **Spring 1996**

In March, ERA40 and the assimilation run again show good correspondence in eastern North America, and reasonable agreement to the west of the continent. In Eurasia, the dipole is again present in both patterns, and while the pattern of positives and negatives is similar further east, once more the assimilation run anomalies are larger than those in ERA40. Agreement is also seen with SSM/I across much of North America, although in Eurasia the widespread positive anomaly is not seen in any other dataset. Agreement between SSM/I and ERA40 improves further east. The November

1995 hindcast again compares reasonably around Hudson Bay, but less so across the rest of North America. The dipole in western Eurasia has changed sign in the November hindcast, corresponding to the change in sign of the NAO for this month, although further east agreement with ERA40 improves.

ERA40, SSM/I and the assimilation run again agree over North America in April. The western Eurasian dipole is weakening in ERA40, though not in the assimilation run where anomalies are still very large. Agreement with ERA40 extends across Siberia. The large positive anomaly is still present in SSM/I however and is not seen elsewhere. Some agreement is seen between the November 1995 hindcast and ERA40 around Hudson Bay, but there is little agreement elsewhere. The May 1995 hindcast shows even less agreement with observations.

In May, ERA40, SSM/I and the assimilation run all agree in northern Eurasia, with positive anomalies in northern Siberia and Scandinavia. ERA40 and SSM/I also show some agreement in North America, although the assimilation run produces large positive anomalies in the Canadian Arctic which are not seen in the observations. The November 1995 hindcast has the positive anomalies in northern Russia, although they extend too far east, but not those in Scandinavia. Agreement is also reduced over North America. For this month, the May 1995 hindcast shows some similarities with the assimilation run, but after such an extended period of differences, and being in a month with limited snow extent, this is most likely due to chance.

#### **6.4.2 Positive ENSO event: 1997-8**

The winter of 1997-8 exhibited a large positive ENSO event. The assimilation and short hindcast runs both reproduce the sea surface temperature anomalies in the Nino3.4 region during the 1997-8 ENSO event very well (reported in Haines (2007)). The No assimilation runs are ENSO-neutral and are therefore not expected to reproduce any of the relevant land surface anomalies.

Figure 2.1 in chapter 2 showed the expected pattern of climate anomalies during a positive ENSO event. Warmer weather is brought to Pacific Asia and northwestern and northeastern North America, which suggests negative SWE anomalies. Wetter and cooler weather, and hence positive anomalies, are found in the United States.

Figure 6.11 shows the spatial correlations between ERA40 SWE anomalies and those from the assimilation run, no assimilation ensemble mean, hindcast released in May 1997, hindcast released in November 1997 and SSM/I. In general, the assimilation run shows the greatest correlation with ERA40 ( $>0.4$  for most months). Again, SSM/I shows fairly high correlation with ERA40 in September and spring, but this drops to zero and even becomes negative during the winter months. The No assimilation run is

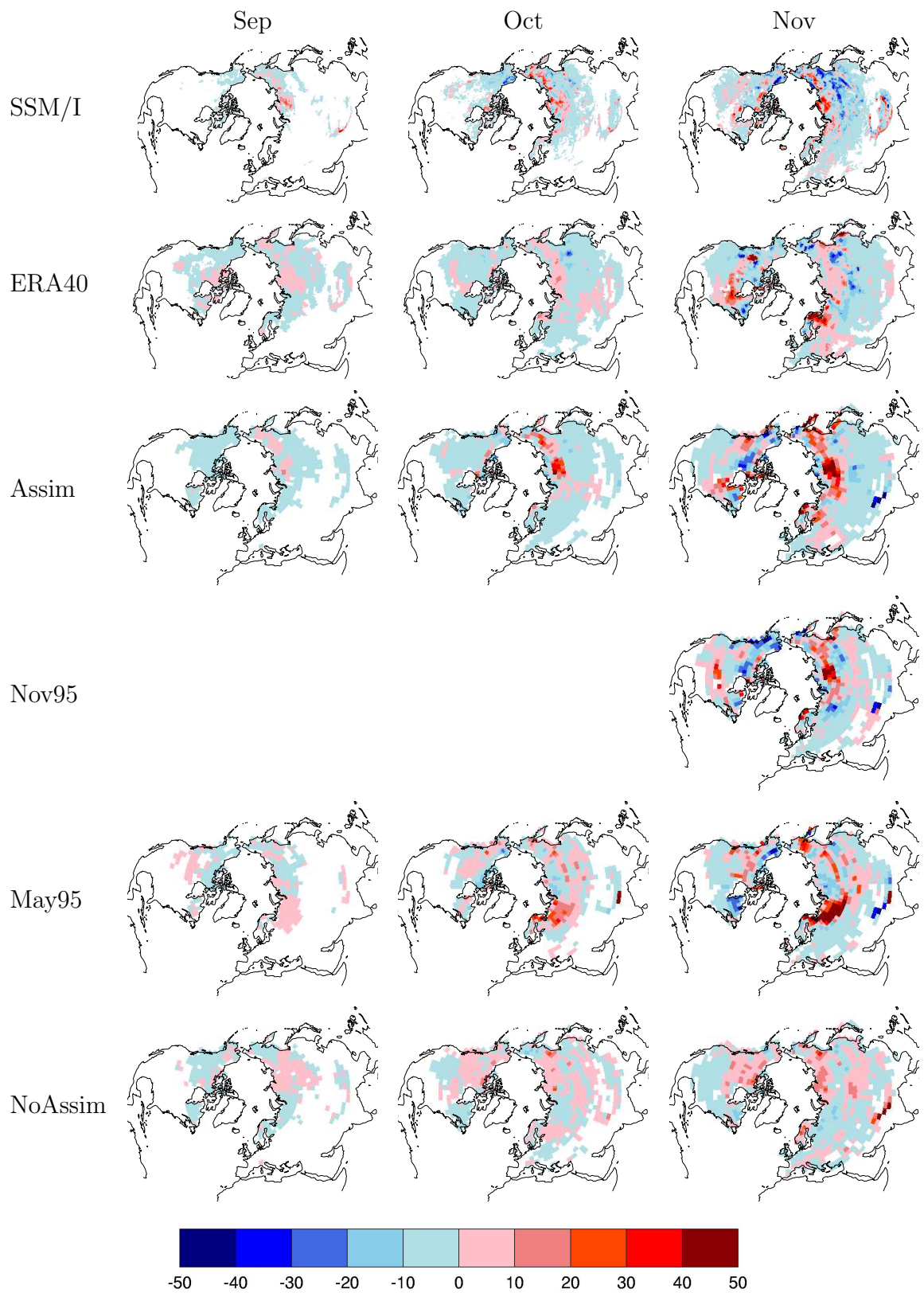


Figure 6.10: Negative NAO event 1995-6: monthly SWE anomalies (mm) from SSM/I, ERA40, assimilation run, hindcasts and no assimilation ensemble mean

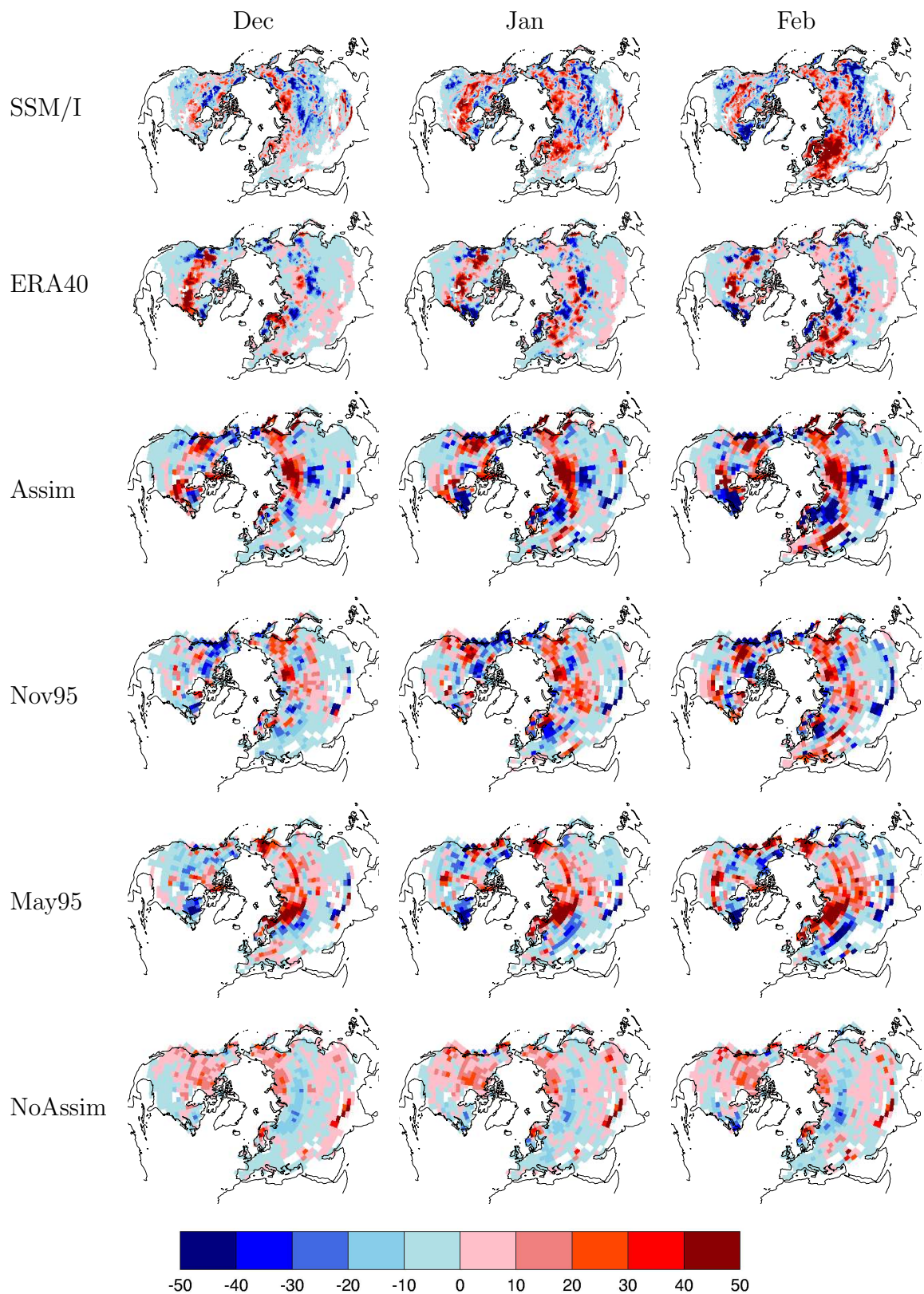


Figure 6.10: (cont) Negative NAO event 1995-6: monthly SWE anomalies (mm) from SSM/I, ERA40, assimilation run, hindcasts and no assimilation ensemble mean

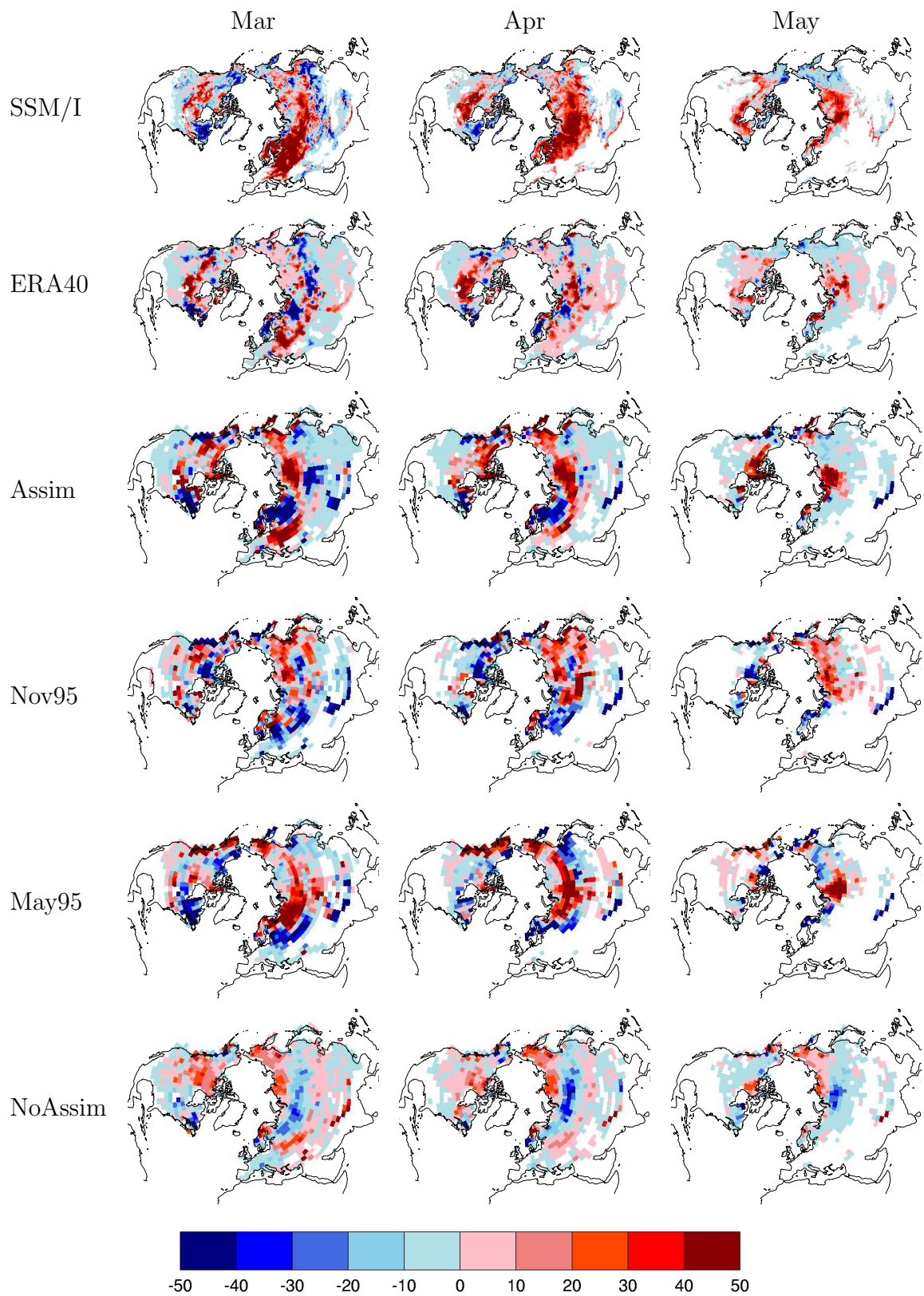


Figure 6.10: (cont) Negative NAO event 1995-6: monthly SWE anomalies (mm) from SSM/I, ERA40, assimilation run, hindcasts and no assimilation ensemble mean

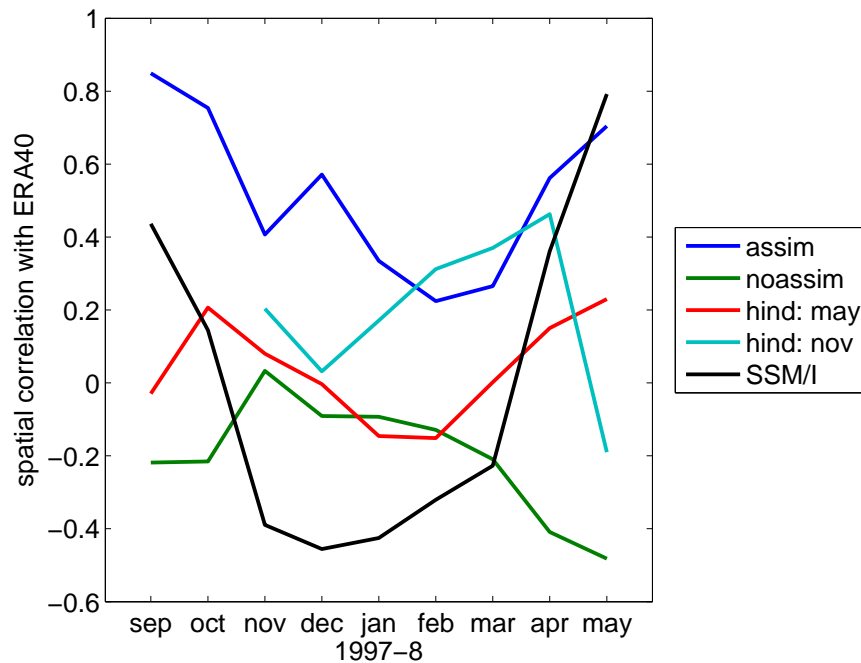


Figure 6.11: Spatial correlation between SWE anomalies of ERA40 and the assimilation run, no assimilation ensemble mean, hindcasts launched in May 1997 and November 1997 and SSM/I, for the positive ENSO event in 1997-8

negatively correlated with ERA40 for most of the period. The hindcasts both have low correlations with ERA40 in 1997, but the correlations increase in 1998 to a maximum for both hindcasts in April.

The spatial distribution of SWE anomalies during the case study period are now examined. Figure 6.12 shows SWE anomalies from the model runs, SSM/I and ERA40.

## Autumn 1997

In September, all anomalies are small. The spatial extent of SWE anomalies is slightly lower in the assimilation run than ERA40, though not as low as in SSM/I. ERA40 and SSM/I do agree about a small area of positive anomalies in northeastern Siberia. In October, positive anomalies develop in North America in ERA40, the assimilation run and in the May 1997 hindcast, although they are not seen in SSM/I. In November, the assimilation run, ERA40 and SSM/I agree about a positive anomaly just east of Scandinavia, although there is disagreement both further east in Eurasia and in North America. The November 1997 hindcast is very similar to the assimilation run, having been released at the beginning of the month, but more surprisingly, the May 1997 hindcast also looks similar to the assimilation run, 7 months after release. SSM/I

also bears more resemblance to the assimilation run than ERA40, with large positive anomalies in eastern Siberia. There is perhaps more agreement this month over North America between SSM/I and ERA40.

## **Winter 1997-8**

In December, more agreement is seen in North America between ERA40 and the assimilation run, with a band of negative anomalies stretching across Canada with positive anomalies to the north. This band is also seen in SSM/I. Differences are larger across Eurasia, particularly to the east where ERA40 shows negative anomalies while those in the assimilation run and SSM/I are positive. More agreement between the assimilation run and ERA40 is seen in western Eurasia. Very little agreement in either continent is seen when looking at the hindcasts, and indeed the spatial correlations between the hindcasts and ERA40 for December are around zero (figure 6.11).

In January, agreement is seen between ERA40 and the assimilation run around Hudson Bay, although little is seen over the rest of North America. ERA40 and SSM/I show a little more agreement in this case. The May 1997 hindcast still shows remarkable agreement with the assimilation run in North America, with the November 1997 hindcast looking quite different (though, in fact, more similar to ERA40). In Eurasia, little large-scale agreement is seen between any of the runs.

By February, the assimilation run and ERA40 look more similar in North America, with positive anomalies at high latitudes and negative anomalies further south, with some positive anomalies on the east and west coasts. SSM/I also shows some similarities, although the large positive anomalies in Alaska are not seen in ERA40. In Eurasia, ERA40 shows positive anomalies in northwest Russia and northern Scandinavia, with negative anomalies further south. In the assimilation run these signs are reversed, though there is more agreement around the Black Sea. SSM/I is in better agreement with ERA40 in this area, as is the November 1997 hindcast. Again, the May 1997 hindcast looks much like the assimilation run in North America, though less so over Eurasia.

## **Spring 1998**

In March, agreement is still reasonable over North America between ERA40 and the assimilation run. SSM/I, however, shows a very different pattern of anomalies to the west, though the east agrees better. The November 1997 hindcast does a good job in eastern North America, although the anomalies on the west coast are too large. The May 1997 hindcast is again similar to the assimilation run. In Eurasia, ERA40 has a

band of positive anomalies going from northern Scandinavia down towards Kazakhstan, surrounded by negative anomalies. A similar pattern is seen in the assimilation run, although shifted further west. A similar but much thinner band of positive anomalies is seen in SSM/I, but there is little overall agreement in Eurasia. The November 1997 hindcast shows the best agreement with ERA40 in Eurasia, and particularly Europe, out of all the model runs.

In April, a large positive anomaly has developed over northwestern Russia in ERA40, and is also present in the assimilation run and SSM/I, though with a smaller spatial extent in the latter. The feature is also present in both hindcast runs, though it is small in the May hindcast. Agreement is also good further east in Eurasia between the assimilation run and ERA40, although SSM/I is still showing much larger positive anomalies in far eastern Siberia. In North America, negative anomalies across Canada are seen in ERA40, the assimilation run and SSM/I, though the latter has larger positive anomalies towards both coasts, and the assimilation run has large positive anomalies in the Canadian Arctic which are not seen in the observations. The May 1997 hindcast is the closer of the two hindcasts to the assimilation run over North America.

In May, the assimilation run, ERA40 and SSM/I are all very similar over the whole hemisphere. Again it is the May 1997 hindcast that performs the better of the two hindcasts in this case.

## 6.5 Discussion

In this chapter, results have been presented from an assimilation scheme using atmospheric and oceanic reanalysis data to reproduce SWE anomalies with the HadCM3 GCM. By assimilating only atmospheric and ocean temperature, ocean salinity, sea level pressure and wind fields, the model was able to reproduce ERA40 SWE anomalies between 1995 and 2001 with a good degree of success (spatial correlations  $> 0.6$  for much of the period). However, RMSE scores were higher than for the No assimilation ensemble mean, as the statistic is biased by some large gridbox-to-gridbox differences between ERA40 and the assimilation run (despite correspondence in the spatial patterns). The No assimilation ensemble mean shows much lower anomaly values than the assimilation run, a sign of the SWE anomaly field having spatial noise across the No assimilation ensemble members which is smoothed out with the averaging.

The largest biases in the assimilation run are seen in winter and spring, with positive biases in Europe, eastern Siberia, the Canadian Arctic and the west coast of North America, and negative biases in central North America, central Eurasia and

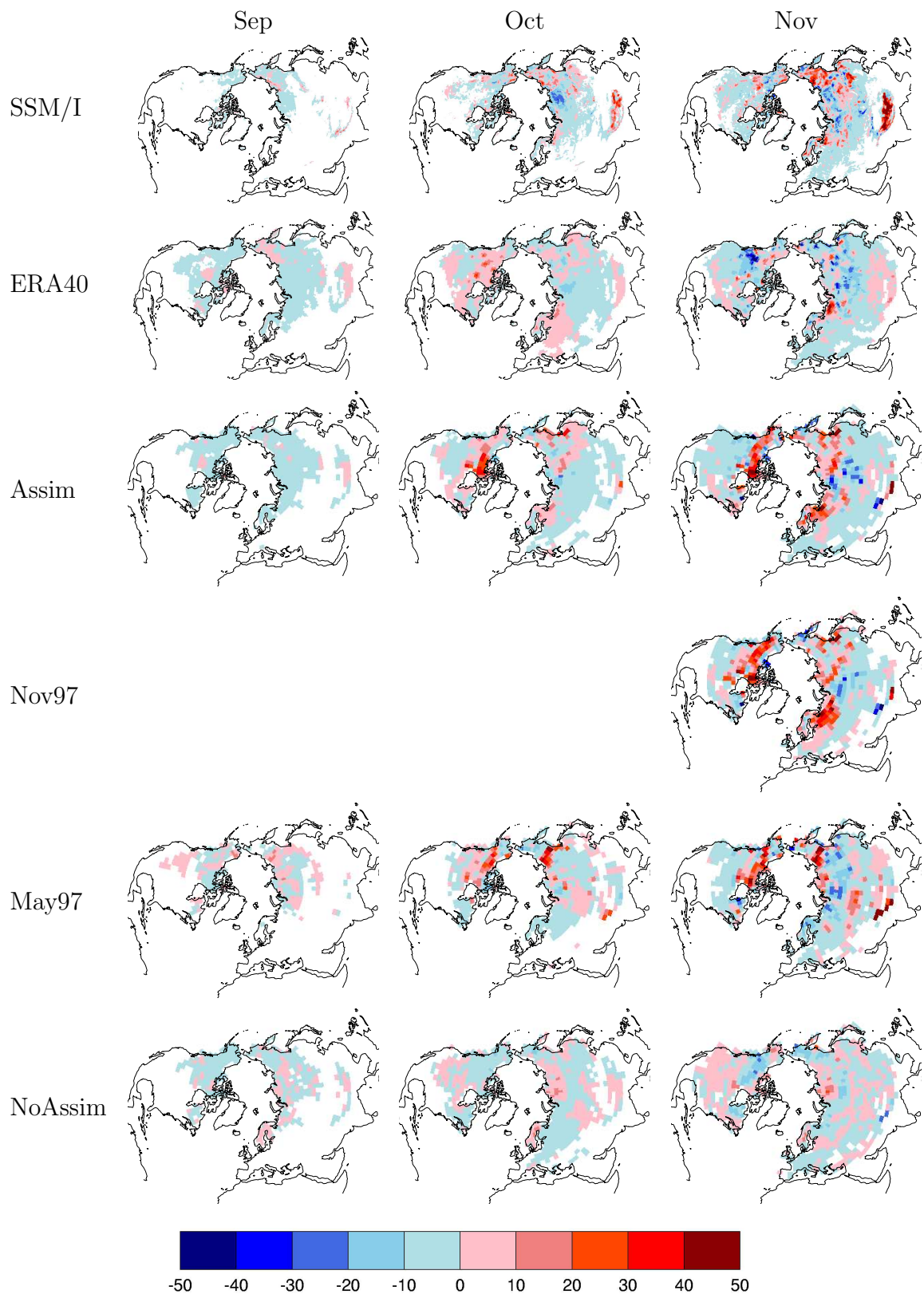


Figure 6.12: Positive ENSO event 1997-8: monthly SWE anomalies (mm) from SSM/I, ERA40, assimilation run, hindcasts and no assimilation ensemble mean

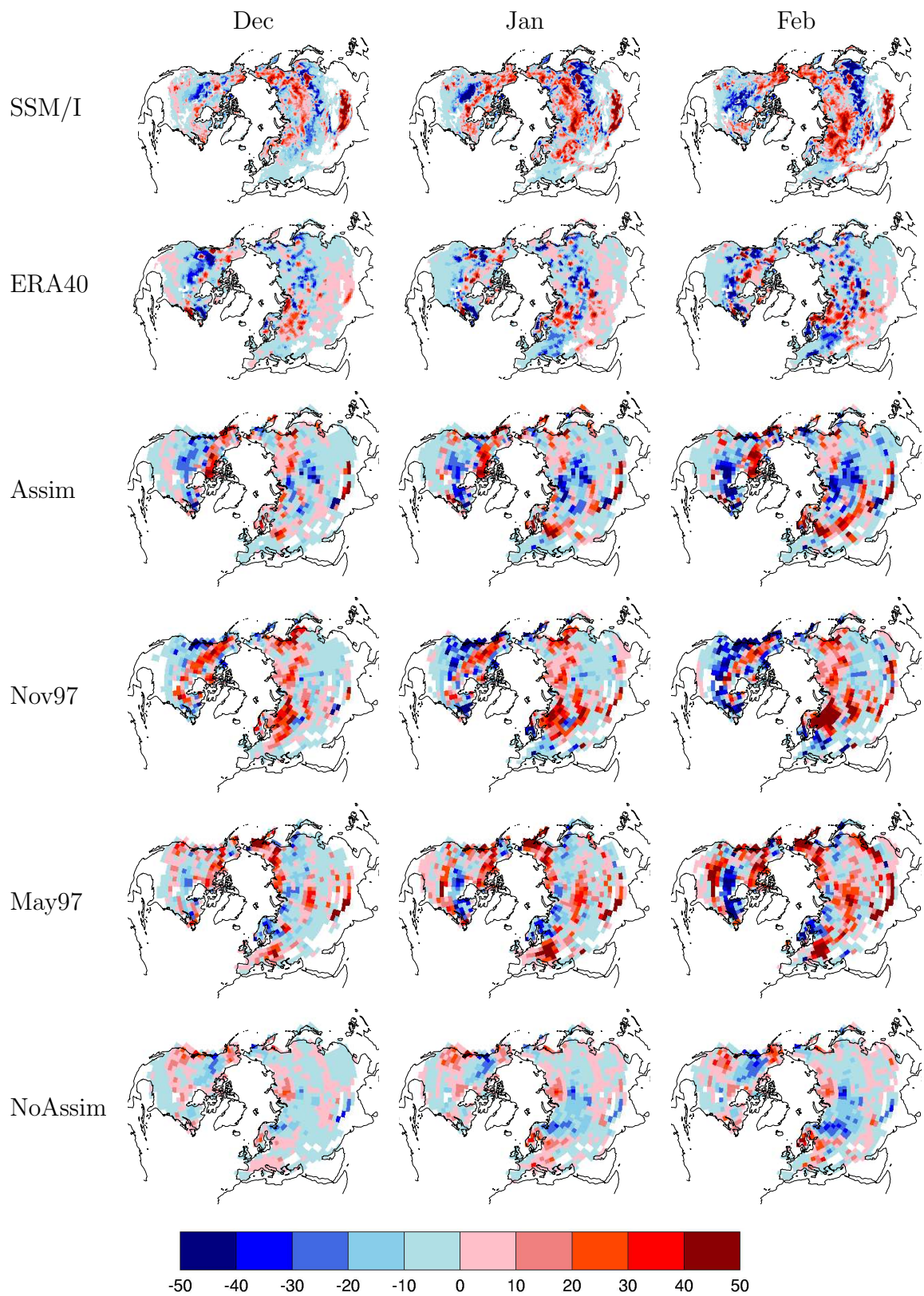


Figure 6.12: (cont) Positive ENSO event 1997-8: monthly SWE anomalies (mm) from SSM/I, ERA40, assimilation run, hindcasts and no assimilation ensemble mean

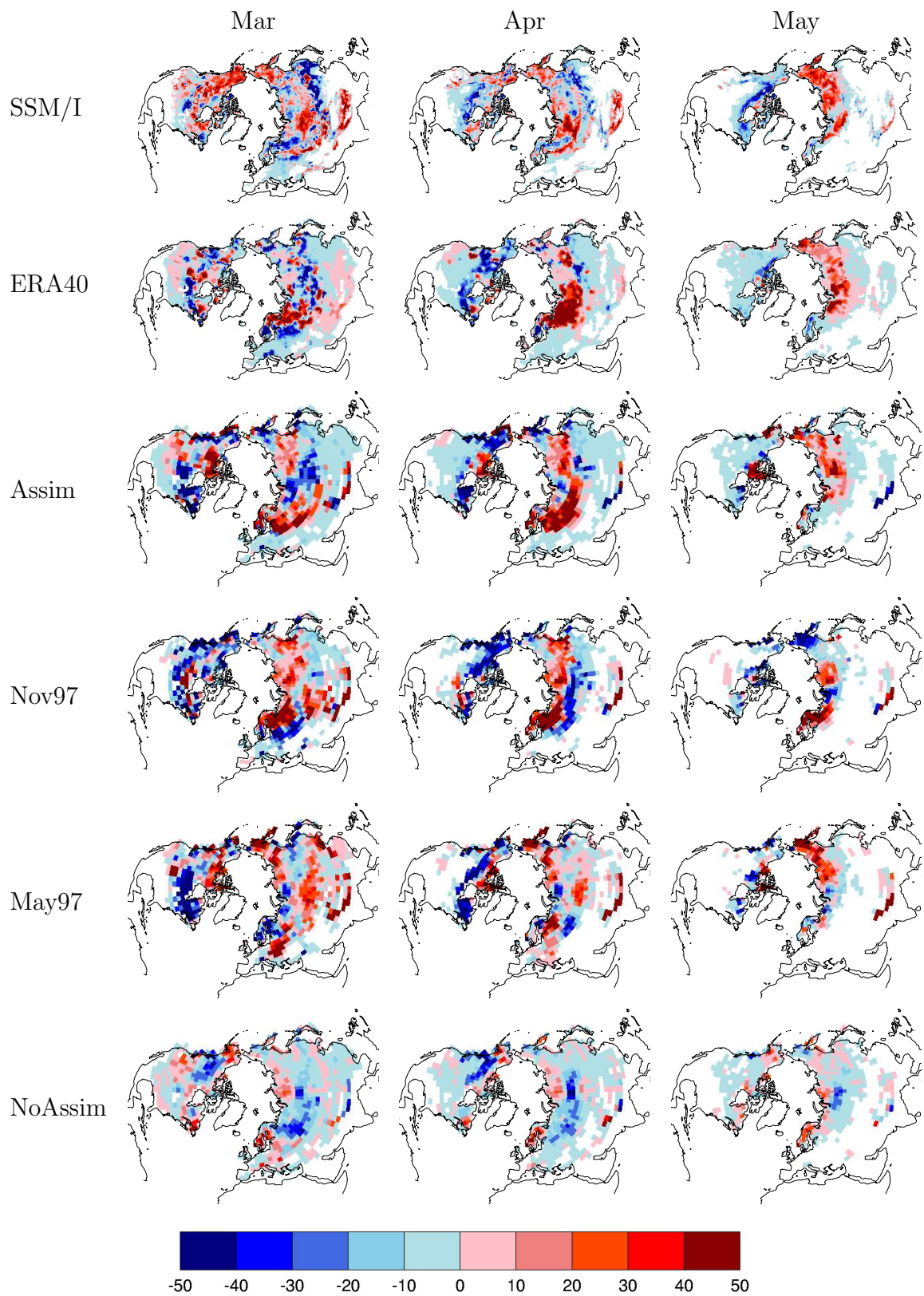


Figure 6.12: (cont) Positive ENSO event 1997-8: monthly SWE anomalies (mm) from SSM/I, ERA40, assimilation run, hindcasts and no assimilation ensemble mean

the Himalayas. It is interesting to note that these areas roughly correspond with areas of differences in the ERA40 and HadCM3 climatologies: in particular HadCM3 has much deeper snow along the west coast of North America, and much shallower snow in central Siberia (see figure 5.2 in chapter 5). As the size of SWE anomalies are related to the SWE climatology (larger values in an area in the climatology make larger SWE anomalies more possible), removing the climatologies does not eliminate the differences due to the basic SWE distributions.

As both surface temperature and sea level pressure are assimilated fields, it is likely that most of the bias comes from precipitation differences. The SWE field in ERA40 is also not purely model-generated, as in situ data are assimilated into the reanalysis, so there may be imbalances in the water and energy cycles.

The success of the assimilation run in reproducing SWE patterns is encouraging, although there are still differences in the characteristics of the anomalies between the different datasets. The ERA40 anomaly field is more speckled, with lots of ‘bullseye’ structures which could be a consequence of interpolation from sparse in situ data. The SSM/I data is at a much higher resolution and hence has much fine structure in it, but the spatial coherence is much higher than for ERA40. The model anomalies, with the lowest resolution examined here, are much more zonal than either of the observational datasets.

To assess the skill of the system in forecasting mode, SWE anomalies from ensembles of hindcasts were also examined. The hindcasts were released every year in May and November and run for 2 years, leading to a total of 10 hindcasts spanning the period 1995-2001. Correlations of hindcast anomalies, both with the assimilation run and with ERA40, drop to around zero by the time a new snow season starts. This suggests that there is little memory from season to season for SWE, unlike the results previously shown with DePreSys and GCEP for surface temperature. However, when the standard deviations of the hindcast runs with and without assimilation are compared, there are areas that show more skill in the hindcasts with assimilation, even by year 2 (although with the small number of hindcasts, this is unlikely to be significant).

Two case studies, spanning the snow seasons of 1995-6 (a large negative NAO event) and 1997-8 (a large positive ENSO event) were examined. While the correlations between the hindcast and ERA40 drop quickly after release, on examining the spatial patterns there is often still some correspondence. During the case studies, the anomalies from SSM/I correlate best with ERA40 during the autumn and spring. Examining the spatial patterns shows that there is better correspondence between these two datasets over North America than Eurasia. This is not surprising, as North America has more snow observations which will better constrain ERA40, and most calibration for the

SSM/I retrieval has been performed using data from the Great Plains. The spatial correlations across the Northern hemisphere will also be most influenced by the larger Eurasian land mass, so although the overall correlation for the ENSO case study was lower than that of the NAO case study, the correspondence in North America is better. ENSO would be expected to influence the SWE distribution in North America more significantly than the NAO.

Agreement is good in western Eurasia between the assimilation run, hindcasts and ERA40 when the sign of the NAO is also the same. Although ENSO has greater impact on the world's weather, on the basis of these case studies snow distribution in the Northern hemisphere (in particular around the North Atlantic) is more sensitive to the NAO index. However the NAO is variable between hindcasts, showing that for this example, the assimilation scheme is not able to generate good forecasts of the NAO.

Snow affects regional temperatures, and since snow in the Northern hemisphere is also likely to undergo changes in distribution with climate change, so an ability to forecast snow distribution will be an important advance in the predictability of global temperatures. While the results in this chapter show that the snow distribution in a climate model can be relatively well-constrained by assimilation, forecasts diverge rapidly once that assimilation ceases. Collins and Allen (2002) found that temperatures over the land surface were not predictable over lead times greater than about a month, and this limited predictability is also seen here in hindcasts of SWE. SSTs however showed predictability at longer timescales, so if links between SST-driven variability, such as ENSO, on snow distribution can be found, there is potential to extend the lead times on snow anomaly forecasts. More work is required to understand the controls on snow distribution in models, such as precipitation patterns and the NAO in particular, and this is the subject of the next chapter.

# Chapter 7

## Predictability of snow anomalies in HadCM3

### 7.1 Introduction

#### 7.1.1 Predictability and seasonal forecasting

Advance information on snow distribution would be useful information for hydrological and climate applications. The previous chapter showed that when constrained by some observed initial condition anomalies such as temperature, the snow anomaly distribution was only predictable a month or two ahead. Longer term predictions could be possible, however, if the controls on snow distribution by boundary conditions such as ocean conditions could be determined. Understanding more about the effect of climate modes such as the El Niño-Southern Oscillation (ENSO) and the North Atlantic Oscillation (NAO) on the rest of the climate system is an important step in delivering useful forecasts.

Few published studies have attempted to link these climate indices to forecastable patterns of snow distribution. Clark and Serreze (1999) examine observed snow extent, and find strong links in Europe with the NAO. Links with other climate modes, such as the Siberian high, cannot be obtained by examining only snow extent as these areas are entirely snow-covered during winter, so anomalies will only be evident in snow depth, for which there are few observations.

Global precipitation was analysed by Dai et al. (1997) using a gridded dataset derived from station data for the years 1900-1988 inclusive. The first EOF of the dataset is a pattern related to ENSO, centred over the Tropics, and ENSO is also shown to be the single largest cause of global extreme precipitation events. The authors also consider the effect of the NAO on precipitation, which they show accounts for 10% of

the DJF precipitation variance in the North Atlantic region. They confirm that positive NAO periods bring increased rainfall to northern Europe ( $> 50^\circ N$ ), the East coast of the United States, northern Africa and the Mediterranean, with decreased rainfall in southern Europe, eastern Canada and western Greenland. The authors also find trends in the global data (which are consistent with model-derived responses to increasing  $\text{CO}_2$  levels) together with an increase in the period between dry events over the United States. This presence of trend in the observed data, together with the difficulty of making accurate precipitation measurements with good spatial coverage, makes the patterns and mechanisms of interannual variability difficult to discern. GCMs become an important tool for generating very long datasets with idealised forcings that can be used for this sort of investigation. This model-based approach is the subject of this chapter.

Most studies relating to snow and climate indices such as ENSO and the NAO have been performed from a meteorology and atmospheric dynamics perspective: exploiting snow information in order to predict the behaviour of the atmosphere some weeks ahead (see references in chapter 2). However, HadCM3 has low land-atmosphere coupling (Koster et al., 2002) so is poorly suited to these kinds of experiments. In this study, the objective is reversed: can knowledge of the current snowpack and/or certain climate modes be used to predict the state of the snowpack later in the season, or the following one? This would represent an important advance in improving the lead times for both hydrological and climate applications.

## 7.2 Data and methodology

### 7.2.1 The long HadCM3 control run

In order to understand the model's internal variability, a long control run with fixed external forcings (such as greenhouse gases) has been studied. This control run was done on the computing cluster at ESSC, and was initialised from a much longer control run performed at the Met Office, to ensure the model components had reached equilibrium and there was no climatology drift. This run will be referred to as the 'control run'.

The run is 545 years long, and fields are output at timesteps of one month. Snow-covered area (SCA) is derived from the SWE field. For a gridbox to be completely snow-covered, a threshold of 6.25mm SWE is required (following the method of Frei et al. (2003) as part of the Atmospheric Model Intercomparison Project). Below this threshold the fractional snow coverage of a gridbox decreases linearly with SWE.

In all of the results that follow, North America and Eurasia have been treated separately, as analysing the Northern hemisphere in its entirety leads to results heavily biased by the larger Eurasian land mass. In the discussion that follows, NA refers to North America and EU to Eurasia. Continental mean indices for SWE and SCA show no trend in the 545 years (not shown).

## 7.2.2 Experiments

### Extreme events

Extremely high or low snow years are important to predict for both hydrological and climate forecasting. It may be that years with very high or very low amounts of snow have an impact on the following year's snowpack development, or that they may be preconditioned in some way by events the previous year. To test this, ensembles of high and low snow years (both SWE and SCA) are created from the long control run, by extracting the years with the highest and lowest continental mean conditions respectively. Ensembles of preceding and following SWE distributions can also be compiled, at various lags, so the effect of particular conditions can be established. Mean February SWE or SCA is used as representative of the snowpack for the winter. To assess the signature of extreme years in the earlier part of the season, composites of monthly SWE from the September to December preceding the extreme February will also be analysed.

Student's t-test is used to determine whether the distributions in different cases are significantly different from the mean distribution in the run. A threshold for significance of 99% is used, as the length of the run provides enough data to justify a high threshold. The implication of the threshold is that only one case (e.g. one gridbox) in a hundred will pass the test for significance by chance, so we can be 99% sure that the cases that pass are indeed statistically significant.

### ENSO

ENSO events have impacts on weather patterns across the globe, which may extend far enough to modulate the characteristics of Northern hemisphere snow distribution. While little has been published on the relationship of ENSO to snow distribution, this approach has been used to analyse precipitation data. Ropelewski and Bell (2008) examined the shift in the statistics of daily rainfall in South America with ENSO phase. They find that useful information about the character of the rainfall season can be extracted, and extend this to gridded datasets and the NCEP-NCAR reanalysis product. They use the Kolmogorov-Smirnov test to determine whether the frequency

distributions in positive and negative phases of ENSO are significantly different, and this approach will be replicated here with snow data. Clark et al. (2001) also use station data to examine the influence of ENSO events, this time on snowpack evolution in two North American river basins. Composites of mean anomalous snow in warm and cold phases are compared, and then used to predict runoff. This approach showed that with the inclusion of ENSO information, there was skill in predicting Spring runoff even before the snow begins to accumulate in Autumn. Here, this anomaly composite approach is extended to hemispheric snow distribution, by employing a GCM.

The representation of ENSO in HadCM3 is discussed in Slingo et al. (2003). The response of the Indian Ocean to an ENSO event is well modelled, but an exaggerated response exists in the tropical Atlantic. The model reproduces the high-frequency component (with a return period of  $\sim 3$  years) of the variability successfully, but does not generate the additional lower frequency response (with a return period of  $\sim 3 - 8$  years) seen in the observations. Nevertheless, the representation of ENSO in HadCM3 is generally good (Collins et al., 2001). The ENSO index used here is the seasonal SST anomaly in the Nino3.4 box (defined as between 5S, 5N and 170W, 120W), with an anomaly of greater than  $0.5^{\circ}\text{C}$  denoting a positive ENSO event and less than  $-0.5^{\circ}\text{C}$  being negative.

The frequency distributions of continental mean values are generated and examined. The Kolmogorov-Smirnov (K-S) test is used to determine whether the frequency distribution of SWE at a gridbox is significantly different when the ENSO is in opposite phases. The K-S test uses the maximum separation distance between the two cumulative frequency curves to determine whether the distributions are statistically different.

Composite seasonal anomalies are also created to assess the impact of ENSO on SWE distribution. Four separate composites are created, based on the phase of the ENSO in the four seasons leading up and coincident with the SWE anomaly. For example, the February SWE anomalies are grouped based on whether ENSO was positive in the MAM, JJA, SON or DJF leading up to that February. Likewise, composites are formed for negative phases of ENSO. As an ENSO event will last for consecutive seasons, each February anomaly can be in several groups. This will suggest whether the distribution of snow in February can be predicted in any way from the ENSO phase in the preceding seasons.

## NAO

Analogous experiments to those described above for ENSO can also be constructed for the NAO. In this study, the NAO has been chosen as the index to use rather than the AO, partly for the simplicity with which it can be extracted from model data (i.e. without performing an EOF analysis). The NAO index is calculated seasonally by subtracting mean sea level pressure in an Azores box (5 gridboxes wide, centred on 26W, 37.5N) minus that in an Iceland box (also 5 gridboxes wide, but centred on 34W, 60N). Positive events are defined as those seasons where the index is more than one standard deviation above the control run mean, and negative events are those seasons where the index is more than one standard deviation below the seasonal mean.

Collins et al. (2001) compare the NAO in HadCM3 to that in observations. The model captures the observed variability well, though the amplitude is underestimated. However, there is too much teleconnection to the Pacific sector, and the signature is not strong enough over western Europe. In general, the representation of winter storm tracks in HadCM3 is good (Slingo et al., 2003). The relevant storm tracks for this study, the Atlantic, Eurasian and Mediterranean tracks, are all represented, although weaker than observed in both density of tracks and their intensity.

As for the ENSO case described above, frequency distributions are calculated for February SWE anomalies, stratified by NAO index in preceding seasons. Likewise, a K-S test is performed, and spatial anomaly distributions are also composited.

## 7.3 Results

### 7.3.1 Extreme snow events

Figure 7.1a shows the frequency distribution of continental mean February SWE for North America. The distribution has a mean value of 83mm, a standard deviation of 5mm, and a slightly positive skew (0.16). Table 7.1 shows the number of extreme events that coincide with ENSO or NAO events. 7 years make up the ensemble of extremely low snow years, with 12 years in the high snow years ensemble. 3 of the low years are during positive ENSO events, 2 are neutral and 2 are negative. These proportions are roughly the same as the control run as a whole. Of the 12 high years, 4 are during positive events, 3 neutral and 5 negative. The proportion of extremely high snow years that are ENSO-positive are roughly the same as for the control run as a whole, while proportionally more extremely high snow years are during ENSO-negative events.

The frequency distribution for Eurasia is shown in figure 7.1b. The mean is lower at 58mm (which is expected as the continental area is much larger), with a smaller

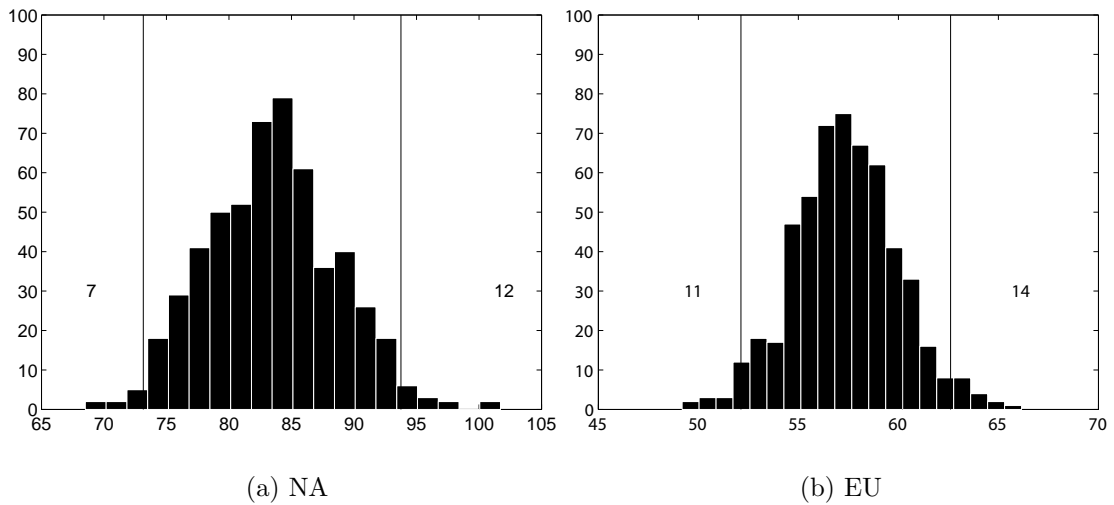


Figure 7.1: Frequency distribution of continental mean February SWE (mm) from all 545 years of control run for North America (left) and Eurasia (right). Vertical lines are shown at  $\pm 2\sigma$  away from the mean, with the number of years with SWE outside this range indicated.

Table 7.1: Extreme events coincident with ENSO or NAO

Continent	Extreme	Total	ENSO			NAO		
			Pos	Neutral	Neg	Pos	Neutral	Neg
NA	High SWE	12	4	3	5	2	8	2
	Low SWE	7	3	2	2	2	5	0
EU	High SWE	14	6	5	3	3	10	1
	Low SWE	11	0	3	8	1	9	1

standard deviation and skewness (2.6mm and 0.08 respectively). As shown in table 7.1, 11 years make up the low snow ensemble, with 14 years in the high snow ensemble. Of the 11 low years, none are during positive ENSO events, 3 neutral and 8 negative. This means an extremely low snow year is much more likely to be during an ENSO-negative event than not, and the proportion of extreme events that are during negative ENSO years is much higher than for the control run as a whole. The spread over ENSO positive and negative events is more even for high years, with 6 during positive events, 5 neutral and 3 negative. Hardly any of the extreme years occur during positive or negative NAO events.

First we examine the SWE distribution in extreme years. Figure 7.2 shows the spatial distribution of February SWE for the ensembles of extremes for the two continents. In high snow years, significant anomalies are seen in North America in Alaska, central Canada, the Canadian East Coast and the American Rockies. In low

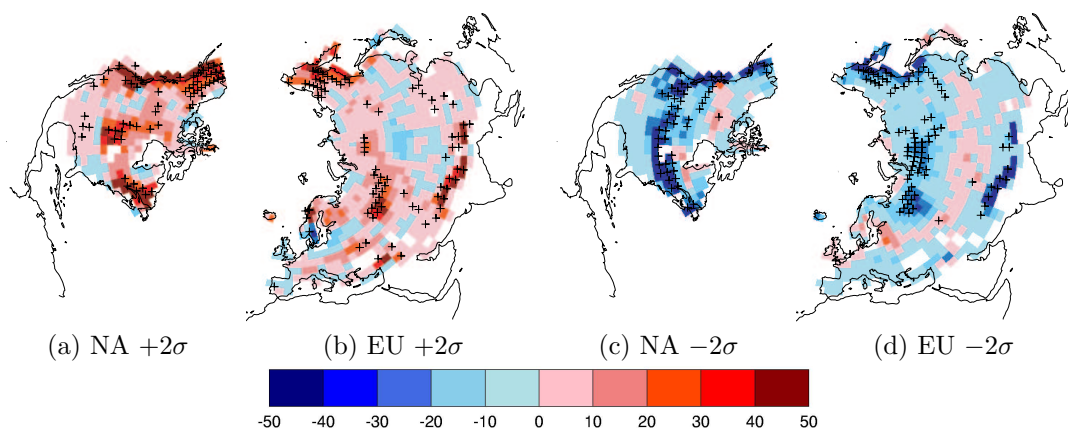


Figure 7.2: Mean February SWE (mm) from highest and lowest SWE years expressed as the difference between these and the mean (crosses showing pixels with differences significant at 99%).

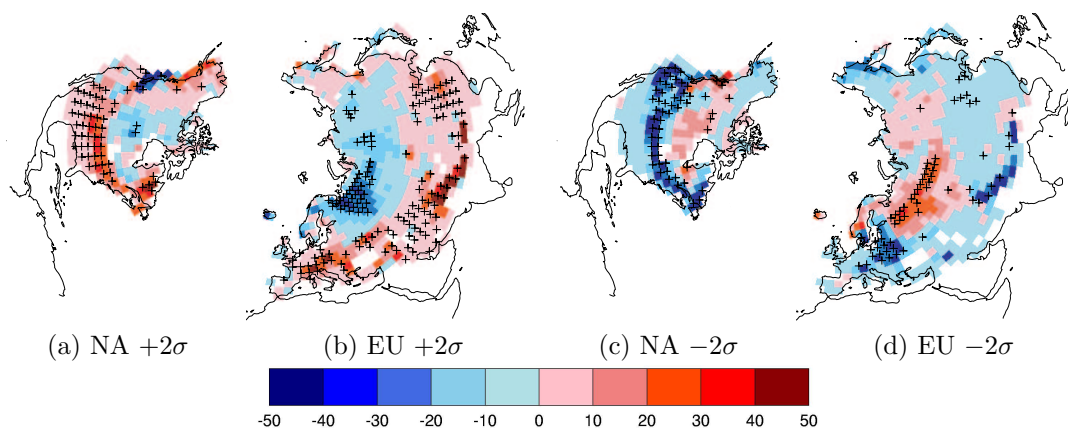


Figure 7.3: Mean February SWE (mm) from the winters coincident with the highest and lowest SCA years expressed as the difference between these and the mean (crosses showing pixels with differences significant at 99%).

SWE years, significance in North America is found more zonally, with a wide band of negative anomalies across the US. This suggests that extremely low snow years in North America come about from a reduction in snow along the southern snow line, whereas extremely high snow years have extra snow in mountainous and maritime areas. Over Eurasia, high snow years bring significant anomalies to the Himalayas, far eastern Siberia and the Urals. The pattern is reversed in low snow years, so both extremes in continental mean SWE over Eurasia are driven by the amount of snowfall in mountainous and maritime areas.

Figure 7.3 shows SWE anomalies in extreme SCA years. As would be expected, large areas of significant anomalies are found along the fringes of the SWE distribution where the anomalous SCA is found, but significant anomalies of the opposite sign are

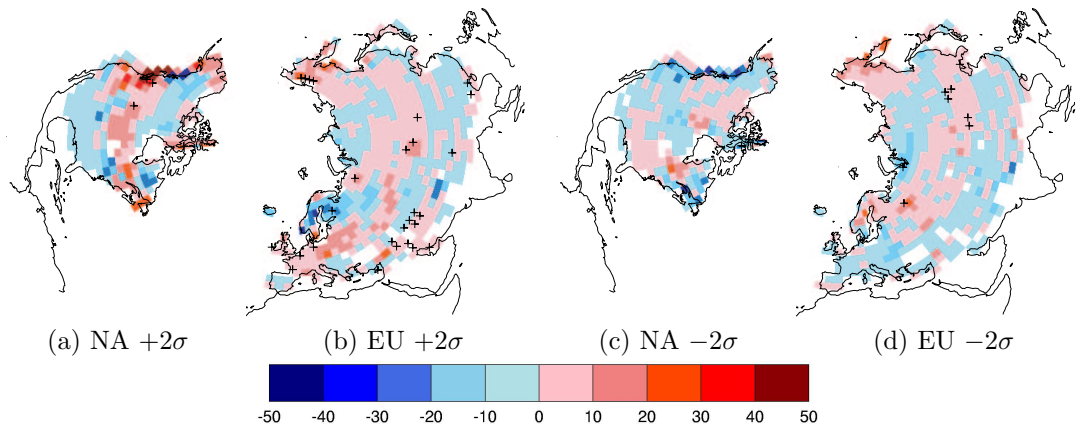


Figure 7.4: Mean February SWE distribution (mm) from the ensemble of years preceding the highest and lowest SWE years. Expressed as the difference between these and the mean (crosses showing pixels with differences significant at 99%).

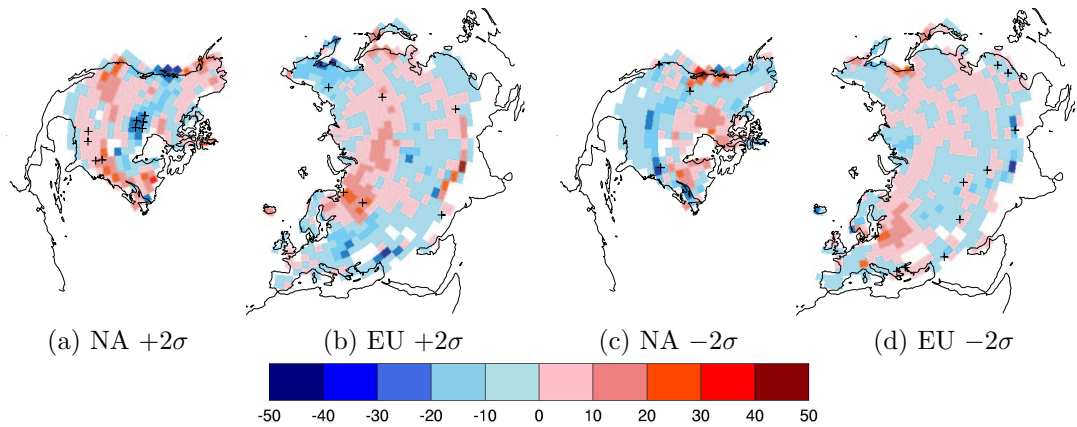


Figure 7.5: Mean February SWE distribution (mm) from the ensemble of years following the highest and lowest SWE years. Expressed as the difference between these and the mean (crosses showing pixels with differences significant at 99%).

also seen in a large area of western Russia. So, low extent years are associated with higher SWE in western Russia, and vice versa. This could be indicative of an NAO-type pattern, where storm tracks shift, bringing more snow to southern areas and less to the north, and vice versa.

Now we examine seasons either side of the extremes. Figures 7.4 and 7.5 show the ensemble of years preceding and following the highest and lowest SWE years respectively. Little significance of the distribution of SWE anomalies is seen in the Februaries following high or low SWE or SCA years (latter not shown). Some scattered gridboxes are statistically significant, but 1 in 100 are expected to appear by chance as part of the statistical test.

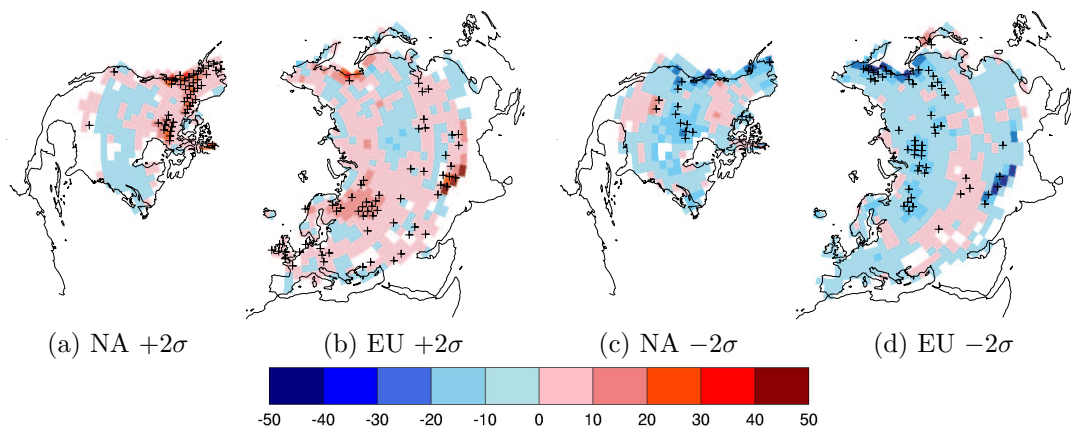


Figure 7.6: Mean SWE (mm) from the autumn/winter months preceding the highest and lowest SWE years expressed as the difference between these and the mean (crosses showing pixels with differences significant at 99%).

From left to right, October SWE in NA, November SWE in EU, December SWE in NA and EU.

As the preceding year's snowpack has no influence on an extreme year's distribution, we now examine the SWE distribution in the months leading up to the extreme February (figure 7.6). For extremely high years in North America, widespread significance is first seen in October, with more than average SWE found in Alaska and west of Hudson Bay. In Eurasia, it is not until November that widespread significance begins to appear, with more SWE in the Urals and Himalayas. For both continents, these areas remain significant through to February.

Examining now the extremely low years (figures 7.6c and 7.6d), it is not until December that significance is seen on either continent. In North America, some low SWE values are significant in the centre of the continent, though not nearly as extensive as the significant low values in the February distribution (figure 7.2c). In Eurasia, significance is seen in December at high latitudes in Russia, with some significance in the Himalayas, all areas that have reduced SWE in February (figure 7.2d).

### 7.3.2 ENSO

Figures 7.7 and 7.8 show the effect of ENSO episodes on the frequency distribution of February SWE during the control run. The frequency distribution of continental mean February SWE values are shaded according to the ENSO index in different seasons leading up to February. For instance, shown in red in figure 7.7a are the February values that occurred when the preceding year's MAM ENSO index was positive. The mean, standard deviation and skewness for each of the distributions are listed in table 7.2.

For North America, February SWE anomalies show a much more positive skew than the rest of the control run when composited by warm ENSO phase in DJF, SON or JJA. February anomalies in cold ENSO phases also show a more positive skew when composited by MAM and JJA ENSO phase, though the skew is reduced when ENSO is negative in the coincident DJF. The February anomalies that occur when ENSO is positive in DJF have the lowest mean, a high standard deviation and the most positive skew, while those that occur when ENSO is negative in DJF have the highest mean, lowest standard deviation and most negative skew. Hence the generally warmer climate in ENSO positive phases is generally leading to less snow over North America, but the high standard deviation and long positive tail of the distribution (as shown by the positive skew) show that there are not consistently low snow values in every positive ENSO event: there are still many ENSO-positive years with positive snow anomalies. The same pattern is true for ENSO negative years, in that while the climate is cooler and snow anomalies are generally positive, the negative skew means there are still a lot of low snow years amongst them.

For Eurasia, the statistics are mainly the opposite to the North American case: the positive ENSO phase in DJF brings a higher mean SWE and lower standard deviation, and vice versa for the negative phase. The changes in skewness however are similar to North America: the positive phase displays a more positive skew, while the negative phase shows a negative skew. It is interesting to note this difference between the continents: the warmer climate of ENSO positive events leads to deeper snow in Eurasia. It is therefore expected that the changes due to ENSO in Eurasia are to increase precipitation in areas where it must fall as snow, namely those areas at high latitudes or high elevation. It also appears that the response of Eurasian snow to ENSO may be more predictable than for North America, as the skewness is in the same direction as the change in mean values: for example, with both a higher mean and more positive skew in ENSO-positive years, it is likely that a year with positive ENSO index also has a positive SWE anomaly.

ENSO phase is clearly having an effect on the expected continental mean SWE values for both North America and Eurasia. To see which areas are most affected by ENSO phase, the cumulative frequency distribution of SWE at each gridbox is calculated for both positive and negative ENSO phases (using the value in the coincident DJF for simplicity, though the results are very similar whichever season is used). These gridbox distributions are compared using the K-S test. In this study, a significance threshold of 99% is used.

Figure 7.9 shows the K-S plot for SWE anomalies. The gridboxes which have significantly different frequency distributions during opposite ENSO phases are shaded:

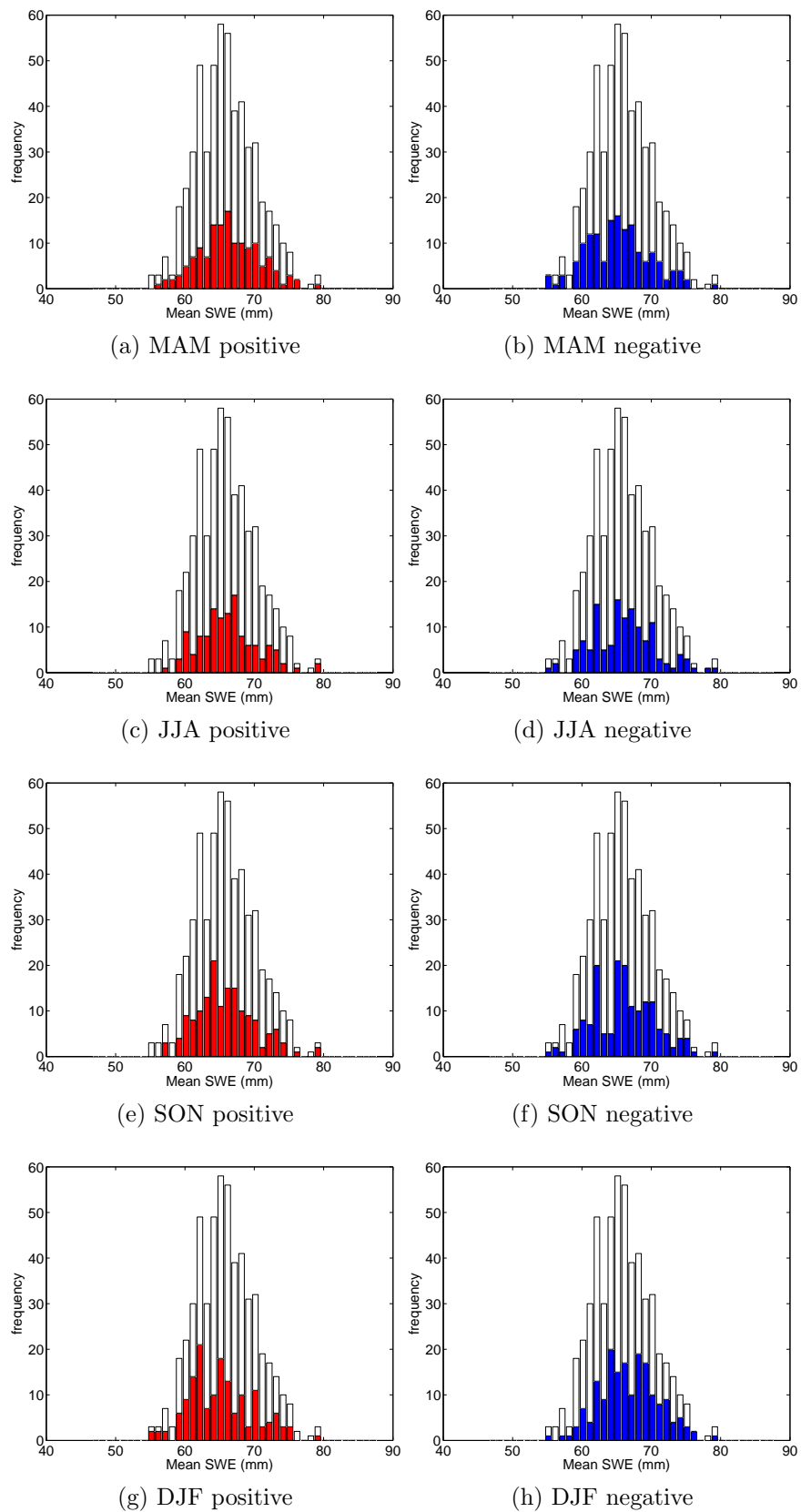


Figure 7.7: Frequency distribution of North American mean February SWE (mm) with ENSO index in preceding MAM, JJA, SON and coincident DJF. Left panel: ENSO positive, right panel: ENSO negative.

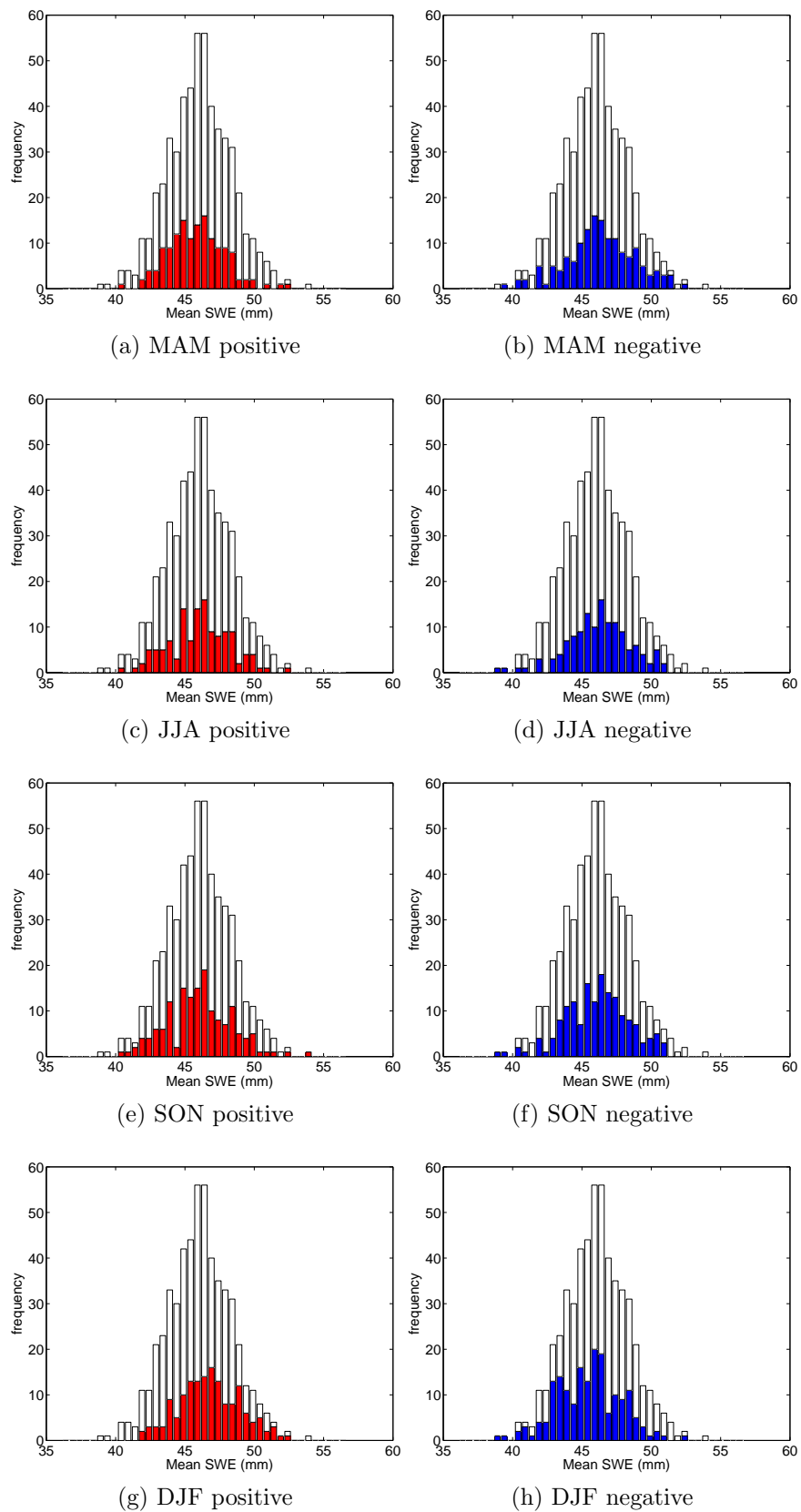


Figure 7.8: Frequency distribution of Eurasian mean February SWE (mm) with ENSO index in preceding MAM, JJA, SON and coincident DJF. Left panel: ENSO positive, right panel: ENSO negative.

Table 7.2: Statistics of February SWE distribution with ENSO index in preceding MAM, JJA, SON and coincident DJF.

		No of years	mean (mm)	std (mm)	skewness	
NA	whole run	545	83.4	5.15	0.16	
	MAM	<i>pos</i>	<i>143</i>	<i>84.0</i>	<i>5.03</i>	<i>0.02</i>
		<i>neg</i>	152	82.8	5.52	0.27
	JJA	<i>pos</i>	<i>128</i>	<i>83.9</i>	<i>4.94</i>	<i>0.50</i>
		<i>neg</i>	132	83.3	5.54	0.32
	SON	<i>pos</i>	<i>155</i>	<i>83.5</i>	<i>4.97</i>	<i>0.41</i>
		<i>neg</i>	164	83.5	5.37	0.10
	DJF	<i>pos</i>	<i>154</i>	<i>81.9</i>	<i>5.45</i>	<i>0.54</i>
		<i>neg</i>	179	84.9	4.90	-0.07
EU	whole run	545	57.7	2.62	0.08	
	MAM	<i>pos</i>	<i>143</i>	<i>57.1</i>	<i>2.36</i>	<i>0.34</i>
		<i>neg</i>	152	57.7	2.84	-0.13
	JJA	<i>pos</i>	<i>128</i>	<i>57.3</i>	<i>2.51</i>	<i>0.18</i>
		<i>neg</i>	132	57.7	2.58	-0.29
	SON	<i>pos</i>	<i>155</i>	<i>57.1</i>	<i>2.70</i>	<i>0.30</i>
		<i>neg</i>	164	57.6	2.61	-0.28
	DJF	<i>pos</i>	<i>154</i>	<i>58.2</i>	<i>2.39</i>	<i>0.16</i>
		<i>neg</i>	179	56.7	2.75	0.06

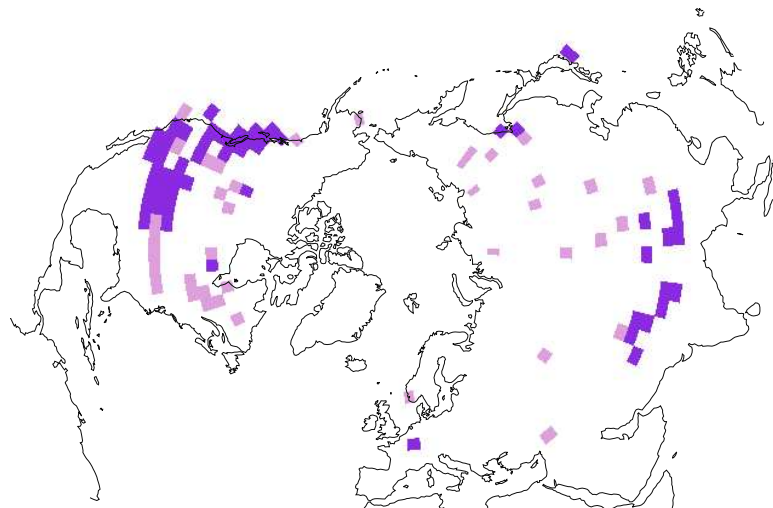


Figure 7.9: Gridboxes with significantly different frequency distribution of SWE during positive and negative ENSO phases are shaded (light: threshold = 95%, dark: threshold = 99%). Significance assessed using the Kolmogorov-Smirnov test.

dark shading represents a threshold of 99%, while lighter shading represents a threshold of 90%. In North America, significant differences are found along the west coast and the southern US. In Eurasia, differences are seen across the Himalayas, China and Japan. These are areas of low latitude but high elevation, which are could see increased snow even in a warmer global climate, if this is driving anomalously large precipitation. An area of gridboxes significant at 95% is also seen in northeastern Canada. Single significant gridboxes are found in other locations such as Europe; again, these are likely to be the 1/100 (or 5/100) gridboxes that pass the test by chance. The shaded areas correspond to regions that are highlighted in figure 2.1 as influenced by ENSO but also have large amounts of seasonal snow.

Figure 7.10 shows the February SWE anomaly composites according to the ENSO index of a particular season (preceding MAM, JJA, SON and coincident DJF respectively). Examining first the SWE anomalies when the coincident DJF is positive (figure 7.10d), large positive anomalies are seen over the Himalayas which are significantly different from those years when ENSO is not positive in DJF. In North America a dipole pattern is seen, with large negative anomalies along the west coast and positive anomalies in the southern central US, both of which show widespread statistical significance. This pattern is reproduced when considering DJF anomalies following positive ENSO phase in SON and JJA (figures 7.10c and 7.10b respectively), but not for positive ENSO phase in MAM (figure 7.10a).

Figure 7.11 shows the anomaly composites for February SWE following negative ENSO phases. The spatial pattern is very similar to that for the positive ENSO phase shown in figure 7.10, except with the sign of the anomalies reversed. Large negative anomalies over the Himalayas are significant, though there are also significant negative anomalies further east in China. Significance is also found in North America, with a similar dipole pattern of opposite-signed anomalies on the west coast and central US. Again the same pattern is seen whether considering ENSO phase in the coincident DJF or preceding JJA and SON (figures 7.11b to 7.11d). In this case, the pattern and significance in Eurasia is seen even when considering ENSO phase in the MAM leading up to the February anomalies, though there is little significance in North America (figure 7.11a). There are also significant negative anomalies in Europe in figures 7.11c and 7.11a.

These results suggest that if a developing ENSO event can be detected or predicted in JJA or SON, the characteristics of the snowpack the following February can also be forecast.

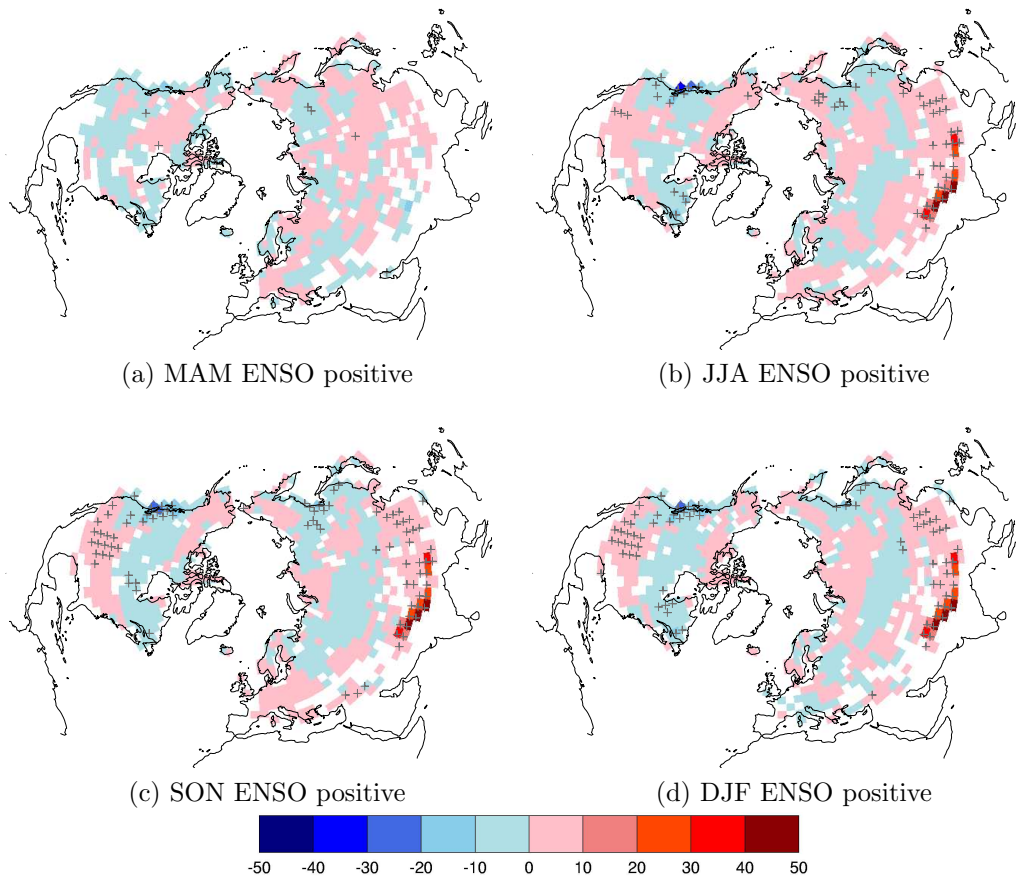


Figure 7.10: February SWE anomaly distribution (mm) from years with positive ENSO index in the previous MAM, JJA, SON and coincident DJF respectively. Crosses show pixels with significant differences from non-positive Februaries at 99%.

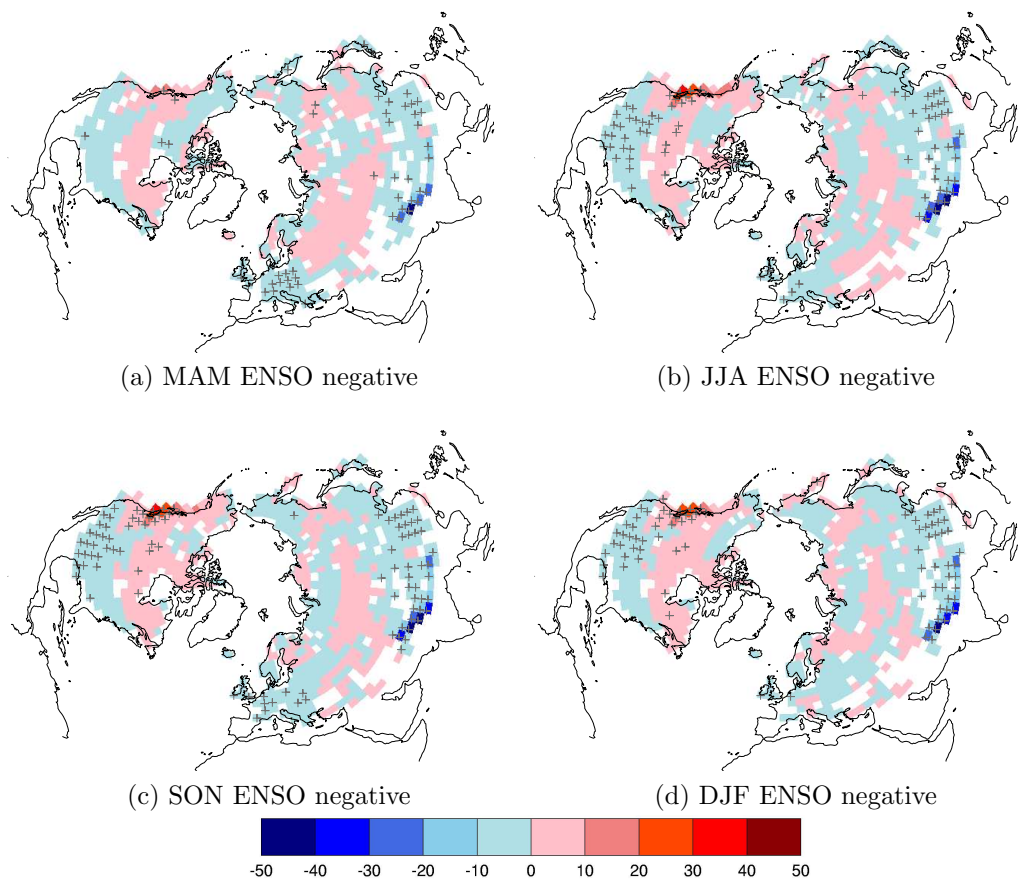


Figure 7.11: February SWE anomaly distribution (mm) from years with negative ENSO index in the previous MAM, JJA, SON and coincident DJF respectively. Crosses show pixels with significant differences from the mean at 99%.

Table 7.3: Statistics of February SWE distribution with NAO index in preceding MAM, JJA, SON and coincident DJF.

		No of years	mean (mm)	std (mm)	skewness	
NA	whole run	545	83.4	5.15	0.16	
	MAM	<i>pos</i>	90	82.7	5.31	0.19
		<i>neg</i>	96	83.6	4.32	0.22
	JJA	<i>pos</i>	83	83.0	5.29	0.38
		<i>neg</i>	89	83.4	4.83	0.19
	SON	<i>pos</i>	90	82.7	4.99	-0.07
		<i>neg</i>	75	83.8	4.98	0.06
	DJF	<i>pos</i>	91	82.8	5.02	0.31
		<i>neg</i>	92	83.8	4.77	0.11
	EU	whole run	545	57.7	2.62	0.08
MAM		<i>pos</i>	90	57.8	2.74	0.29
		<i>neg</i>	96	57.2	2.59	-0.06
JJA		<i>pos</i>	83	57.5	2.79	0.14
		<i>neg</i>	89	57.4	2.47	0.06
SON		<i>pos</i>	90	57.2	2.64	0.18
		<i>neg</i>	75	56.9	2.18	-0.06
DJF		<i>pos</i>	91	57.6	2.66	0.17
		<i>neg</i>	92	56.9	2.33	0.05

### 7.3.3 NAO

Figures 7.12 and 7.13 show the effect of the NAO index on the frequency distribution of February SWE during the control run. The frequency distribution of continental mean February SWE values are shaded according to the NAO index in different seasons leading up to February. The mean, standard deviation and skewness for each of the distributions are listed in table 7.3.

For North America, the mean SWE is reduced in Februaries composited by positive NAO index, and increased in composites with negative NAO index. The standard deviation is also reduced in negative cases. No consistent pattern is seen with respect to skewness. Over Eurasia, the continental mean SWE is very similar in each case, showing that, as expected, the total amount of snow does not change with NAO index, simply the tracks of the storms. The standard deviation is raised for positive cases, and lowered for negative ones. There is also more positive skew in positive cases, and very little skew in negative cases.

Figure 7.14 shows the result of the K-S test for the NAO, with the same shading as in figure 7.9. SWE anomalies with significantly different frequency distributions with opposite NAO index are shaded. Significant gridboxes are more widespread in this case

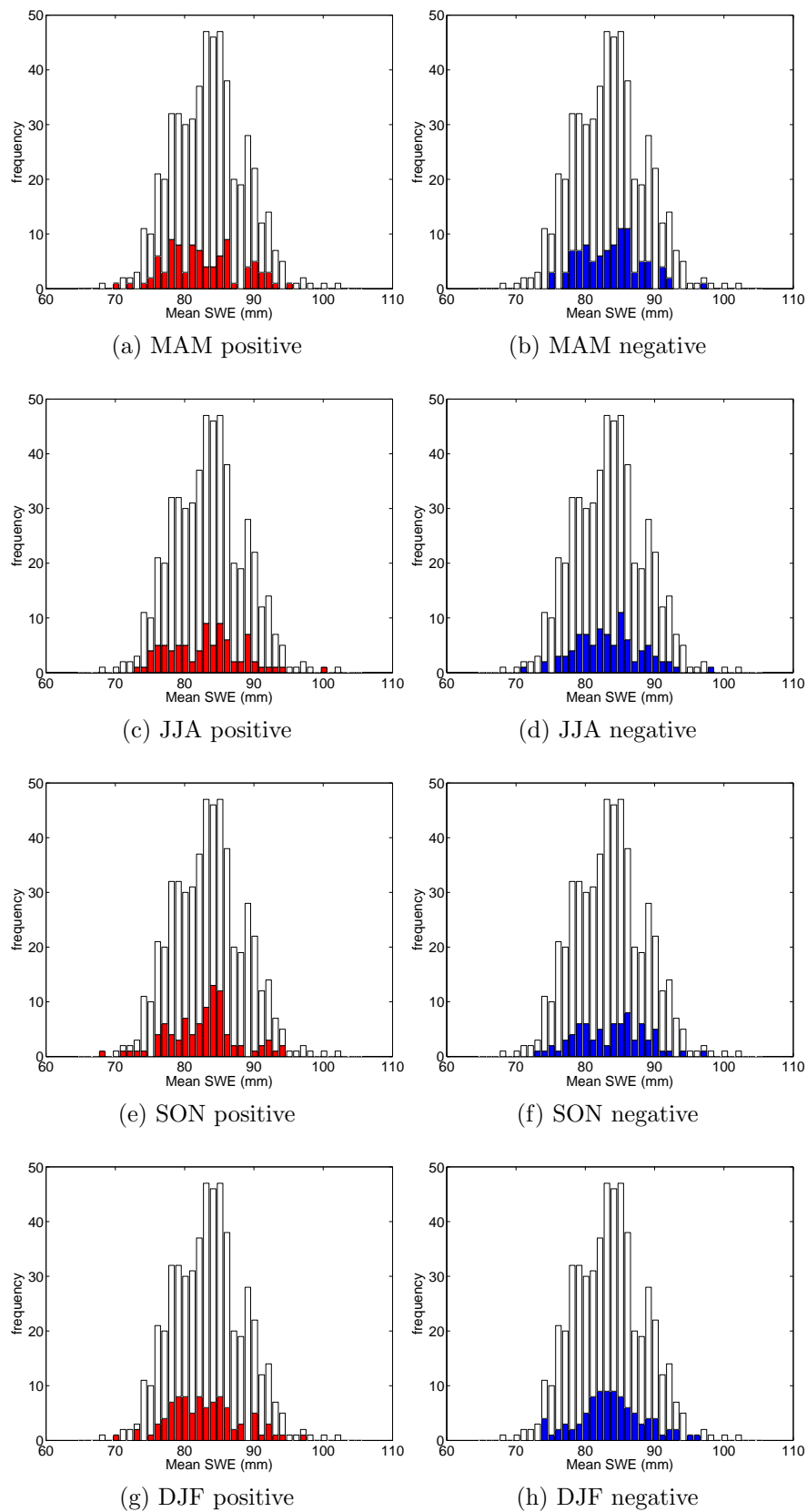


Figure 7.12: Frequency distribution of North American mean February SWE (mm) with NAO index in preceding MAM, JJA, SON and coincident DJF. Left panel: NAO positive, right panel: NAO negative.

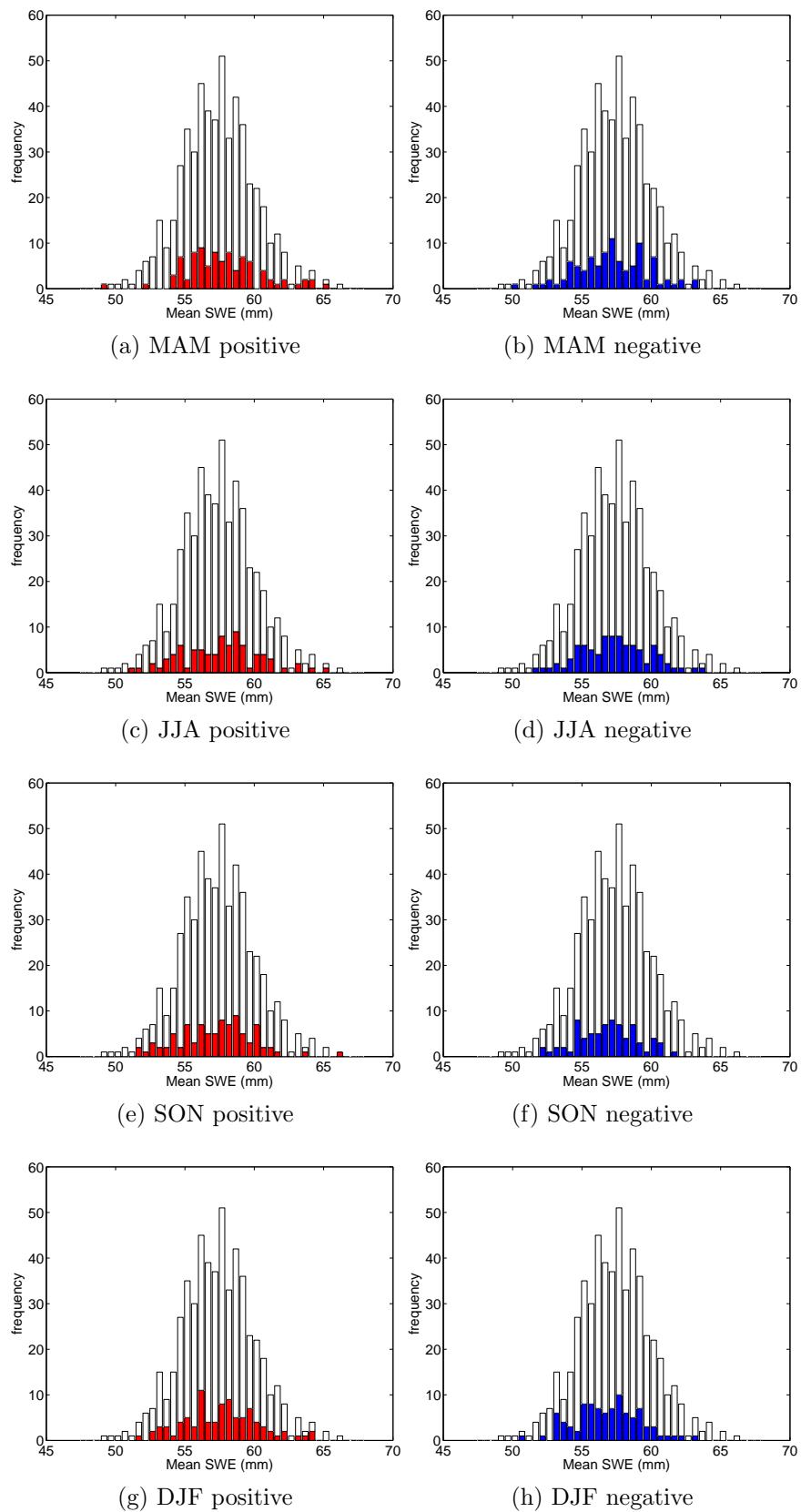


Figure 7.13: Frequency distribution of Eurasian mean February SWE (mm) with NAO index in preceding MAM, JJA, SON and coincident DJF. Left panel: NAO positive, right panel: NAO negative.

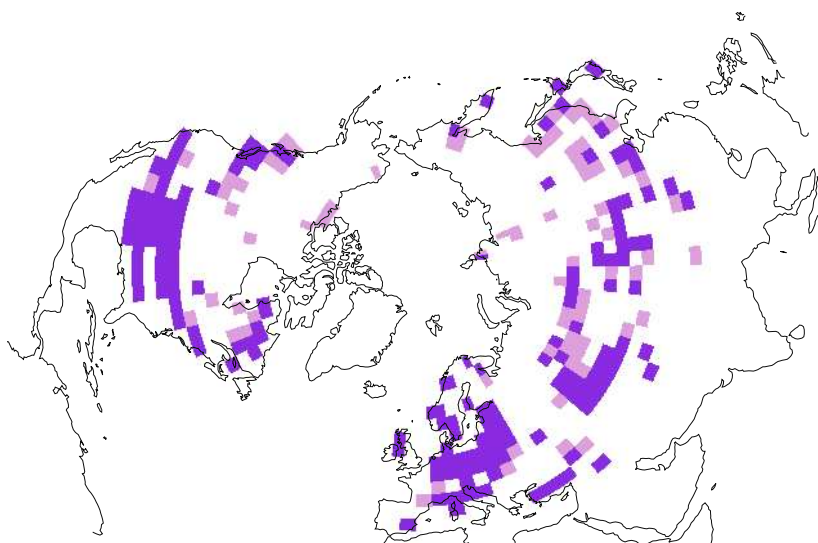


Figure 7.14: Gridboxes with significantly different frequency distribution of SWE during positive and negative NAO phases are shaded (light: threshold = 95%, dark: threshold = 99%). Significance assessed using the Kolmogorov-Smirnov test.

compared to ENSO (figure 7.9), which is to be expected given that the main influence of ENSO is the Tropics, whereas the NAO directly impacts higher latitudes which have more snow. Significance is seen in the United States, the coasts of Canada, most of Europe and midlatitude Asia.

Figure 7.15 shows the composite of February anomalies by NAO phase. When the NAO is positive in DJF (figure 7.15d, European SWE anomalies are negative and significant. Significant positive anomalies are found further east around the Black Sea and much of central Asia. Widespread significant negative anomalies are also seen across the United States, with some large positive anomalies found on the west coast. This pattern of anomalies reflects the expected pattern of the NAO from the illustration in figure 2.2. Some significance at high latitudes in Europe is seen when the NAO is positive in SON (figure 7.15c), along with far eastern Russia/northern China and the east coast of North America. Very little significance is evident in composites based on other seasons.

The picture is almost exactly reversed when the NAO is negative in DJF (figure 7.16d), with widespread positive SWE anomalies in Europe and the United States. Again, significant negative anomalies are seen in central Eurasia. In addition, northeastern Canada shows a cluster of significant positive anomalies. Figure 7.16c shows significant positive anomalies in Scandinavia and Mongolia, with large significant negative anomalies on the west coast of North America. Once more, no significance is seen when considering JJA and MAM NAO index (figures 7.16b and 7.16a respectively).

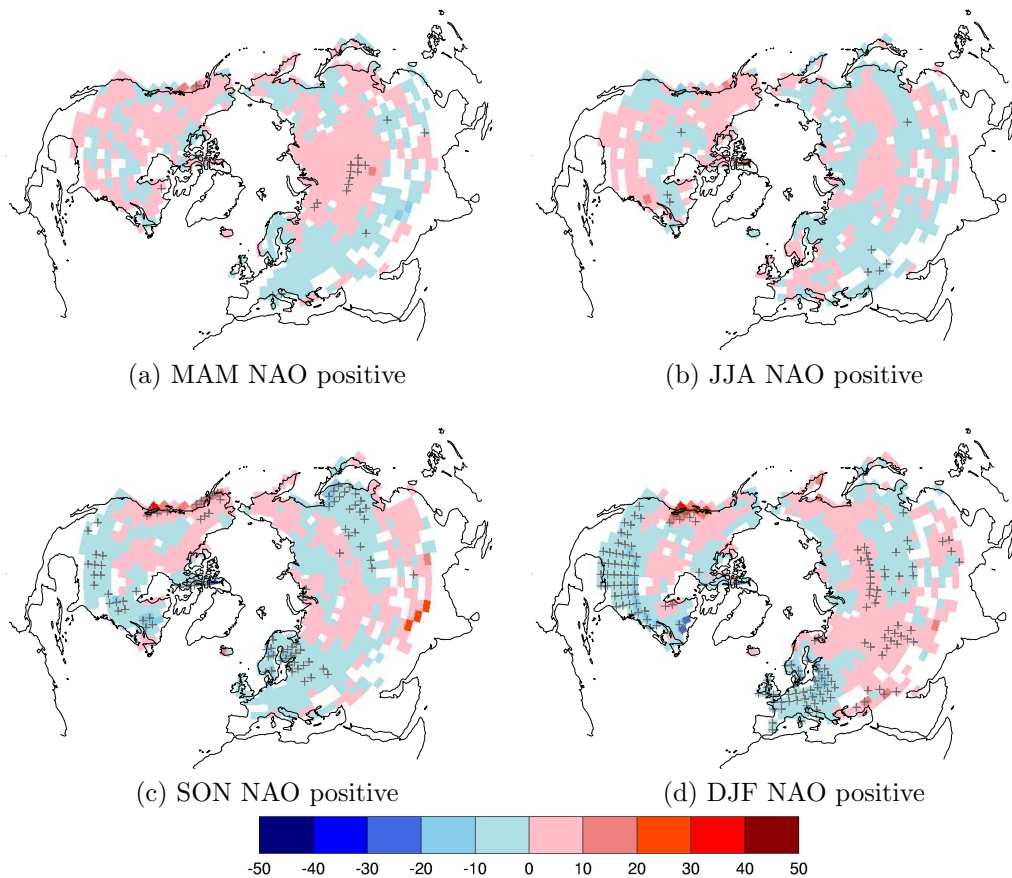


Figure 7.15: February SWE anomalies (mm) from years with positive NAO index in the previous MAM, JJA, SON and coincident DJF respectively. Crosses show pixels with significant differences from the mean at 99%.

The results show that some information on February SWE distribution can be obtained from the NAO index in SON, but more widespread significance is seen when using the coincident DJF NAO index.

## 7.4 Discussion

An investigation of the distribution of SWE anomalies in extreme years and during ENSO and NAO events has been made, in order to see where potential predictability of SWE anomalies may exist. The most extreme years, in terms of highest and lowest continental mean SWE, have a similar pattern (with opposite sign) over Eurasia in both cases, with the largest anomalies occurring in the Urals, central Siberia, the Himalayas and northeastern Siberia. In North America, however, the opposite extremes look quite different. Extremely high snow years have more snow along the coasts and in the central states, while extremely low snow years have a zonal pattern of less snow

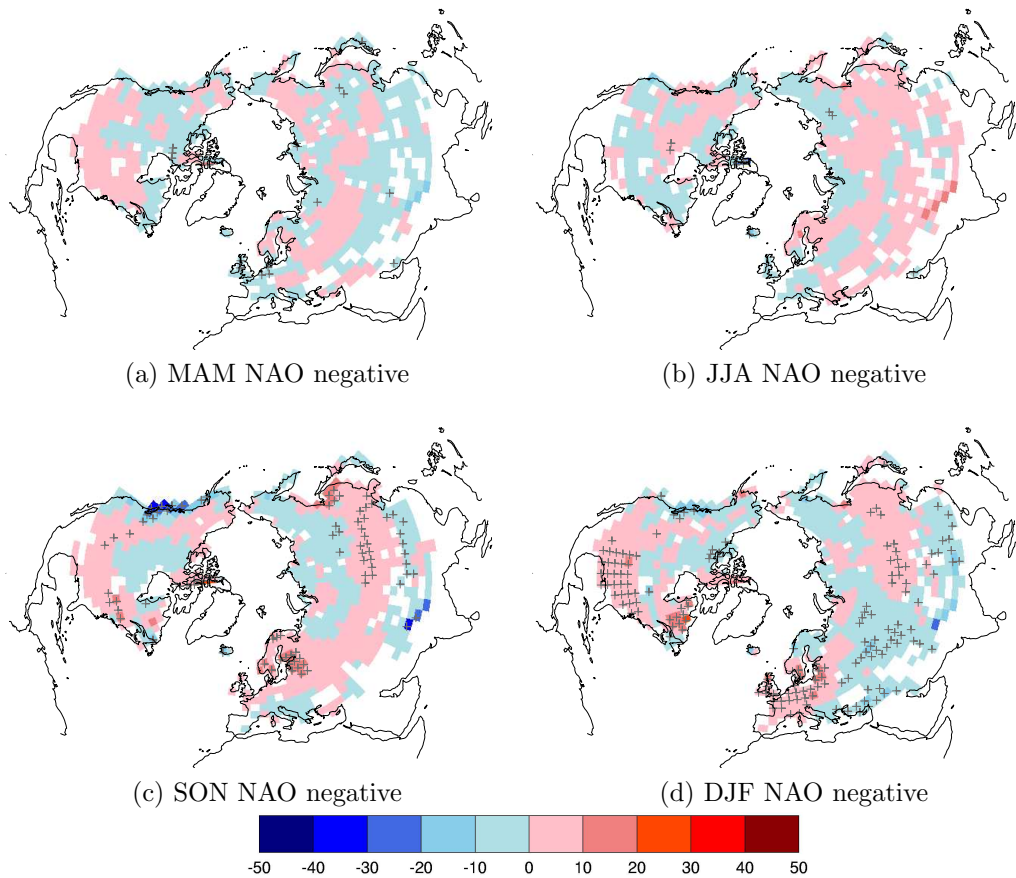


Figure 7.16: February SWE anomalies (mm) from years with negative NAO index in the previous MAM, JJA, SON and coincident DJF respectively. Crosses show pixels with significant differences from the mean at 99%.

across the United States. The high years also show significance earlier in the season, while for both continents there is little sign, even by December, that the mean SWE for February will be extremely low. No significance was found in years before or after extremes of continental mean SWE, so in HadCM3 at least there is no preconditioning of extreme SWE by the previous year's snowfall, and no memory of an extreme year in the following year's snowfall. La Niña events are more common amongst high snow years in North America and low snow years in Eurasia than for the run as a whole, although the spatial SWE distribution in either case does not look the same as the average La Niña pattern for the run. This suggests that other factors are involved in driving the extremes of continental SWE. As was shown by Sobolowski et al. (2007) the forcing effects of snow and orography are likely to combine non-linearly and hence are very difficult to predict.

The effect of ENSO on the frequency distribution of SWE in North America is to reduce the mean SWE and skew the distribution slightly towards lower values when ENSO is positive in DJF, and to shift the mean higher and skew the distribution towards higher values when DJF is negative. This is associated with a dipole anomaly structure, with significant anomalies of opposite sign centered in western Canada and the central United States. This dipole structure reduces the effect of ENSO on continental mean values: a further study which analyses these two regions of North America separately may show enhanced predictability. In Eurasia the effect of ENSO on the frequency distribution of SWE is somewhat reversed: while warm episodes still lead to a more positively skewed distribution, the mean value is raised. Again, the opposite effect is seen during cold episodes. In Eurasia the significant anomalies are concentrated in the Himalayas, and it is this area that dominates the effect on continental mean values. The areas showing significance during both positive and negative events correspond to the regions with significantly different SWE distributions found using the K-S test. As expected, it is the high elevation areas of Eurasia that dominate the Eurasian SWE response, while the high elevation region of North America shows an opposite response. At this higher latitude it is the warmer climate of the positive event that dominates (and vice versa for negative events), while the lower latitude region of North America responds similarly to Eurasian regions.

While most of the anomaly patterns were as expected, the clear link between Himalayan snow in HadCM3 and ENSO was more surprising. However, a recent study by Mariotti (2007) of a combination of station data and reanalysis products finds a similar relationship between SON precipitation and ENSO in this region, driven by anomalous moisture flux from the Arabian Sea and tropical Africa. The relationship is important if using HadCM3 to investigate, for instance, the Blanford

hypothesis, although ENSO-monsoon links in HadCM3 are somewhat weaker than in reality (Turner et al., 2005).

The link with February SWE distribution is seen to exist from the previous JJA ENSO index onwards. This suggests that if there is a positive or negative ENSO event occurring in JJA, characteristics of the February SWE distribution in certain regions can be forecast. This represents a long lead time for hydrological applications such as flood and wildfire forecasting. It also makes sense in terms of an ENSO event lasting several seasons, and impacting on precipitation during the Northern hemisphere snow accumulation period. This seasonal dependence within predictability studies has been noted before, with lowest predictability occurring in spring (MAM) e.g. Latif et al. (1998). This ‘spring predictability barrier’ is not well understood, and it has been suggested that it is an artifact of models.

The results of NAO composites also show significant impacts on SWE distribution, particularly in Europe and eastern North America. Significant areas also occur along the west coast of North America and eastern Russia, which could be a consequence of the exaggerated teleconnection between the NAO and the Pacific in HadCM3, as documented in Collins et al. (2001). The NAO does not show potential for seasonal forecasting beyond the coincident DJF, and some limited areas using SON; this is not surprising, as the NAO index is more a measure of current storm activity. While this is important for SWE accumulation, the NAO index is not so much a driver of longer term variability as a measure of that variability itself. To exploit this behaviour, the mechanism that drives the NAO index (perhaps longer term ocean variability) needs to be understood. Recently, the utility of the NAO index was put into doubt by Ambaum (2008), who showed that the seemingly bimodal distribution into positive and negative states in the last 30 years could be explained by sampling variability alone, and that the underlying behaviour is in fact Gaussian. Clearly, more investigation is required into mechanisms that drive mid- to high latitude variability if we are to produce reliable snow forecasts.

The study presented here shows that ENSO has the most promise as a predictor of February SWE. Applying the results to real world predictions requires confidence in both the model’s representation of climate dynamics and its snow component, and the latter has been shown earlier in this thesis to be crude. While a GCM will always be an incomplete representation of reality, it is an appropriate tool for this kind of study as long time series with prescribed forcing can be produced, allowing more statistical confidence in the output and an examination of purely the internal variability. The results in this section do mirror other similar studies that have been performed using other models and observational datasets, which lends confidence to these conclusions.

# Chapter 8

## Conclusions

### 8.1 Summary of results

The GCEP project aims to test a method of producing seasonal predictions of climate. Results for the land surface, and in particular snow, are an important aspect of this research, as they will help to inform many aspects of economic and social policy. A number of aims were set out at the start of this thesis, and a summary of these and the results are presented below.

- I. *To investigate the variability of Northern hemisphere snow data as observed by satellites.*

The SSM/I dataset used in this thesis is the only long-term, global observation-based SWE product available. The retrieval used to derive SWE was developed in 1987 by Chang et al., and this simple empirical difference equation has changed little in twenty years. Despite many newer approaches being proposed, this type of static retrieval is often found to be the most consistently reliable choice at large scales (Koenig and Forster, 2004; Armstrong and Brodzik, 2002; Foster et al., 1997). An EOF analysis of the data from 1987-2005 revealed a coherent annual cycle. The most prominent interannual anomaly pattern is active over central Eurasia, and accounts for 1.3% of the variance of the entire dataset, and 13% with the seasonal cycle removed. This interannual pattern is most active in the boreal forest region (figure 3.9).

- II. *To investigate the variability of Northern hemisphere snow data as modelled by a GCM.*

The GCM used in GCEP is HadCM3, developed by the UK Met Office in the 1990s. This makes it a relatively old model, but it does a good job of simulating the Earth's climate compared to other coupled climate models (see, for instance

the CMIP3 study by Covey et al. (2003)). Many aspects of HadCM3 have been well-studied, in particular the tropical oceans, but the representation of the land surface, and snow in particular, is crude. As GCMs become more sophisticated and represent more physical processes, further investigation of this crucial aspect of the climate system is required to build on the success of HadCM3 in the future.

The climatology of a long control run of HadCM3 shows deep SWE along the Pacific coasts of North America and Eurasia, and also in the western half Eurasia and northeastern Canada (figure 4.5). Little snow is seen in Siberia. The SWE distribution is little changed in a transient run with increasing greenhouse gases when compared to a pre-industrial control (figure 4.6). A run with flux adjustments generally reduces SWE across the hemisphere, with increases confined to the higher latitudes (figure 4.9).

The ERA40 reanalysis product is used to provide the atmospheric data for the GCEP project to constrain and validate HadCM3. It is a synthesis between meteorological observations and a GCM, and its snow fields are constrained by the assimilation of (albeit sparse) in situ snow data. The SWE climatology for 1958-2001 (figure 4.14) shows maximum SWE in March in central Siberia and northeastern Canada.

III. *To understand the differences between the observed and modelled snow data.*

Having generated climatologies of SWE from HadCM3, SSM/I and ERA40, it is clear that these datasets are very different, particularly over Siberia. It is difficult to validate the data in this region, as there are few in situ observations to constrain SWE, and precipitation estimates are particularly inaccurate at high latitudes, due to the problem of gauge undercatch (Guntner et al., 2007). Boreal forests are a challenging environment for both the satellite retrievals and the GCM, not least because the behaviour of snow in the boreal forests is not well understood. Using summer runoff as an integrated measurement of winter snow amount, the Lena shows a large snowmelt peak in June not replicated in the HadCM3-derived hydrograph. Having compared a range of other models and retrieval techniques, the SSM/I product is more likely to be an overestimate in this region (due to assumptions inherent in the retrieval algorithm), while HadCM3 is more likely to be an underestimate. The ERA40 climatology lies somewhere in between, and is constrained by available observations, so this could well be a more reliable SWE distribution.

---

IV. *To assess the ability of a GCM to reproduce observed snow anomalies.*

Having established the differences between the climatologies, for this chapter ERA40 is taken as ‘truth’. The model’s ability to reproduce the distribution of ERA40 SWE anomalies is tested via an anomaly assimilation scheme, as used in the Met Office’s DePreSys project (Smith et al., 2007). The SWE anomaly distribution is well reproduced in assimilation mode, but when hindcasts are released from this run and allowed to evolve freely, the pattern diverges from both ERA40 and assimilation run. The memory of the initial conditions (the point of release from the assimilation run) is lost at the start of the following snow season. Unfortunately, a statistically robust analysis of the biases in the hindcasts was limited by the small ensemble size, which was necessary due to the errors in the ERA40 reanalysis for 1989-1994. As an alternative, two case studies were examined in detail.

A case study of a large negative NAO event in 1995-6 shows that SWE anomalies are well reproduced in Europe when the sign of the NAO is the same in the hindcast and the observations, but predictions of the index are not reliable in the cases examined here. An examination of the 1997-8 ENSO event showed better reproduction of SWE anomalies over North America, despite the hemispheric spatial correlations being lower than for the NAO case study (the larger Eurasian land mass dominates the hemispheric calculation).

V. *To assess the predictability of snow anomalies.*

The results from the assimilation and hindcast experiments suggest that the SWE anomaly distribution is governed more by the boundary conditions of the assimilated fields (temperature, pressure, winds and ocean salinity) than the initial state at the point of release. In the final results chapter, the model is allowed to evolve according to its own internal variability over a multi-century run, and the SWE distribution examined. Years of extremely high or low SWE and snow-covered area were shown to have no memory from one season to the next, and were not preconditioned by the previous year’s snow distribution. ENSO and NAO events had a much more obvious impact on the SWE distribution, with ENSO driving significant anomalies in the Himalayas and North America, and the NAO impacting North America and Europe.

While significant connections with NAO index were only present in DJF (and to an extent SON), the link with February SWE distribution was seen to exist from the previous JJA ENSO index onwards. This suggests a lead time of 6-8 months on SWE anomaly distribution during ENSO events.

Chapter 1 of this thesis set out three hypotheses to be tested:

1. Information on the distribution of SWE in the Northern hemisphere can be reliably obtained from remote sensing and GCMs
2. Snow distribution in coupled models will be better forecast from an initial state that is constrained by observations of fields such as surface temperature.
3. Seasonal forecasts of SWE anomalies can be made with knowledge of large scale patterns of climate variability such as the El Niño-Southern Oscillation

Hypothesis 1 is rejected. Hypothesis 2 is supported only for a few months, as at longer lead times the hindcasts released from the assimilation run show similar characteristics to those released from the No assimilation ensemble mean. Hypothesis 3 has been accepted within HadCM3, as SWE anomalies show predictability with ENSO at lead times of over 6 months. However, this hypothesis has yet to be tested with observational data.

## 8.2 Discussion

The first notable result in this work is the large disagreement in the SWE distribution between the available datasets: it appears that we do not know how the snow is distributed across the Northern hemisphere. In many respects this is unsurprising; the very presence of snow can make a location inhospitable and inaccessible, and ground truth data difficult to retrieve. What is more surprising is the lack of remarks on this in the literature. Yang et al. (1999) make a comparison of GCM SWE distribution and SMMR-derived SWE, and conclude that “the available datasets and models are not yet ready to fulfil this objective [a rigorous evaluation of snow simulations in coupled land-atmosphere models]”. Most studies of remotely sensed SWE (Derksen and LeDrew, 2000; Derksen et al., 2005; Langlois et al., 2004; Mognard and Josberger, 2002; Parde et al., 2007; Pulliainen and Hallikainen, 2001) have understandably concentrated on studying limited areas with good ground-based data, often the Great Plains in North America. However, comparing the large scale distributions highlights the gulf between the datasets.

Neither dataset can be established *a priori* as the truth. HadCM3 is a large, complex model which, while physically-based and extensively studied, will always be an incomplete approximation to a complex system. On the other hand, the SSM/I radiometer measures brightness temperatures, not SWE, and a model is required to

retrieve one from the other. Examining both together should enable more conclusions to be drawn about each individually.

If the SWE distribution within HadCM3 is correct, then the assumptions used in deriving the SWE retrieval algorithm are critically flawed, and the algorithm should not be applied globally. If the SWE distribution from SSM/I is more correct, then the model is not snowing enough over Siberia, suggesting that there are large circulation biases occurring in this region. The work of Gong and Entekhabi (2003) and Cohen et al. (2007) highlight snow in Siberia as having an important role in the circulation patterns of the Northern hemisphere, so errors in the region are likely to have important consequences downstream. Additionally, if the modelled snow and hence modelled runoff is wrong, then this will be affecting the amount and distribution of sea ice, which has an important role in climate feedbacks. There appears to be agreement across GCMs about the Siberia ‘hole’ in SWE (see figure 5.17), so if this SWE distribution does diagnose a circulation problem, it is widespread. Additionally, this is also an area where GCMs predict large changes in precipitation amounts with climate change (figure 5.18), so an understanding of the basic state in the models is critical for the interpretation of these future changes.

An important caveat that emerges from this line of thought is that the results one obtains when investigating SWE distribution and its links to the rest of the climate system could depend heavily on the source of the SWE data. Taking the Blanford hypothesis as an example, as discussed in chapter 2, recent studies have produced contradictory results as to the sign of the snow anomaly correlation with the monsoon, the region of Eurasian snow that has the most influence, and whether it is depth or extent anomalies that are most influential (Bamzai and Shukla, 1999; Kripalani and Kulkarni, 1999; Robock et al., 2003). Could these contradictions be a consequence purely of the contradictions between the different sources of snow data?

With these issues in mind, the approach taken in chapter 6 of this thesis is to take ERA40 as ‘truth’, and to test HadCM3’s ability to reproduce the ERA40 SWE anomalies when given other ERA40 anomaly fields as input. Assimilation of temperature, salinity, sea level pressure and winds was shown to be broadly successful in reproducing the correct SWE anomaly distribution. The main drivers of SWE distribution are temperature and precipitation, so since the temperature fields are assimilated, the remaining biases must come from differences in precipitation. The CMIP3 study showed that GCMs have been shown generally to have difficulty in reproducing accurate precipitation fields (Covey et al., 2003).

The results of the hindcast runs showed that, for HadCM3 at least, boundary conditions are more important for reproducing snow anomalies than correct initial

states of the assimilated fields in the schemes tested. Biases in this case come from both those fields that had biases during the assimilation period (such as precipitation) and those that diverge quickly from the constrained initial state. Land surface temperatures have previously been shown to be predictable only up to a month ahead (Collins and Allen, 2002), although other results from GCEP suggest that after bias correction there may in this case be some skill in air temperature over land at longer lead times (Haines et al., 2008). The NAO case study in particular showed the sensitivity of European snow anomaly distribution to the sign of the NAO index, which was variable across the hindcasts.

Despite reduced skill over land, GCEP results show multi-annual predictions are possible for other fields such as ocean heat content, and relate initial conditions of these storage variables to predictability in other fields such as mean sea level pressure (Hermanson and Sutton, 2008). The results of chapter 7 show that there are links between large scale modes and snow anomalies in HadCM3, and if long term predictions of ENSO could be made, this may be a more useful way of obtaining snow predictions at long lead times.

However, the land surface component of HadCM3 is crude, and improvements are required (such as, perhaps, an explicit snow layer and surface tiling to better partition the flux calculations) for the results from the model to carry greater confidence. Nevertheless, these results are an encouraging step in understanding snow variability. In order to both develop better snow models and apply these model-derived results to the real world, more reliable long-term snow observations are required. Once greater confidence is reached in the global snow observations, assimilation of these observed SWE fields into models would be an important next step in understanding the feedbacks between the land surface and climate in interannual predictions.

Remote sensing is the only way to achieve large scale snow mass measurements with high temporal and spatial resolution, yet existing satellite-derived SWE estimates are often rejected because of their perceived unreliability. The limitations of the static SWE retrieval method are well-known, so why is it still used, and why is it believed to perform better than the other retrievals that have been developed since? Microwave retrievals at a point are extremely sensitive to the snow grain size parameter, which in reality will vary across a snowpack both vertically and horizontally. Derksen et al. (2005) found that by subsampling a single SSM/I grid cell, the microwave estimate lay in the centre of a highly variable but normally distributed set of in situ measurements. This suggests that the spatial averaging performed over a pixel by the radiometer cancels out the high variability of the grain size (and other varying parameters to which the retrieval is sensitive). This scaling is not well understood, and improved understanding could

provide more insight into how the retrieval works. If the properties of the snowpack and its interaction with radiation were better understood at the scale of a satellite pixel, which may be up to tens of kilometres across, a more physically-based retrieval could be applied to over 30 years of existing satellite measurements and deliver an important dataset for use in many applications.

An alternative approach in using the remotely sensed data would be to assimilate the radiance measurements from the radiometer directly. This is common in variational data assimilation schemes, but in order to understand the radiance measurements we would still have to develop a better understanding of the surface interaction with radiation. Additionally, while radiance assimilation is common in numerical weather prediction, there will always be applications which require a derived product (SWE, snow depth, or snow mass) either for input into a model or for comparison with in situ data.

New satellite missions that are scheduled for launch in the future could also benefit from the SWE information that SSM/I could provide. One such mission is the Global Precipitation Measurement mission (GPM)<sup>1</sup>, due to be launched in 2013. The aim of this mission is to measure precipitation, including solid precipitation at mid- and high-latitudes using high frequency passive microwave channels. Validation of high latitude solid precipitation estimates will be challenging, and while one of the mission's aims is to improve passive microwave retrievals over land, it would surely be a benefit to this mission if reliable high latitude lying snow estimates were already available. Precipitation reconstruction from snow depth measurements combined with a model has already been tested (*e.g.* Cherry et al. (2005)), and while reliable ground measurements of snow depth or SWE are not easy, these quantities are more measurable than snowfall. The accumulation of snow on the ground would provide a simple first order check on the retrievals from GPM, and help to validate estimates of global precipitation that are so lacking at the moment.

### 8.3 Future work

The work in this thesis has tested the hypotheses as set out, but inevitably, these answers lead on to new questions. In particular, the following areas could be addressed:

- I. *Improvements to microwave SWE retrievals*

There are a number of issues with the microwave retrievals that need to be addressed. A better understanding of how retrievals at a point scale up to the

---

<sup>1</sup><http://gpm.gsfc.nasa.gov/index.html>

size of the radiometer footprint is essential for dealing with subpixel variability, for instance with grain size. More investigation of how vegetation interacts with microwaves is also required, along with more appropriate ways of characterising the vegetation than simply the fraction of forested pixel (for instance canopy closure or stem volume). A more physically-based, forward modelling approach would be a start to addressing these issues, and yield results that would be more applicable to regions outside the calibration areas.

## II. *Testing predictability links with real data*

Links between ENSO and snow distribution have been found in models, but these need to be applied to the real world. Clearly, a 545-year observational dataset is unrealistic, so to test these results with real-world data requires a different approach. One method could be to break the control run down into many shorter runs, of a length more similar to observational datasets, and assess the statistical likelihood of detecting the ENSO-SWE or NAO-SWE signals in any one run of this length. Results could then be compared with the observations themselves. The presence of trends in the real world (for instance due to climate change) will also need to be understood in this context in order to apply these results.

## III. *Evaluation of MSLP and precipitation in hindcast runs*

Up till now, the assessment of hindcast performance within GCEP has been mainly in terms of surface temperature, and ocean fields such as sea surface temperature and heat content. Mean sea level pressure is a field that is assimilated as part of the scheme presented here, and an evaluation of the scheme's success in forecasting circulation patterns would provide a useful context for the lack of predictability that was seen for snow. Precipitation is not assimilated, but a similar assessment of the global field would provide further information on areas in which the model is having difficulty.

## IV. *Extension of the method to other storage/memory variables*

The same methods presented here could be applied to other important storage fields such as soil moisture and sea ice. Soil moisture presents additional challenges, as there are even fewer observations available than for SWE. ESA's SMOS (Soil Moisture-Ocean Salinity) mission, and the NASA mission SMAP (Soil Moisture Active Passive) are due to be launched in the coming years, and aim to provide global soil moisture fields for analysis. Sea ice observational datasets are more readily available, though as for snow, extent datasets are more common and cross-validated than depth data.

## 8.4 Concluding remarks

In order to plan for the years and decades ahead, knowledge of the internal variability of the climate system is required. Policy makers need to make decisions now, so it is important to make best use of the tools which are currently available, while appreciating the limitations of each. SSM/I has been providing data for twenty years, and the time series extends back further if the SMMR instrument is included. This represents an important resource in characterising the climate system, and how it has changed in the last decades. Even if the established SWE retrieval is flawed, the brightness temperature data are real, and have been responding to the surface environment. Linking this data source with studies using models such as HadCM3 is vital for understanding how these changes may affect our climate in the future.

# References

- Ambaum, M. (2008). Unimodality of wave amplitude in the Northern hemisphere. In *EGU General Assembly, Vienna*.
- Ambaum, M., Hoskins, B., and Stephenson, D. (2001). Arctic Oscillation or North Atlantic Oscillation? *Journal of Climate*, 14:3495–3507.
- Andreadis, K. and Lettenmaier, D. (2006). Assimilating remotely sensed snow observations into a macroscale hydrology model. *Advances in Water Resources*, 29:872–886.
- Armstrong, R. and Brodzik, M. (2002). Hemispheric-scale comparison and evaluation of passive microwave snow algorithms. *Annals of Glaciology*, 34:38–44.
- Armstrong, R., Brodzik, M., Knowles, K., and Savoie, M. (2005). Global monthly EASE-Grid snow water equivalent climatology. Digital media. Boulder, CO: National Snow and Ice Data Center.
- Armstrong, R., Brodzik, M., Wang, J., Savoie, M., Frauenfeld, O., and Zhang, T. (2004). Solutions to the snow cover mapping anomaly over the Tibetan plateau (poster). In *Fall Meet. Suppl. Abstract C31A-0282*. Eos Trans. AGU.
- Armstrong, R., Chang, A., Rango, A., and Josberger, E. (1993). Snow depths and grain-size relationships with relevance for passive microwave studies. *Annals of Glaciology*, 17:171–176.
- Armstrong, R. L. and Brodzik, M. J. (2001). Recent Northern hemisphere snow extent: a comparison of data derived from visible and microwave satellite sensors. *Geophysical Research Letters*, 28(19):3673–3676.
- Bagnoud, N., Pitman, A., McAveney, B., and Holbrook, N. (2005). The contribution of the land surface energy balance complexity to differences in means, variances and extremes using the AMIP-II methodology. *Climate Dynamics*, 25:171–188.

- 
- Bamzai, A. and Shukla, J. (1999). Relation between Eurasian snow cover, snow depth and the Indian summer monsoon: an observational study. *Journal of Climate*, 12:3117–3132.
- Bjornsson, H. and Venegas, S. (1997). A manual for EOF and SVD analysis of climatic data. Technical report, McGill University, CCGCR Report No. 97-1, Montreal, Qubec, 52pp.
- Blanford, H. (1884). On the connection of the Himalaya snowfall with dry winds and seasons of drought in India. *Proceedings of the Royal Society, London*, 37:3–22.
- Boone, A., Mognard, M., Decharme, B., Douville, H., Grippa, M., and Kerrigan, K. (2006). The impact of simulated soil temperatures on the estimation of snow depth over Siberia from SSM/I compared to a multi-model climatology. *Remote Sensing of Environment*, 101:482–494.
- Bowling, L., Lettenmaier, D., Nijssen, B., Graham, L., Clark, D., El Maayar, M., Essery, R., Goers, S., Gusev, Y., Habets, F., van den Hurk, B., Jin, J., Kahan, D., Lohmann, D., Ma, X., Mahanama, S., Mocko, D., Nasonova, O., Niu, G.-Y., Samuelsson, P., Shmakin, A., Takata, K., Versegny, D., Viterbo, P., Xia, Y., Xue, Y., and Yang, Z.-L. (2003a). Simulation of high-latitude hydrological processes in the Torne-Kalix basin: PILPS phase 2(e) 1: Experiment description and summary intercomparisons. *Global and Planetary Change*, 38:1–30.
- Bowling, L., Lettenmaier, D., Nijssen, B., Polcher, J., Koster, R., and Lohmann, D. (2003b). Simulation of high-latitude hydrological processes in the torne-kalix basin: Pilps phase 2(e) 3: Equivalent model representation and sensitivity experiments. *Global and Planetary Change*, 38:55–71.
- Brasnett, B. (1999). A global analysis of snow depth for numerical weather prediction. *Journal of Applied Meteorology*, 38:762–740.
- Brodzik, M. and Knowles, K. (2002). EASE-grid: a versatile set of equal-area projections and grids. In *Discrete Global Grids*. Santa Barbara, CA, USA: National Center for Geographic Information & Analysis. [http://www.ncgia.ucsb.edu/globalgrids-book/ease\\_grid/](http://www.ncgia.ucsb.edu/globalgrids-book/ease_grid/).
- Brown, R., Brasnett, B., and Robinson, D. (2003). Gridded North American monthly snow depth and snow water equivalent for GCM evaluation. *Atmosphere-Ocean*, 41:1–14.

- 
- Brown, R. and Frei, A. (2007). Comment on “Evaluation of surface albedo and snow cover in AR4 coupled models by a. roesch”. *Journal of Geophysical Research*, 112:doi:10.1029/2006JD008339.
- Brown, R. and Mote, P. (2008). The response of Northern hemisphere snow cover to a changing climate. Submitted to *Journal of Climate*.
- Brown, R. D. (2000). Northern hemisphere snow cover variability and change, 1915 - 1997. *Journal of Climate*, 13:2339–2355.
- Carroll, T., Cline, D., Berkowitz, E., and Savage, D. (2003). Snow economics and the NOHRSC snow information system (SNOW-INFO) for the united states. In *European Geophysical Union General Assembly, Vienna*.
- Cess, R., Potter, G., Zhang, M.-H., Blanchet, J., Chalita, S., , Colman, R., Dazlich, D., Genio, A. D., Dymnikov, V., Galin, V., Jerrett, D., Keup, E., Lacis, A., Treut, H. L., Liang, X.-Z., Mahfouf, J.-F., McAveney, B., Meleshko, V., Mitchell, J., Morcrette, J.-J., Norris, P., Randall, D., Rikus, L., Roeckner, E., Royer, J.-F., Schlese, U., Sheinin, D., Slingo, J., Sokolov, A., Taylor, K., Washington, W., Wetherald, R., and Yagai, I. (1991). Interpretation of snow-climate feedback as produced by 17 general circulation models. *Science*, 253(5022):888–892.
- Chang, A., Foster, J., and Hall, D. (1987). Nimbus-7 derived global snow cover parameters. *Annals of Glaciology*, 9:39–44.
- Chang, A., Kelly, R., Josberger, E., Armstrong, R., Foster, J., and Mognard, N. (2005). Analysis of ground-measured and passive-microwave-derived snow depth variations in midwinter across the northern Great Plains. *Journal of Hydrometeorology*, 6:20–33.
- Chen, C.-T., Nijssen, B., Guo, J., Tsang, L., Wood, A., Hwang, J.-N., and Lettenmaier, D. (2001). Passive microwave remote sensing of snow constrained by hydrological simulations. *IEEE Transactions on Geoscience and Remote Sensing*, 39:1744–1756.
- Cherry, J., Tremblay, L., Dery, S., and Stieglitz, M. (2005). Reconstructing solid precipitation from snow depth measurements and a land surface model. *Water Resources Research*, 41:doi:10.1029/2005WR003965.
- Clark, M., Serreze, M., and McCabe, G. (2001). Historical effects of El Nino and La Nina events on the seasonal evolution of the montane snowpack in the Columbia and Colorado river basins. *Water Resources Research*, 37:741–757.
-

- Clark, M. and Serreze, M.C. and Robinson, D. (1999). Atmospheric controls on Eurasian snow extent. *International Journal of Climatology*, 19:27–40.
- Clark, M. and Serreze, M. (2000). Effects of variations in east Asian snow cover on modulating atmospheric circulation over the North Pacific ocean. *Journal of Climate*, 13:3700–3710.
- Cohen, J., Barlow, M., Kushner, P., and Saito, K. (2007). Stratosphere-troposphere coupling and links with Eurasian land surface variability. *Journal of Climate*, 20:5335–5343.
- Cohen, J. and Entekhabi, D. (1999). Eurasian snow cover variability and Northern hemisphere climate predictability. *Geophysical Research Letters*, 26(3):345–348.
- Collins, M. and Allen, M. R. (2002). Assessing the relative roles of initial and boundary conditions in interannual to decadal climate predictability. *Journal of Climate*, 15:3104–3109.
- Collins, M., Booth, B. B., Harris, G., Murphy, J., Sexton, D., and Webb, M. (2006). Towards quantifying uncertainty in transient climate change. *Climate Dynamics*, 27:127:147.
- Collins, M., Tett, S., and Cooper, C. (2001). The internal climate variability of HadCM3, a version of the Hadley Centre coupled model without flux adjustments. *Climate Dynamics*, 17:61–81.
- Covey, C., AchutaRao, K., Cubasch, U., Jones, P., Lambert, S., Mann, M., Phillips, T., and Taylor, K. (2003). An overview of results from the Coupled Model Intercomparison Project (CMIP). *Global and Planetary Change*, 37:103–133.
- Cox, P., Betts, R., Bunton, C., Essery, R., Rowntree, P., and Smith, J. (1999). The impact of new land surface physics on the GCM simulation of climate and climate sensitivity. *Climate Dynamics*, 15:183–203.
- Dai, A., Fung, I., and Del Genio, A. (1997). Surface observed global land precipitation variations during 1900–88. *Journal of Climate*, 10:2943–2962.
- Derksen, C., Brown, R., and Walker, A. (2004). Merging conventional (1915–92) and passive microwave (1978–2002) estimates of snow extent and water equivalent over central North America. *Journal of Hydrometeorology*, 5:850–861.

- 
- Derksen, C. and LeDrew, E. (2000). Temporal and spatial variability of North American prairie snow cover (1988-1995) inferred from passive microwave-derived snow water equivalent imagery. *Water Resources Research*, 36:255–266.
- Derksen, C. and MacKay, M. (2006). The Canadian boreal snow water equivalent band. *Atmosphere-Ocean*, 44:305–320.
- Derksen, C., Misurak, K., LeDrew, E., Piwowar, J., and Goodison, B. (1997). Relationship between snow cover and atmospheric circulation, central North America, winter 1988. *Annals of Glaciology*, 25:347–352.
- Derksen, C., Walker, A., and Goodison, B. (2005). Evaluation of passive microwave snow water equivalent retrievals across the boreal forest/tundra transition of western Canada. *Remote Sensing of Environment*, 96:315–327.
- Derksen, C., Walker, A., LeDrew, E., and Goodison, B. (2002). Time-series analysis of passive-microwave-derived central North American snow water equivalent imagery. *Annals of Glaciology*, 34:1–7.
- Derksen, C. and Walker, A. E. (2003). Identification of systematic bias in the cross-platform (SMR and SSM/I) EASE-Grid brightness temperature time series. *IEEE Transactions on Geoscience and Remote Sensing*, 41(4):910–915.
- Deser, C. (2000). On the teleconnectivity of the “Arctic Oscillation”. *Geophysical Research Letters*, 27:779–782.
- Dirmeyer, P. A. (2005). The land surface contribution to the potential predictability of boreal summer season climate. *Journal of Hydrometeorology*, 6:618–632.
- Domine, F., Salvatori, R., Legagneux, L., Salzano, R., Fily, M., and Casacchia, R. (2006). Correlation between the specific surface area and the short wave infrared (SWIR) reflectance of snow. *Cold Regions Science and Technology*, 46(1):60–68.
- Dommenget, D. and Latif, M. (2002). A cautionary note on the interpretation of EOFs. *Journal of Climate*, 15:216–225.
- Dong, J., Walker, J., Houser, P., and Sun, C. (2007). Scanning multichannel microwave radiometer snow water equivalent assimilation. *Journal of Geophysical Research*, 112:doi:10.1029/2006JD007209.
- Dong, J., Walker, J. P., and Houser, P. R. (2005). Factors affecting remotely sensed snow water equivalent uncertainty. *Remote Sensing of Environment*, 97:68–82.
-

- 
- Dumenil Gates, L., Hagemann, S., and Golz, C. (2000). Observed historical discharge data from major rivers for climate model validation. Technical report, Max-Planck-Institut für Meteorologie, Hamburg.
- Dye, D. (2002). Variability and trends in the annual snow-cover cycle in Northern hemisphere land areas, 1972-2000. *Hydrological Processes*, 16:3065–3077.
- Entekhabi, D., Asrar, G., Betts, A., Beven, K., Bras, R., Duffy, C., Dunne, T., Koster, R., Lettenmaier, D., McLaughlin, D., Shuttleworth, W., van Genuchten, M., Wei, M.-Y., and Wood, E. (1999). An agenda for land surface hydrology research and a call for the second international hydrological decade. *Bulletin of the American Meteorological Society*, 80:2043–2058.
- Essery, R. (1998). Boreal forests and snow in climate models. *Hydrological Processes*, 12:1561–1567.
- Essery, R., Best, M., Betts, R., Cox, P., and Taylor, C. (2003). Explicit representation of subgrid heterogeneity in a GCM land surface scheme. *Journal of Hydrometeorology*, 4:530–543.
- Essery, R., Blyth, E., Harding, R., and Lloyd, C. (2005). Modelling albedo and distributed snowmelt across a low hill in Svalbard. *Nordic Hydrology*, 36:207:218.
- Etchevers, P. e. a. (2004). Validation of the energy budget of an alpine snow pack simulated by several snow models (SnowMIP project). *Annals of Glaciology*, 38:150–158.
- Falloon, P. and Betts, R. (2007). Validation of river flows in HadGEM1 and HadCM3 with the TRIP river flow model. Submitted to Journal of Hydrology.
- Fasullo, J. (2004). A stratified diagnosis of the Indian Monsoon-Eurasian snow cover relationship. *Journal of Climate*, 17:1110–1122.
- Fletcher, C., Kushner, P., and Cohen, J. (2007). Stratospheric control of the extratropical circulation response to surface forcing. *Geophysical Research Letters*, 34:doi:10.1029/2007GL031626.
- Foster, D. and Davy, R. (1988). Global snow depth climatology. USAF Publ. USAFETAC/TN-88/006. U.S. Air Force Environ. Tech. Appl. Cent., Scott Air Force Base, Ill.
- Foster, J. and Chang, A. (1993). *Atlas of satellite observations related to global change*, chapter 7, pages 361–370. Cambridge University Press.

- 
- Foster, J., Chang, A., and Hall, D. (1997). Comparison of snow mass estimates from a prototype passive microwave snow algorithm, a revised algorithm and a snow depth climatology. *Remote Sensing of Environment*, 62:132–142.
- Foster, J., Hall, D., and Chang, A. (1987). Remote sensing of snow. *Eos, Transactions of the American Geophysical Union*, 68(32):682–684.
- Foster, J., Hall, D., Chang, A., Rango, A., Wergin, W., and Erbe, E. (1999). Effects of snow crystal shape on the scattering of passive microwave radiation. *IEEE Transactions on Geoscience and Remote Sensing*, 37:1165–1168.
- Foster, J., Liston, G., Koster, R., Essery, R., Behr, H., Dumenil, L., Verseghy, D., Thompson, S., pollard, D., and Cohen, J. (1996). Snow cover and snow mass intercomparisons of general circulation models and remotely sensed datasets. *Journal of Climate*, 9:409–426.
- Foster, J., Owe, M., and Rango, A. (1983). Snow cover and temperature relationships in North America and Eurasia. *Journal of Climate and Applied Meteorology*, 22:460–469.
- Foster, J. L., Sun, C., Walker, J. P., Kelly, R., Chang, A., Dong, J., and Powell, H. (2005). Quantifying the uncertainty in passive microwave snow water equivalent observations. *Remote Sensing of Environment*, 94:187–203.
- Frei, A., Brown, R., Miller, J. A., and Robinson, D. A. (2005). Snow mass over North America: observations and results from the second phase of the Atmospheric Model Intercomparison Project. *Journal of Hydrometeorology*, 6:681–695.
- Frei, A. and Gong, G. (2005). Decadal to century scale trends in North American snow extent in coupled atmosphere-ocean general circulation models. *Geophysical Research Letters*, 32:10.1029/2005GL023394.
- Frei, A., Miller, J. A., and Robinson, D. A. (2003). Improved simulations of snow extent in the second phase of the Atmospheric Model Intercomparison Project (AMIP-2). *Journal of Geophysical Research*, 108:10.1029/2002JD003030.
- Frei, A. and Robinson, D. (1999). Northern hemisphere snow extent: regional variability 1972-1994. *International Journal of Climatology*, 19:1535–1560.
- Frei, A. and Robinson, D. A. (1998). Evaluation of snow extent and its variability in the Atmospheric Model Intercomparison Project. *Journal of Geophysical Research*, 103:8859–8871.
-

- 
- Fukutomi, Y., Igarashi, H., Masuda, K., and Yasunari, T. (2003). Interannual variability of summer water balance components in three major river basins of northern Eurasia. *Journal of Hydrometeorology*, 4:283–296.
- Ge, Y. and Gong, G. (2008). Observed inconsistencies between snow extent and snow depth variability at regional/continental scales. *Journal of Climate*, 21:1066–1082.
- Gibson, J., Kallberg, P., Uppala, S., Nomura, A., Hernandez, A., and Serrano, E. (1997). ERA description. Technical report, European Centre for Medium-Range Weather Forecasts.
- Gong, G. and Entekhabi, D. (2002). A large-ensemble model study of the wintertime AO-NAO and the role of interannual snow perturbations. *Journal of Climate*, 15:3488–3499.
- Gong, G. and Entekhabi, D. (2003). Relative impacts of Siberian and North American snow anomalies on the winter Arctic Oscillation. *Geophysical Research Letters*, 30:doi:10.1029/2003GL017749.
- Gong, G., Entekhabi, D., and Cohen, J. (2003). Modeled Northern hemisphere winter climate response to realistic Siberian snow anomalies. *Journal of Climate*, 16:3917–3931.
- Gong, G., Entekhabi, D., Cohen, J., and Robinson, D. (2004). Sensitivity of atmospheric response to modeled snow anomaly characteristics. *Journal of Geophysical Research*, 109:doi:10.1029/2003JD004160.
- Goodison, B., Banga, A., and Halliday, R. (1984). Canada-United States prairie snow cover runoff study. *Canadian Water Resources Journal*, 9:99–107.
- Gordon, C., Cooper, C., Senior, C., Banks, H., Gregory, J., Johns, T., Mitchell, J., and Wood, R. (2000). The simulation of SST, sea ice extents and ocean heat transports in a version of the Hadley Centre coupled model without flux adjustments. *Climate Dynamics*, 16:147:168.
- Grippa, M., Mognard, N., and Le Toan, T. (2005). Comparison between the interannual variability of snow parameters derived from SSM/I and the Ob river discharge. *Remote Sensing of Environment*, 98:35–44.
- Grippa, M., Mognard, N., Le Toan, T., and Josberger, E. (2004). Siberia snow depth climatology derived from SSM/I data using a combined dynamic and static algorithm. *Remote Sensing of Environment*, 93:30–41.
-

- Groisman, P., Karl, T., Knight, R., and Stenchikov, G. (1994). Changes of snow cover, temperature and radiative heat balance over the Northern hemisphere. *Journal of Climate*, 7:1633–1656.
- Guntner, A., Stuck, J., Werth, S., Doll, P., Verzano, K., and Merz, B. (2007). A global analysis of temporal and spatial variations in continental water storage. *Water Resources Research*, 43:W05416.
- Gupta, R., Haritashya, U., and Singh, P. (2005). Mapping dry/wet snow cover in the Indian Himalayas using IRS multispectral imagery. *Remote Sensing of Environment*, 97:458–469.
- Hahn, D. and Shukla, J. (1976). An apparent relationship between Eurasian snow cover and Indian monsoon rainfall. *Journal of Atmospheric Science*, 33:2461–2462.
- Haines, K. (2007). ECMWF seminar series: Recent developments in the use of satellite observations in NWP. In *Ocean Data Assimilation, 3-7 Sept.*
- Haines, K., Hermanson, L., Liu, C., Putt, D., Sutton, R., Iwi, A., and Smith, D. (2008). Decadal Climate Prediction (project GCEP). Submitted to Philosophical Transactions of the Royal Society A.
- Hall, D., Foster, J., Salomonson, V., Klein, A., and Chien, J. (2001). Development of a technique to assess snow-cover mapping errors from space. *IEEE Transactions on Geoscience and Remote Sensing*, 39:432–438.
- Hall, D., Kelly, R., Riggs, G., Chang, A., and Foster, J. (2002). Assessment of the relative accuracy of hemispheric-scale snow-cover maps. *Annals of Glaciology*, 34:24–30.
- Hamlet, A., Mote, P., Clark, M., and Lettenmaier, D. (2005). Effects of temperature and precipitation variability on snowpack trends in the western United States. *Journal of Climate*, 18:4545–4561.
- Hermanson, L. and Sutton, R. (2008). Climate predictability in the second year. Submitted to Philosophical Transactions of the Royal Society A.
- Jin, J., Miller, N., Sorooshian, S., and Gao, X. (2006). Relationship between atmospheric circulation and snowpack in the western USA. *Hydrological Processes*, 20:753–767.

- 
- Jones, H., Pomeroy, J., Walker, D., Hoham, R., Aitchison, C., Begin, Y., Billings, W., Boivin, S., Brun, E., Davies, T. D., Duval, B., Groisman, P. Y., de Molenaar, J., Tranter, M., and Zlotin, R. I. (2001). *Snow Ecology*. Cambridge University Press.
- Josberger, A. and Mognard, M. (2002). A passive microwave snow depth algorithm with a proxy for snow metamorphism. *Hydrological Processes*, 16:1557–1568.
- Kalnay, E., Kanamitsu, M., Kistler, R., Collins, W., Deaven, D., Gandin, L., Iredell, M., Saha, S., White, G., Woollen, J., Zhu, Y., Leetmaa, A., Reynolds, B., Chelliah, M., Ebisuzaki, W., Higgins, W., Janowiak, J., Mo, K., Ropelewski, C., Wang, J., Jenne, R., and Joseph, D. (1996). The NCEP/NCAR 40-year reanalysis project. *Bulletin of the American Meteorological Society*, 77(3):437–471.
- Kanamitsu, M., Ebisuzaki, W., Woollen, J., Yang, S.-K., Hnilo, J., Fiorino, M., and Potter, G. (2002). NCEP-DEO AMIP-II Reanalysis (R-2). *Bulletin of the American Meteorological Society*, 83(11):1631–1643.
- Kelly, R., Chang, A., Tsang, L., and Foster, J. (2003). A prototype AMSR-E global snow area and snow depth algorithm. *IEEE Transactions on Geoscience and Remote Sensing*, 41:230–242.
- Kitaev, L., Forland, E., Razuvaev, V., Tveito, O., and Krueger, O. (2005). Distribution of snow cover over northern Eurasia. *Nordic Hydrology*, 36(4-5):311–319.
- Koenig, L. and Forster, R. (2004). Evaluation of passive microwave snow water equivalent algorithms in the depth hoar-dominated snowpack of the Kuparuk River Watershed, Alaska, USA. *Remote Sensing of Environment*, 93:511–527.
- Koster, R., Dirmeyer, P., Hahmann, A., Ijpelaar, R., Tyahla, L., Cox, P., and Suarez, M. (2002). Comparing the degree of land-atmosphere interaction in four atmospheric general circulation models. *Journal of Hydrometeorology*, 3:363–375.
- Krenke, A. (1998, updated 2004). Former Soviet Union hydrological snow surveys, 1966-1996. Digital media. Edited by NSIDC. Boulder, CO: National Snow and Ice Data Center/World Data Center for Glaciology.
- Kripalani, R. and Kulkarni, A. (1999). Climatology and variability of historical Soviet snow depth data: some new perspectives in snow-Indian monsoon teleconnections. *Climate Dynamics*, 15:475–489.
- Langlois, A., Royer, A., Fillol, E., and Laprise, R. (2004). Evaluation of the snow cover variation in the Canadian Regional Climate Model over eastern Canada using passive microwave satellite data. *Hydrological Processes*, 18:1127–1138.

- 
- Latif, M., Anderson, D., Barnett, T., Cane, M., Kleeman, R., Leetma, A., O'Brien, J., Rosati, A., and Schneider, E. (1998). A review of the predictability and prediction of ENSO. *Journal of Geophysical Research*, 103:14375–14393.
- Latif, M., Sterl, A., Maier-Reimer, E., and Junge, M. (1993). Structure and predictability of the El Niño/Southern Oscillation phenomenon in a coupled ocean-atmosphere general circulation model. *Journal of Climate*, 6:700–708.
- Leathers, D. and Robinson, D. (1993). The association between extremes in North American snow cover extent and United States temperatures. *Journal of Climate*, 6:1345–1355.
- Liston, G. and Elder, K. (2006). A distributed snow-evolution modeling system (SnowModel). *Journal of Hydrometeorology*, 7:1259–1276.
- Loveland, T. R., Reed, B. C., Brown, J. F., Ohler, D. O., Zhu, J., and Yang, L. (2000). Development of a global land cover characteristics dataset. *International Journal of Remote Sensing*, 21:1303–1330.
- Mariotti, A. (2007). How ENSO impacts precipitation in southwest central Asia. *Geophysical Research Letters*, 34:doi:10.1029/2007GL030078.
- Marshall, S., Oglesby, R., and Nolin, A. (2003). The predictability of winter snow cover over the western United States. *Journal of Climate*, 16:1062–1073.
- Matson, M. and Wiesnet, D. (1981). A new data base for climate studies. *Nature*, 289:451–456.
- Mognard, N. and Josberger, E. (2002). Northern Great Plains 1996/7 seasonal evolution of snowpack parameters from satellite passive-microwave measurements. *Annals of Glaciology*, 34:15–23.
- Neale, R. and Slingo, J. (2003). The maritime continent and its role in the global climate: a GCM study. *Journal of Climate*, 16:834–848.
- Palmer, T., Alessandri, A., Andersen, U., Cantelaube, P., Davey, M., Delecuse, P., Deque, M., Diez, E., Doblas-Reyes, F., Feddersen, H., Graham, R., Gualdi, S., Gueremy, J.-F., Hagedorn, R., Hoshen, M., Keenlyside, N., Latif, M., Lazar, A., Maisonnave, E., Marletto, V., Morse, A., Orfila, B., Rogel, P., Terres, J.-M., and Thomson, M. (2004). Development of a European multi-model ensemble system for seasonal to inter-annual prediction (DEMETER). *Bulletin of the American Meteorological Society*, 85:853–872.
-

- 
- Parde, M., Goita, K., and Royer, A. (2007). Inversion of a passive microwave snow emission model for water equivalent estimation using airborne and satellite data. *Remote Sensing of Environment*, 111:346–356.
- Pulliainen, J. (2006). Mapping of snow water equivalent and snow depth in boreal and sub-arctic zones by assimilating space-borne microwave radiometer data and ground-based observations. *Remote Sensing of Environment*, 101:257–269.
- Pulliainen, J. and Hallikainen, M. (2001). Retrieval of regional snow water equivalent from space-borne passive microwave observations. *Remote Sensing of Environment*, 75:76–85.
- Randall, D., Wood, R., Bony, S., Colman, R., Fichefet, T., Fyfe, J., Kattsov, V., Pitman, A., Shukla, J., Srinivasan, J., Stouffer, R., Sumi, A., and Taylor, K. (2007). Climate models and their evaluation. In *Climate Change 2007: The physical science basis. Contribution of working group 1 to the fourth assessment report of the intergovernmental panel on climate change*. Cambridge University Press, Cambridge, UK and New York, NY, USA.
- Reichler, T. and Kim, J. (2008). Uncertainties in the climate mean state of global observations, reanalyses, and the GFDL climate model. *Journal of Geophysical Research*, 113:doi:10.1029/2007JD009278.
- Rikiishi, K., Hashiya, E., and Imai, M. (2004). Linear trends of the length of snow-cover season in the Northern hemisphere as observed by the satellites in the period 1972-2000. *Annals of Glaciology*, 38:229–237.
- Robock, A., Mu, M., Vinnikov, K., and Robinson, D. (2003). Land surface conditions over Eurasia and Indian summer monsoon rainfall. *Journal of Geophysical Research*, 108:doi:10.1029/2002JD002286.
- Rodell, M. and Houser, P. (2004). Updating a land surface model with MODIS-derived snow cover. *Journal of Hydrometeorology*, 5:1064–1075.
- Ropelewski, C. and Bell, M. (2008). Shifts in the statistics of daily rainfall in South America conditional on ENSO phase. *Journal of Climate*, 21:849–865.
- Schlosser, C. and Mocko, D. (2003). Impact of snow conditions on spring dynamical seasonal predictions. *Journal of Geophysical Research*, 108:doi:10.1029/2002JD003113.
- Sellers, P., Hall, F., Kelly, R., Black, A., Baldocchi, D., Berry, J., Ryan, M., Ranson, K., Crill, P., Lettenmaier, D., Margolis, H., Cihlar, J., Newcomer, J., Fitzjarrald,

- 
- D., Jarvis, P., Gower, S., Halliwell, D., Williams, D., Goodison, B., Wickland, D., and Guertin, F. (1997). BOREAS in 1997: experiment overview, scientific results and future directions. *Journal of Geophysical Research*, 102:28731–28770.
- Slater, A., Schlosser, C., Desborough, C., Pitman, A., Henderson-Sellers, A., Robock, A., Vinnikov, K., Mitchell, K., Boone, A., Braden, H., Chen, F., Cox, P., de Rosnay, P., Dickinson, R., Dai, Y.-J., uan, Q., Entin, J., Etchevers, P., Gedney, N., Gusev, Y., Habets, F., Kim, J., Koren, V., Kowalczyk, A., Nasonova, O., Noilhan, J., Schaake, S., Shmakin, A., Smirnova, T., Verseghy, D., Wetzell, P., Xue, Y., Yang, Z.-L., and Zeng, Q. (2001). The representation of snow in land surface schemes: results from PILPS 2(d). *Journal of Hydrometeorology*, 2:7–25.
- Slingo, J., Guilyardi, E., Hodges, K., Hoskins, B., Inness, P., Lawrence, D., Neale, R., Osborne, T., Spencer, H., and Yang, G.-Y. (2003). *How good is the Hadley Centre climate model? Research at CGAM in identifying and understanding model systematic errors: 1999-2002*. Hadley Centre.
- Smith, D., Cusack, S., Colman, A., Folland, C., Harris, G., and Murphy, J. (2007). Improved surface temperature prediction for the coming decade from a global climate model. *Science*, 317:796–799.
- Smith, D. and Murphy, J. (2007). An objective ocean temperature and salinity analysis using covariances from a global climate model. *Journal of Geophysical Research*, 112:doi:10.1029/2005JC003172.
- Sobolowski, S., Gong, G., and Ting, M. (2007). Northern hemisphere winter climate variability: response to North American snow cover anomalies and orography. *Geophysical Research Letters*, 34.
- Stockdale, T. (1997). Coupled ocean-atmosphere forecasts in the presence of climate drift. *Monthly Weather Review*, 125:809–818.
- Strack, J., Liston, G., and Pielke, R. (2004). Modelling snow depth for improved simulation of snow-vegetation-atmosphere interactions. *Journal of Hydrometeorology*, 5:723–734.
- Sturm, M., Holmgren, J., and Liston, G. (1995). A seasonal snow cover classification system for local to global applications. *Journal of Climate*, 8:1261–1283.
- Su, F., Adam, J., Bowling, L., and Lettenmaier, D. (2005). Streamflow simulations of the terrestrial Arctic domain. *Journal of Geophysical Research*, 110:doi:10.1029/2004JD005518.
-

- 
- Sun, C., Walker, J., and Houser, P. (2004). A methodology for snow data assimilation in a land surface model. *Journal of Geophysical Research*, 109:10.1029/2003JD003765.
- Tapley, B., Bettadpur, S., Watkins, M., and Reigber, C. (2004). The gravity recovery and climate experiment: Mission overview and early results. *Geophysical Research Letters*, 31:doi:10.1029/2004GL019920.
- Trujillo, E., Ramirez, J., and Elder, K. (2007). Topographic, meteorologic and canopy controls on the scaling characteristics of the spatial distribution of snow depth fields. *Water Resources Research*, 43(7):409.
- Turner, A., Inness, P., and Slingo, J. (2005). The role of the basic state in the ENSO-monsoon relationship and implications for predictability. *Quarterly Journal of the Royal Meteorological Society*, 131:781–804.
- Uppala, S., Kallberg, P., Simmons, A., Andrae, U., Da Costa Bechtold, V., Fiorino, M., Gibson, J., Haseler, J., Hernandez, A., Kelly, G., Li, X., Onogi, K., Saarinen, S., Sokka, N., Allan, R., Andersson, E., Arpe, K., Balmaseda, M., Beljaars, A., Van De Berg, L., Bidlot, J., Bormann, N., Caires, S., Chevallier, F., Dethof, A., Dragosavac, M., Fisher, M., Fuentes, M., Hagemann, S., Holm, E., Hoskins, B., Isaksen, L., Janssen, P., Jenne, R., McNally, A., Mahfouf, J.-F., Morcrette, J.-J., Rayner, N., Saunders, R., Simon, P., Sterl, A., Trenberth, K., Untch, A., Vasiljevic, D., Viterbo, P., and Woollen, J. (2005). The ERA-40 re-analysis. *Quarterly Journal of the Royal Meteorological Society*, 131:2961–3012.
- van den Hurk, B., Viterbo, P., Beljaars, A., and Betts, A. (2000). Offline validation of the ERA40 surface scheme. Technical report, European Centre for Medium-Range Weather Forecasts.
- Viterbo, P. and Betts, A. (1999). Impact on ECMWF forecasts of changes to the albedo of the boreal forests in the presence of snow. *Journal of Geophysical Research*, 104:27803–27810.
- Walker, G. (1910). On the meteorological evidence for supposed changes of climate in India. *Mem. Indian Meteor.*, 21:1–21.
- Walker, J., Houser, P., and Reichle, R. (2003). New remote sensing technologies require advances in hydrologic data assimilation. *Eos, Transactions of the American Geophysical Union*, 84:545–551.
- Wallace, J. (2000). North Atlantic Oscillation/annular mode: two paradigms - one phenomenon. *Quarterly Journal of the Royal Meteorological Society*, 126:791–805.
-

- Wang, J. and Tedesco, M. (2007). Identification of atmospheric influences on the estimation of snow water equivalent from AMSR-E measurements. *Remote Sensing of Environment*, 111:398–408.
- Xie, P. and Arkin, P. (1997). Global precipitation: A 17-year monthly analysis based on gauge observations, satellite estimates, and numerical model outputs. *Bulletin of the American Meteorological Society*, 78:2539–2558.
- Yang, D., Kane, D., Hinzman, L., Zhang, X., Zhang, T., and Ye, H. (2002). Siberian Lena river hydrologic regime and recent change. *Journal of Geophysical Research*, 107:doi:10.1029/2002JD002542.
- Yang, D., Zhao, Y., Armstrong, R., Robinson, D., and Brodzik, M.-J. (2007). Streamflow response to seasonal snow cover mass changes over large Siberian watersheds. *Journal of Geophysical Research*, 112:doi:10.1029/2006JF000518.
- Yang, F., Kumar, A., Wang, W., Juang, H.-M. H., and Kanamitsu, M. (2001). Snow-albedo feedback and seasonal climate variability over North America. *Journal of Climate*, 14:4245–4248.
- Yang, Z.-L., Dickinson, R., Hahmann, A., Niu, G.-Y., Shaikh, M., Gao, X., Bales, R., Sorooshian, S., and Jin, J. (1999). Simulation of snow mass and extent in general circulation models. *Hydrological Processes*, 13:2097–2113.
- Zhu, C., Lettenmaier, D., and Cavazos, T. (2005). Role of antecedent land surface conditions on North American Monsoon rainfall variability. *Journal of Climate*, 18:3104–3121.